

On the Properties and Design of Organic Light-Emitting Devices

A DISSERTATION
SUBMITTED TO THE FACULTY OF THE GRADUATE SCHOOL
OF THE UNIVERSITY OF MINNESOTA
BY

Nicholas C. Erickson

IN PARTIAL FULFILLMENT OF THE REQUIREMENTS
FOR THE DEGREE OF
DOCTOR OF PHILOSOPHY

Russell. J. Holmes, Advisor

17 January 2014

© Nicholas C. Erickson 2014

Acknowledgements

I would like to thank my research advisor, Prof. Russell J Holmes for his expert direction and support of my development as a scientist and my research work. I would like to thank the Holmes research group members, past and present, for challenging and supporting me.

I would like to thank my parents for their constant support of my academics and for encouraging me to find balance.

Finally, I would like to thank my wife for her unwavering support; without her, none of this would have been possible.

X-ray reflectivity measurements in this thesis were carried out by Dr. M. Manno in the Characterization Facility, University of Minnesota, which receives partial support from NSF through the MRSEC program.

Dedication

To my wife.

Abstract

Organic light-emitting devices (OLEDs) are attractive for use in next-generation display and lighting technologies. In display applications, OLEDs offer a wide emission color gamut, compatibility with flexible substrates, and high power efficiencies. In lighting applications, OLEDs offer attractive features such as broadband emission, high-performance, and potential compatibility with low-cost manufacturing methods. Despite recent demonstrations of near unity internal quantum efficiencies (photons out per electron in), OLED technology adoption lags conventional counterparts, particularly in large-area display and general lighting applications.

This thesis seeks to understand the optical and electronic properties of OLED materials and device architectures which lead to not only high peak efficiency, but also reduced device complexity, high efficiency under high excitation, and optimal white-light emission. This is accomplished through the careful manipulation of organic thin film compositions and the introduction of a novel device architecture, the graded-emissive layer (G-EML). This device architecture offers a unique platform to study the electronic properties of varying compositions of organic semiconductors.

This thesis also introduces an experimental technique to measure the spatial overlap of electrons and holes within an OLED's emissive layer. This overlap is an important parameter which is affected by the choice of materials and device design, and greatly impacts the operation of the OLED, particularly at high excitation densities. Overall this thesis relies on a careful understanding of materials properties, and their connection to device operation, to design novel organic light-emitting devices.

Table of Contents

Chapter 1	A Review of the Optical and Electronic Properties of Organic Semiconducting Materials	1
1.1	What is an Organic Semiconductor?	1
1.2	What is an Organic Thin Film?	2
1.3	Character of the Excited State	3
1.3.1	<i>Singlet and Triplet Excitons</i>	4
1.3.2	<i>Electronic Transitions in Organic Semiconductors</i>	5
1.3.3	<i>Fluorescence</i>	8
1.3.4	<i>Phosphorescence</i>	9
1.4	Energy Transfer and Exciton Diffusion	11
1.4.1	<i>Cascade Energy Transfer</i>	12
1.4.2	<i>Förster Energy Transfer</i>	12
1.4.3	<i>Dexter Energy Transfer</i>	14
1.4.4	<i>Exciton Diffusion</i>	15
1.5	Charge Transport in Organic Semiconductors	15
1.5.1	<i>Band Transport</i>	16
1.5.2	<i>Hopping Transport</i>	17
Chapter 2	Introduction to Organic Light-Emitting Devices	19
2.1	Thin Film and Device Fabrication	19
2.1.1	<i>Vacuum Thermal Evaporation</i>	20
2.1.2	<i>Formation of Cathode</i>	23
2.1.3	<i>Complete OLED Fabrication Process</i>	25
2.2	OLED Characterization and Data Analysis	25
2.2.1	<i>Units of Optical Output in OLEDs</i>	25
2.2.2	<i>External Quantum Efficiency</i>	28
2.2.3	<i>Power Efficiency</i>	32
2.2.4	<i>Measurement and Calculation of Device Parameters</i>	32
2.3	Basic OLED Operation and Design	35
2.3.1	<i>The First OLED</i>	36
2.3.2	<i>The Use of an Emissive Guest</i>	38
2.3.3	<i>Achieving Broadband Emission</i>	39
2.3.4	<i>Multilayer OLED Operation</i>	39
2.3.5	<i>Typical Device Operation</i>	40
2.3.6	<i>Requirements for High-Efficiency OLEDs</i>	42
2.3.7	<i>White-Light Emitting OLEDs</i>	44
2.3.8	<i>State of the Art</i>	46
2.4	Overview of This Thesis	46

Chapter 3	Graded Composition Emissive Layer Light-Emitting Devices.....	48
3.1	Evolution of OLED Architectures.....	48
3.2	Graded-Composition Emissive Layer.....	49
3.3	Optimizing Red G-EML OLEDs.....	56
3.3.1	<i>Red-Light Emitting G-EML OLEDs for Display Applications.....</i>	<i>57</i>
3.3.2	<i>Red-Light Emitting G-EML OLEDs for Lighting Applications.....</i>	<i>59</i>
3.4	Optimizing Blue G-EML OLEDs.....	60
3.4.1	<i>Blue Light-Emitting Devices with TPBi as an ETL.....</i>	<i>62</i>
3.4.2	<i>Blue Light-Emitting Devices with 3TPYMB as an ETL.....</i>	<i>64</i>
3.4.3	<i>Multilayer FIrpic-Based OLEDs.....</i>	<i>65</i>
3.5	Conclusion.....	67
Chapter 4	Depth Profiling.....	68
4.1	X-Ray Photoelectron Spectroscopy.....	70
4.2	Experimental Techniques.....	70
4.3	XPS Study of Host Materials.....	71
4.4	Depth Profiling of OLED Architectures.....	74
4.4.1	<i>Resolution of the Unique Identification of TCTA and BPhen.....</i>	<i>74</i>
4.4.2	<i>Characterization of the Mixed-Emissive Layer.....</i>	<i>75</i>
4.4.3	<i>Characterization of the Graded-Emissive Layer.....</i>	<i>76</i>
4.5	Conclusion.....	78
Chapter 5	Electronic Properties of G-EML OLEDs.....	80
5.1	Measurement of the Charge Carrier Mobility.....	80
5.2	Single-Carrier Experimental Design.....	81
5.3	Optimized Red- and Green-Emitting Devices.....	83
5.3.1	<i>Performance of Red- and Green-Emitting G-EML OLEDs.....</i>	<i>83</i>
5.3.2	<i>Charge Transport in Green and Red G-EML OLEDs.....</i>	<i>85</i>
5.4	Optimized Blue-Light Emitting Devices.....	91
5.4.1	<i>Performance of Blue Light-Emitting G-EML devices.....</i>	<i>91</i>
5.5	Conclusions.....	94
Chapter 6	Measurement of the Recombination Zone of Organic Light-Emitting Devices.....	96
6.1	Conventional Methods to Measure the Recombination Zone.....	98
6.2	Sensing Excitons via Energy Transfer.....	100
6.2.1	<i>Theory of Exciton Sensitization.....</i>	<i>101</i>
6.2.2	<i>Theory of the Electronic Model of G-EML OLEDs.....</i>	<i>104</i>
6.3	Experimental Methods.....	108
6.4	Measurements of the Exciton Recombination Zone.....	109
6.5	Electronic Model of G-EML OLEDs.....	115

6.6	Impact of Recombination Zone on Efficiency Roll-Off.....	118
6.7	Conclusions and Acknowledgments.....	119
Chapter 7 Engineering Efficiency Roll-Off in Organic Light-Emitting Devices.....		121
7.1	Density-Driven Exciton Quenching Processes.....	121
7.2	Experimental Design.....	123
	7.2.1 <i>Device Architectures of Interest</i>	123
	7.2.2 <i>Device Fabrication and Test Film Design</i>	125
7.3	Characterizing Triplet-Triplet Annihilation.....	126
7.4	Characterizing Triplet-Polaron Quenching.....	128
7.5	Predicting Efficiency Roll-Off in OLEDs.....	130
	7.5.1 η_{EQE} Predictions for D-EML and G-EML Devices.....	130
	7.5.2 Transient Electroluminescence of D-EML and G-EML Devices.....	133
	7.5.3 η_{EQE} Predictions for Large-Recombination Zone G-EML Devices.....	135
7.6	Conclusions.....	137
Chapter 8 Optical Modeling of OLEDs.....		138
8.1	Theory of Optical Fields in OLEDs.....	138
	8.1.1 <i>Transfer-Matrix Model of Optical Electric Fields</i>	138
	8.1.2 <i>Dipole Emission within OLEDs</i>	141
8.2	Optical Modeling Results for D-, M-, and G-EML OLEDs.....	142
	8.2.1 <i>Optical Electric Field Results</i>	142
	8.2.2 <i>Predictions of Outcoupling Efficiency</i>	143
8.3	Summary.....	146
Chapter 9 Single-Dopant, Single-Layer White Light-Emitting OLEDs.....		147
9.1	Simultaneous Monomer and Excimer Emission.....	147
9.2	Pt-17 in Single-Layer G-EML Devices.....	149
	9.2.1 <i>G-EML Devices with Pt-17</i>	149
	9.2.2 <i>G-EML Devices with 10 wt. % Pt-17</i>	151
	9.2.3 <i>Summary of Pt-17 Performance in G-EML Devices</i>	152
9.3	Conclusions.....	155
Chapter 10 Future Research Directions.....		156
10.1	Summary of This Thesis.....	156
10.2	Simple, High-Quality White OLEDs.....	157
10.3	Understanding Device Operating Lifetimes.....	163
	10.3.1 <i>Characterizing Degradation-Induced Exciton Quenching</i>	164
	10.3.2 <i>Characterizing Degradation-Induced loss of Charge Balance</i>	165
10.4	Mitigating Efficiency Roll-Off.....	166

10.4.1 <i>Extraordinary Recombination Zone Widths</i>	166
10.4.2 <i>Engineering Exciton Lifetime through Device Design</i>	166
Chapter 11 Bibliography	169
Appendix	177
A: List of Publications, Presentations, and Patents.....	177
B: G-EML Electronic Simulation Code.....	179
C: Optical Simulation Code.....	182
<i>Optical Field Simulation</i>	182
<i>Optical Emission and Outcoupling Simulation</i>	191
D: Copyright Notices.....	200

Chapter 1 - A Review of the Optical and Electronic Properties of Organic Semiconducting Materials

1.1 What is an organic semiconductor?

Organic materials are broadly classified as chemical compounds which contain carbon.¹ Virtually millions of compounds which fit this definition have been discovered. Those which are used in optical, electronic, and optoelectronic devices, however, typically show some semiconducting properties due to a chemical bonding scheme of alternating single and double bonds, termed *conjugation*. These organic semiconductors are further classified by molecular weight, those with ‘small’ molecular weights, $m_w < 1$ kg/mol, and those with larger molecular weights, which are typically polymers (chains of repeat molecular units). This work will focus on the use of small molecule organic semiconductors which are typically capable of sublimation or evaporation without degradation.

Conjugation in these molecules is the result of the hybridization of the carbon 2p and 2s electronic orbitals. Three sp^2 orbitals are formed with a single, unhybridized p_z orbital left over. This remaining p_z orbital is oriented out of the plane and may overlap with neighboring p_z orbitals, forming a π -bond and resulting in a delocalization of the electron cloud. The unhybridized p_z orbitals of the simple molecule benzene, chemical structure shown in Figure 1.1a, are shown in Figure 1.1b, with the resulting delocalized π -bond shown in Figure 1.1c. The overlapping π -bonds in a conjugated molecule result in the formation of an array of available *molecular* energy levels.² Of most importance

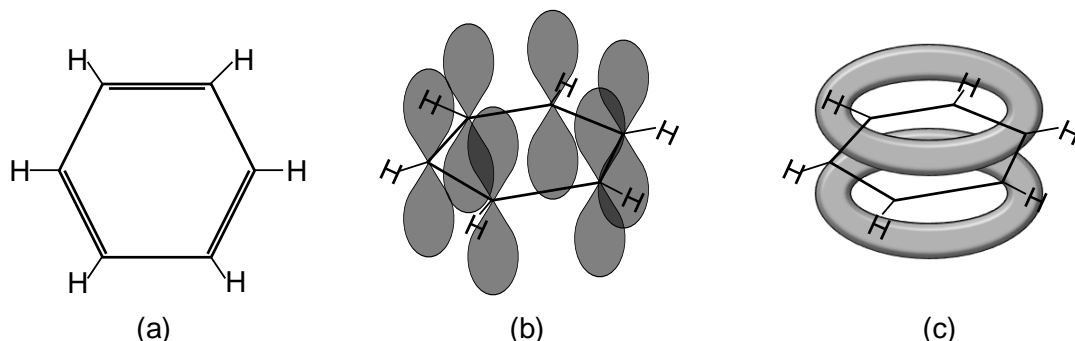


Figure 1.1: (a) The chemical structure of benzene showing the alternating single and double carbon-carbon bonds. (b) Schematic representation of the unhybridized p_z orbitals, oriented orthogonal to the plane of the benzene ring. (c) Representation of the resulting π -bond electron delocalization.

are the highest occupied molecular orbitals (HOMO) and lowest unoccupied molecular orbitals (LUMO).^{3,4} These energy levels are conceptually similar to the valence and conduction bands, respectively, of an inorganic semiconductor. Excess electrons, which are the result of either electrical or optical exciton, are transported through the LUMO levels, while excess holes (actually an unpaired electron in the HOMO, leading to the formation of a positively charged vacancy) are transported through the HOMO levels. The distance, in energy, between the HOMO and LUMO levels is termed the electronic energy gap, and the character of these energy levels strongly determines the optical and electronic properties of organic semiconductors. These properties will be discussed in greater detail in below.

1.2 What is an Organic Thin Film?

A thin film is typically defined as a layer of material which has a thickness of ~1-1000 nm. Small molecule organic semiconductors form thin films which are bonded via relatively weak van der Waals forces.¹ These forces arise from intermolecular, dipole-dipole interactions. There are three distinct mechanisms: induced dipole-induced dipole,

permanent dipole-induced dipole, and permanent dipole-permanent dipole. The first mechanism, termed the London dispersion force, is due to the instantaneous fluctuations of the electron density surrounding a molecule, resulting in an instantaneous polarization. The polarization of one molecule may induce an instantaneous polarization in a nearby molecule, resulting in an overall attraction between the two molecules. In this way molecules with no permanent dipole may form stable films. The permanent dipole-induced dipole (Debye force) and the permanent dipole-permanent dipole (Keesom force) mechanisms occur when one or more of the constituent molecules has a permanent dipole, a not uncommon feature of some molecules. The net result of the weak bonding in a thin film of organic material is that the electronic properties of a thin film are often similar to those of a single molecule. Additionally, the weak intermolecular bonding renders the typical organic thin films mechanically soft.^{5,6}

1.3 Character of the Excited State

An important precursor to the emission of light from an organic thin film is the formation of an excited state. The excited state, termed an ‘exciton,’ consists of an electron in the LUMO which is bound via a Coulomb force to a hole in the HOMO. Due to the low relative dielectric constant of organic semiconductors ($\epsilon_R \sim 3$), the exciton is highly localized and has a large binding energy, >100 meV.¹ An exciton which is confined to a single molecule is termed a “Frenkel” exciton, while an exciton which spans adjacent molecules is referred to as a “charge-transfer” exciton.^{1,7,8} Excitons which are yet larger in spatial extent (“Wannier-Mott” excitons) are not typically encountered in organic semiconductors.⁹ The large exciton binding energy found in organic

semiconductors allows them to persist at room temperature for a period of time (the exciton “lifetime,” τ), before deactivation through the emission of a photon (light), the emission of phonons (heat), or the transfer of energy to another molecule (energy transfer).^{10–14} The characteristics and behavior of this energy-carrying, charge-neutral quasiparticle is a principal factor in determining the operation and performance of OLEDs.

1.3.1 Singlet and Triplet Excitons

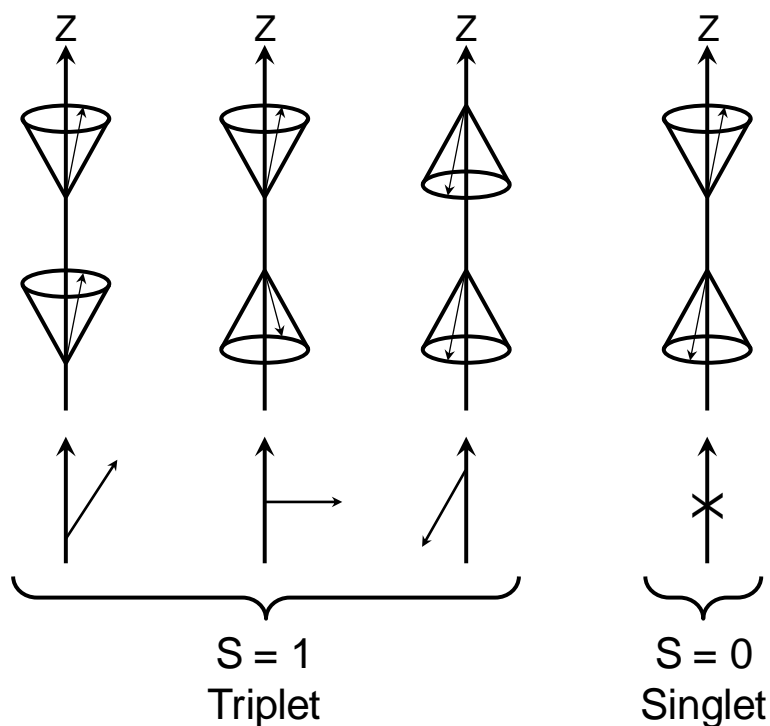


Figure 1.2: Vector depiction of the four possible spin states of an electron-hole pair. There are three permutations which give a net spin of $S = 1$, termed “triplet” excitons, and one variation which has a net spin of $S = 0$, termed “singlet” excitons.

As Fermions, electrons and holes have associated spins of $S = \pm 1/2$. The four possible combinations of electron and hole spin in an exciton are depicted as rotating vectors in Figure 1.2.¹⁵ An exciton, therefore, may have a total spin of magnitude $S = 0$,

when the spin vectors are out of phase (the anti-symmetric state), or $S = 1$, when the spin vectors are in phase (the symmetric state). The degeneracy of each total spin state gives the exciton its name, the $S = 0$ state being a ‘singlet’ exciton of single degeneracy, the $S = 1$ state being a ‘triplet’ exciton of triple degeneracy. Under electrical excitation, electrons and holes with uncorrelated spins bind to form excitons, therefore all four configurations of exciton spin are produced. Simple statistics show that a population of excitons formed this way will be 75% triplets and 25% singlets.^{16,17} The available and dominant electronic transitions of an exciton are greatly affected by its spin state, a matter addressed in the following sections.

1.3.2 Electronic Transitions in Organic Semiconductors

The energy levels and electronic transitions of an organic semiconductor are illustrated in Figure 1.3. The ground state is S_0 ; higher-lying singlet excited states are labeled S_1 , S_2 , etc. Similarly, T_1 and T_2 indicate higher-lying triplet excited states. Each state consists of a manifold of vibronic states which are close in energy to the primary state, denoted by a second subscript ($S_{1,0}$ indicates the lowest level vibronic in the first excited state).

The rate of transition (k_{obs}) between initial (subscript i) and final (subscript f) state can be given by Fermi’s Golden rule:¹⁵

$$k_{obs} = \rho |\langle \Psi_f | P_{i \rightarrow f} | \Psi_i \rangle|^2, \quad (1.1)$$

where P is the strength of a perturbation acting on an initial wavefunction (Ψ_i) and ρ is the density of resonant states for the transition. The Born-Oppenheimer approximation states that the motion of electrons in the molecular orbitals is more rapid than the

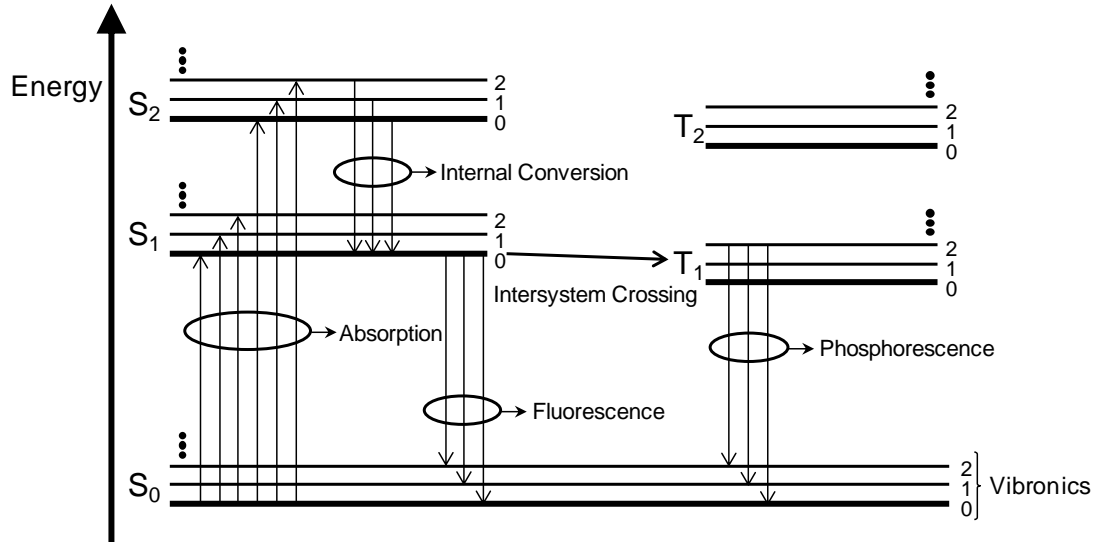


Figure 1.3: Energy level diagram of an organic semiconductor. S_0 is the ground state, while the first and second singlet and triplet excited states are S_1 and S_2 , and T_1 and T_2 , respectively. The vibronic sub-level of each electronic level are indicated as 0, 1, 2. The available electronic transitions for a molecule are: absorption, internal conversion, fluorescence, intersystem crossing, and phosphorescence.

vibration of the nuclei. This allows the total wave function, Ψ , to be separated into an electronic wave function, ϕ , and a nuclear wave function, χ .¹⁸ This assumption is generally valid for organic molecules, where the mass of the nuclei is much greater than that of the electrons in the outer orbitals. Effectively, this requires that electronic transitions occur on a time scale which is much shorter than the reorganization of the nucleus in response to the transition.

The rate of an optical transition between states may be written in a Fermi's golden rule notation as:¹⁵

$$k_{obs} = \frac{\langle \phi_f | P_{d-d} | \phi_i \rangle^2}{\Delta E_{if}^2} \times \langle \chi_i | \chi_f \rangle, \quad (1.2)$$

where the first term is due to a dipole-dipole interaction and ΔE_{if} is the separation in energy of the two states, and the second term is due to the overlap of the vibrational

(nuclear) wave functions, termed the Franck-Condon factor; this factor is discussed in greater detail below.^{15,18} The dipole operator, P_{d-d} , is itself symmetric, meaning it cannot mix states which do not share spin symmetry. This requires that an optical transition between Ψ_i and Ψ_f must be a singlet-singlet or triplet-triplet transition. Generally, molecules in the ground state have filled HOMO energy levels, requiring that the constituent, paired electrons have opposite spins, i.e. the anti-symmetric state. Under first-order approximations, optical transitions from an excited, anti-symmetric state (singlet exciton) are allowed, while optical transitions from excited symmetric states (triplet excitons) are not.¹⁵

A schematic of an optical transition is depicted in Figure 1.4, where the energy levels of a ground state and first singlet excited state are depicted together with their vibronic manifolds. In Figure 1.4a, a photon is absorbed by an electron in the ground state and is promoted to the vibronic level of a higher singlet energy state. The strength of the transition is determined by the overlap of the ground state level ($S_{0,0}$) with each vibronic level. The strength of the transition determines the “intensity” of absorption, depicted in Figure 1.4b. Once in an excited singlet state, an electron with excess energy (energy above the lowest vibronic energy level in the S_1 state) rapidly cools to the lowest energy singlet level, $S_{1,0}$ (rate $\sim 10^{12}\text{s}^{-1}$),¹⁵ in a process termed internal conversion. This process occurs with the emission of phonons as a means to dissipate the excess energy. From the Born-Oppenheimer approximation, the electronic transitions may be assumed to occur while the nuclei are stationary, termed the Franck-Condon principle. Following the electronic transitions, the nuclei may react to the new arrangement in electronic charge.

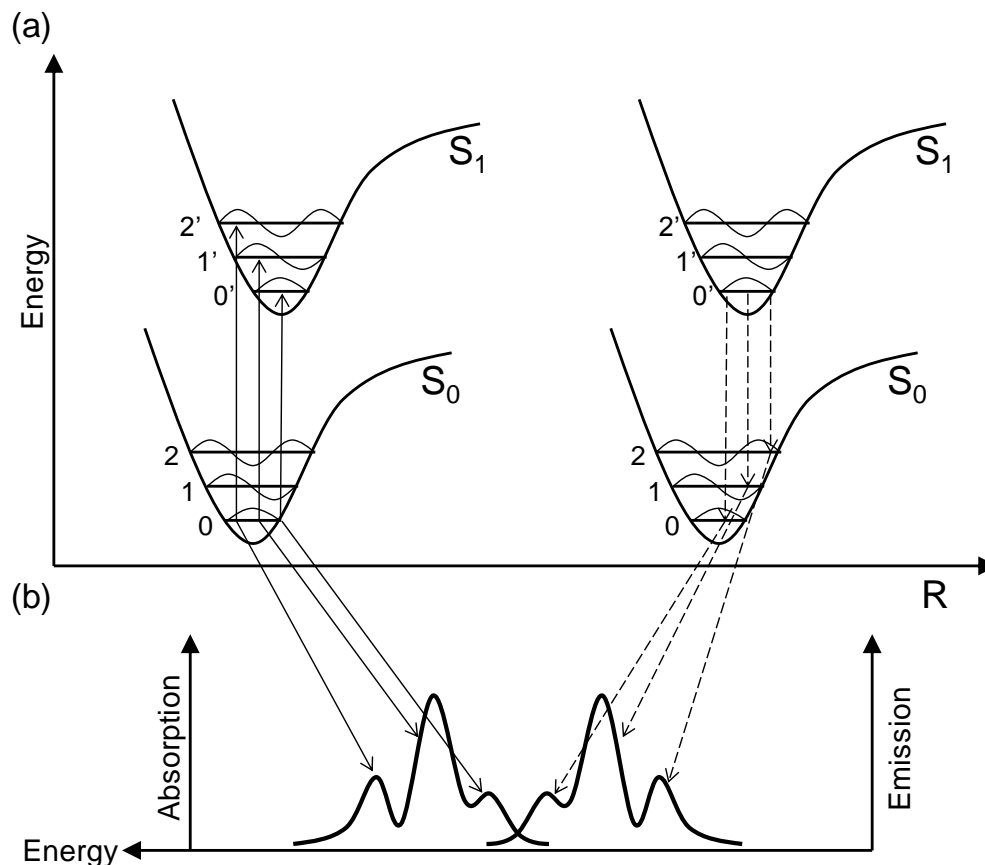


Figure 1.4: (a) Energy level schematic depicting absorption transitions from the ground state, $S_{0,0}$ to higher-lying states, $S_{1,n}$. After absorption, nuclear reorganization occurs and emission transitions from $S_{1,0}$ to vibronic levels in the ground state, $S_{0,n}$ may occur. (b) The spectral shift in emission from absorption is the Franck-Condon shift. The intensity of the absorption and emission transitions are determined by Fermi's golden rule

This shift in nuclear geometry is depicted in Figure 1.4a as a shift in the reaction coordinate, R .¹⁵

1.3.3 Fluorescence

Once in the $S_{1,0}$ state, an exciton may undergo radiative (emission of photons) or nonradiative (emission of phonons) decay to a vibronic level in the ground state ($S_{0,1}$, $S_{0,2}$...). The emission of a photon during the transition of $S_1 \rightarrow S_0$ is called fluorescence. The strength of the fluorescence transition, or intensity of emission, is determined by the

overlap of the $S_{1,0}$ state and the vibronic energy levels of the ground state. The tendency of electronic transitions to begin at the lowest vibronic energy level ($S_{0,0}$ for absorption, $S_{1,0}$ for fluorescence) is known as Kasha's Rule.¹⁹ Due to the nuclear reorientation following the excitation of a molecule, the fluorescence of a molecule is shifted to lower energy relative to absorption, termed the Franck-Condon shift.¹⁵ Absorption spectroscopy, therefore, is an experimental technique which reveals the vibronic character of the excited states in a molecule, while fluorescence spectra reflect the vibronic character of the ground state. The efficiency with which fluorescence occurs, η_{fl} , may be constructed as an equation of relative rates:

$$\eta_{fl} = \frac{k_R}{k_R + k_{NR}} = \frac{k_R}{k_T}, \quad (1.3)$$

where k_R is the rate of radiative fluorescence decay, k_{NR} is the rate of nonradiative decay, and k_T is the total radiative decay rate. The magnitude of η_{fl} may be quite high, indeed experimental values which approach unity have been observed. Clearly, with Eqns. 1.1-1.3, the strength of the fluorescent transition, the overlap of the initial and final wave functions, and any perturbations between the initial and final states are strong determining factors in the ability of a molecular excited state to emit light.

1.3.4 Phosphorescence

A third process which may occur after the formation of an excited state (in addition to fluorescence and nonradiative decay), is the transfer of that singlet excited state energy to a triplet state ($S_{1,0} \rightarrow T_{1,n}$), termed intersystem crossing.¹⁵ This process requires one of the constituent electrons to "flip" its spin. In terms of Fermi's golden rule, the rate at which the transition occurs (k_{ISC}) requires a mechanism to perturb the

spin state of an electron and is often very small, though non-zero. Once a triplet state has been excited, both radiative and nonradiative decay pathways (to the ground state vibronic manifold, $S_{0,n}$) may be possible, the latter through the emission of phonons, the former through the emission of photons. The process of photon emission from a triplet state is termed phosphorescence. Again, the transition from $T_{1,0}$ to $S_{0,n}$ requires a spin flip, and therefore is seldom seen in typical organic semiconductors.

Given the small fraction of singlet excitons formed under electrical excitation ($\sim 25\%$),¹⁶ there has been much effort aimed at harnessing triplet excitons in the process of light emission. One way to achieve stronger emission from triplet excitons is to introduce a perturbation to the electron spin states, effectively mixing the singlet and triplet exciton spin states. This has been achieved through the use of cyclometallic organic molecules, which have heavy transition metal atom constituents.²⁰ These materials make use of the strong coupling of the electron spin angular momentum (\mathbf{S}) and the orbital angular momentum of the electron (\mathbf{L}), due to the relative motion of the nucleus of the atom. This coupling is termed spin-orbit coupling, and its effect on the observable rate of phosphorescence, k_{ph} , can be included in a Fermi's golden rule rate equation (from Eqn. 1.2):

$$k_{ph} = \frac{\langle \phi_f | P' | \phi_i \rangle^2}{\Delta E_{if}^2} \times \langle \chi_i | \chi_f \rangle \times \frac{\langle \phi_f | P_{so} | \phi_i \rangle^2}{\Delta E_{if}^2}, \quad (1.4)$$

where P' is now a perturbation to the electronic wavefunctions, and P_{so} is the spin-orbit coupling operator. The spin-orbit interaction of an electron in a hydrogen potential is given by:^{15,18}

$$H_{SO} = \frac{e^2}{8\pi\epsilon_0} \frac{1}{m^2 c^2 r^3} \mathbf{L} \cdot \mathbf{S}, \quad (1.5)$$

Where e is the elementary charge, ϵ_0 is the permittivity of free space, m is the mass of the electron, c is the speed of light, and r is the radius of motion. Ignoring the front factors, a two-electron system will have a spin-orbit interaction:

$$H_{SO} \propto \mathbf{L}_1 \cdot \mathbf{S}_1 + \mathbf{L}_2 \cdot \mathbf{S}_2, \quad (1.6)$$

which becomes:

$$H_{SO} \propto \frac{1}{2} (\mathbf{L}_1 + \mathbf{L}_2) \cdot (\mathbf{S}_1 + \mathbf{S}_2) + \frac{1}{2} (\mathbf{L}_1 - \mathbf{L}_2) \cdot (\mathbf{S}_1 - \mathbf{S}_2). \quad (1.7)$$

The $(\mathbf{S}_1 + \mathbf{S}_2)$ operator is commutative with the total spin \mathbf{S} , while $(\mathbf{S}_1 - \mathbf{S}_2)$ is not. It is this second term which will give rise to a commutator of the electron spin states, i.e. it will mix the singlet and triplet states. With strong spin-orbit coupling, k_{ph} may be enhanced such that it competes with nonradiative decay pathways. The efficiency of phosphorescence may be written similarly to η_{fl} :

$$\eta_{ph} = \frac{k_{ph}}{k_{ph} + k_{NR}}. \quad (1.8)$$

Experimental work has shown that with proper molecule design, η_{ph} may approach unity.^{21,22}

1.4 Energy Transfer and Exciton Diffusion

While the previous sections have dealt with *intramolecular* excited state transitions, there are several key *intermolecular* excited state transitions. These ‘energy transfer’ processes transport the energy of an initial molecular exciton (the “donor” molecule) to a second molecular exciton (the “acceptor” molecule). These processes occur over a wide range of length scales and can be critical to OLED operation and

Chapter 1: A Review of the Optical and Electronic Properties of Organic Semiconducting Materials

performance. There are three primary mechanisms which are responsible for energy

transfer: cascade energy transfer, Förster energy transfer, and Dexter energy transfer

1.4.1 Cascade Energy Transfer

Cascade energy transfer (or trivial energy transfer) is a mechanism which relies on emission of a photon by the donor molecule and the subsequent absorption of that photon by an acceptor molecule. The physical processes for this type of energy transfer are readily explained in the context of the previous sections: an excited state radiatively transitions to the ground state, some time later, a molecule absorbs the photon, and an electron is promoted to a higher-lying singlet exciton state. The important parameters are the efficiency of fluorescence (or phosphorescence) and the overlap of the emission spectra with the acceptor absorption cross-section. The later takes into account both the magnitude of the photon energy required and the strength of the absorption transition of the acceptor molecule into various singlet excited state vibronics. This process may occur over very large distances (10-100nm or more), provided the photon is allowed to propagate in the intervening media.^{1,15}

1.4.2 Förster Energy Transfer

Förster energy transfer (or Förster resonance energy transfer, FRET) is a mechanism by which the energy of an exciton is transferred from a donor molecule to an acceptor molecule via their overlapping dipole fields.^{1,15} This process may be approximated as two interacting point dipoles and functions much like a simple transmitting antenna-receiving antenna: an exciton in the donor produces an oscillating electric field which drives the electrons of the acceptor in to resonance, shown in Figure

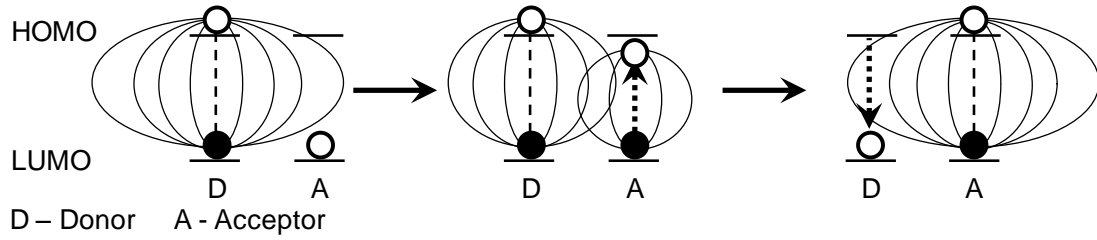


Figure 1.5: Schematic diagram of the Förster energy transfer process. An exciton on the donor molecule (D) sets up an oscillating electric field, which excites an electron on the accepting molecule (A), resulting in an exciton on the acceptor and a donor molecule in the ground state.

1.5. The energy of the exciton is fully transferred from donor to acceptor, which leaves the donor in the ground state. This process may occur through occupied space; though, as in the antenna analogy, the distance between the dipoles has a large effect on the energy transfer process.

The rate of Förster energy transfer (k_F) is given by:²³

$$k_F[d] = \frac{1}{\tau} \left(\frac{R_0}{d} \right)^6, \quad (1.9)$$

where τ is the exciton lifetime, d is the donor-acceptor molecular separation, and R_0 is the characteristic radius of Förster energy transfer, defined as the separation of the donor and acceptor molecules where the rate of Förster energy transfer is equal to the rate of all the other energy loss mechanisms. The Förster radius for a donor-acceptor pair is:^{15,23}

$$R_0^6 = \frac{9 \eta_{PL} \kappa^2}{128 \pi^5 n^4} \int \lambda^4 F_D[\lambda] \sigma_A[\lambda] d\lambda, \quad (1.10)$$

where η_{PL} is the photoluminescence efficiency of the donor, κ is the dipole orientation factor, n is the index of refraction of the medium between the donor and acceptor, λ is the wavelength, F_D is the area-normalized donor emission spectrum, and σ_A is the absorption cross-section of the acceptor. Equation 1.10 can be viewed much like a Fermi's golden rule equation, the integral (weighted to include the strength of the acceptor's absorption

transitions) is the overlapping density of states while the front factors determine the magnitude of the transition operator. Like the Fermi's golden rule equations describing fluorescence, the initial and final states must have the same spin configuration, as the dipole-dipole coupling transition does not include an operator which perturbs the spin states. Thus, Förster energy transfer is typically restricted to singlet excitons, whose fluorescence transitions do not require a spin flip. Given that a photon is a quantum of the electromagnetic field, the coupling between the donor and acceptor molecule is often described as the emission and absorption of a 'virtual photon.' The typical length scales of Förster energy transfer are ~1-10 nm,¹ though the properties of both the donor and acceptor are important in determining the rate (and therefore efficiency) of energy transfer.

1.4.3 Dexter Energy Transfer

Dexter energy transfer is process which physically transfers the excited state electron from a donor molecule to an acceptor. This process is, therefore, a much shorter-range energy transfer mechanism than the previously described processes. The rate of Dexter energy transfer (k_D) is:^{1,15}

$$k_D = \frac{4\pi^2}{h} |\beta_{DA}|^2 \int E_D(E) A_A(E) dE, \quad (1.11)$$

where h is Planck's constant, β_{DA} is the exchange energy interaction between molecules, E is the energy, E_D is the normalized donor emission spectrum, and A_A is the normalized acceptor spectrum. The dependence of Dexter energy transfer on donor-acceptor separation can be included by assuming that the electron clouds of each molecule fall off exponentially.¹⁵

$$k_D = K e^{-2R_{DA}/R_0} \int E_D(E) A_A(E) dE. \quad (1.12)$$

Here K is related to the specific orbital interactions, R_{DA} is the donor-acceptor separation, and R_0 is defined as the separation at which the energy transfer process is equal to the other rates of energy loss.

In comparison to Förster energy transfer, Dexter energy transfer also requires a resonance of the density of states, represented by the integrals in Eqns. 1.11 and 1.12. Also like Förster energy transfer, the process of the physical exchange of electrons maintains the spin throughout the transfer. However, unlike Förster energy transfer, the exchange process does not require mediation by a virtual photon, thus the exchange may occur for excited states which do not have any wave function overlap with the ground state. Dexter energy transfer is, therefore, the dominant mechanism by which triplet excitons are transferred from donor to acceptor molecules.

1.4.4 Exciton Diffusion

The term exciton diffusion describes the net motion of exciton energy throughout space. The diffusion process consists of multiple energy transfer events. Both Förster and Dexter may contribute, though one process will typically dominate due to the spin character of the exciton or the optical properties of either the donor or acceptor molecules. In future chapters the impacts of exciton diffusion on OLED device design, operation, and performance will be discussed.

1.5 Charge Transport in Organic Semiconductors

The topic of charge transport in organic semiconductors is an active area of research.^{24,25} Typically, the nature of charge transport falls between two extremes: a

band transport model and a ‘hopping’ model. Band transport is most likely in materials with long-range order, typically characteristic of crystalline thin films, where excess electrons are greatly delocalized in space. A hopping model is more appropriate for materials which are highly disordered, typically characteristic of materials where there is little orientation of the molecules, i.e. amorphous thin films, where excess electrons in the LUMO are highly localized in space.²⁶ The balance of these transport regimes, and their relevance to OLED device operation are discussed in the following sections.

1.5.1 Band Transport

The theory of band transport was initially developed to describe the electronic properties of inorganic crystalline materials (now sometimes extended to crystalline organic materials). It based on the premise that a long-range, periodic potential is formed by the symmetry and order of an atomic (or molecular) lattice. The periodic potential sets up an electronic wave function in the conduction band (or LUMO) that has a large spatial extent, overlapping many lattice sites. The electron in a crystalline material is able to travel rapidly through the conduction band in response to an applied electric field. This is observed experimentally as a high mobility, $\mu = F/v$, where v is the velocity of the electron and F is the applied field. The temperature (T) dependence of the mobility in the limit of band transport is:¹⁵

$$\mu \propto T^{-n}, \quad (1.13)$$

where $n > 1$, and is a material dependent parameter. A signature of band transport, therefore, is a decrease in mobility with increasing temperature. This is due to an increase in the interactions of conduction-band electrons and phonons of the lattice.

1.5.2 Hopping Transport

Organic thin films, as discussed previously, are typically bonded via weak van der Waals forces. This bonding scheme leads to very weak interactions between adjacent molecules and results in a thin film which molecular orientations and spacings are highly disordered. This disorder prevents the formation of a delocalized electronic band; instead, carriers are confined to individual molecules. Due to the weak interaction between molecules there is a barrier for electron transfer from one molecule to another. Carrier conduction is thus an activated process, where an electron must overcome a barrier in order to ‘hop’ to an adjacent site. Unlike the band transport limit, the carrier in the hopping process spends enough time on each molecule to polarize the surrounding lattice. The polarized lattice reconfigures to a new equilibrium state. Together, the polarization field and the charge carrier are known as a “polaron.”^{9,26} This process is diagrammed in Figure 1.6. The mobility, μ , in such a system is now dependent on a range of factors, including the barrier height (E_A), and the temperature of the lattice (T):¹

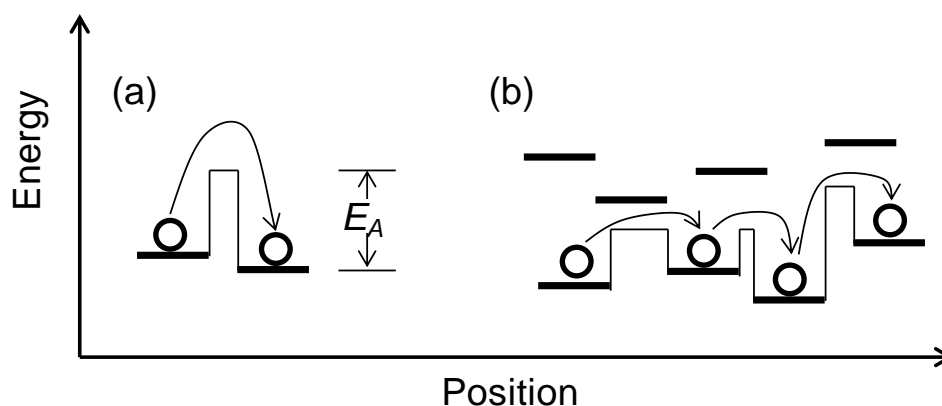


Figure 1.6: (a) Schematic of hopping transport showing the energy barrier, E_A , that must be overcome in order transport charge. (b) The path of a carrier typically transports through the lowest energy states available for conduction.

$$\mu \propto e^{-E_A/k_B T}, \quad (1.14)$$

where k_B is Boltmann's constant. Given the disorder in many organic thin films, hopping transport is expected to be the dominant charge transport mechanism. Further studies of the mobility of organic thin films are presented in Chapter 5.

Chapter 2 Introduction to Organic Light-Emitting Devices

2.1 Thin Film and Device Fabrication

There are several ways to achieve a thin film of a small molecule organic semiconductor. Methods have been developed which are based on both liquid phase and vapor phase processing,^{5,27,28} with powdered solids as the typical starting material. Liquid phase processing requires soluble materials and appropriate solvents. Once in solution, films may be formed by a variety of techniques, including: spin coating, ink-jet printing, spray-coating, and doctor-blading. There is significant current interest in developing materials which are compatible with the above techniques as they may present paths to high-throughput, low-cost manufacturing on flexible substrates, such as roll-to-roll processing.^{29,30} One current challenge in liquid phase processing is achieving high performance multi-layered device structures, where each layer must be immune to dissolution in subsequent liquid processing techniques.^{31,32}

Vapor phase processing requires a method to transition the initial powdered material from the solid to the gas phase. This is usually accomplished by heating the material, either directly, with the use of a crucible or special boat, or through the use of a hot carrier gas, as is the case in organic vapor phase deposition (OVPD).^{33,34} In OVPD, the organic source material is heated in to the vapor phase, where it is transported, via the hot carrier gas, through a heated reactor to a cooled substrate. This technique has many benefits, such as high material utilization, high deposition rates, and compatibility with

roll-to-roll processing. However, film uniformity and control of mixed film composition are still challenges.

2.1.1 Vacuum Thermal Evaporation

The most common method used to form the layers necessary for OLEDs (shown schematically in Figure 2.1) is vacuum thermal evaporation (VTE).³⁵ This

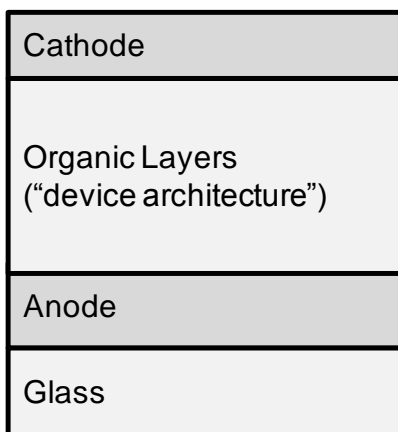


Figure 2.1: Cross-sectional schematic of an OLED on a glass substrate. The anode is typically pre-coated on the substrate.

technique relies on heating the source powder in a crucible or folded metal source boat (Tantalum or Tungsten are commonly used). An electrical current is passed through the boat, causing resistive heating of the boat, which in turn heats the enclosed powder. Under high-vacuum and applied heating, organic materials may evaporate from a melt, or may sublime directly from the solid phase to the vapor phase. The deposition rate of the VTE process is controlled by the heating of the boat. The opening of the boat behaves as a surface source, with a vapor plume shape that has cosine dependence, similar to Lambert's cosine law. The substrates in such a system are placed a significant distance from the source boat and are often on a rotation stage, to ensure uniform film thicknesses,

the “throw distance” between the source boats and substrates is typically ~ 1 meter. A schematic of a typical deposition system is shown in Figure 2.2a, a source boat is shown

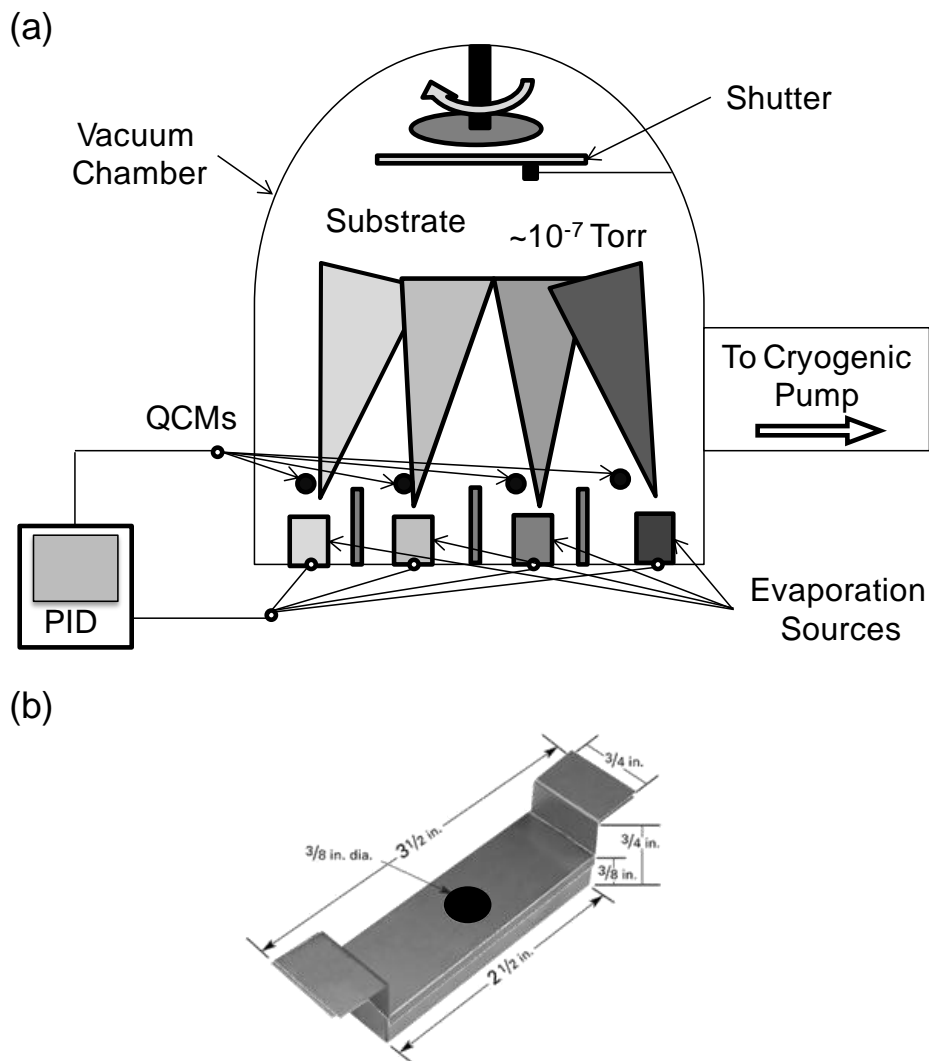


Figure 2.2: (a) Schematic of a typical vacuum thermal evaporation system. Organic source powders are placed in the evaporation source boats, shown in (b) with common dimensions (R.D. Mathis Co., evaporation source model: SB-6 (bottom) SB-6A (lid)). Upon heating, the organic powders evaporate or sublime, leaving the source boat with a Lambertian plume shape.

in Figure 2.2b, with typical dimensions labeled.

Chapter 2: Introduction to Organic Light-Emitting Devices

Deposition rates in such a system are measured via quartz crystal microbalance (QCM). Highly crystalline quartz undergoes a strong piezoelectric effect in response to an applied voltage. Under an AC bias, a quartz crystal of a known thickness has a stable frequency resonance; the resonant frequency shifts as the mass of the crystal is increased via the deposition of organic molecules (or metal atoms) on the QCM surface. With a simple assumption about the relationship of mass to film thickness, a rate of deposition (thickness over time) is achieved.^{36,37} As the exact ratio of mass to thickness is difficult to quantify for all materials of interest, a tooling factor is used. This factor is the ratio of the actual, measured thickness to the desired thickness. With the use of an accurate technique for deposition rate measurement and computer control of the power provided to each deposition boat, an active feedback control loop may be established. With each loop a computer, via a proportional-integral-derivative (PID) controller, is able to measure the error between an intended rate and measured rate, and may adjust the applied power. Changes in applied power will heat or cool the deposition boat, which will in turn adjust the temperature, and deposition rate, of the target material. With accurate tooling factors and PID settings, a target deposition rate which changes over time is attainable. Deposition rates are typically on the order of $\sim 1\text{-}4 \text{ \AA/s}$ with an experimental error of $\pm 0.04 \text{ \AA/s}$.

Overall, this technique allows for very careful control of deposition rates, and thus also film thickness and film composition. Multi-layered structures are trivial in such a system, source boats are heated (and allowed to cool) in succession, allowing structures

with any number of layers to be fabricated. For these reasons, the VTE system is most often used in settings where the utmost control over film mixing, thickness, etc. is required. Devices reported in this thesis are exclusively fabricated via the VTE method.

2.1.2 Formation of Cathode

One important step in the production of an OLED is the fabrication of the top metal electrode, typically the cathode of the device. The cathode is responsible for the injection of electrons in to the device. Therefore, a metal with a low work function is often desired to minimize the LUMO-work function energy difference. There are several metals which are currently used, such as Al, Ag, and alloys of Mg:Ag.^{10,38} The most common, however, is Al, due to its effectiveness, environmental stability, and low cost. The Al deposition process is a high-vacuum thermal evaporation process, similar to the deposition of organic materials. Al pellets (~4 mm in diameter) are placed in a tungsten-wire basket. The basket is resistively heated, causing the Al pellets

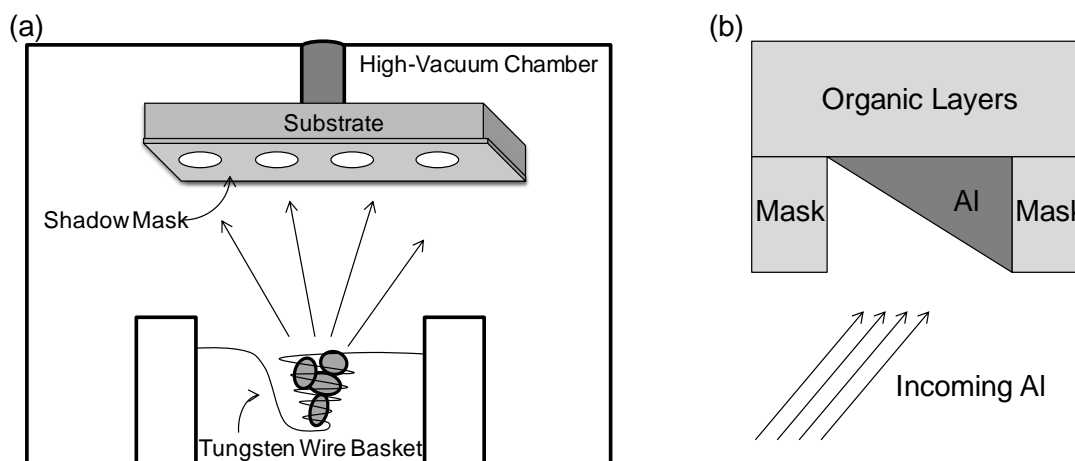


Figure 2.3: (a) Schematic of the cathode deposition through a shadow mask. (b) If the mask is too thick, or the angle of the incoming Al vapor is large, edge effects may occur, resulting in non-uniform electrodes.

to melt and evaporate. To define the active area of OLED on a substrate, a shadow mask is used to allow Al deposition to occur only in a specified area, shown schematically in Figure 2.3a. It is important that the mask is very thin and flat, so that mask edge effects and shadowing do not occur; an example of a mask edge effect is shown in Figure 2.3b.

One important development in the performance of OLEDs is the use of an interface-modifying layer at the organic/cathode interface. This layer is typically LiF, and is deposited sequentially after the last organic layer and before the deposition of Al. Effectively, the work function of the LiF/Al cathode is reduced for LiF thicknesses of ~1 nm. This greatly enhances electron injection into organic layers and has been shown to enhance the performance of OLEDs.^{39,40} There are two ways in which LiF might reduce the effective work function of the cathode. The first occurs with the dissociation of the lithium and fluorine atoms by the incoming, energetic Al atoms. The free atoms may then bond with either the organic molecules or Al atoms at the interface, resulting in a smaller energy barrier between the Al and organic layers.^{41,42} A second route depends on the large dipole moment measured for LiF thin films. It has been proposed that a thin film of LiF would form a large interface dipole, enhancing the injection of electrons through a reduction in the tunneling barrier.⁴³ The latter mechanism would be highly dependent on orientation of the LiF molecule and is considered unlikely. However, measurements of the chemistry present at the organic-metal interface are difficult on thin layers, particularly after Al deposition.⁴⁴ Regardless of mechanism, the inclusion of LiF in the formation of cathodes has become convention in OLEDs.

Chapter 2: Introduction to Organic Light-Emitting Devices

2.1.3 Complete OLED Fabrication Process

The fabrication of an OLED begins with a clean substrate. Dust, grease from the manufacturing process, and oils from the skin all serve to reduce device operation and yield. Substrate cleaning follows a standard procedure: sonication in a non-ionic surfactant (Tergitol, Sigma Aldrich), sonication in deionized water, sonication in acetone, and boiling in isopropyl alcohol. In this thesis, all OLEDs were fabricated on glass substrates pre-coated with a 150-nm-thick layer of indium-tin oxide (ITO), a highly transparent and conductive material, having a sheet resistance of $15 \Omega/\square$. The ITO-coated substrates were treated in UV-ozone ambient prior to loading in the VTE system. All organic layers were grown using vacuum thermal sublimation ($<10^{-7}$ Torr) without breaking vacuum. Devices were defined by evaporating a cathode consisting of a 1-nm-thick layer of LiF and a 100-nm-thick layer of Al through a shadow mask with 1 mm diameter openings.

2.2 OLED Characterization and Data Analysis

Typical OLED operation and performance may be reported in the form of a few figures of merit. These numbers may reflect the efficiency of luminescence, the optical output of the device, the operating voltage of the device, as well as metrics which are related to display or lighting applications. The sections below discuss these metrics, as well as their use in understanding device operation, together with the experimental data and equipment needed to achieve these metrics.

2.2.1 Units of Optical Output in OLEDs

The efficiency of an OLED is reported as optical output divided by electrical input. A metric may be as simple as optical power out (W_{OPT}) divided by input electrical power (W_{OLED}), referred to as the “wall-plug efficiency.” This efficiency, however, does not reflect how well the device may operate as light source, intended for viewing with human eyes. Indeed, the spectral sensitivity of the human eye (the “photopic” response, $\Phi[\lambda]$), in daylight conditions, has a narrow wavelength-response which is centered in the green-yellow region of the visible spectrum (Figure 2.4).⁴⁵ A useful characterization,

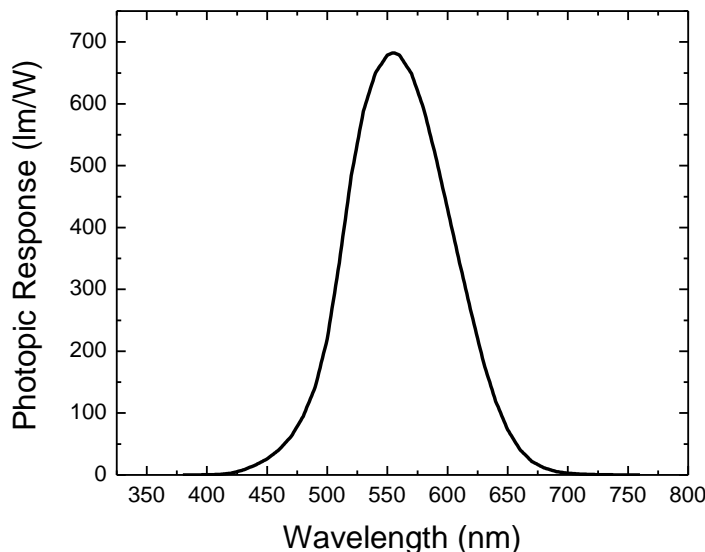


Figure 2.4: Photopic response of the standard human eye. The peak wavelength of sensitivity is ~555nm

then, is to compare the emitted power spectrum of the OLED (or electroluminescence, $EL[\lambda]$) to the photopic response of the human eye. This is done by calculating an average wavelength of overlap factor, ϕ :

$$\phi = \frac{\int \Phi[\lambda]EL[\lambda]d\lambda}{\int EL[\lambda]d\lambda}. \quad (2.1)$$

The units of ϕ are *lumens* (lm), which is an SI unit of luminous flux. Noting the output of an OLED in terms of lumens is useful, as it automatically adjusts for emitted spectral components that are not visible to the human eye. This is especially important for OLEDs which are intended for display or lighting applications – the emission of ultraviolet, or infra-red light is inherently a source of loss. Closely related to the lumen is the candela (cd). This SI unit is defined as the power (in lumens) emitted by a source in to a particular solid angle, and is a measure of brightness. For an OLED, the relevant solid angle is the hemisphere directly above the substrate (Figure 2.5a), light which

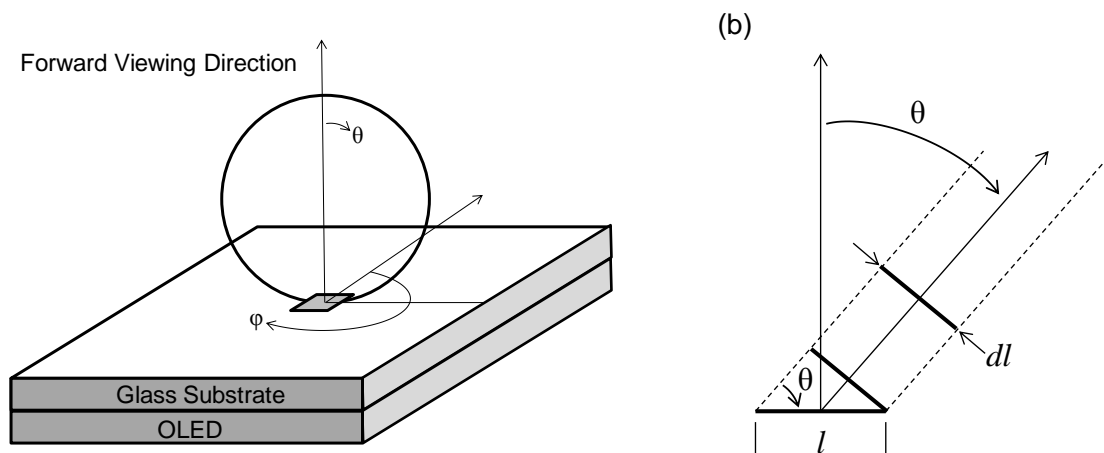


Figure 2.5: (a) Schematic of the forward hemisphere of light emission. All light which escapes into this hemisphere escapes in the “forward viewing direction.” The angle θ is defined from the normal to the source surface area, while ϕ is defined from the plane which is parallel to the source surface area. (b) Schematic of the effective viewing aperture for a surface source as a function of viewing angle θ .

escapes into this hemisphere is travelling into the “forward viewing direction,” and is light which is useful for display and lighting applications. To calculate candelas, the luminous flux (in lumens) is integrated over the forward viewing hemisphere with the important consideration that the OLED is not a point source, but is rather a surface

emitter. The power emitted versus viewing angle from a surface source follows Lambert's cosine law, which states that the brightness per solid angle, per unit area is constant with changes in angle; as θ increases, the emission intensity decreases but the solid angle decreases as well, this can be seen schematically in Figure 2.5b. Conceptually, the surface area of the emitter can be thought of as an aperture through which the luminous flux is observed. At off-normal angles, the intensity falls by a factor of $\cos[\theta]$, but the effective aperture size (dl , in Figure 2.5b) falls by a factor of $\sin[\theta]$. Experimentally, all output in the forward hemisphere is collected, so the conversion of intensity in lumens to candelas, requires factoring in the Lambertian angular dependence and the changing solid angle:

$$cd = \frac{lm}{\int_0^{\pi/2} \int_0^{2\pi} \cos[\theta] \sin[\theta] d\varphi d\theta} = \frac{lm}{\pi}, \quad (2.2)$$

where the angles θ and φ are defined in Figure 2.5a. The unit of candela is often normalized to the surface area of the emitting device and is reported as cd/m^2 , this unit has sometimes been referred to as a “nit.” Throughout this thesis, the luminescent output of an OLED will be described units of cd/m^2 , and will be referred to as “brightness.”

2.2.2 External Quantum Efficiency

A fundamental of measure of the OLED efficiency is the external quantum efficiency, or η_{EQE} . The η_{EQE} , as the name suggests, is the ratio of quantum output (photons) to quantum input (electrons). The η_{EQE} metric only counts photons which escape in to the forward viewing hemisphere. The conceptual definition for η_{EQE} is:¹⁰

$$\eta_{EQE} = \chi \times \gamma \times \eta_{OC} \times \eta_{PL}, \quad (2.3)$$

where χ is the spin fraction, γ is the charge balance factor, η_{OC} is the outcoupling efficiency, and η_{PL} is the photoluminescence efficiency. The spin fraction, χ , of a device is defined as the fraction of excitons which are allowed to decay radiatively. In the language of Chapter 1, this is the fraction of excited states which have wave function overlap with the ground state and do not require a spin flip (i.e. singlet excitons). For typical fluorescent materials, $\chi = 0.25$. However, from Chapter 1 section 3.4, strong spin-orbit coupling allows for the radiative decay of triplet excited states; therefore, for phosphorescent materials, $\chi = 1.0$.

One recent development which challenges the above framework for χ , is the demonstration of thermally activated delayed fluorescence (TADF).^{46,47} In this system, a metal-free organic molecule is engineered so that the singlet and triplet energy levels have a small energy gap (ΔE_{ST}), such that the reverse intersystem crossing rate from triplet to singlet, R_{ISC} , is enhanced. Despite the formation of triplet excitons under electrical excitation, an enhanced R_{ISC} increases the probability that triplet excitons will convert to singlets and undergo radiatively decay with an efficiency of η_{FL} . This leads to an effective increase in χ , though the ratio of singlets to triplets formed is not impacted. Molecules designed for TADF have recently been used to achieve high peak efficiency in OLED.⁴⁸

The charge balance factor, γ , is defined as the fraction of electrons injected into the device which form excitons in the emissive region of the device. This parameter quantifies loss mechanisms due to the charge which ‘leaks’ through the entire device

without forming excitons, and due to the formation of excitons outside of the intended spatial region. The γ of a particular device is dependent on many aspects of the overall device design and it is often used to assess the quality of device operation. For particularly well designed OLEDs, γ may approach unity. The outcoupling factor, η_{OC} , is the fraction of photons formed in the device which escape in to the far field in the forward viewing direction. Due to the index of refraction contrast between the organic layers, ITO, glass, and air, light generated in the active layers of the OLED may undergo total internal reflection and be lost to horizontal wave guide or plasmon absorption modes, shown in Figure 2.6. The exact calculation of the fraction of outcoupled light will

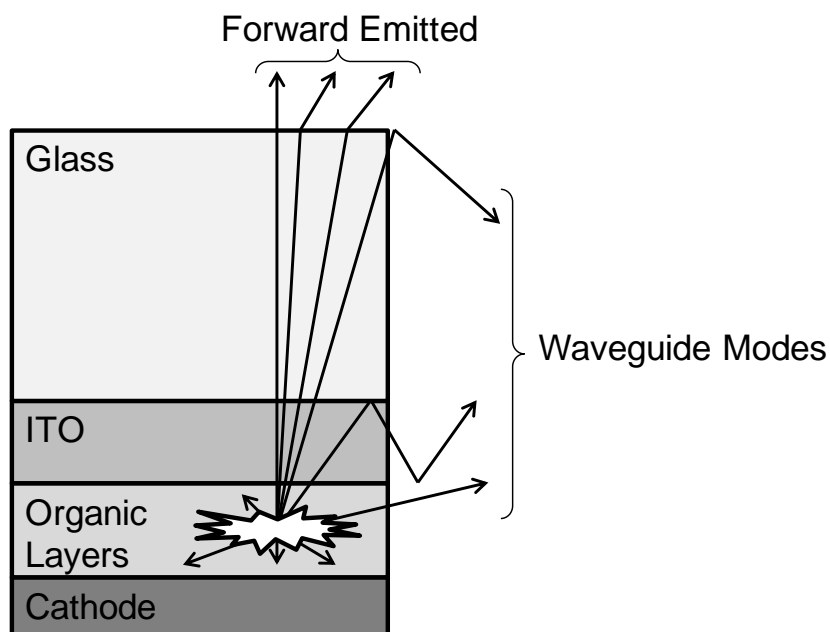


Figure 2.6: The outcoupling factor, η_{OC} , for an OLED results from the internal reflection of some of the generated light. This is due to the index of refraction contrast between the organic thin films, ITO, glass substrate, and air layers.

be addressed in Chapter 7, though a value of $\eta_{OC} = 0.2$ is often quoted. An initial guess for η_{OC} can be made using Snell's law to calculate the critical angles for total internal

reflection for light transiting the ITO-glass and glass-air interfaces. Using the indices of refraction for ITO, glass, and air (~ 2.2 , 1.5 , 1.0), the critical angle for the ITO-glass interface is:

$$\text{ArcSin} \left[\frac{1.5}{2.2} \right] \approx 43^\circ.$$

Assuming that photons are emitted equally in all directions, the fraction of photons which are not total internally reflected at this interface is $\sim (43^\circ \times 2)/180^\circ \approx .48$. Similarly, the critical angle for total internal reflection at the glass-air interface is:

$$\text{ArcSin} \left[\frac{1.0}{1.5} \right] \approx 42^\circ.$$

Again, assuming that photons are approaching this interface at all angles, the fraction of photons which are transmitted is $\sim (42^\circ \times 2)/180^\circ \approx .47$. Thus the total fraction of photons which are transmitted across the ITO-glass and glass-air interfaces is $= .48 \times .47 \approx .22$, or 22%. This maximum η_{OC} drastically reduces the maximum η_{EQE} achievable in a standard OLED (where no attempt is made to enhance η_{OC}).

The final factor in eqn. 2.3 is the photoluminescence efficiency, η_{PL} . This factor was addressed in the previous chapter for fluorescent (η_f) and phosphorescent (η_{ph}) materials. Conceptually, it is defined as the fraction of excitons formed in the emissive regions which undergo radiative decay, rather than nonradiative decay. With the proper selection of emissive material, this factor may approach unity.²¹ All together, these four factors conceptually define η_{EQE} . We can see from the maximum values of each of the constituent parts ($\chi = 1.0$, $\gamma = 1.0$, $\eta_{OC} \approx 0.2$, $\eta_{PL} \sim 1.0$), η_{EQE} may approach a maximum of 0.20, or 20% for phosphorescent-based OLEDs. If we account for the typical optical loss

in an OLED due to η_{OC} , we may define an *internal* quantum efficiency, $\eta_{IQE} = \chi \times \gamma \times \eta_{PL}$, which represents the efficiency with which a particular device converts injected charge carriers to generated photons.

2.2.3 Power Efficiency

While η_{EQE} may be a good metric of an OLED's ability to convert charge to light, it does not account for the power used by the OLED in the process, nor is it calibrated to the response of the human eye. Therefore, it is beneficial to define a luminous power efficiency, η_P , which is the ratio of optical power output (in lumens), per unit electron power (W). This metric then has the units of lm/W and accounts for the spectral output of the device relative to the photopic response, as well as the current injected into – and the voltage used by – the OLED. This metric is defined in terms of the η_{EQE} as:

$$\eta_P = \eta_{EQE} \times \phi \times \frac{V_{photon}}{V_{OLED}}, \quad (2.4)$$

where ϕ is defined in Eqn. 2.1, V_{photon} is the energy of the average photon emitted (in eV), and V_{OLED} is the voltage used by the device. The use of η_P implicitly assumes the use of the OLED in display or lighting applications meant for observation by the human eye. As it also accounts for the power used by the device, it is a definitive measure of display and lighting OLED efficiency.

2.2.4 Measurement and Calculation of Device Parameters

The characterization of OLED operation and performance necessitates three main measurements: the device current (I_{OLED} , mA, often transformed to current density, J , mA/cm²) versus voltage (V_{OLED} , V), the brightness (B , cd/m²) versus voltage, and the

spectral distribution of emitted light ($EL[\lambda]$, W/cm^2). Once collected, this data is transformed and calibrated to produce the figures of merit and metrics used to characterize OLEDs: the spectra (typically used as recorded, in W/cm^2), the current density-voltage characteristics (J - V plot), the brightness-voltage characteristics (B - V), and the η_P and η_{EQE} of the device versus J , V , and/or B . The first plot is relatively straight forward to achieve, a source-measurement unit with sufficient sensitivity (such as the Agilent 4155C used throughout this thesis), and capable of sourcing and measuring both current and voltage, is used to directly measure the current of the device at each applied voltage. The EL spectrum of the device is measured via a fiber-coupled spectrometer (an Ocean Optics HR4000 is used to cover a wavelength range of 300-900nm). A measurement of brightness is achieved through the use of a large-area photodetector (a Hamamatsu detector, model S3584-08 is used here). This detector is large enough such that every photon emitted in the forward viewing direction is assumed to be collected. An aperture is used to ensure that light which escapes through horizontal waveguide modes is not collected (as it should not contribute to η_{EQE}), a schematic of this is shown

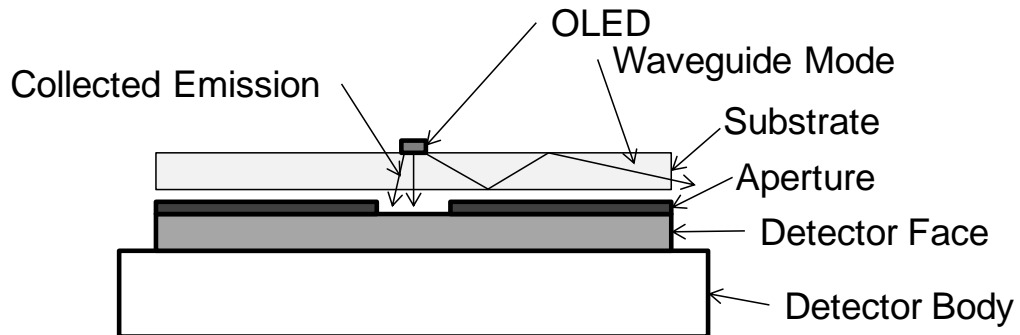


Figure 2.7: Schematic of OLED testing setup for collection of JV and BV data. An aperture prevents waveguide modes from contributing to measured output.

in Figure 2.7. The output of the photodiode, however, is not given in units of optical power. Instead the detector outputs a current (I_{ph}) which is proportional to the optical power incident on the face of the detector. The proportionality constant is the “responsivity” of the detector, in units of A/W. Each detector has a wavelength dependent responsivity, $R[\lambda]$, shown in Figure 2.8 for the detector used in this work. Similar to the calculation of the spectral overlap with the average wavelength of photopic response, the responsivity of the average wavelength is calculated:

$$\bar{R} = \frac{\int R[\lambda] \times EL[\lambda] d\lambda}{\int EL[\lambda] d\lambda}. \quad (2.5)$$

From this, the actual optical power may be calculated by $P_{OPT} = I_{ph} \times 1/\bar{R}$ at each applied voltage. Using Eqns. 2.1 and 2.2, the luminance output (in lm) and B (in cd/m^2) may be calculated. With the luminance output calculated, η_p may now be computed at each applied voltage (and current density). An alternative method of testing the

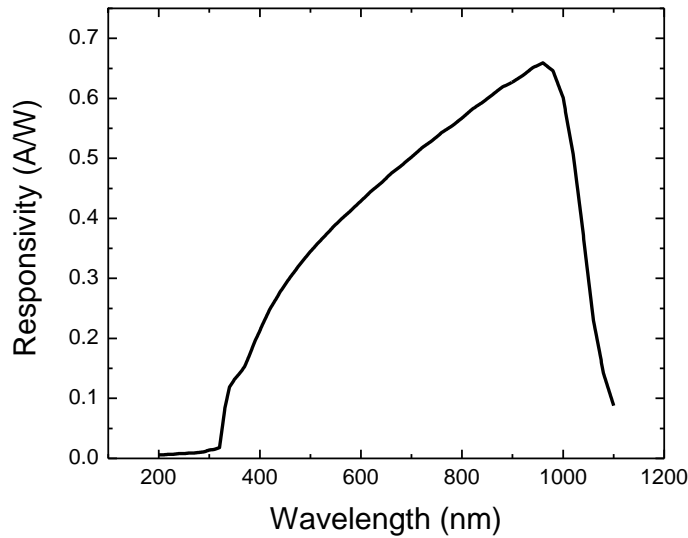


Figure 2.8: Responsivity of the Hamamatsu S3584-08 silicon photodiode used in this work

optical output of the device makes use of a spectroradiometer. This device is capable of measuring the EL spectrum of the device and the total power output of the device simultaneously. This measurement is often made at some distance from the substrate, so an assumption of the angular distribution of the output is needed in order to properly calculate output power.

A calculation of η_{EQE} is not made by measuring the parameters of Eqn. 2.3; instead, the actual flux of photons emitted in to the forward viewing direction is measured and compared to the flux of injected electrons. The latter part of this measurement is made directly by the source measurement unit (the current of the device, I_{OLED} , being the number of charges per second, q/s). The flux of photons may be calculated with P_{OPT} and a conversion from power to number of photons. This is done by calculating the average wavelength of the spectral output:

$$\bar{\lambda} = \frac{\int EL[\lambda]d\lambda}{\int \frac{1}{\lambda} EL[\lambda]d\lambda}. \quad (2.6)$$

The photon flux is then, P_{flux} :

$$P_{flux} = \frac{I_{ph} \times \frac{1}{\bar{\lambda}}}{hc \times \frac{1}{\bar{\lambda}}}, \quad (2.7)$$

where h is Planck's constant and c is the speed of light. A complete calculation of η_{EQE} can now be written:

$$\eta_{EQE} = \frac{\frac{I_{ph} \times \frac{1}{\bar{\lambda}}}{hc \times \frac{1}{\bar{\lambda}}}}{I_{OLED}/q}. \quad (2.8)$$

2.3 Basic OLED Operation and Design

2.3.1 The First OLED

The first demonstration of electroluminescence (EL), that is luminescence based on the injection of both electrons and holes from exterior contacts, was by Helfrich and Schneider in 1965.⁴⁹ They used a single crystal of anthracene with liquid metal contacts formed from positive and negative ions of anthracene. The device required operating voltages of $\sim 10^2$ - 10^4 V and achieved an efficiency of $\sim 0.1\%$ (W/W). While this was an important demonstration of EL in organic materials, the high voltages and low efficiency of the device made it impractical for use in commercial applications. The revolutionary report of efficient, low-voltage operation of an OLED came in 1987 from the Eastman Kodak Company.⁵⁰ Tang and VanSlyke, developed a bilayer structure formed from two different organic semiconductors, a diamine, now known as di-[4-(N,N-ditolyl-amino)-phenyl]cyclohexane (TAPC) and tris-(8-hydroxyquinoline)aluminum (Alq_3). Importantly, they were able to use ITO and a Mg:Ag alloy to attain efficient injection of holes and electrons, respectively, into the organic layers (Figure 2.9a). They also thermally evaporated both the organic active materials as well as the Mg:Ag cathode via VTE, a much simpler method than previous demonstrations of organic EL which relied on the use of single crystals. The η_{EQE} of the bilayer device reached a peak value of $\sim 1.0\%$ with a brightness as high as 10^3 cd/m^2 at voltages less than 10V. The operation of the device is best described using an energy diagram of the structure, shown in Figure 2.9b. Upon application of an applied voltage, holes are injected from the ITO anode and

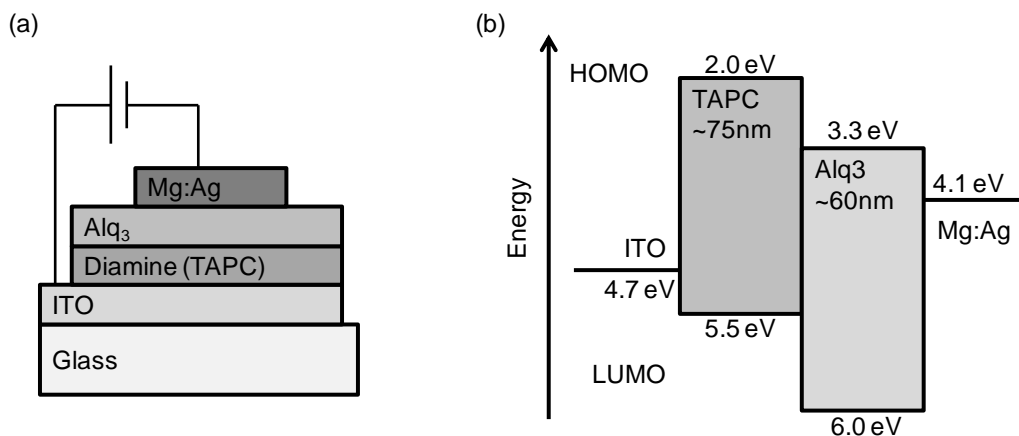


Figure 2.9: (a) Diagram of the Tang and VanSlyke bilayer OLED. The organic layers (TAPC, Alq₃) are sandwiched by electrodes formed from ITO and Mg:Ag. (b) The bilayer OLED diagram on an energy landscape, without the application of a voltage bias. The HOMO and LUMO and work function values are taken from literature.

electrons are injected by the Mg:Ag cathode. Holes are transported by the electric field across the TAPC, which serves as a hole transport layer (or HTL); similarly electrons are transported across the Alq₃, which is the electron transport layer (ETL). When both carriers reach the interface one of three things may happen: a hole is injected on to the HOMO of Alq₃, an electron is injected on to the LUMO of TAPC, or an exciton is formed across the two adjacent molecules, with the hole residing on the HOMO of the TAPC, the electron on the LUMO of Alq₃ (such an exciton is referred to as an “exciplex”). Tang and VanSlyke observed only emission from the Alq₃ species; therefore it is likely that excitons were primarily formed on that species, according to the first option. Had electrons been injected into the TAPC layer, excitons would have likely formed there, leading to some radiative decay of TAPC excitons and a spectral output with contributions from both TAPC and Alq₃ would have been observed. Had an exciplex formed, any radiative decay of that species would have been observed in the EL

as a broad emission feature red-shifted from the emission of either TAPC or Alq₃, no such emission was observed.

2.3.2 The Use of an Emissive Guest

An important progression from the use of pure layers of organic materials (or “neat” layers) as emissive regions was the introduction of luminescent guest molecules doped in to a host matrix. This was also demonstrated by Tang et al.,⁵⁰ who were motivated by the high η_{PL} observed for organic laser dyes in dilute solution. In that work, they used variety of coumarin and dicyanomethylene-based (DCM) molecules in devices which yielded η_{EQES} as high as 2.5%, an enhancement of 250% over previous devices. The use of emissive guests has since been a hallmark of OLED design. Much work has been dedicated to the synthesis and characterization of emissive guests with high η_{PL} , environmental stability, and wide color gamut.^{21,51}

One important advance in the development of OLEDs came with the introduction of efficiency phosphorescent dopant molecules.^{10,20,22,52–54} Several reports of very high peak η_{EQE} , above the threshold for fluorescent materials in a standard OLED ($\eta_{EQE} = 5\%$, given $\eta_{OC} = 20\%$ and $\chi = 25\%$) confirmed that these organic species do indeed utilize triplet excitons in the emission of light. These phosphorescent molecules may also be engineered to have very high η_{PL} , approaching unity efficiency at low concentration.²¹ Recent studies have shown phosphorescence-based OLEDs with peak η_{EQES} which reach the optical limit of $\sim 20\%$.^{55–58} The requirements for achieving these high efficiencies are discussed in greater detail below.

2.3.3 Achieving Broadband Emission

One potential application for OLEDs is in broadband, or white, light-emitting devices. To achieve a high-quality white light source, the majority of visible wavelengths must be represented in the EL spectrum, which is typically achieved through the use of multiple emissive guests.^{29,59–61} The photophysical properties of the molecules must be considered in the design of high-efficiency devices. Energy transfer from blue light-emitting molecules may be efficient if a narrow-gap molecule (such as a red light-emitting molecule) is nearby. Additionally, all emissive dopant molecules must undergo excitation, either through exciton formation on the molecules or energy transfer, in order to contribute to the EL. There are several emissive layer designs which have been developed to address these intermingled issues.

2.3.4 Multilayer OLED Operation

The devices which have shown the highest peak η_{EQES} often have a multilayer structure which often is comprised of at least three layers and four materials. A conceptual version of such a device is presented in Figure 2.10a. In this device, an emissive layer (EML) is comprised of a host molecule and an emissive dopant. The host is typically responsible for charge injection and charge transport, though the guest may participate if it is present in high enough concentration. The EML is sandwiched between two transport layers, an HTL on the anode side and an ETL on the cathode side. With the application of an applied bias (shown in Figure 2.10b), electrons are injected from the cathode to the ETL, while holes are injected into the HTL. The charges are

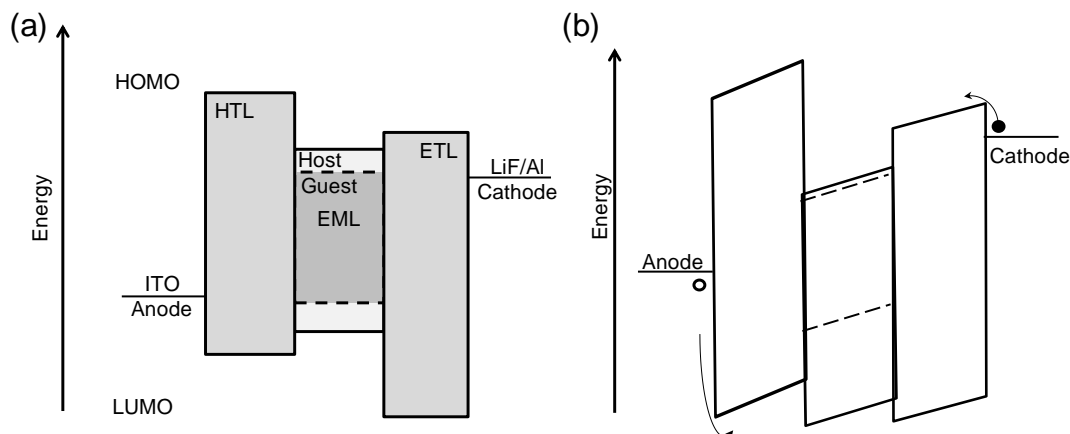


Figure 2.10: (a) Energy diagram of prototypical three layer OLED at zero applied bias. (b) Energy diagram of a device under bias, the exact degree of band bending is not well characterized. The dilute-doped guest energy levels are represented by dashed lines.

transported across their respective transport layers to the EML. Once at the EML, the charges are injected on to the host, or directly on to the guest if, as shown, the guest energy levels fall inside those of the host material. Given the often dilute concentration of guest molecule present, only charges which reside on the host material are mobile. When both charges are present in the EML, an exciton is either formed on the host, or directly on the guest where they decay radiatively. Ideally, excitons formed on the host are energy transferred to the guest molecule via the mechanisms described previously, where they decay radiatively with high η_{PL} .

2.3.5 Typical Device Operation

To illustrate the operation of a typical OLED, a device structure (shown in Figure 2.11 with the molecular structures of the constituent materials) of ITO / NPD (30 nm) / CBP:Ir(ppy)₃ (20 nm, 10wt. % guest) / BPhen (40 nm) / LiF/Al (1 nm/100 nm) has been fabricated, where NPD: N, N'-bis(naphthalene-1-yl)-N, N'-bis(phenyl)-benzidine, CBP:

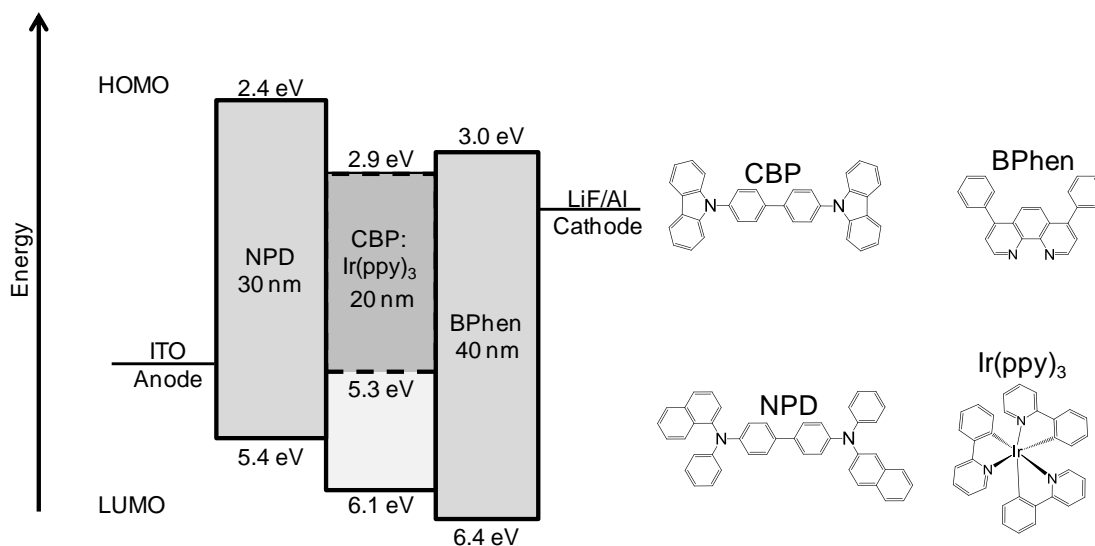


Figure 2.11: Energy band diagram of an archetypical three-layer OLED with a phosphorescent dopant, Ir(ppy)₃. The chemical structures of the materials of interest are also shown.

4,4'-bis(9-carbazolyl)-1,1'-biphenyl, Ir(ppy)₃: tris(2-phenylpyridine)iridium(III), and BPhen: 4,7-diphenyl-1,10-phenanthroline. The EL spectral output in the green portion of the spectrum, shown in Figure 2.12a, is characteristic of the phosphorescent guest, Ir(ppy)₃, a commonly used dopant capable of high η_{PL} . The current density-voltage and brightness-voltage characteristics of the device are presented in Figure 2.12b. From this data, η_{EQE} and η_P are calculated, shown in Figure 2.12c as a function of current density. Given that the EL spectra closely matches the known spectra for Ir(ppy)₃ with no observable host emission, we can begin to describe the operation of this device. Charges injected from the electrodes travel through the respective transport layers. Given the favorable HOMO level alignment of BPhen and CBP,^{3,62} it is likely the electrons are efficiently injected into the EML. Holes from NPD, however, have a large energy barrier to injection on to CBP.⁶³ With the HOMO level of Ir(ppy)₃ falling inside that of NPD

and CBP,⁶⁴ it is likely that holes are injected directly on to Ir(ppy)₃, where they capture electrons from the LUMO of CBP to form excitons which radiatively decay with high η_{PL} .

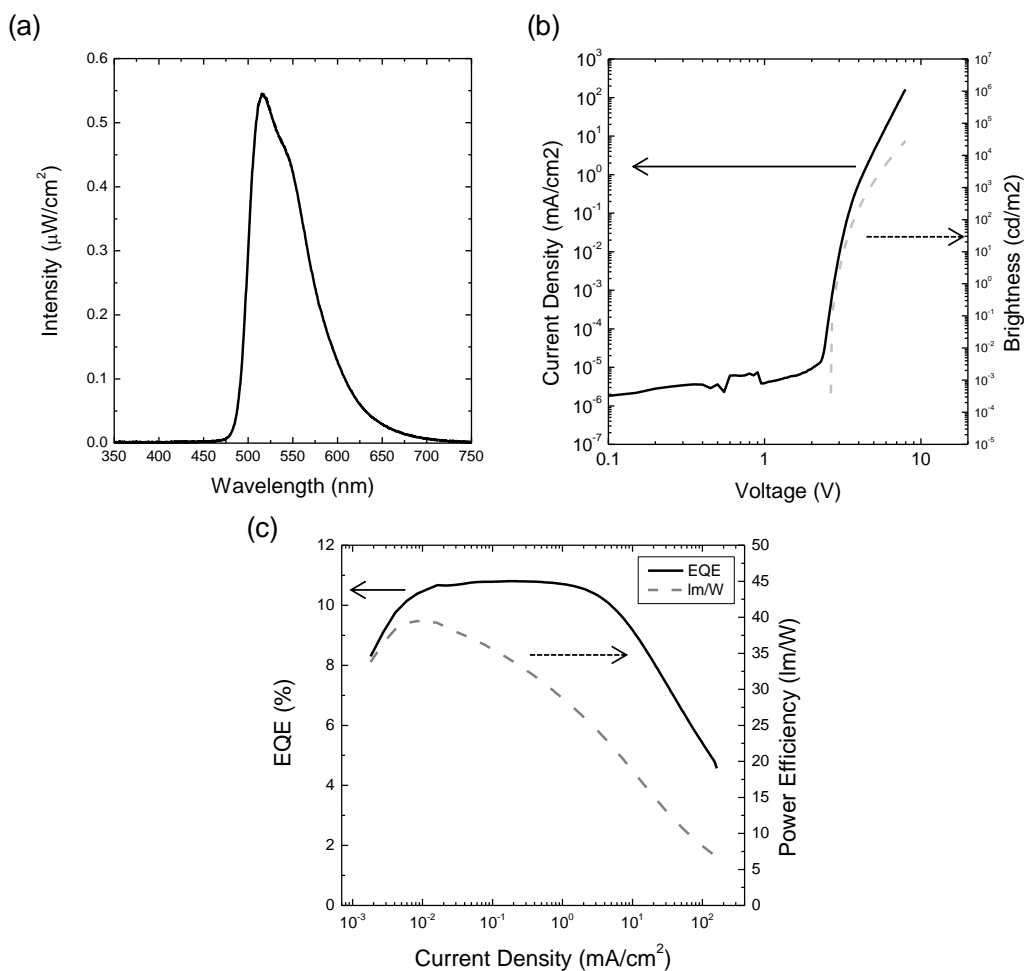


Figure 2.12 (a) Electroluminescent spectral output of the Ir(ppy)₃-based device. (b) Current density-voltage and brightness-voltage characteristics of the device of Figure 2.11. (c) calculated η_{EQE} and η_p . Peak values efficiencies are: $\eta_{EQE} = 10.8\%$ and $\eta_p = 39.5$ lm/W .

2.3.6 Requirements for High-Efficiency OLEDs

The design of OLEDs for high-efficiency can be mostly understood from Figure 2.10 and the conceptual equation for η_{EQE} , eqn. 2.3. First, hole transport materials

(HTMs) and electron transport materials (ETMs) must be selected such that they have high or matched carrier mobilities, the former to reduce driving voltage, the latter to equalize the flux of hole and electrons into the emissive layer (i.e. to improve γ). Additionally, the transport layers should have large singlet and triplet exciton energies,^{65,66} such that excitons on nearby guest molecules do not energy transfer to the transport layer, resulting in a reduction in γ . Second, a host material must be selected (or constructed from multiple materials, as discussed in subsequent chapters) which is able to efficiently transport carriers of both charge, i.e. high electron and hole mobilities.^{67–69} The host material must also have high singlet and triplet exciton energies, and the appropriate optical properties to ensure both that excitons formed on the host are efficiently energy-transferred to the guest and that excitons formed on the guest do not back-transfer to the host.^{13,53,66} Third, an emissive guest should be selected for the desired spectral output as well as for high η_{PL} and χ .

These concepts may be condensed in to two main concepts: materials selection and management of charge (and subsequently, excitons). Proper materials selection at the onset will ensure that the device efficiency is not initially hampered, by maximizing η_{PL} and χ , where γ may be affected (and maximized) by device design. The management of charge is equally crucial, though it will depend on the materials chosen. Careful consideration of the desired spatial location of charge may allow precise engineering of the exciton formation region (where the spatial distribution of electrons and holes overlap), and can mitigate many of the potential loss mechanisms: leakage of charge

through the emissive layer and device, energy transfer of guest excitons to nearby transport molecules, and loss of guest excitons to back-energy transfer to the host.

2.3.7 White-Light Emitting OLEDs

The use of OLEDs for solid-state lighting (SSL) applications requires broadband visible, or white-light, emission. A quality white-light source must have every wavelength of visible light represented, such that reflections, absorptions, etc. of that

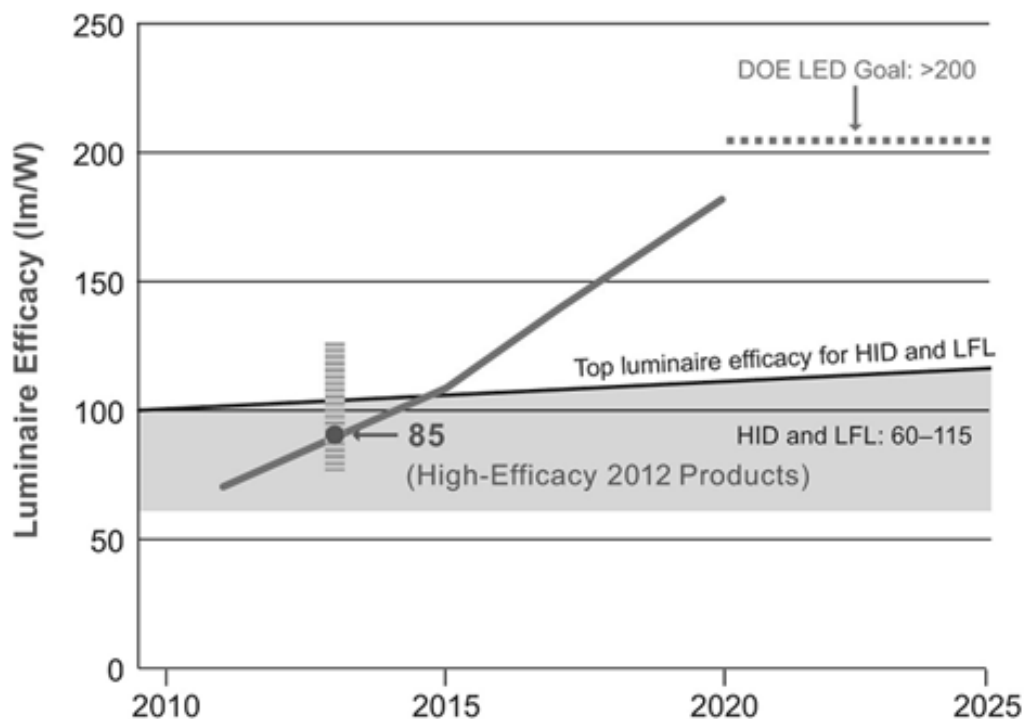


Figure 2.13: Efficiency progress and goals for solid-state OLED lighting. The US DOE goal for both inorganic LED and OLED luminaires is 200lm/W by 2025. From the “Solid-State Lighting Research and Development Multi-Year Program Plan,” U.S. DOE/EERE-0961

source on everyday objects are ‘true’ to the objects color. This has been standardized by comparing the emitted spectrum of a white light source with an ideal blackbody which radiates with a similar color temperature (or color-coordinated temperature, “CCT”).

More so than many other applications of OLEDs, SSL requires the highest possible efficiency, with the lowest possible manufacturing cost. While consumers may be willing to pay a premium for a next-generation cell phone or television display, OLED-based SSL requires cost-competitiveness with current technologies. The U.S. Department of Energy has set efficiency targets for both inorganic LEDs and OLEDs which reach as high as 200lm/W by 2025 (see Figure 2.13) for the whole luminaire (or total lighting package).⁷⁰

Broadband emission may be achieved via several routes; incorporating a combination of blue-, green-, yellow, orange-, and red-light emitting molecules has typically been the most common. Some white OLEDs have been demonstrated with a

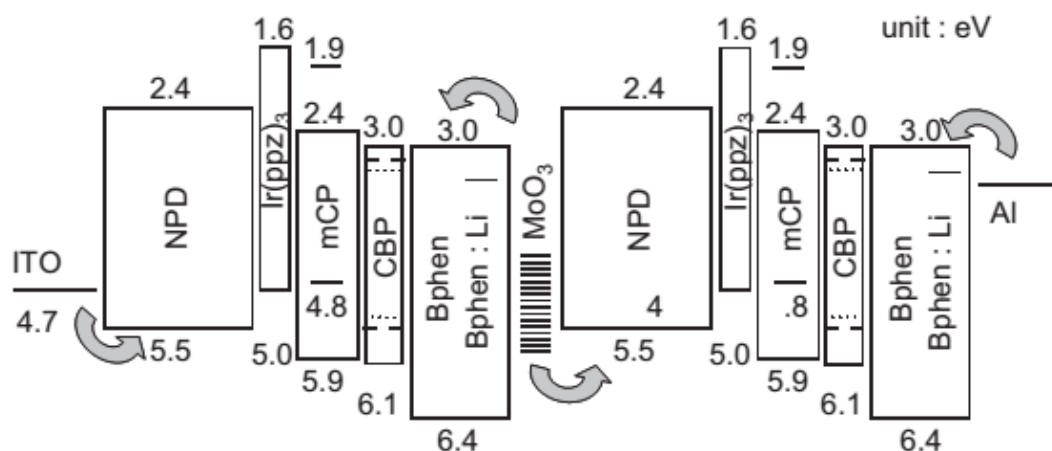


Figure 2.14: A white-light emitting tandem OLED. Copyright WILEY-VCH Verlag GmbH & Co. KGaA, Weinheim, from Kanno et al.

‘tandem’ device architecture,^{71–73} where internal charge generation layers serve as internal contacts. A schematic of one such device is shown in Figure 2.14.⁷² Recently, a new class of molecules which emit from both a blue-light emitting phosphorescent monomer as well as an aggregation-induced red-light emitting excimer have been

demonstrated.^{74,75} Devices incorporating this type of molecules are discussed in greater detail in Chapter 9.

2.3.8 State of the Art

Current best-in-field devices (single-wavelength, which *have not* incorporated mechanisms to improve η_{OC}) have shown η_{EQES} which approach the optical outcoupling limit of $\eta_{EQE} = 20\%$.^{22,54–56,58,76,77} The power efficiencies of these devices are also high, nearing values of 100 lm/W.⁵⁵ These are peak efficiencies, however; the efficiencies of the devices at lighting and display relevant brightness levels (10^2 - 10^3 cd/m²) are often much lower,^{65,78} due to a decrease in the efficiency of the device as the current density is increased, an affect termed the “efficiency roll-off.”⁷⁹ These devices are often comprised of complicated designs, having multiple, doped transport and blocking layers.

2.4 Overview of This Thesis

This thesis seeks to elucidate the structure-property-device operation relationships which govern efficacious organic light-emitting device (OLED) operation. Credence is given not only to peak efficiency, but also to other important factors, such as lighting and display relevant efficiencies, efficiency roll-off parameters, device structure complexity, and others. This thesis will examine a variety of device architectures in an effort to identify and engineer the key materials and device structure parameters which govern device operation and performance.

Chapter 3 introduces a novel device architecture, the graded-emissive layer (G-EML) structure, which achieves high performance in a single-layer device structure.

Chapter 2: Introduction to Organic Light-Emitting Devices

Chapter 4 examines the post-deposition composition of a variety of OLED structures, while Chapter 5 explores the electrical properties of the G-EML devices. Chapter 6 presents an experimental technique capable of measuring the spatial extent of electron-hole charge density overlap in an OLED. Chapter 7 examines the outcoupling efficiency of OLED structures, and means to increase the far-field extraction of generated light. Chapter 8 examines the important parameters which govern efficiency roll-off and discusses methods and device architectures which may improve device operation. Chapter 9 presents work on white-light emitting devices, aimed at achieving high-efficiency operation with simple device structures. Chapter 10 describes important future directions for organic optoelectronic and OLED work.

Chapter 3 Graded Composition Emissive Layer Light-Emitting Devices

3.1 Evolution of OLED Architectures

Historically, the development of organic light-emitting device architectures has sought to separate and assign the necessary device operation processes (charge injection, charge transport, exciton formation, light emission, etc.) to individual materials and/or device layers.^{10,21,80} In Chapter 2, the progression to a bilayer device from a discrete single-crystal was discussed, as well as the use of a dilute luminescent guest. As the OLED field grew and important device operating conditions were identified, additional materials and layers were developed and included in the layer stack.⁷⁷ Exciton blocking layers with high singlet and triplet energies were included to prevent exciton energy transfer out of the emissive layer. Charge transport layers were developed which had high mobilities and which did not re-absorb the emitted light. Charge injection layers were incorporated for enhanced charge injection from the contacts. All the while, various emissive layer architectures were developed to improve charge balance.^{77,78,81–83} One high-efficiency device architecture which embodies these developments is shown in Figure 3.1.⁷⁷ Here, conductivity-doped transport layers (designated p- or n-doped) are utilized to reduce the voltage drop across these layers. Electron and hole blocking layers (EBL and HBL, respectively) are used to prevent energy transfer from the emissive layer host or guest molecules to the transport layers. A two-layer emissive layer is used, where one material is an electron transporting host, the other a hole transporting host, and both

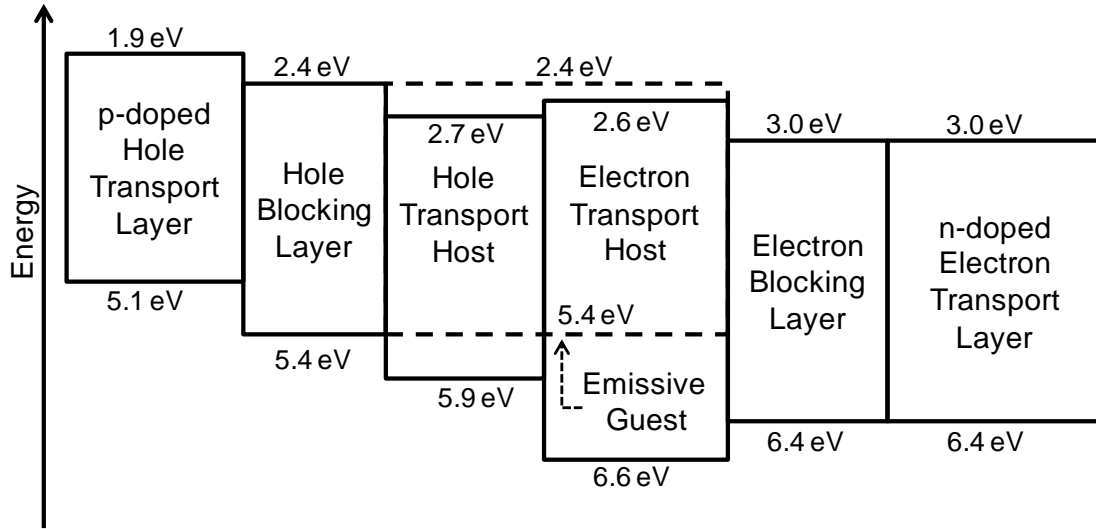


Figure 3.1: Energy level diagram of a high-efficiency OLED. This device is comprised of two transport layers, two charge/exciton blocking layers, and has an emissive layer which contains two host materials in addition to an emissive guest.

are doped uniformly with the emissive guest. This emissive layer configuration is known as the “double emissive layer” or D-EML.⁸¹ This device achieves $\eta_{EQE} = 19.3\%$, very near the limit set by η_{OC} ($\sim 20\%$) and reaches $\eta_P = 77$ lm/W. While this demonstration of performance is important, it requires six layers, nine different materials (including the p- and n-type dopants in the doped transport layers), and is fabricated in six steps. Other devices which have shown improved efficiencies have utilized layers interposed between the anode and HTL. These layers are designed to improve hole-injection (hence the name, hole-injection layer, “HIL”) in multilayer OLEDs and may be polymer, metal-oxide,⁸⁴ or small-molecule based.^{85,86} This chapter introduces a novel device design which seeks to simplify the traditional architecture, while maintaining high efficiency and stable device operation.

3.2 Graded-Composition Emissive Layer

The device architecture presented here was conceived as an exercise in controlling the efficiency of exciton formation through the manipulation of injected charge carriers in the emissive layer. To control the spatial extent of charge carriers in the device, a layer whose composition varies continuously, from nearly 100% HTM at the anode to nearly 100% ETM at the cathode, was fabricated with a constant doping of a luminescent guest (Figure 3.2a). This layer structure was termed the “graded-emissive layer” or G-EML. The fabrication of this layer was achieved through the co-deposition of the three constituent materials using time-varying deposition rates, described in Figure 3.2b. This was made possible through the use of a VTE system where each material, and

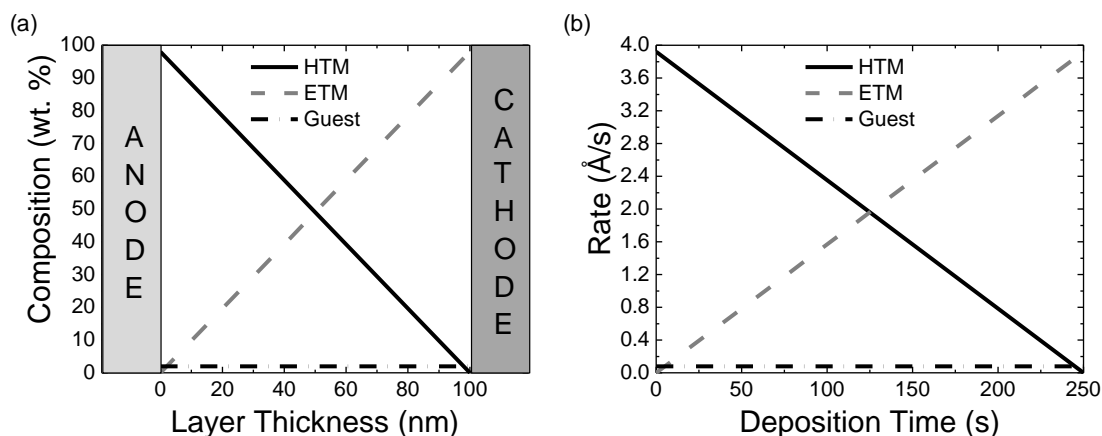


Figure 3.2: (a) Schematic of a graded-composition layer. The HTM and ETM host materials have a continuously-varying composition across the layer: from nearly 100% at the respective electrode to 0% at the opposing electrode. The emissive guest concentration is kept constant throughout the layer. (b) The deposition rate profiles of the constituent materials.

rate monitor, is isolated from the others, and a carefully tuned PID controller with a programmed, linear deposition rate ramp profile. Devices were fabricated in a single process, using 4,4',4''-tris(carbazol-9-yl)triphenylamine (TCTA) as the HTM, 4,7-diphenyl-1,10-phenanthroline (BPhen) as the ETM, and the archetypal green

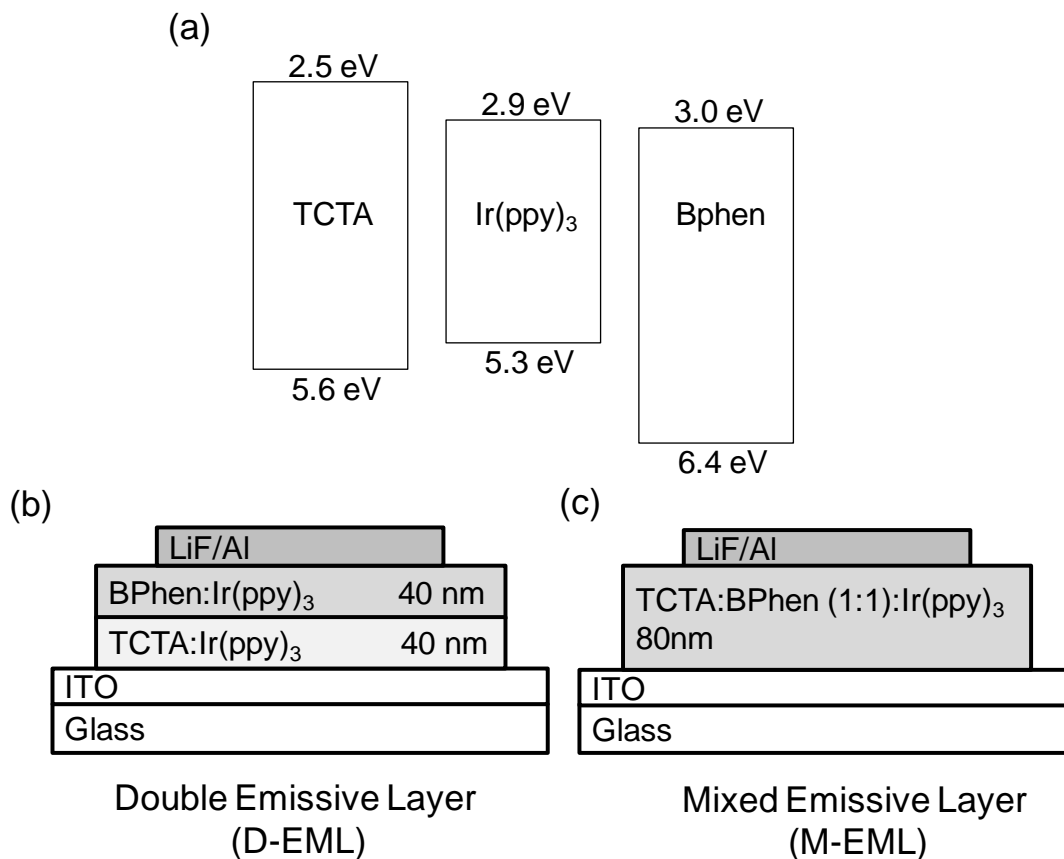


Figure 3.3: (a) Energy levels of the green light-emitting G-EML device. Layer structure of the simplified (b) double-emissive layer, and (c) mixed emissive layer devices.

phosphorescent guest, *fac*-tris(2-phenylpyridine) iridium (III) [Ir(ppy)₃], as the emitter at an optimized concentration of 2 wt.%. The energy levels of these materials are shown in Figure 3.3a.^{87,88} These host materials are well matched for optimum charge balance as both are characterized by charge carrier mobilities of $\sim 10^{-4} \text{ cm}^2 \text{ V}^{-1} \text{ s}^{-1}$ at an applied field of $\sim 10^5 \text{ V cm}^{-1}$.^{89,90}

The G-EML structure was sandwiched between typical OLED electrodes: ITO as an anode and LiF/Al as a cathode. For comparison, simplified OLEDs based on a D-EML or a mixed-host emissive layer (M-EML) architecture were also fabricated. The M-EML architecture consists of a uniformly mixed distribution of ETM, HTM, and the

phosphorescent emitter in a set composition ratio. The result is a large interface area between the ETM and HTM, creating favorable conditions for exciton formation.⁸³ The layer structures for these additional devices is: 40 nm TCTA:Ir(ppy)₃ (5 wt. %)/40 nm BPhen:Ir(ppy)₃ (5 wt.%) for the D-EML (Figure 3.3b), and 80 nm TCTA:BPhen:Ir(ppy)₃ (1:1: 5 wt. %) for the M-EML (Figure 3.3c). The optimum Ir(ppy)₃ doping concentration was separately determined to be 5 wt.% for each of these comparison architectures.

Previous work has demonstrated that the η_{PL} of phosphorescent materials may approach unity in dilute-doped films (<2 wt. %).²¹ Unfortunately, conventional devices using such low doping levels often show low efficiency and significant host luminescence.^{22,54} This has been attributed to incomplete host-guest energy transfer or inefficient charge trapping on the guest. In the G-EML, injected charge carriers are initially carried by the respective transport materials into the device. At very low concentration it is unlikely that Ir(ppy)₃ participates in charge injection from the electrodes or contributes significantly to charge transport. Due to the HOMO level alignment between Ir(ppy)₃ and TCTA, Ir(ppy)₃ may act as a hole trap with excitons forming directly on Ir(ppy)₃.^{66,80,91} The combination of charge transport on the host materials with direct exciton formation on the guest allows for the use of low doping concentrations and thus the ability to realize a high η_{PL} for the guest. Figure 3.4a shows the electroluminescence (EL) from OLEDs consisting of the D-EML, M-EML, or G-EML already described. In each case Ir(ppy)₃ emission is observed, with no emission from either host material. For the G-EML Figure 3.4b, the EL spectrum does not vary

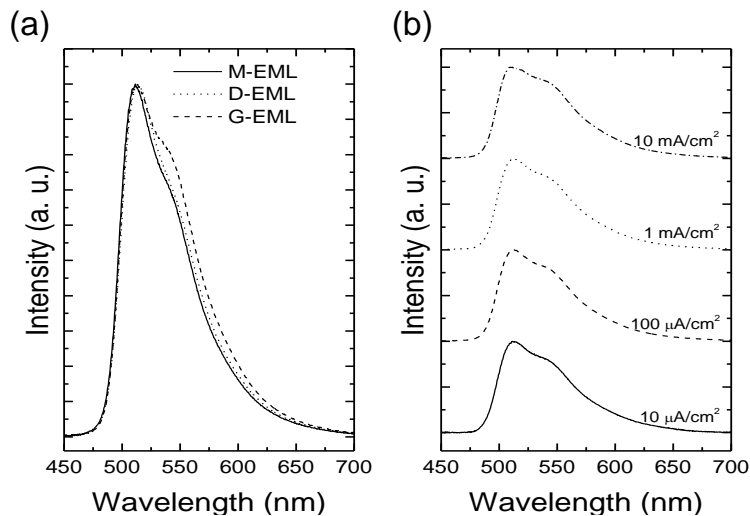


Figure 3.4: (a) Normalized EL spectra of M-EML, D-EML and G-EML OLEDs at a brightness of 1000 cd/m². (b) EL spectra of a G-EML OLED as a function of current density with the applied current density. The lack of host emission supports a model of direct charge-trapping for the excitation of Ir(ppy)₃.

To further test this hypothesis, a 1:1 TCTA:BPhen G-EML OLED was fabricated *without* Ir(ppy)₃. This device was intended to explore the favored excited state of a G-EML device without the emissive guest. Rather than exciting either of the host materials independently, an exciplex (or excited complex) was formed; the EL spectrum is shown in Figure 3.5. Given the HOMO/LUMO energy level alignment of TCTA with BPhen, it is likely that the exciplex hole resides on a TCTA molecule and the electron on an adjacent BPhen molecule. This is confirmed by comparing the TCTA-HOMO / BPhen-LUMO energy gap, ~2.6 eV and the peak emission energy, $\lambda \sim 470$ nm (corresponding to an energy of ~2.65 eV). This energy is well above the triplet excited state energy of Ir(ppy)₃ ~ 2.4 eV.⁹² This supports the model assumption that it is energetically unfavorable

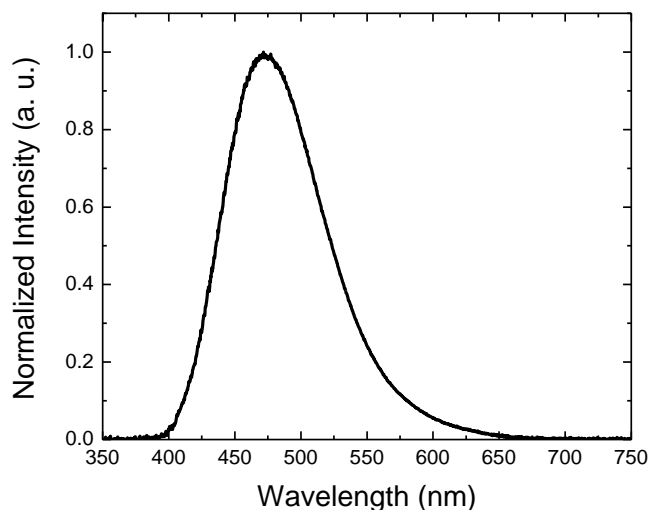


Figure 3.5: Electroluminescence spectrum of a 1:1 TCTA:BPhen G-EML OLED without any emissive guest.

to from a host exciton; indeed, the lowest energy state in an Ir(ppy)₃-doped G-EML OLED is the guest exciton.

Figure 3.6a shows the current density-voltage characteristics of the three Ir(ppy)₃-based devices under consideration. Devices consisting of an M-EML exhibit the largest leakage current at low voltage. Given that the M-EML devices have HTM and ETM dispersed throughout the device, continuous conduction pathways for both holes and electrons likely exist, permitting leakage currents to flow through the organic layer. In the devices containing a D-EML, the separate layers of TCTA:Ir(ppy)₃ and BPhen:Ir(ppy)₃ present large energetic barriers for the leakage of electrons and holes, respectively. This effectively confines charge carriers to the interface between the two emissive layers.^{77,81} In the G-EML device, large concentrations of TCTA near the anode and BPhen near the cathode also prevent charge carriers from leaking across the device, confining them to the central region of the G-EML.

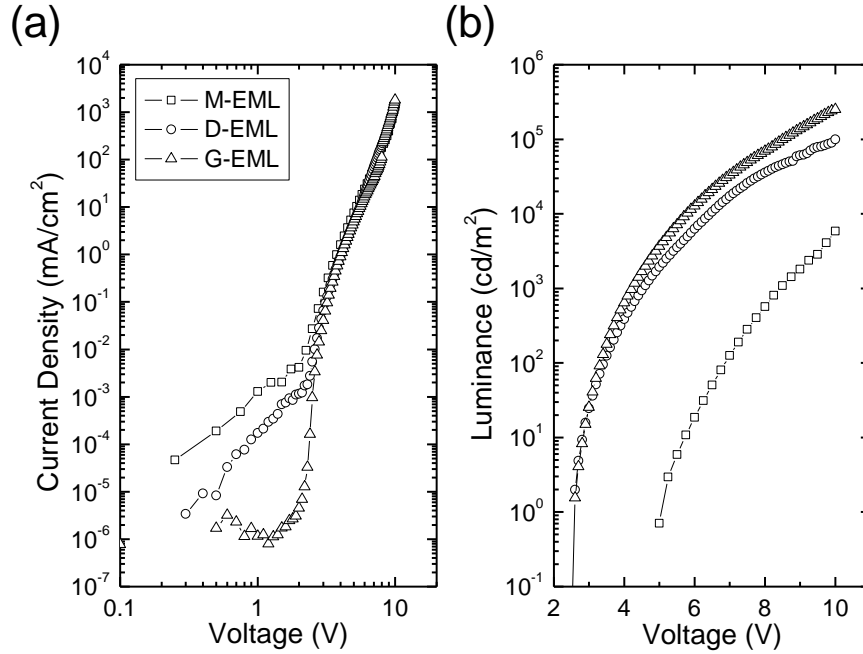


Figure 3.6: (a) Current density-voltage and (b) luminance-voltage characteristics for M-EML (square), D-EML (circle), and G-EML (triangle) OLEDs.

Figure 3.6b shows the luminance-voltage characteristics of OLEDs consisting either of an M-EML, D-EML, or G-EML. The M-EML device requires the largest voltage to realize measureable luminescence, having a turn-on voltage (“ V_{TO} ” defined as the voltage at which the brightness reaches $1 \text{ cd}/\text{m}^2$) of $V_{TO} = 5.0 \text{ V}$. The combination of low brightness and a high leakage current is an indication that the M-EML device suffers from poor charge balance. The D-EML and G-EML architectures reach luminance levels of $\sim 100,000 \text{ cd}/\text{m}^2$ and $\sim 250,000 \text{ cd}/\text{m}^2$ at a voltage of 10 V, respectively. These devices show high luminance at low voltage, with $V_{TO} = 2.6 \text{ V}$. Exciton formation on either TCTA or BPhen would require an input energy at least as large as the optical energy gap of each material, 3.3 eV and 3.4 eV respectively. These values are much larger than the observed turn-on voltage. Additionally, the energetic barriers for electron injection into TCTA and hole injection into BPhen are large, while it is favorable for holes to reside on

Ir(ppy)_3 . This is additional evidence for the direct formation of excitons on Ir(ppy)_3 . The G-EML device shows an enhancement in brightness at high voltage, indicating that charge balance is improved over the D-EML device.

The dependence of the external quantum efficiency and power efficiency on current density is shown in Figure 3.7a and 3.7b. The poor charge balance in the M-EML device has a detrimental effect on its overall performance, with an $\eta_{EQE} = (0.22 \pm 0.03) \%$ and $\eta_P = (0.25 \pm 0.03) \text{ lm/W}$. Improved charge confinement in the D-EML enhances charge balance compared to the M-EML device, leading to peak efficiencies of

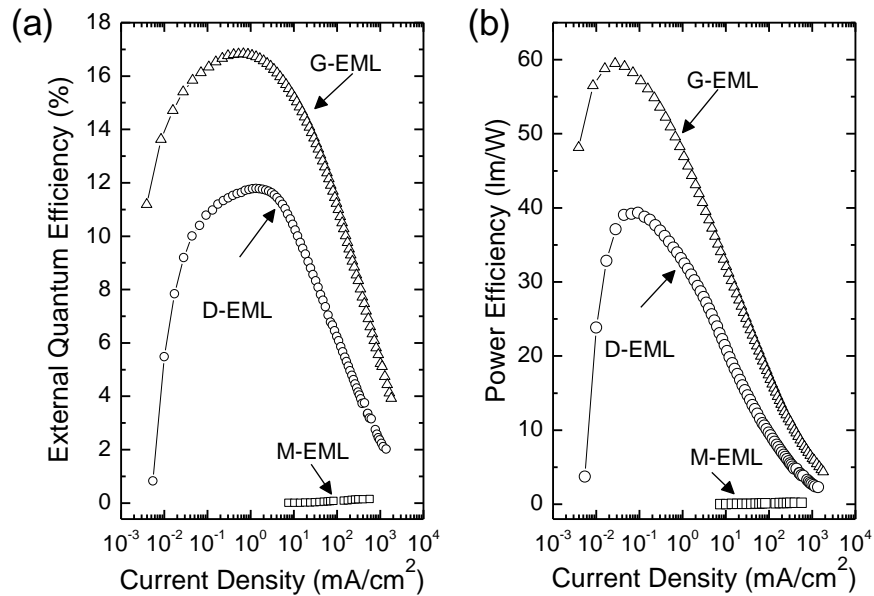


Figure 3.7: External quantum (a) and power (b) efficiency versus current density for M-EML (square), D-EML (circle), and G-EML (triangle) OLEDs. At 1000 cd/m^2 the D-EML OLED has $\eta_{EQE} = 11.7\%$ and $\eta_P = 28.7 \text{ lm/W}$, while the G-EML OLED has $\eta_{EQE} = 16.7\%$ and $\eta_P = 44.4 \text{ lm/W}$.

$\eta_{EQE} = (11.8 \pm 0.3) \%$ and $\eta_P = (39.4 \pm 2.6) \text{ lm/W}$. Owing to the self-balancing nature of the G-EML, charge balance is nearly maximized. This leads to a high external quantum efficiency of $(16.9 \pm 0.4) \%$ and a power efficiency of $(61.0 \pm 1.1) \text{ lm/W}$.

3.3 Optimizing Red G-EML OLEDs

In addition to the green-light emitting G-EML devices, it is also desirable to achieve high efficiency operation in both red- and blue-light emitting devices. Taken together, these three, “primary colors of light,” allow for a spectral distribution which spans the visible wavelength region, enabling both display and white-light applications. Display applications require saturated color spectra; that is, they require deep blue, deep red, and green emission to cover the whole range of spectra needed to display colors. Lighting applications, however, require that all wavelengths of visible light are produced, so that reflections off of objects accurately reflect their color (as compared to a blackbody source, like the sun). Thus, the optimal spectrum of colors differs for lighting and display applications and different emitting molecules are required. The optimization of these structures depends on the constituent materials chosen, and is discussed below.

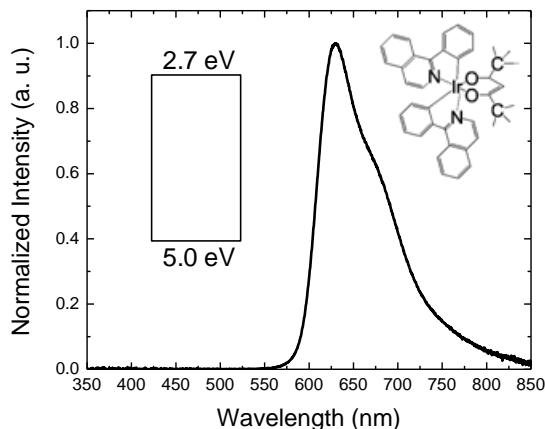


Figure 3.8: EL spectrum of PQIr in a G-EML OLED. The inset shows the chemical structure together with the HOMO and LUMO energy levels, taken from literature.

3.3.1 Red-Light Emitting G-EML OLEDs for Display Applications

Red light-emitting G-EML OLEDs were fabricated using bis(1-phenylisoquinoline)-(acetylacetonate) iridium (III) [PQIr] as the emissive guest. The EL

spectrum of the molecule is shown in Figure 3.8, together with the molecular structure and energy levels. The spectrum peaks at ~630 nm and has spectral components which extend into the deep red and near-IR regions of the electromagnetic spectrum. This spectrum makes PQIr a good candidate for display applications. Given that the energy levels of this molecule fall within those of Ir(ppy)₃, it follows that a similar G-EML host configuration should also permit efficient device performance. Indeed, peak performance is achieved for the same host structure shown in Figure 3.2b, with TCTA and BPhen as HTM and ETM, with a slightly higher optimal doping concentration of 7 wt. %

The current density-voltage and brightness voltage-characteristics of the device are shown in Figure 3.9a. Like the Ir(ppy)₃-based G-EML devices, the PQIr-based G-EML OLEDs show a low leakage current at low voltage, with a steep increase in current

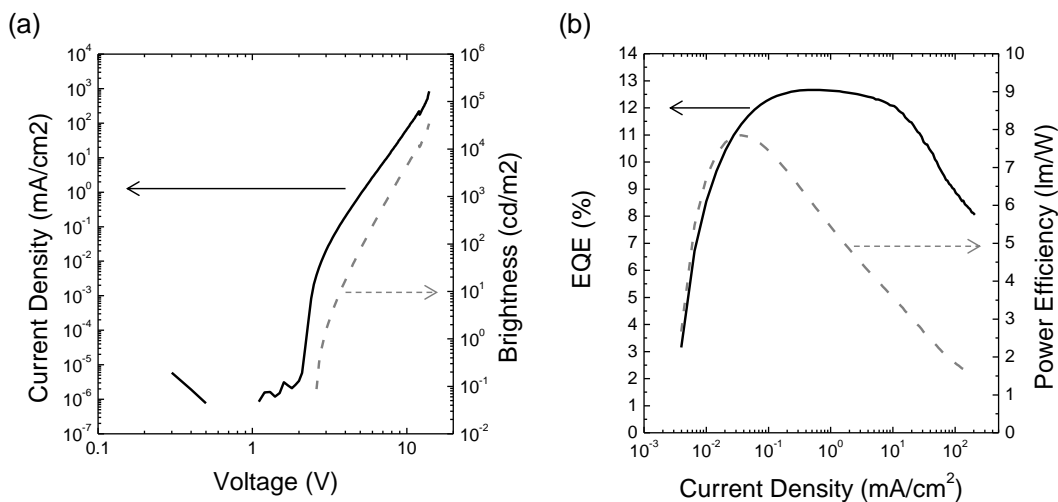


Figure 3.9: (a) Current density-voltage and brightness-voltage characteristics of PQIr-based G-EML OLED. (b) η_{EQE} and η_P versus current density. Peak $\eta_{EQE} = 12.7\%$ and $\eta_P = 7.5$ lm/W are achieved.

density which coincides with a steep increase in the luminance of the device. The turn-on voltage of the device is $V_{TO} = 2.9$ V, indicating an efficient use of voltage. The η_{EQE} and

η_P of the PQIr-based device are shown in Figure 3.9b. Given that the η_{PL} of PQIr is ~60% and with an initial guess that η_{OC} ~20%, an $\eta_{EQE} = 12.7\%$ represents a near unity η_{IQE} .²¹ The relatively low value of η_P for this device is the result of the poor overlap in the spectrum of PQIr with the photopic response function. Given the deep-red EL spectrum, PQIr would be a good candidate for display applications, though the IR components would represent a loss in white-lighting applications.

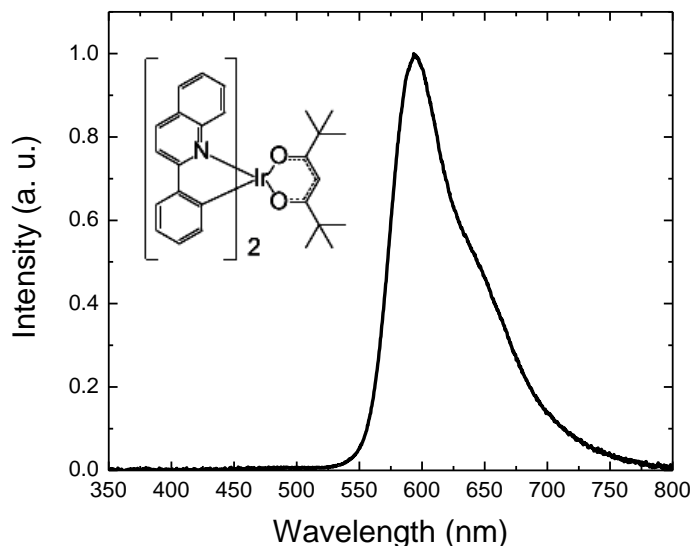


Figure 3.10: EL spectrum of PQIr in a G-EML OLED. The inset shows the chemical structure

3.3.2 Red-Light Emitting G-EML OLEDs for Lighting Applications

To address the need for lighting application-specific devices, a new red-orange emissive guest is chosen, Bis(phenylisoquinoline)(2,2,6,6-tetramethylheptane-3,5-dionate) iridium(III) [Ir(dpm)pq₂]. The EL spectrum for this molecule is shown in Figure 3.10 with the chemical structure. While the shape is similar to PQIr, the spectrum is shifted to higher energies, with a peak wavelength of ~600 nm and much less emission in the near-IR. The current density-voltage and brightness-voltage characteristics of a 1:1 G-

EML device with TCTA and BPhen are shown in Figure 3.11a. The current density-voltage characteristics of the Ir(dpm)pq₂-based devices show the low leakage current characteristic of the optimized G-EML device. Likewise, a low $V_{TO} = 2.75$ V is achieved,

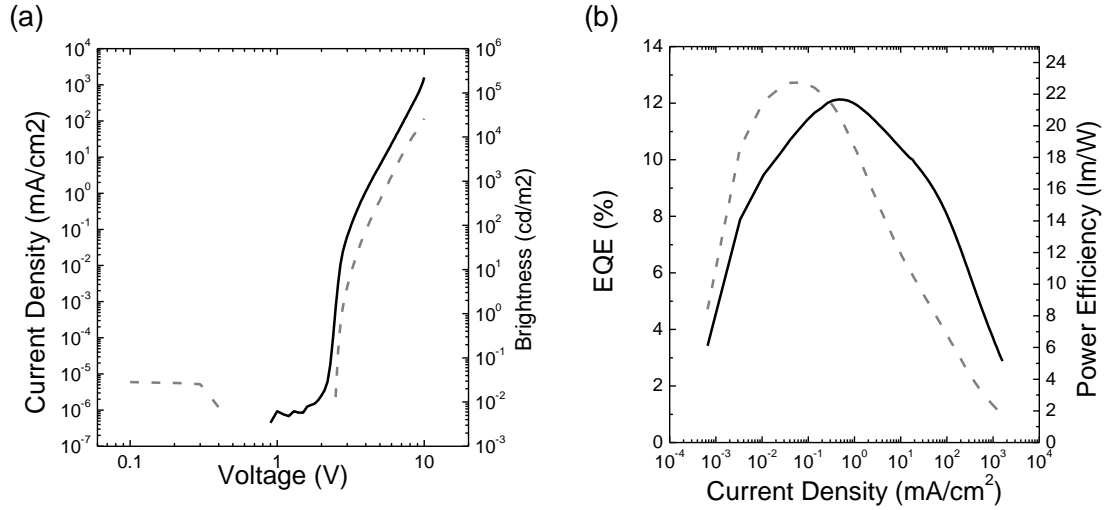


Figure 3.11: (a) Current density-voltage and brightness-voltage characteristics of Ir(dpm)pq₂-based G-EML OLED. (b) η_{EQE} and η_P versus current density. Peak $\eta_{EQE} = 12.1\%$ and $\eta_P = 23.0$ lm/W are achieved.

indicating very efficient voltage use. The η_{EQE} and η_P of the device are shown in Figure 3.11b. With $\eta_{PL} \approx 70\%$, a peak $\eta_{EQE} = 12.1\%$ represents a very high $\eta_{IQE} \approx 85\%$.⁹³ With the improved spectral overlap of the EL spectrum with the photopic response function, a peak $\eta_P = 23$ lm/W is achieved. All together, the η_{EQE} , η_P , and red-orange spectra of the Ir(dpm)pq₂-based G-EML OLEDs render these devices promising candidates for inclusion into white lighting applications.

3.4 Optimizing Blue G-EML OLEDs

Blue-light emitting devices have been a topic of continued research, as it is difficult to find host materials with large enough singlet and triplet energy levels to confine high-energy, blue-light emitting excitons to the emissive guest. It is yet more

difficult to find materials that have large exciton energies and high carrier mobilities. High-efficiency blue OLEDs have often required complex device architectures with additional transport layers, as it is difficult to achieve charge balance using the host materials alone. One aspect of the G-EML device architecture which has not been utilized with the green and red OLEDs, is the ability to tune the gradient profile. Thus far, the optimum gradient profile has been one which contains, overall, an equal ratio of HTM to ETM, so named a “1:1” gradient. However, G-EML architectures which contain larger relative ratios of one transport material are possible. Figure 3.12a shows a G-EML deposition process (deposition rate over time) which results in a structure with an overall relative ratio of 1:2 HTM to ETM, the compositional structure of the device is shown in Figure 3.12b.

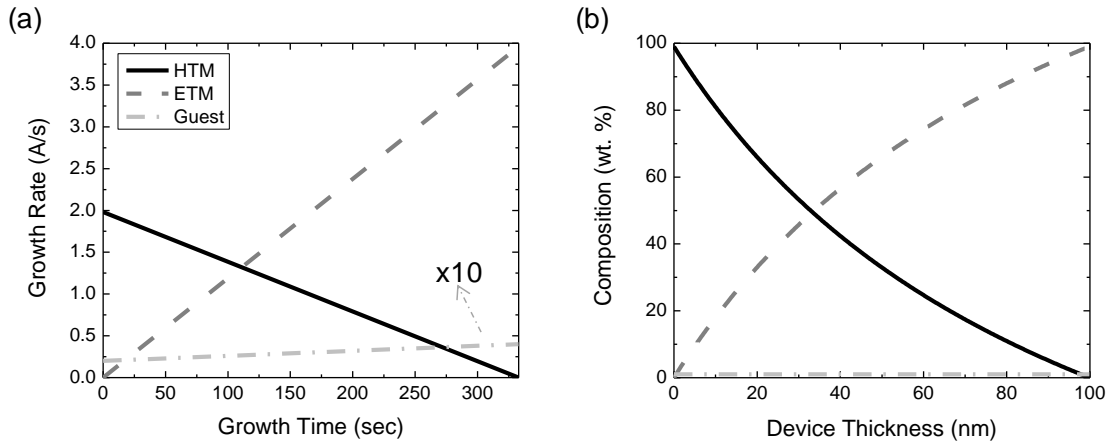


Figure 3.12: (a) Deposition process for a 1:2 G-EML OLED, the growth rate of the dopant is multiplied by a factor of 10 for visibility. (b) the resulting composition profile of the device in (a)

Indeed, a continuous range of gradient profiles which favor one type of host material are possible with a naming convention which refers to the overall ratio of the

host materials, HTM:ETM. Importantly, these devices retain the nearly 100% host composition at each respective electrode and continuously vary to nearly 0% composition at the opposing electrode. This tunability allows for the use host materials which have desirable exciton energy levels, but which may not have optimal charge carrier mobilities. This flexibility widens the library of possible host material combinations, where particular materials are desired.

3.4.1 Blue Light-Emitting Devices with TPBi as an ETL

To achieve blue light emission, the phosphorescent guest molecule bis[(4,6-difluorophenyl)-pyridinatoN,C^{2'}]picolate (FIrpic) was chosen. The EL spectrum of this molecule is shown in Figure 3.13 with the energy levels and chemical structure. The triplet energy of this emitter is ~ 2.65 eV, with a peak EL emission wavelength of ~ 475 nm. As per the discussion above, a suitable host must have a triplet energy at least equal

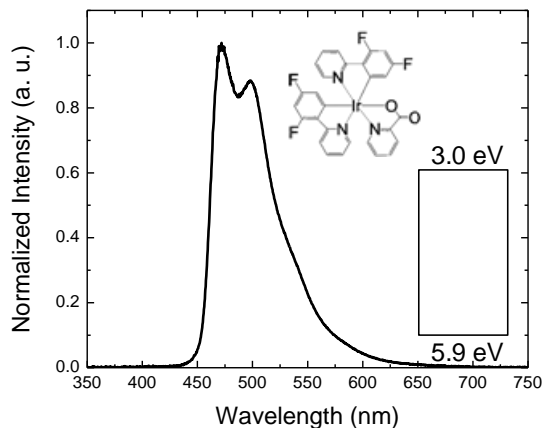


Figure 3.13: Electroluminescent spectrum of FIrpic, the energy levels and molecular structure are inset.

to, but preferably higher than, the triplet energy of FIrpic. While TCTA qualifies ($E_T \approx 2.9$ eV), BPhen does not ($E_T \approx 2.5$ eV). A recently developed molecule with high triplet energies and suitable HOMO and LUMO energies was chosen as an ETM: 2,2',2''-

(1,3,5-benzinetriyl)-tris(1-phenyl-1-H-benzimidazole) (TPBi, $E_T = 2.7$ eV, HOMO = 2.8 eV, LUMO = 6.3 eV).⁸³

A series of G-EML devices were constructed with varying gradient profiles to determine the optimal balance of HTM:ETM, the peak η_{EQE} of each device is plotted in Figure 3.14a with the chemical structure of TPBi inset. The performance of the G-EML improves with increasing TPBi concentration up to a critical threshold where performance rolls off steeply. The best performing device has a 1:2 gradient profile, with peak $\eta_{EQE} = 10.9\%$, and peak $\eta_P = 28.1$ lm/W. To better understand the origin of this performance trend, the V_{TO} and the voltage at 1000 cd/m² for each device are plotted in Figure 3.14b. The V_{TO} shows a weak dependence on composition, except for extreme

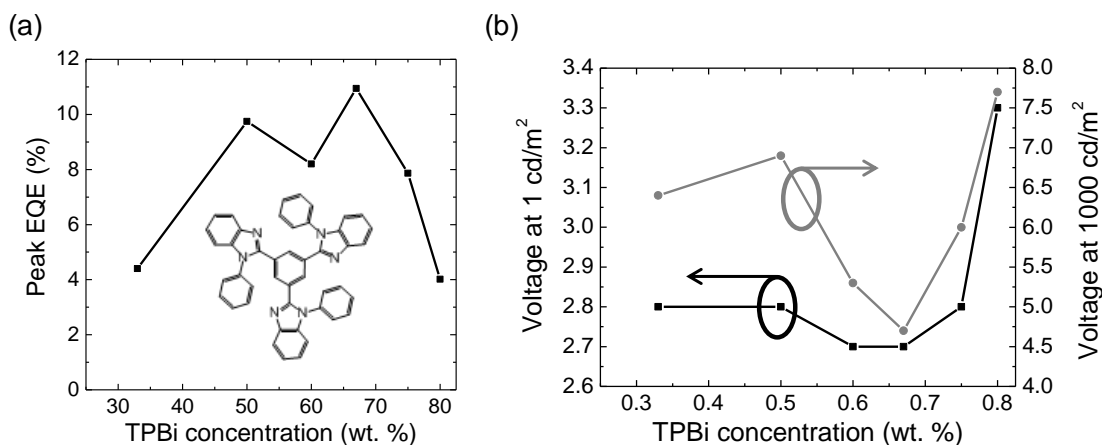


Figure 3.14: (a) Peak η_{EQE} of varying composition profile of FIrpic-based G-EML devices. TCTA is used as an HTM with TPBi as an ETM. The molecular structure of TPBi is shown in the inset. (b) The turn-on voltage (voltage at 1 cd/m²) and the voltage required to produce 1000 cd/m² as a function of overall TPBi concentration.

gradient profiles. This likely reflects the fact that injection into the device is not affected, until extreme gradient profiles render the active layer a vast majority of ETM. The voltage at higher output, however, shows a strong trend with composition, with the optimal gradient for efficient voltage use matching the gradient profile for η_{EQE} . This

indicates that tuning the gradient profile not only influences the charge carrier distributions and the ease with which they may form excitons (indicated by lower voltage), but also the degree of charge carrier confinement in the device. With FIrpic doped throughout the device, excitons formed anywhere within the organic layers will decay with high η_{PL} (this is further confirmed by the lack of host emission in these devices); thus, reductions in the peak η_{EQE} must come from a loss in charge balance, which in these single-layer devices, is manifested as the transport of a carrier from one electrode, across the layer, to the opposite electrode. The electrical properties of these G-EML devices will be explored more in Chapter 5.

3.4.2 Blue Light-Emitting Devices with 3TPYMB as an ETL

The peak η_{EQE} of the previous FIrpic-based devices is well below the theoretical limit, considering $\eta_{OC} \approx 20\%$ and $\eta_{PL} \approx 95\%$ at low concentration (giving a peak $\eta_{EQE} = 19.0\%$).²¹ The η_{PL} of FIrpic doped in to TPBi has recently been discussed, where it was found that the η_{PL} reached a maximum value of only 32% at a concentration of 10 wt.%.⁶¹ This low efficiency was attributed to a back-transfer of excitons from FIrpic to TPBi, given the relatively close triplet energy levels. Thus, to achieve higher peak efficiencies using FIrpic, a wider-gap ETM was chosen to replace TPBi: Tris(2,4,6-trimethyl-3-(pyridin-3-yl)phenyl)borane (3TPYMB). A series of gradient profiles (2:1, 1:1, and 1:2) were fabricated using TCTA and 3TPYMB as the HTM and ETM hosts, respectively, with 2 wt.% FIrpic. The current density-voltage characteristics of the three devices are shown in Figure 3.15a along with the molecular structure and energy levels of 3TPYMB. The resulting η_{EQE} of the various devices are shown in Figure 3.15b.

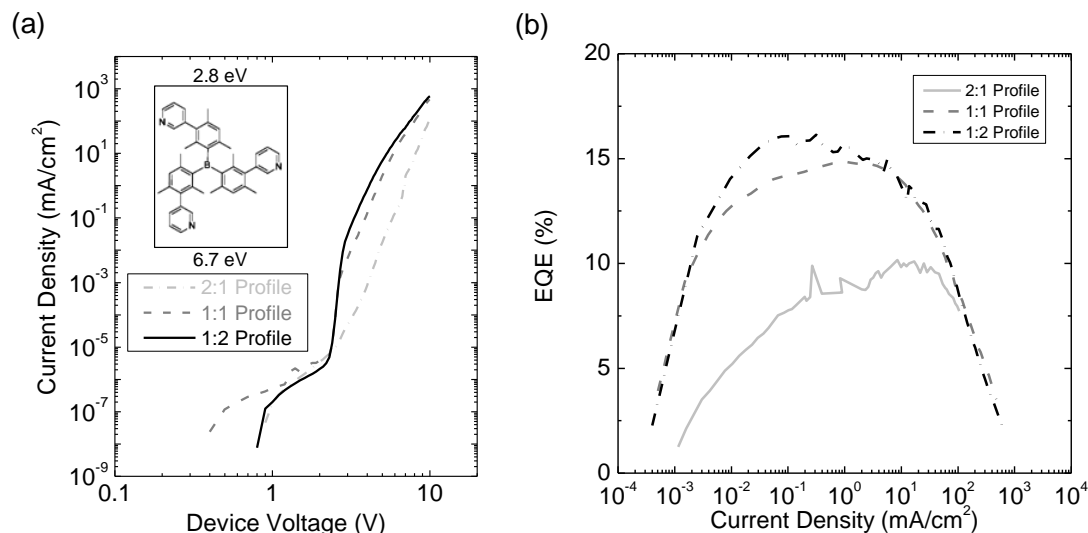


Figure 3.15: (a) Current density-voltage characteristics of the TCTA:3TPYMB-based FIrpic G-EML devices. The molecular structure and energy levels of 3TPYMB are shown in the inset. (b) The η_{EQE} of the three gradient profiles versus current-density. The 1:2 gradient profile shows the highest peak $\eta_{EQE} = 16.1\%$

Again, the 1:2 gradient profile shows the lowest voltage ($V_{TO} = 2.75$ V) and highest peak performance ($\eta_{EQE} = 16.1\%$ and $\eta_P = 35.5$ lm/W) of the three devices. This performance represents an enhancement in η_{EQE} of nearly 50% over the TPBi-based devices.

3.4.3 Multilayer FIrpic-Based OLEDs

Given the high η_{PL} of FIrpic, a device was fabricated which replicated a known, highly efficient OLED. This device replaced TCTA with another wide-gap HTM: Di-[4-(N,N-ditolyl-amino)-phenyl]cyclohexane (TAPC) and utilized a newly synthesized ETM: 2,8-bis(diphenylphosphoryl)dibenzothiophene (PO15), obtained from Pacific Northwest National Labs (PNNL).^{76,94} The PNNL-optimized structure was: ITO / TAPC (35 nm) / TAPC:PO15:FIrpic [55:40:5] (15 nm) / PO15 (50nm). The resulting current density-voltage and brightness-voltage are shown in Figure 3.16a, with the spectral output shown in Figure 3.16b, along with the chemical structures of these host materials. The η_{EQE}

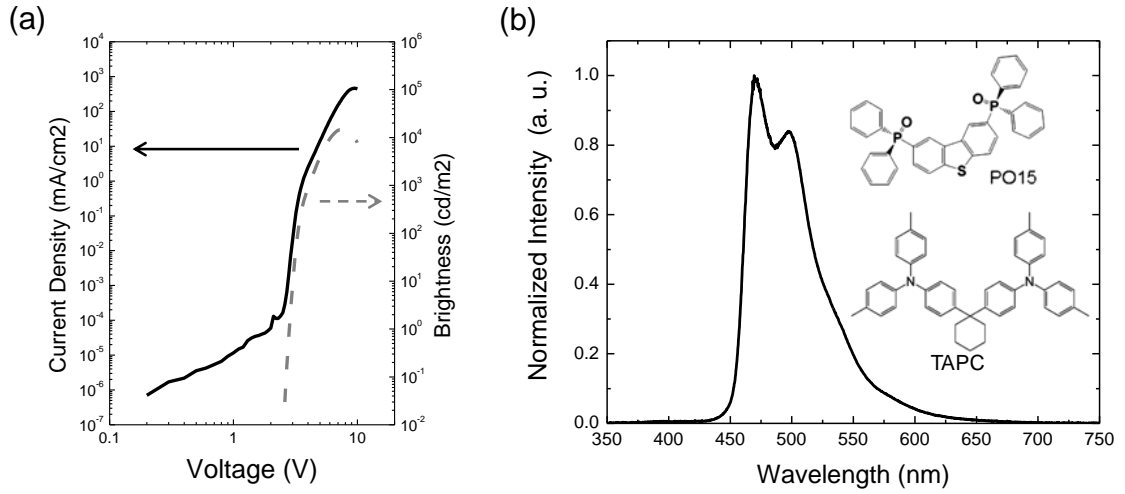


Figure 3.16: (a) Current density-voltage and brightness-voltage characteristics of the multilayer PNNL OLED. (b) Electroluminescent spectral output of the multilayer PNNL OLED, with the molecular structures of PO15 and TAPC inset.

and η_P of this device is shown in Figure 3.17 versus current density. The device exhibits very high peak quantum- and power-efficiencies of $\eta_{EQE} = 20.3\%$, $\eta_P = 34.3 \text{ lm/W}$. The comparison of this data to the previously fabricated Flrpic-based G-EML devices indicates that an enhancement of $\sim 20\%$ is achievable through further optimization. This

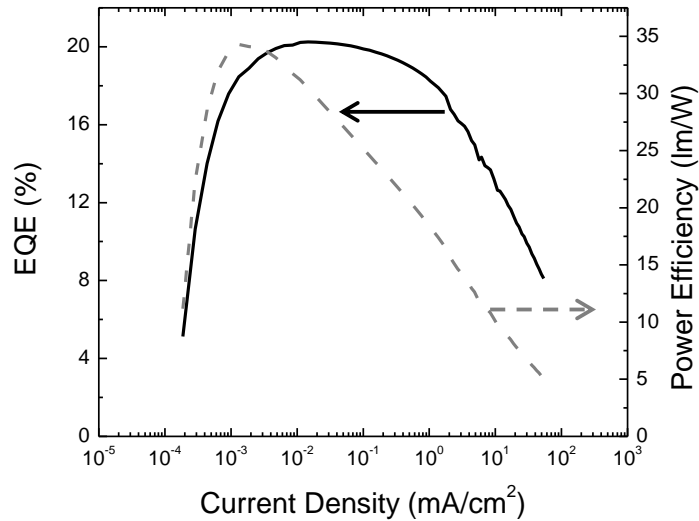


Figure 3.17: The η_{EQE} and η_P of the PNNL Flrpic-based OLED are shown versus current density.

optimization will likely come from minor changes to the device such as small changes in doping concentration, which will not drastically alter the operation of the G-EML device.

3.5 Conclusion

In summary, a graded-emissive layer device architecture has been presented which achieves high-efficiency device operation and is fabricated in a single deposition process. The efficiencies achieved here approach those of state-of-the-art, multilayer devices, despite the simple device architecture. Through the use of various emitting molecules, the G-EML architecture may be extended to devices of all visible-wavelength emission colors. The importance of host selection and gradient profile has been demonstrated experimentally. Clearly, the change in host material is responsible for the improvement in η_{EQE} observed in the FIrpic-based G-EML OLEDs presented here. Further, tuning the gradient profile allows for a wide variety of host materials to be considered. Imbalances in the charge carrier mobilities of the hosts may be overcome through tuning of the composition profile. The impact of gradient profile on charge carrier mobility is examined in greater detail in Chapter 4.

Chapter 4 Depth Profiling of Organic Thin Films

The previous chapters have demonstrated the important role of device and emissive layer engineering in OLED operation and performance. Highly efficient organic light-emitting devices (OLEDs) often contains layers which are comprised of multiple materials with different functionalities. This is particularly true for the emissive layer, where a dilute emissive guest molecules is doped into a host material or mixture of host materials,^{10,53,81,95} though composite transport layers are also used.^{58,77,96} The overall composition and composition profile of these layers have proven difficult to probe,^{97–99} as the thin films are typically soft and the different materials are often composed only of carbon, hydrogen, and nitrogen.⁸⁰ The performance of these composite layers has been shown to be strongly dependent on the mixing ratio and spatial distribution of the constituent materials. This is especially evident in devices employing a mixed-emissive layer (M-EML), where the mixing ratio of hole- and electron-transport materials (HTM and ETM, respectively) significantly impacts device performance.^{76,83,100–102} In chapter 3, a graded-emissive layer (G-EML) architecture was introduced where the emissive layer is comprised of a continuously varying composition of HTM, ETM, and emissive guest. The G-EML device architecture was shown to achieve high performance in a single-layer device architecture.^{103–106} The G-EML devices show a strong dependence of performance on the exact composition profile, and the optimized blue light-emitting structures from Chapter 3 have been demonstrated with composition profiles which contain relatively larger amounts of ETM.¹⁰⁴

Typically, devices with composite layers are fabricated via vacuum thermal co-evaporation. While this fabrication technique allows for careful control over the relative deposition rates of the constituent materials, the spatial composition of these films have proven difficult to examine post-deposition. Given the demonstrated connection between film composition and device performance, there is strong interest in developing techniques to accurately probe the exact post-deposition composition profile. Characterization of the depth profile requires a means to determine both the identity and quantity of chemical species present at the surface of the film (or within a very shallow volume near the surface), so that exact ratios of the constituent materials may be determined. Additionally, a process to remove thin, uniform layers of material is required. This process must not damage the underlying layers nor chemically interact with the exposed surface.

Until recently, the sputtering of organic thin films has focused on the use of C_{60}^{+} ion beams to remove thin layers of material.^{97,99} Though this method has shown some positive results, it is not applicable to many organic systems where the deposition of amorphous carbon and chemical interactions at the surface render analysis of the underlying layers impossible.^{97,107} Promising results, however, have been obtained using large-clusters of Ar ions as the primary beam in gas-cluster ion beam (GCIB) milling with time-of-flight secondary ion mass spectrometry (TOF-SIMS) analysis. The Ar-GCIB process has shown large sputtering yields of organic materials with little signs of degradation of the exposed layers.^{98,108} One of the primary drawbacks of the TOF-SIMS

chemical analysis technique is its inability to easily quantify the various chemical states without elaborate standards and calibration processes.

4.1 X-ray Photoelectron Spectroscopy

An alternative technique, which allows for a quantitative measurement of the chemical makeup of the surface of an organic thin film is X-ray photoelectron spectroscopy (XPS).^{109,110} In this technique, high energy monochromatic X-rays are focused to small spot on the surface of the sample. The X-rays are generated through the use of an electron gun aimed at an Al target. Electron impact on the Al target generates X-rays with an energy of 1486.6 eV. These X-rays penetrate the organic sample and interact with the electron orbitals of the atomic elements of each molecule. Electrons near the sample surface are ejected with kinetic energies characteristic of their binding energies in each molecule. The XPS technique is non-destructive and is capable of detecting very small differences in the chemical makeup of many organic semiconducting materials. In this work, sequential Ar-based GCIB sputtering is paired with XPS measurements to allow for the composition depth profile of an organic thin film to be determined.

4.2 Experimental Techniques

All organic thin films and devices were fabricated according to the previously reported methods, using 4,4',4''-tris(carbazol-9-yl)triphenylamine (TCTA) as an HTM, 4,7-diphenyl-1,10-phenanthroline (BPhen) as an ETM, and *fac*-tris(2-phenylpyridine) iridium (III) (Ir(ppy)₃) as the emissive guest. Samples were packed in a nitrogen

environment and transported to the composition depth profiling system where they were loaded from ambient to a load-locked antechamber. The samples of interest were characterized in a PHI *VersaProbe* II Scanning XPS system equipped with an Ar⁺ Gas Cluster Ion Beam source for depth profiling. Since the device structures were large and uniform, XPS measurements were done with a 200 μm monochromatic Al K α (1486.6 eV) X-rays focused on the area of interest. The photoelectron takeoff angle was 45° and the pass energy in the spherical capacitance analyzer was fixed at 23 eV for this analysis to obtain good energy resolution to clearly define both the C 1s and N 1s species in TCTA and BPhen. The GCIB source can be operated with beam energies from 2.5 kV to 20 kV and Ar cluster size from <1000 to 5000. For this study we used Ar₁₅₀₀ clusters at 10 kV, 2 nA corresponding to 4 eV per Ar⁺ atom rastering over a 2 mm x 2 mm area. The PHI *VersaProbe* II Scanning XPS system has a dual beam charge neutralization (7 eV Ar⁺ ions and 1 eV electrons) capability to prevent differential surface charging at various interfaces.

4.3 XPS Study of Host Materials

Initial C 1s and N 1s XPS spectra of pure films of TCTA and BPhen are shown in Figures 4.1a with the chemical structures shown in the inset. Though both materials are comprised of only carbon, hydrogen, and nitrogen, a distinct chemical signature is recorded. The N 1s peak of TCTA is shifted by 1.8 eV relative to BPhen (Figure 4.1b), this is due to the difference in electronic environments of the nitrogen atom in each molecule. This shift serves as a unique identification of the two materials in subsequent

measurements and highlights the high resolution chemical state characterization of the XPS technique.

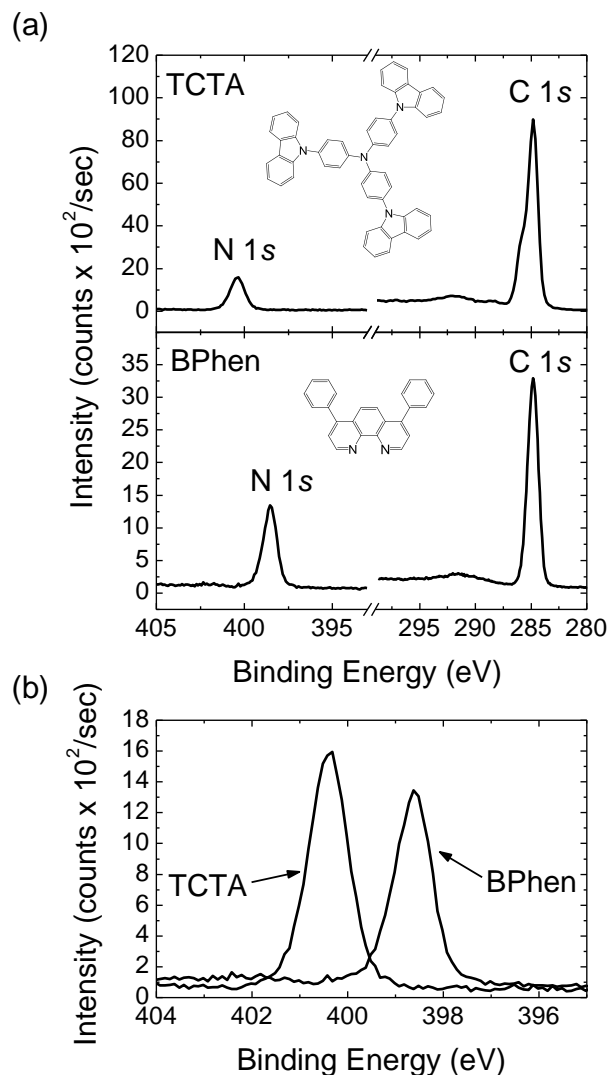


Figure 4.1: XPS spectra of the N 1s and C 1s of (a) TCTA and (b) BPhen. The N 1s peaks are shifted, relative to each other, by 1.8 eV.

It is interesting to view the complete XPS scan of BPhen on an ITO/glass substrate, Figure 4.2. Here, signal from the ITO substrate is apparent in the initial BPhen scan, *before* the first Ar-GCIB sputter process. This is likely due to the crystallization of BPhen after exposure to atmosphere, which results in the formation of voids. According

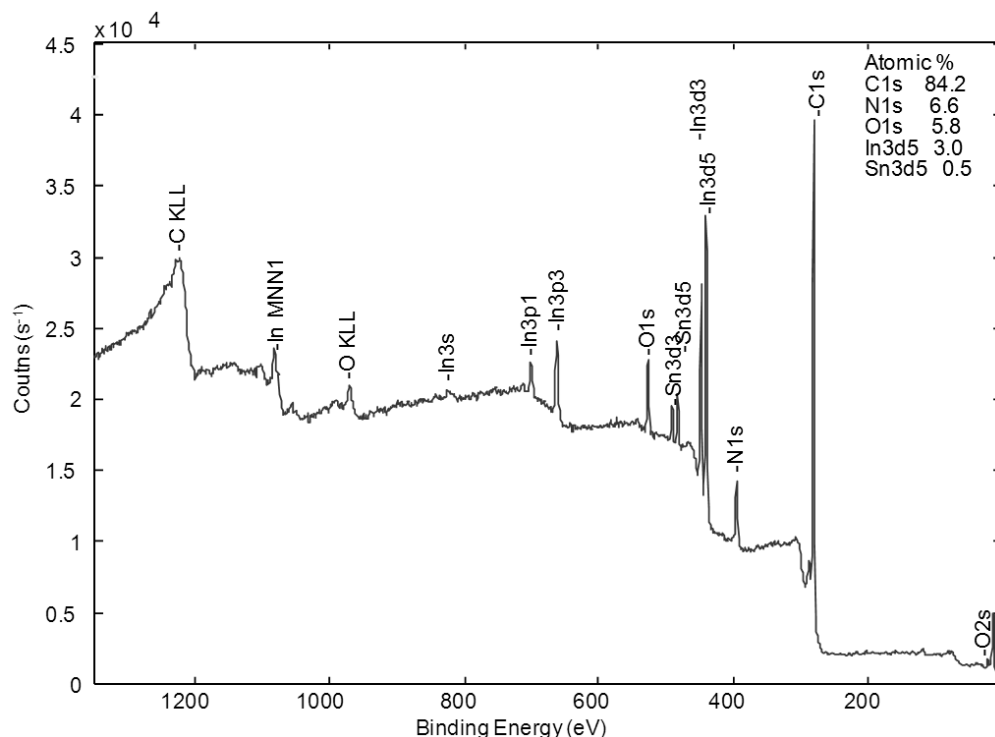


Figure 4.2: Full XPS spectra of a 100-nm-thick layer of BPhen on ITO.

to Figure 4.2, these voids are present throughout the entire depth of the sample. To protect the BPhen layer a sample was grown on TCTA which was capped with a thin (10nm) layer of TCTA to encapsulate and protect the BPhen surface. The stack was subjected to the depth profiling process; the resulting composition profile is presented in Figure 4.3. It is clear that neither the Si substrate used here, nor the underlying TCTA layer, are detected in the initial scan or in subsequent depth scans, until most of the BPhen layer has been sputtered. This indicates the role of ambient atmosphere in inducing crystallization in BPhen and suggests that BPhen crystallization does not occur during growth, but rather is an environmental effect which may be mitigated with the use

of a capping layer.

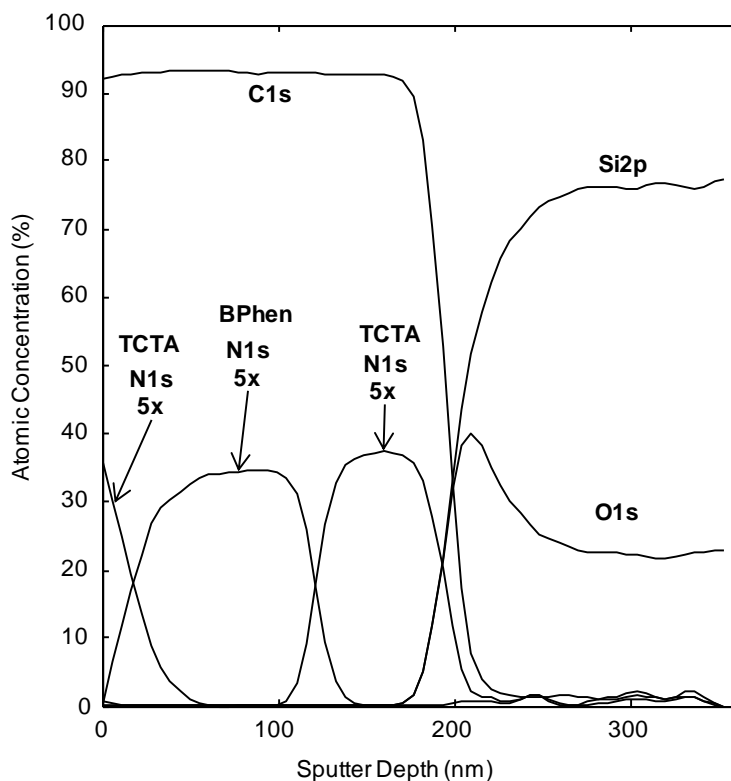


Figure 4.3: Sputter depth profile of a TCTA (10 nm) / BPhen (100 nm) / TCTA (100 nm) / ITO / glass stack. Signal from the Si substrate and from the TCTA N 1s peak is *not* observed during the majority of the depth profiling of the BPhen layer.

4.4 Depth Profiling of OLED Architectures

4.4.1 Resolution of the Unique Identification of TCTA and BPhen

To demonstrate the ability of XPS to distinguish the host materials, a double-emissive layer (D-EML) structure of BPhen on TCTA on a Si substrate was examined; the resulting depth profile is shown in Figure 4.4a. Tracking the different N 1s peaks clearly shows the layered structure of the D-EML. Mapping of the exact interface between the layers is limited in resolution by both the penetration depth of the XPS technique and the uniformity of the Ar-GCIB sputtered region. Non-uniformity caused by

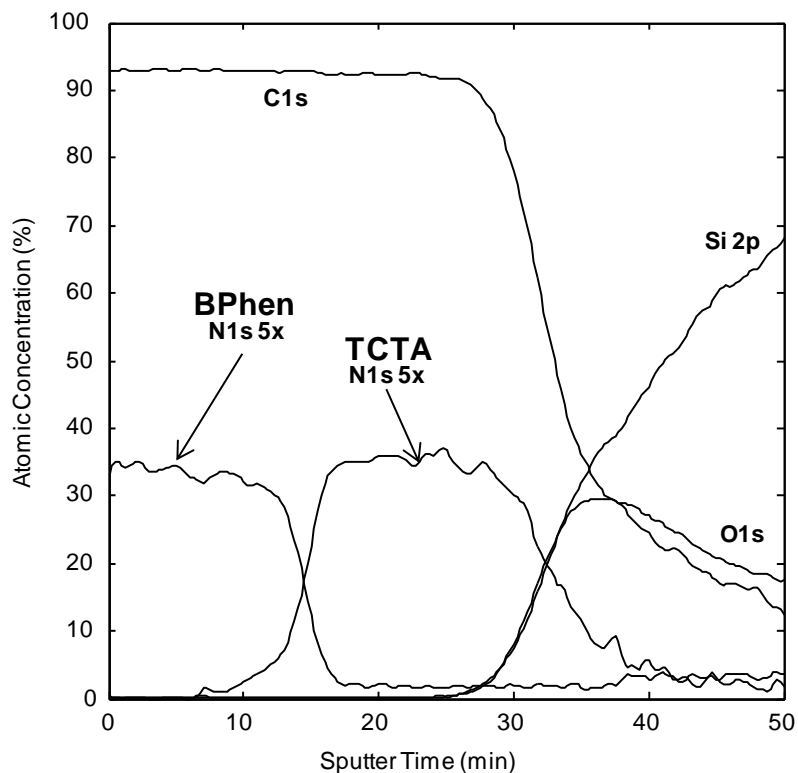


Figure 4.4: Depth profile of a BPhen / TCTA D-EML structure.

sputtering was mitigated by using compucentric Zalar ([®] Physical Electronics) rotation of the sample during the sputter cycle.

4.4.2 Characterization of the Mixed-Emissive Layer

The XPS spectra for the C 1s and N 1s peaks of a M-EML device on ITO are shown as a function of sputter depth in Figure 4.5a and 4.5b, respectively. The XPS spectra clearly show the 400.4 eV peak present in TCTA and the 398.6 eV peak of BPhen. The π - π^* shake-up transition for each sputter depth is clearly identifiable. The persistence of this peak throughout the sputter depth of the organic film demonstrates that the depth profiling process does not damage the conjugation of the target molecules. The complete depth profile of the M-EML is shown in Figure 4.5c. The composition of the

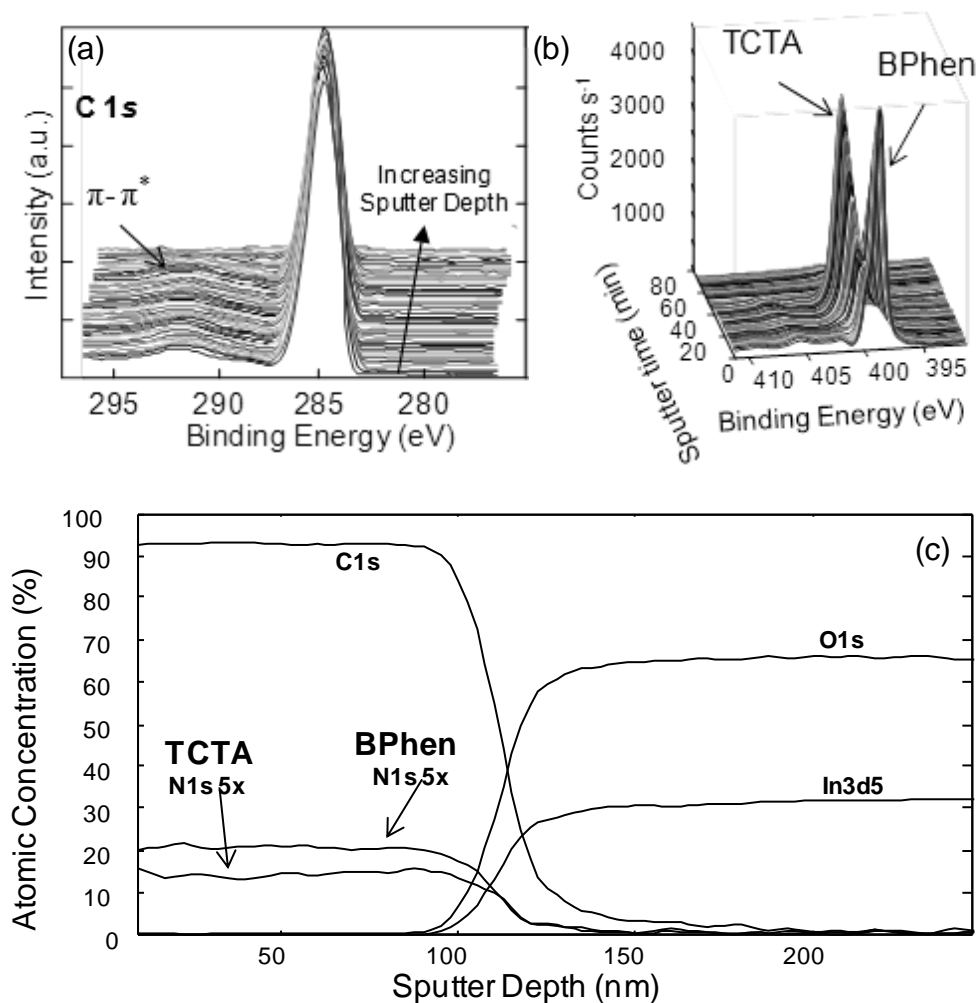


Figure 4.5: XPS spectra for (a) C 1s and (b) N 1s peaks for a M-EML device on an ITO substrate. The complete depth profile of the device is shown in (c).

M-EML device clearly shows that the uniform mixing of TCTA and BPhen is maintained throughout the layer and persists post-deposition. No large-scale vertical separation of the two phases is observed within the resolution of the technique.

4.4.3 Characterization of the Graded-Emissive Layer

The composition depth profiles of G-EML devices having 1:1, 1:2, and 1:3 TCTA:BPhen composition ratios are shown in Figures 4.6a, b, and c, respectively, along with the target profiles. It is clear that each composition profile is physically distinct.

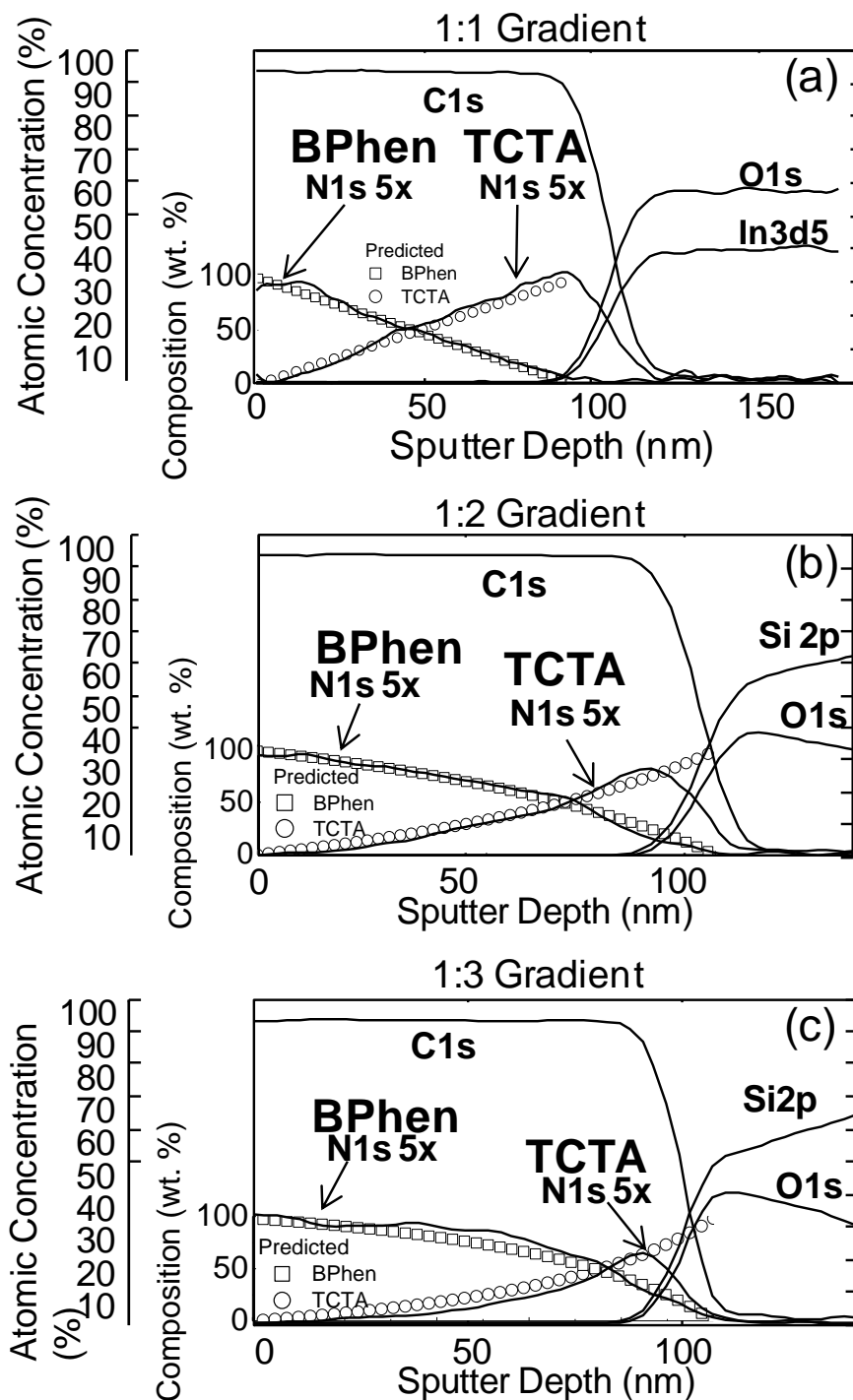


Figure 4.6: Composition depth profiles of (a) 1:1, (b) 1:2, (c) and 1:3 gradient profiles of TCTA:BPhen. The predicted gradient profiles for BPhen (squares) and TCTA (circles) are shown overlaid on the depth profile data.

The measured composition profile matches closely with the intended composition profile, both in the concentration ratio of the host materials at each location and in the zero-concentration endpoints of the intended gradient profile. From this data, it follows that the observed differences in device operation and performance are the product of real differences in the electronic properties of each gradient, which are the result of distinct variations of the spatial composition in each G-EML device. The close matching of the intended and measured composition profiles indicates that vapor-deposition is a reliable way to achieve robust, graded-composition layers that do not greatly phase-separate during growth or post deposition, and whose electronic properties may be tuned by small changes in gradient composition profile.

4.5 Conclusion

In conclusion, the pairing of Ar-GCIB with XPS allows for the examination of the composition depth profile of OLEDs to be examined with great precision. The large-cluster Ar-GCIB process is well-suited for use with soft organic thin-films as it does not contaminate the surface nor damage the underlying layers. The use of XPS allows for precise quantification and identification of the various molecular species found throughout the depth of an OLED device. These techniques have been used to examine the composition depth profiles of a variety of common OLED emissive layer architectures fabricated via vacuum thermal deposition, and confirm that variations in the intended composition profiles of G-EML devices, and uniform mixing ratios in M-EML devices, are physically distinct and are present post-deposition. This technique will allow

Chapter 4: Depth Profiling of Organic Thin Films

for improved understanding of the role of composition in the operation of composite layers and the performance of OLEDs.

Chapter 5 Electronic Properties of G-EML OLEDs

The results of Chapter 3 clearly indicate the strong dependence of G-EML OLED device performance on composition profile, particularly for blue-emitting OLEDs. Chapter 4 shows conclusively that the intended composition profiles of G-EML devices grown by vacuum thermal evaporation match closely with the post-deposition composition profiles, as measured by XPS and Ar-GCIB. With this information, a complete understanding of the operation of G-EML devices requires a detailed examination of the constituent electronic properties of each material and gradient profile system. This is accomplished through the characterization of the electron and hole mobilities of HTM:ETM mixtures of varying composition, containing each phosphorescent guest. It is observed that for green- and red-emitting systems, except at extreme ratios of HTM:ETM, the electron and hole mobilities are well-matched and largely independent of composition. For blue-emitting devices, a mismatch of the electron and hole mobilities is observed. As a result, the optimum gradient profile for blue electrophosphorescence is ETM-rich, while for green and red emission the optimized gradients contain equal amounts of HTM and ETM.

5.1 Measurement of Charge Carrier Mobility

The mobility in an organic thin film may be extracted by measuring the current density-electric field characteristics of devices which pass only electrons or holes (termed “electron-only” or “hole-only” devices, respectively).^{111,112} In these highly disordered films, charges are injected over an energy barrier into localized energy states where

transport occurs via hopping, finally recombining with image charges at the opposing electrode. This regime is termed “injection limited current” (ILC).^(cites) Under these conditions, the net surface recombination current at the interface, under an applied field, can be equated to the bulk current leading to the interface. The expression of the current density (J) on applied field (F) was described by Scott and Malliaras:¹¹¹ $J =$

$$4N_0\psi^2 e\mu[F]e^{-e\phi_B/k_B T}e^{-f^{1/2}} \quad (5.1)$$

where N_0 is the density of states in the organic film, taken here as $\sim 10^{22} \text{ cm}^{-3}$, e is the elementary charge, ϕ_B is the injection barrier height, k_B is the Boltzmann constant, T is the temperature, ψ is a function of the reduced electrical field $f = e^3 F / 4\pi\epsilon\epsilon_0 k_B^2 T^2$, with $\psi = f^{1/2} + f^{1/2} - f^{1/2} (1 + 2f^{1/2})^{1/2}$, where ϵ is permittivity of free space, and ϵ_0 is the relative dielectric constant of the organic active layer. The electric field-dependent mobility ($\mu[F]$) is described by a Poole-Frenkel-like relation:^{113–115}

$$\mu[F] = \mu_0 e^{\gamma\sqrt{F}}, \quad (5.2)$$

where μ_0 is the zero-field mobility and γ is the field-dependence parameter. The field dependence arises from a distribution in hopping site energies whose barriers to charge transport are reduced with the application of an electric field.^{116,117} In order to preserve an analytical solution to Eqn. (5.1), the electric field is approximated as uniform over the organic layer thickness, d , ($F=V/d$).

5.2 Single-Carrier Experimental Design

For measurements of the charge carrier mobility, single-carrier devices were fabricated using LiF/Al (top) and Al (bottom) as electron-only injection and extraction

contacts, and ITO (bottom) and Au (top) as hole-only injection and extraction contacts. Uniform mixtures of HTM:ETM doped uniformly with the phosphorescent guest were prepared by vacuum thermal co-evaporation on glass substrates. A thickness of 275 nm was used for studies of all HTM:ETM compositions. The electron injection barrier height for BPhen is $\phi_B = .83$ eV¹¹⁸ and the hole injection barrier for TCTA is $\phi_B = .75$ eV.⁸⁴ The injection barrier for TPBi was estimated by fitting the J - V data for the 100% TPBi sample, using literature values for the mobility, giving $\phi_B = .70$ eV.¹¹⁹ This injection barrier height was used in subsequent fits of TCTA:TPBi mixtures.

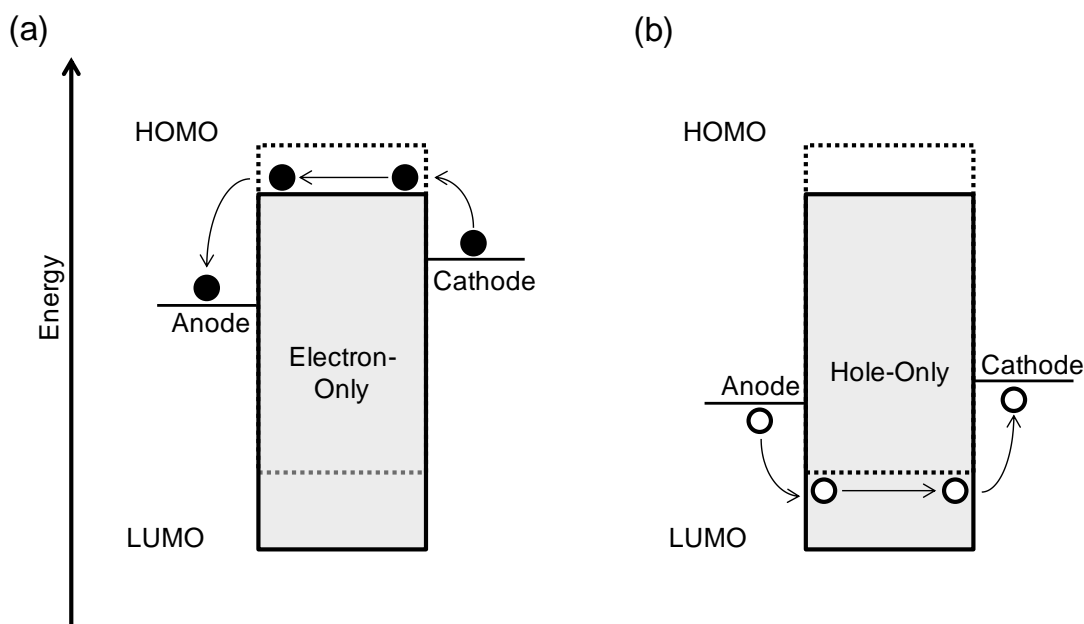


Figure 5.1: Schematic of (a) electron-only and (b) hole-only device operation.

A schematic of the single-carrier device operation is shown in Figure 5.1a for electron-only devices and Figure 5.1b for hole-only devices. Electrons are injected from the cathode and transported across the deepest-energy LUMO, while holes are injected from the anode and transported across the shallowest-energy HOMO.

5.3 Optimized Red- and Green-Emitting Devices

5.3.1 Performance of Red- and Green-Emitting G-EML OLEDs

Electroluminescence spectra collected at a brightness of 1000 cd/m² for optimized green-, red-, and blue-emitting G-EML OLEDs are shown in Figures. 5.2a, 5.2b, and 5.2c, respectively. In each case the EL is characteristic of the phosphorescent dopant, with no emission observed from the HTM or ETM materials. The absence of host emission is an indication that excitons are well-confined to the phosphorescent guest. The dependence of η_{EQE} and η_P on current density for each device is shown in Figures. 5.2d-5.2f. Peak $\eta_{EQE}=(16.7 \pm 0.3)\%$ and $\eta_P=(65.0 \pm 1.1)\text{lm/W}$, are obtained for green

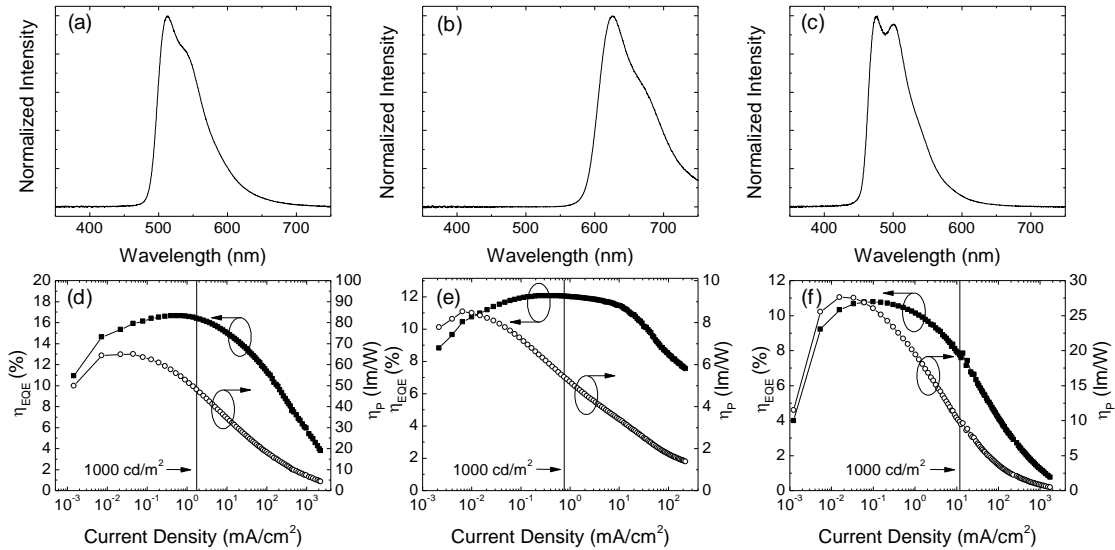


Figure 5.2: Electroluminescence spectra at a brightness of 1000 cd/m² for optimized G-EML devices containing (a) 1:1 TCTA:BPhen with 2 wt.% Ir(ppy)₃, (b) 1:1 TCTA:BPhen with 7 wt.% PQIr, and (c) 1:2 TCTA:TPBi with 4 wt.% FIrpic. Also shown is the dependence of η_{EQE} and η_P on current density for the same optimized G-EML structures containing (d) Ir(ppy)₃, (e) PQIr, and (f) FIrpic. Vertical lines indicate operation at a brightness of 1000 cd/m².

electrophosphorescence. Optimized red- and blue-emitting G-EML OLEDs show peak efficiencies of $\eta_{EQE}=(12.0 \pm 0.4)\%$ and $\eta_P=(8.3 \pm 1.1)\text{lm/W}$; and $\eta_{EQE}=(10.9 \pm 0.3)\%$ and

$\eta_P = (28.1 \pm 1.1) \text{ lm/W}$, respectively. These values of η_{EQE} and η_P are comparable with values previously reported using conventional multi-layer architectures.

The current density-voltage and brightness-voltage characteristics for green, red, and blue G-EML devices are shown in Figures. 5.3a and 5.3b. Overall, the devices exhibit low current leakage levels at low voltage, with a steep increase in the current density after turn-on. The low levels of leakage current are indicative of a high degree

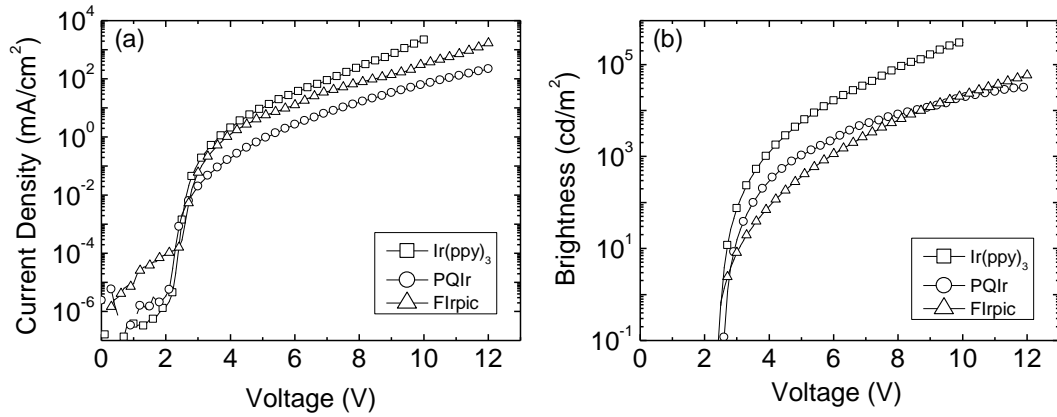


Figure 5.3: (a) Current density-voltage and (b) brightness-voltage characteristics for the G-EML devices.

of charge confinement in the device, and are characteristic of the G-EML architecture. Similar devices based on uniform HTM:ETM mixtures have shown considerable leakage leading to low performance operation, reflecting the substantial improvement that can be realized by engineering the spatial composition of the device. Additionally, the G-EML devices show very low voltage operation, indicated by a steep increase in the brightness as voltage is increased.

The dependence of η_{EQE} on current density for green and red G-EML devices having HTM:ETM compositions of 2:1, 1:1, and 1:2 is shown in Figures. 5.4a and 5.4b,

respectively. It is evident that gradient profile and overall composition ratio strongly determine the peak efficiency, the current density for peak efficiency, and the roll-off in the efficiency, mainly via changes in the electron-hole charge balance. Further studies of the impact of the G-EML profile in reducing bimolecular quenching process that contribute to the efficiency roll-off^{11,12,120–122} are presented in Chapters 6 and 7.

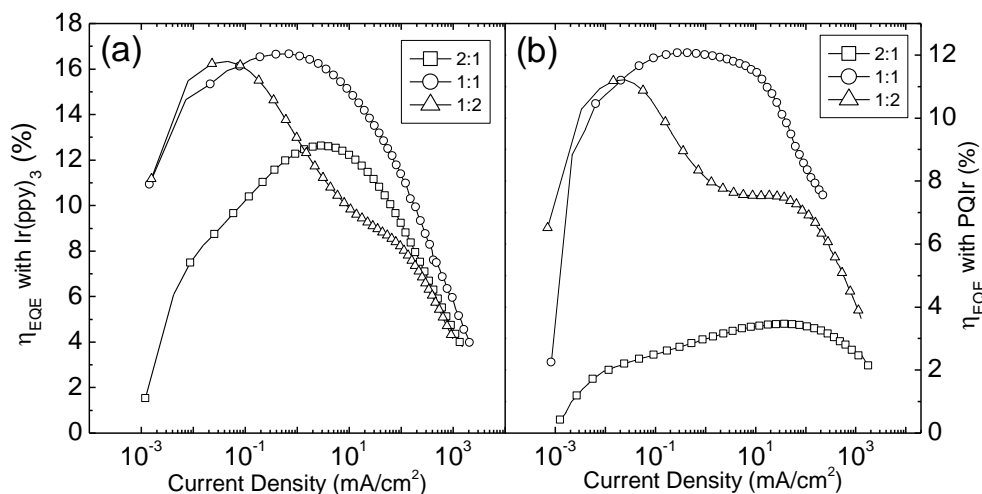


Figure 5.4: External quantum efficiency versus current density for each of the gradient profiles doped with either (a) 2 wt.% Ir(ppy)₃ or (b) 7 wt.% PQIr.

5.3.2 Charge transport in green and red G-EML OLEDs

To characterize the electrical properties of the G-EML, a series of single-carrier devices were prepared containing uniform mixtures of the HTM, ETM, and phosphorescent guest. Characterizing the electron and hole mobilities of these mixtures allows for a comparison of the charge carrier mobilities at different spatial locations within a G-EML device. Characteristic fits of the measured current density-electric field curves to Eqns. (5.1) and (5.2) are shown for electrons in Figures. 5.5a and 5.5b and for holes in Figures. 5.5c and 5.5d, for single-carrier devices containing Ir(ppy)₃ and PQIr,

respectively. Differences in as-deposited film thickness complicate direct comparison of the current density-electric field characteristics due to the complex dependence of Eqns. (5.1) and (5.2) on thickness. Fits to Eqn. (5.1) show good agreement for high fields and diverge slightly at low fields. This divergence could

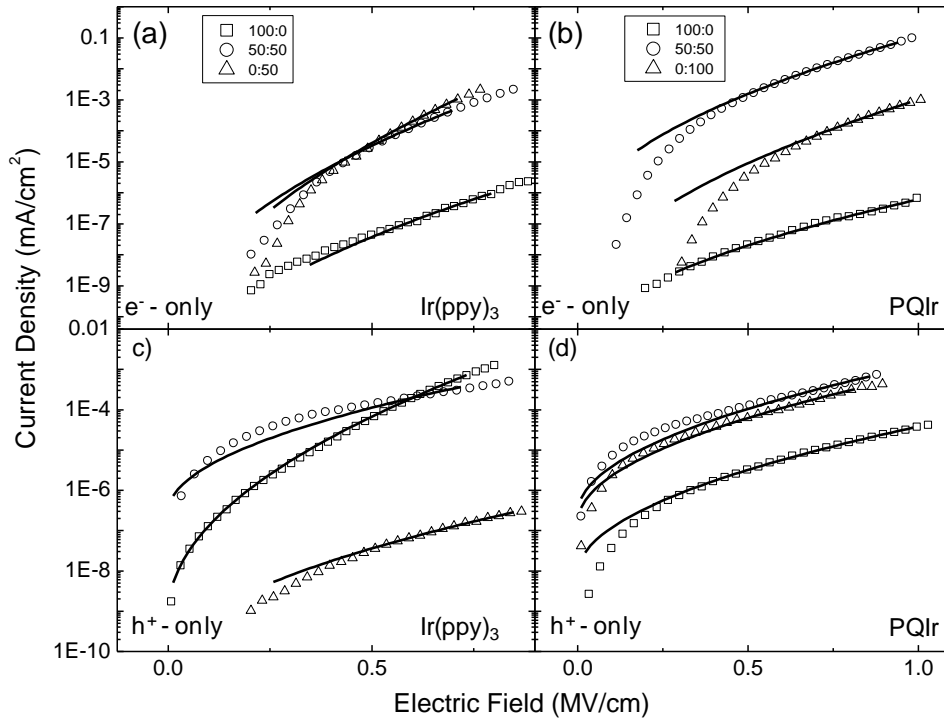


Figure 5.5: Current density-voltage characteristics for 100:0 TCTA:BPhen (squares), 50:50 TCTA:BPhen (diamonds), and 0:100 TCTA:BPhen (triangles) electron-only, (a) and (b), and hole-only, (c) and (d), single-carrier devices. Data for devices with 7 wt. % Ir(ppy)₃ are shown in (a) and (c), while data for devices with 2 wt. % PQIr are shown in (b) and (d). Symbols are experimental data while solid lines are fits to Eqs. 5.1 and 5.2.

potentially be due to Ohmic conduction at low field, or to a change in the field-dependent injection mechanism that is dominant at low voltages.

The materials parameters μ_0 and γ , extracted from fits of Eqns. (5.1) and (5.2) to the single-carrier device data, are shown in Table I for Ir(ppy)₃-based devices and Table II for PQIr-based devices. The extracted values of the field-dependence parameter γ are

comparable to those found in previous studies of charge transport in organic semiconductors based on a Poole-Frenkel-like model of the mobility.^{114,123} The extracted fit parameters may be used in conjunction with Eqn. (5.2) to determine the charge carrier mobility at a given applied field. The dependence of charge carrier mobility on BPhen composition is shown in Figure 5.6a for Ir(ppy)₃-based devices and Figure 5.6b for PQIr-based devices. Mobilities are calculated using an applied field which corresponds to the voltage across each 1:1 G-EML device at peak η_{EQE} , namely 0.37 MV/cm and 0.44 MV/cm for Ir(ppy)₃- and PQIr-based devices, respectively. It is evident that across a wide range of TCTA:BPhen composition ratios the electron and hole mobilities are well-matched in magnitude. Additionally, the mobilities show little dependence on host composition in the range of 80:20 to 20:80 TCTA:BPhen. At extreme ratios of host composition, containing ratios >80 wt.% of either host, the mobilities of both electrons and holes decrease by >2 orders of magnitude.

Table I: Fit parameters for Ir(ppy)₃-based single-carrier devices: Zero-field mobility (μ_0) and field dependence parameter (γ) for electron and hole transport in mixed films as a function of the TCTA:BPhen ratio with 2 wt.% Ir(ppy)₃.

TCTA:BPhen	Electron		Hole	
	μ_0 (cm ² /V-s)	γ (cm/V) ^{1/2}	μ_0 (cm ² /V-s)	γ (cm/V) ^{1/2}
100:0	5.3×10^{-9}	9.2×10^{-3}	3.2×10^{-5}	7.5×10^{-3}
80:20	7.4×10^{-7}	1.1×10^{-2}	2.7×10^{-3}	0
70:30	1.0×10^{-7}	1.2×10^{-2}	5.6×10^{-2}	0
60:40	1.4×10^{-3}	7.3×10^{-3}	9.1×10^{-3}	0
50:50	1.4×10^{-5}	1.2×10^{-2}	1.0×10^{-1}	0
40:60	1.6×10^{-6}	1.4×10^{-2}	4.6×10^{-2}	0
30:70	3.8×10^{-7}	1.6×10^{-2}	3.2×10^{-4}	0
20:80	8.0×10^{-8}	1.5×10^{-2}	1.9×10^{-4}	0
0:100	1.3×10^{-6}	1.6×10^{-2}	3.0×10^{-5}	1.2×10^{-3}

Table II: Fit parameters for PQIr-based single-carrier devices: Zero-field mobility (μ_0) and field dependence parameter (γ) for electron and hole transport in mixed films as a function of the TCTA:BPhen ratio with 7 wt% PQIr.

TCTA:BPhen	Electron		Hole	
	μ_0 (cm ² /V-s)	γ (cm/V) ^{1/2}	μ_0 (cm ² /V-s)	γ (cm/V) ^{1/2}
100:0	4.2×10^{-6}	3.2×10^{-3}	3.0×10^{-4}	0
80:20	6.0×10^{-6}	7.7×10^{-3}	4.9×10^{-3}	0
70:30	2.2×10^{-6}	5.2×10^{-3}	1.4×10^{-3}	0
60:40	1.6×10^{-4}	7.0×10^{-3}	1.5×10^{-2}	0
50:50	8.1×10^{-5}	8.0×10^{-3}	5.9×10^{-4}	0
40:60	4.8×10^{-3}	5.0×10^{-3}	2.7×10^{-2}	0
30:70	2.7×10^{-3}	6.1×10^{-3}	1.3×10^{-2}	0
20:80	2.7×10^{-4}	8.1×10^{-3}	2.7×10^{-3}	0
0:100	4.2×10^{-2}	6.0×10^{-3}	1.0×10^{-2}	0

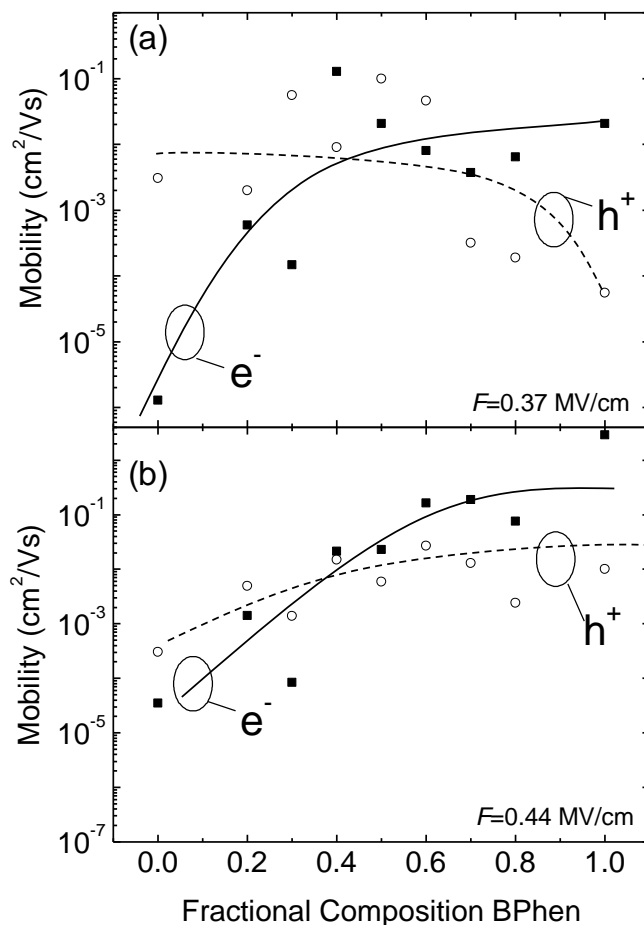


Figure 5.6: Electron (solid symbols) and hole (open symbols) mobility for mixed films as a function of the TCTA:BPhen composition ratio with (a) 2 wt. % Ir(ppy)_3 at a field of 0.37 MV/cm and (b) 7 wt. % PQIr at a field of 0.44 MV/cm. The solid lines are guides to the eye.

The high η_{EQE} achieved in the green and red G-EML devices is likely the result of multiple defining characteristics of the 1:1 TCTA:BPhen gradient profile. Efficient charge injection from the electrodes is maintained by the high composition of each transport material near its respective electrode. Charge carrier mobilities are well-matched at moderate compositions and remain so throughout the center region of the device. The mobility matching over a large range of compositions, and consequently

throughout the 1:1 G-EML, likely leads to increased overlap between the electron and hole charge densities in the device, allowing for efficient exciton formation. An imbalance in the charge carrier mobility may spatially shift the exciton recombination zone in the 2:1 and 1:1 G-EML devices, leading to a shift in the peak η_{EQE} (Figure 5.4a, 5.4b) with respect to applied current density. As electrons (holes) approach the anode (cathode), the mobility decreases significantly, providing charge confinement and reducing charge carrier leakage. Additionally, as charges are injected onto, and transported across, their respective transport material, there exists an energy difference between the HTM-ETM lowest unoccupied molecular orbital energy levels (for electrons), and highest occupied molecular orbital energy levels (for holes), which effectively confine electrons to the ETM, and holes to the HTM. The spatially-varying composition ensures that the high concentration of transport material at the electrodes will effectively block carriers from traveling across the entire device as leakage current, a critical improvement over single-layer, uniformly mixed devices. The role of the luminescent guest in charge transport was separately examined by excluding it from single carrier device studies. For these HTM:ETM structures, the extracted charge carrier mobilities were found to be in good agreement with the data reported here for devices containing the HTM, ETM, and guest. Ultimately, the confluence of efficient charge injection, large spatial overlap of the electron and hole densities, and charge and exciton confinement results in high charge balance, with a 1:1 gradient offering the most symmetric injection and transport conditions and thus the highest η_{EQE} .

5.4 Optimized Blue-Light Emitting Devices

5.4.1 Performance of Blue Light-Emitting G-EML Devices

Blue G-EML OLEDs with 2:1, 1:1, and 1:2 gradient profiles were fabricated using the methods described previously. The resulting dependence of η_{EQE} on applied current density is shown in Figure 5.7 for each gradient. A strong dependence on gradient profile is observed, with the 1:2 G-EML device showing peak performance.

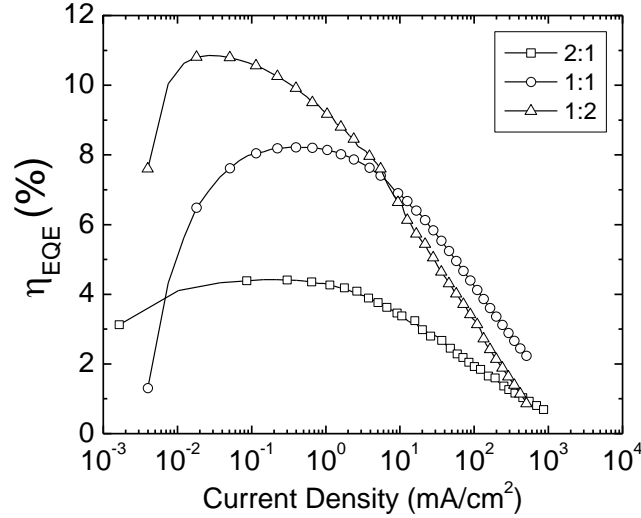


Figure 5.7: External quantum efficiency versus current density for FIrpic-based G-EML devices with varying overall HTM:ETM composition.

The charge carrier mobilities were extracted by fitting single carrier current density-electric field curves for uniform mixtures of varying composition using Eqns. 5.1 and 5.2. Selected electron- and hole-only data and the associated fits are shown in Figures. 5.8a and 5.8b, respectively, with the corresponding μ_0 and γ values listed in Table III. The carrier mobility at an applied field equivalent to the peak in η_{EQE} (0.30 MV/cm) for a 1:2 G-EML is shown versus TPBi composition in Figure 5.9. In contrast to the TCTA:BPhen material system, the TCTA:TPBi material system shows charge carrier mobilities which

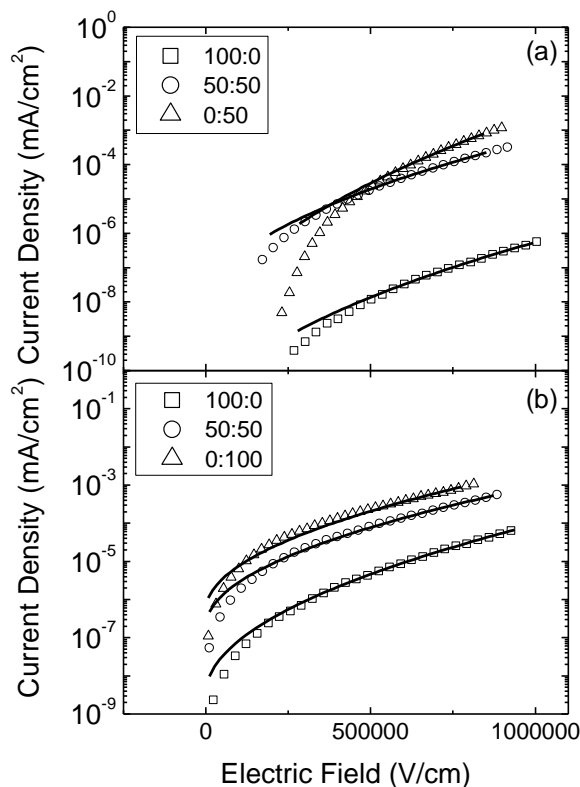


Figure 5.8: Current density-voltage characteristics for 100:0 TCTA:TPBi (squares), 50:50 TCTA:TPBi (diamonds), and 0:100 TCTA:TPBi (triangles) (a) electron-only and (b) hole-only single-carrier devices with 4 wt.% FIrpic. Symbols represent measured data while solid lines are fits to Eqns. 5.1 and 5.2.

are mismatched over a wide range of host compositions. Additionally, no significant decrease is observed for the hole mobility in TPBi-rich devices. TPBi doped with 4 wt.% FIrpic transports holes with a mobility similar to that of TCTA:FIrpic. The lack of a roll-off in hole mobility versus TPBi composition, and thus also position in the G-EML device, may allow for increased hole leakage. The spatial overlap of the electron and hole densities in the 2:1 and 1:1 G-EMLs is likely small due to the low electron mobility in TCTA-rich devices. This likely forces the exciton recombination zone towards the cathode, potentially resulting in additional metal-quenching losses.^{124,125}

Table III: Fit parameters for FIrpic-based single-carrier devices: Zero-field mobility (μ_0) and field dependence parameter (γ) for electron and hole transport in mixed films as a function of the TCTA:TPBi ratio with 4 wt% FIrpic.

TCTA:TPBi	Electron		Hole	
	μ_0 (cm ² /V-s)	γ (cm/V) ^{1/2}	μ_0 (cm ² /V-s)	γ (cm/V) ^{1/2}
100:0	1.0×10^{-8}	4.0×10^{-3}	1.2×10^{-4}	1.8×10^{-3}
80:20	7.6×10^{-8}	4.3×10^{-3}	2.8×10^{-3}	0
70:30	2.0×10^{-6}	3.3×10^{-3}	4.4×10^{-3}	0
60:40	1.3×10^{-5}	2.5×10^{-3}	3.0×10^{-3}	0
50:50	4.9×10^{-5}	2.5×10^{-3}	7.4×10^{-3}	0
40:60	3.1×10^{-7}	6.0×10^{-3}	6.8×10^{-3}	0
30:70	1.4×10^{-6}	5.0×10^{-3}	7.7×10^{-3}	0
20:80	1.2×10^{-4}	6.0×10^{-3}	1.2×10^{-2}	0
0:100	2.5×10^{-3}	7.0×10^{-3}	1.9×10^{-2}	0

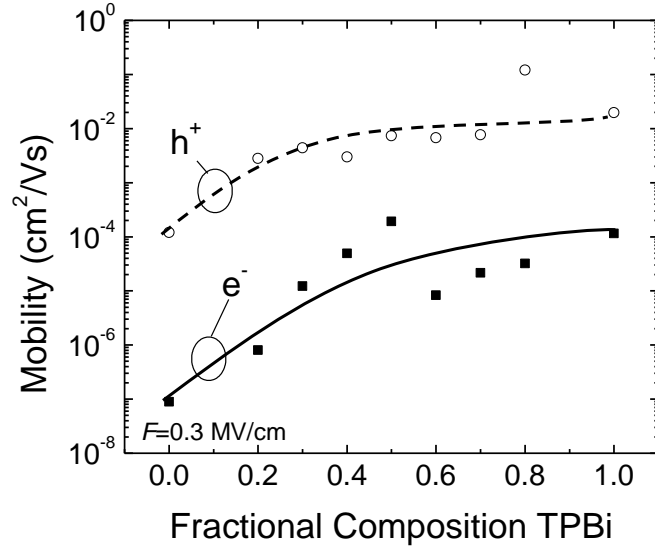


Figure 5.9: Electron (solid symbols) and hole (open symbols) mobility at a field $F = 0.30$ MV/cm for mixed as a function of the TCTA:TPBi composition ratio with 4 wt. % FIrpic. The solid lines are guides to the eye.

In a 1:2 G-EML, a large region of the device is TPBi-rich. As the electron mobility is highest for ETM-rich compositions, the 1:2 device offers a larger spatial extent where both the electron and hole mobilities are maximized. The electron density is thus extended further into the device, improving charge balance and exciton formation. The improved charge balance leads to an enhancement in both η_{EQE} and η_P . In an ideal G-EML device, electron and hole mobilities would be matched over a wide range of compositions, falling only at extreme compositions to aid charge confinement. An ETM with a higher mobility, or conversely, an HTM with a slightly lower mobility, would likely lead to improved charge balance and efficiency in blue-emitting G-EML devices.

5.5 Conclusions

Efficient green, red, and blue OLEDs have been demonstrated which consist of a single, engineered organic layer. The devices exhibit high η_{EQE} and η_P owing to the high charge balance, low-voltage, and tunability of the G-EML device structure. Single-carrier devices are used to extract the field-dependent charge carrier mobilities over a range of HTM:ETM:Guest compositions. The dependence of the electron and hole mobilities on composition, and thus position, is found to strongly influence device operation and performance. The optimal gradient profile is one which both maximizes and balances the electron and hole mobilities, achieving carrier and exciton confinement and large spatial overlap of electron and hole densities. The G-EML device structure is able to overcome a mismatch in HTM and ETM mobilities through careful tuning of the

gradient profile, and thus may be a powerful tool in realizing simplified, high-efficiency OLEDs using a range of active materials.

Chapter 6 Measurement of the Recombination Zone of Organic Light-Emitting Devices

In phosphorescent OLEDs, high external quantum efficiencies (η_{EQE}) have been realized using a variety of device architectures with varying degrees of complexity.^{10,22,58,77,82,83,91,96,103,126,127} As understanding of the fundamental processes relevant for efficient device operation has improved, models of the optical and electronic characteristics of multilayer devices have become increasingly predictive.^{24,128,129} One important feature of OLEDs which has proven difficult to probe experimentally is the spatial extent and location of the exciton recombination zone.¹²⁸ The spatial overlap between the exciton density and the local optical field greatly impacts the efficiency with which photons escape the device,^{71,130,131} as well as the intrinsic radiative decay rate of the exciton.^{128,132–134} The spatial extent of recombination has also been identified as an important parameter that governs the degree to which the η_{EQE} decreases under high excitation,^{11,12,120} termed the efficiency “roll-off.” The mechanisms responsible for the roll-off are separated into two general categories: a reduction in confinement in the emissive layer and bimolecular exciton quenching. The reduction in confinement at high drive current densities reduces the fraction of injected carriers which form excitons, and can be an obstacle to high efficiency operation.¹²⁰ However, such losses can often be mitigated through the use of charge carrier blocking layers that confine injected electrons and holes to the emissive layer. In terms of the bimolecular quenching of excitons, it is understood that in systems which employ long-lifetime phosphorescent emitters, triplet-

triplet annihilation (TTA) and triplet-polaron quenching (TPQ) are the dominant mechanisms for roll-off at device-relevant electric fields, both of which are strongly dependent on the local density of excitons.^{11,12,120–122,135–137}

As already noted, to achieve high peak η_{EQE} in an OLED effective exciton confinement is required in the emissive layer. This is often realized through the use of charge and exciton blocking layers with specific properties, including a shallow lowest unoccupied molecular orbital (LUMO) energy level to block electrons, a deep highest occupied molecular orbital (HOMO) energy level to block holes, or a large energy gap to confine excitons to the emissive layer. One challenge in multilayer devices which incorporate blocking layers is achieving balanced electron and hole injection into the emissive layer. Differences in the barrier heights and charge carrier mobilities for the electron and hole transport pathways inevitably lead to an emissive layer with an excess of one carrier type.¹²⁹ Additionally, the mobilities of electrons and holes often show different field dependencies,^{104,117,138} further complicating charge balance across the useful range of drive voltages. As a result of this relative charge imbalance in the emissive layer, the recombination zone is likely pinned at the interface between the emissive layer and the minority carrier transport layer. In the absence of substantial exciton diffusion or significant exciton quenching effects, the recombination zone is equivalent to the exciton generation profile, and is determined by the spatial overlap of the electron and hole charge densities in the emissive layer.

Device architectures which have shown improved charge balance and charge and exciton confinement often incorporate a double-emissive layer (D-EML) or mixed-emissive layer (M-EML).^{77,78,81–83,139} The D-EML consists of two distinct layers, a hole-transport material (HTM) and an electron transport material (ETM), with an emissive guest uniformly doped throughout both layers. This design strongly confines the charge carriers to a region near the HTM:ETM interface.⁷⁷ The M-EML design consists of a uniformly mixed layer of HTM and ETM that is doped with a luminescent guest. This design has a large interfacial area between HTM and ETM to facilitate exciton formation and the charge carrier mobilities can be tuned by varying the ratio of HTM:ETM.^{102,104,138} Both architectures are usually incorporated into multilayer structures to realize effective charge and exciton confinement.^{83,100}

6.1 Conventional Methods to Measure the Recombination Zone

Conventional experimental determinations of the recombination zone in an OLED have focused on two techniques: translating the position of the guest emitter across the emissive layer while observing large changes in device performance, or monitoring the shape of the emission profile versus viewing angle and deducing the location of exciton generation based on weak microcavity effects.^{138,140–145} While the former technique may give a qualitative determination of the recombination zone location, it gives little information about the recombination zone width and it neglects the often significant role played by the emissive guest in charge transport or charge injection into the emissive layer. This effect may be quite large, especially in devices which employ a single

emissive layer where the host preferentially carries one type of charge, or use large doping concentrations where the guest may participate in charge transport.^{66,143,146} The latter technique compares measured data to fits of optical models and is limited by assumptions present in the optical model.¹⁴⁴ A third technique which has recently been discussed employs a strip-doping method which relies on nearest-neighbor exciton quenching methods.^{12,147} Use of this technique requires a high local concentration of a

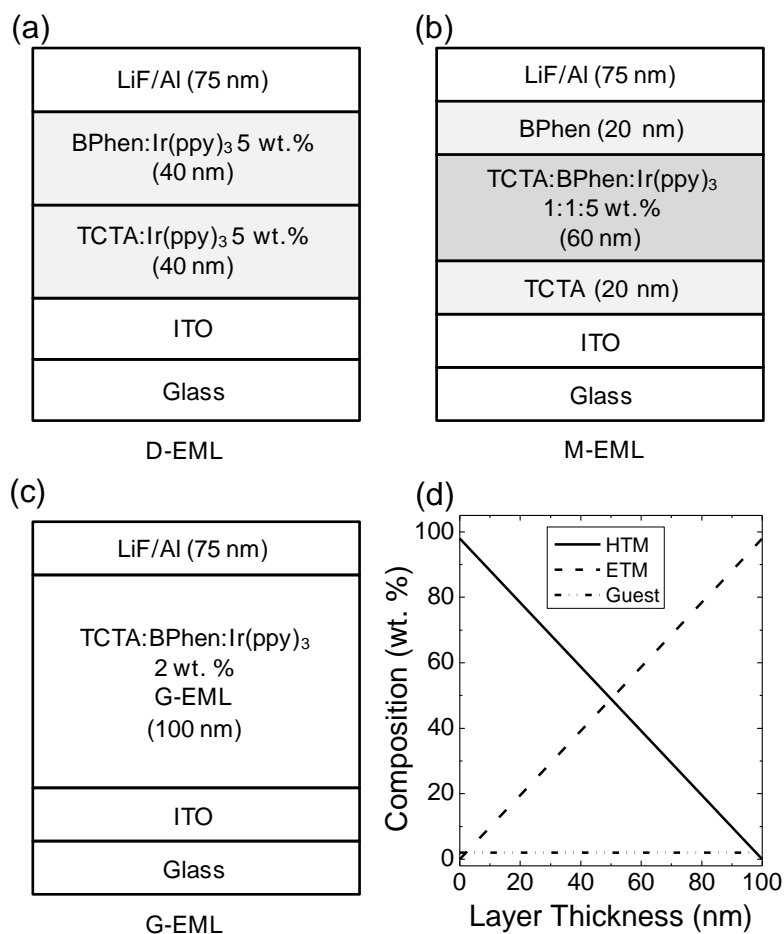


Figure 6.1: Layer structures for the (a) double- (D-EML), (b) mixed- (M-EML), and (c) graded-emissive layer (G-EML) OLED architectures. The spatial composition profile (wt. %) of the G-EML device is shown in (d).

quenching molecule, which may impact the electrical properties of the emissive layer.

6.2 Sensing Excitons via Energy Transfer

In this Chapter, the exciton recombination zone in OLEDs with various emissive layer architectures is probed directly through the addition of a fluorescent sensitizer, capable of quenching excitons formed on the emissive guest, at different locations within the emissive layer. By comparing the overall emission intensity of sensitized devices to control structures containing no sensitizer, a ‘map’ of the local exciton density may be determined. Electrical measurements are performed to ensure that the inclusion of the sensitizer does not alter the electrical characteristics of the devices. This technique is applied to simplified OLEDs containing common emissive layer architectures, namely D-EML and M-EML-type structures, as well as an OLED based on a graded-emissive layer (G-EML), shown schematically in Figures 6.1a-c. The simplified structures facilitate comparisons of the recombination zones in the different devices and show the influence of emissive layer architecture on the recombination zone. The G-EML device offers an architecture which contains no sharp interfaces between HTM and ETM host layers or transport layers, and whose electronic character changes continuously with position within the device (see Figure 6.1d).^{103,104,106} This device has been previously shown to exhibit a high degree of exciton and charge confinement, and is capable of realizing high efficiency in a single-layer device. It is found that the G-EML and M-EML devices exhibit a large recombination zone while the D-EML exhibits a significantly narrower recombination zone centered at the HTM:ETM interface. The larger recombination

Chapter 6: Measurement of the Recombination Zone of Organic Light-Emitting Devices

zones of the G-EML and M-EML may be responsible for an observed reduction in the efficiency roll-off compared to devices containing a D-EML. The efficiency roll-off is considered in greater detail in Chapter 7.

6.2.1 Theory of Exciton Sensitization

Any technique designed to give a quantitative measurement of the exciton recombination zone requires: (i) a high sensitivity to the presence of guest excitons, (ii) a high degree of spatial resolution, and (iii) that it must not substantially alter the natural distribution of charge carriers or excitons within the device. One way to sense the recombination zone is by locally transferring excitons formed on the emissive guest to a second, “sensitizing” molecule.¹² Once the exciton is transferred from the guest to the sensitizer, it may be detected by monitoring emission from the sensitizer, or by selecting a sensitizing material which does not readily luminesce. In the later case the guest exciton is effectively quenched by the sensitizer, resulting in a measurable reduction in luminescence from the guest. Depending on the guest and sensitizing materials, quenching may occur via Dexter- or Förster-type energy transfer.^{1,15} Quenching via Dexter energy transfer requires a physical exchange of electrons between the guest and sensitizer and is therefore a nearest-neighbor process. The rate of Dexter energy transfer falls off steeply with increasing separation between guest and sensitizer molecules.¹⁵ While this mechanism may be a highly localized process, satisfying condition (ii), it requires a high density of sensitizer molecules in order to ensure that the sensitizer is adjacent to the dilute-doped guest, likely influencing the local electronic environment.¹²

Förster energy transfer is a non-radiative dipole-dipole coupling between a donor (i.e. guest) and acceptor (i.e. sensitizer) molecule. This interaction may occur through occupied space, extending the range of energy transfer and quenching. The rate of Förster energy transfer between point dipoles is given by:²³

$$k_F[d] = \frac{1}{\tau} \left(\frac{R_0}{d} \right)^6, \quad (6.1)$$

where τ is the exciton lifetime, d is the donor-acceptor molecular separation, and R_0 is the characteristic radius of Förster energy transfer, given by:^{15,23}

$$R_0^6 = \frac{9 \eta_{PL} \kappa^2}{128 \pi^5 n^4} \int \lambda^4 F_D[\lambda] \sigma_A[\lambda] d\lambda, \quad (6.2)$$

where η_{PL} is the photoluminescence efficiency of the donor, κ is the dipole orientation factor, n is the index of refraction of the medium between the donor and acceptor, λ is the wavelength, F_D is the area-normalized donor emission spectrum, and σ_A is the absorption cross-section of the acceptor. Förster energy transfer between the guest and sensitizer, and thus the spatial resolution of exciton quenching, may be tuned by selecting a sensitizing material with an appropriate overlap of absorption with the guest emission. Quenching may then occur over a small distance (~ 1 -5 nm) and retain a high sensitivity to the presence of guest excitons, allowing a low sensitizer concentration to be used (< 1 wt.%). Such a low doping concentration is unlikely to affect charge transport and leads to only a slight reduction in spatial resolution.

In this chapter, a measurement of the recombination zone in a variety of common emissive layer architectures is realized by including a highly localized, lightly-doped strip of tetraphenyltetrabenzoporphyrin (TPTBP) into a device to quench excitons formed on

the luminescent guest via Förster energy transfer. The composition of the sensitized strip is otherwise matched to the local concentrations of the host and guest materials for a particular structure. Here, TPTBP is selected based on the small overlap of its absorption cross section with the photoluminescence (PL) of the archetypal green phosphor, tris(2-phenylpyridine)iridium(III) (Ir(ppy)_3) (see Figure 6.2a). In a separate measurement, TPTBP showed extremely weak luminescence under electrical excitation, this ensures that excitons transferred from Ir(ppy)_3 predominantly decay non-radiatively.

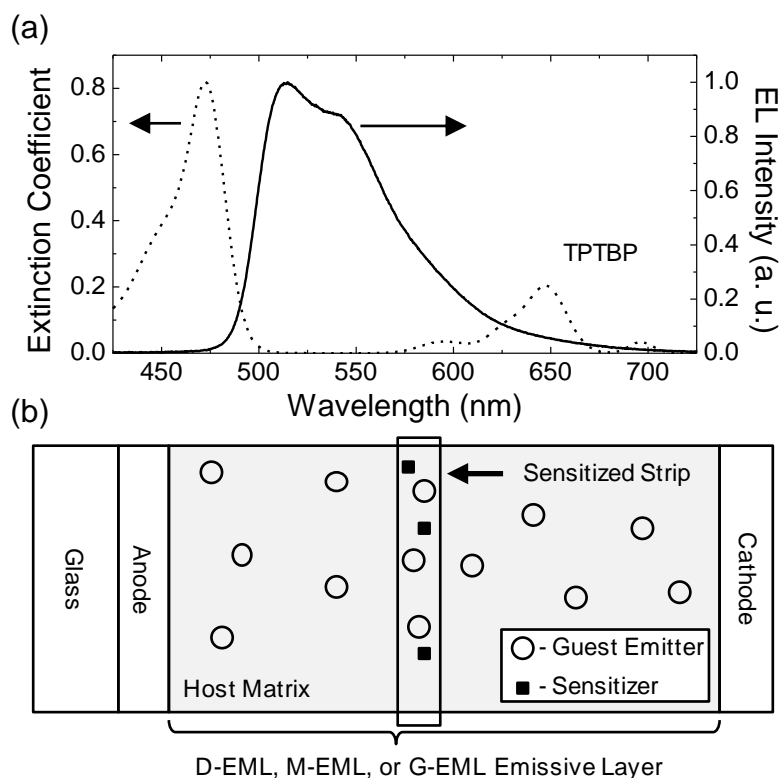


Figure 6.2: (a) Extinction coefficient for the sensitizer, TPTBP, (dashed line) and peak-normalized electroluminescence (EL) spectrum of the emissive guest, Ir(ppy)_3 (solid line). **Inset:** Molecular structure of TPTBP. (b) Schematic representation of the sensitizing strip technique.

Subsequent measurements of the electroluminescence (EL) from sensitized devices

containing both TPTBP and Ir(ppy)₃ showed no observable contribution from TPTBP. Using Eqn. 6.2 and the optical properties of TPTBP and Ir(ppy)₃, an $R_0 = 3.9$ nm is calculated. The Förster quenching distance, and thus the spatial resolution of the measurement, may be tuned by selecting a sensitizer with a small overlap of absorption with guest emission, ensuring a small R_0 and high degree of spatial resolution. The integrated EL intensity of each sensitized device is measured and compared to a control device which does not contain TPTBP, this quantity is termed the “EL ratio” $\equiv \beta$. This ratio is directly proportional to the ratio of quenched excitons and therefore the quantity $1-\beta$ is proportional to the ratio of unquenched excitons, i.e. the local exciton density. A map of the recombination zone is realized by fabricating a series of devices with the sensitizing strip translated throughout the emissive layer, and plotting the local exciton density versus strip position (Figure 6.2b). One factor that is not included but may become important in wide-recombination zone devices is the spatial dependence of the far-field extraction efficiency of excitons at different positions within the EML. The optical field properties, and the effects of optical field on OLEDs, are discussed further in Chapter 8.

6.2.2 Theory of the Electronic Model of G-EML OLEDs

Theoretical models for the spatial charge density in an organic semiconductor have previously been developed for multilayer OLEDs.^{24,129,148} To describe the environment of a single-layer, G-EML device (Figure 6.1c), we adapt a model from Neumann et al.¹⁴⁹ which considers charge carrier drift, diffusion, and recombination to

describe charge densities and the recombination zone. It is important to note that the charge densities, electric field, and mobility are all position dependent in a G-EML,¹⁰⁴ thus we have chosen to make this explicit by including $[x]$ in all subsequent, spatially-dependent equations.

The one-dimensional equations are:

$$\frac{dF[x]}{dx} = \frac{e}{\epsilon\epsilon_0} (p[x] - n[x]) , \quad (6.3)$$

$$\frac{dJ_n}{dx} = e\gamma n[x]p[x] , \quad (6.4)$$

$$\frac{dJ_p}{dx} = -e\gamma n[x]p[x] , \quad (6.5)$$

where Eqn. 6.3 is Poisson's equation. Here, $F[x]$ is the electric field, e is the elementary charge, ϵ is the relative permittivity of the organic layer (taken here as $\epsilon = 3$), ϵ_0 is the permittivity of vacuum, $p[x]$ is the hole density, and $n[x]$ is the electron density. The continuity equations for electrons and holes are given in Eqns. 6.4 and 6.5, respectively, and contain a Langevin-type recombination term. Langevin recombination has been extensively used to describe recombination in OLEDs.^{1,150,151} In this formalism, γ is the recombination coefficient:

$$\gamma = \frac{e}{\epsilon\epsilon_0} (\mu_n[x] + \mu_p[x]) . \quad (6.6)$$

The electron current density is given by:

$$J_n = e n[x] \mu_n[x] F[x] + kT \mu_n[x] \frac{dn[x]}{dx} , \quad (6.7)$$

and contains a field-dependent drift term as well as a diffusion term. Similarly, the hole current density is given by:

$$J_p = e p[x] \mu_p[x] F[x] - kT \mu_p[x] \frac{dp[x]}{dx}. \quad (6.8)$$

In these expressions we have assumed the validity of the Einstein relation relating the drift and diffusion of charge. To simplify the evaluation of the continuity equations, dimensionless quantities are used to describe the position, the electric field, and the charge densities:

$$X = \frac{1}{L} x, \quad (6.9)$$

$$E[X] = \frac{L}{V} F[X], \quad (6.10)$$

$$N[X] = n[X] \frac{L^2 e}{\epsilon \epsilon_0 V}, \quad (6.11)$$

$$P[X] = p[X] \frac{L^2 e}{\epsilon \epsilon_0 V}, \quad (6.12)$$

where L is the width of the G-EML layer and V is the applied voltage. Using the continuity equations and the electron and hole current densities defined in Eqns. 6.3-6.8, together with the dimensionless variables defined above, we derive four steady-state, coupled equations for the voltage, electric field and the carrier densities:

$$V[X] = -\frac{dE[X]}{dX}, \quad (6.13)$$

$$E[X] = P[X] - N[X], \quad (6.14)$$

$$0 = -N[X]^2 + N[X]E[X] \frac{d\mu_n[X]}{dX} \frac{1}{\mu_n[X]} + E[X] \frac{dN[X]}{dX} + \frac{kT}{eV} \frac{d\mu_n[X]}{dX} \frac{1}{\mu_n[X]} \frac{dN[X]}{dX} + \frac{kT}{eV} \frac{d^2 N[X]}{dX^2} - N[X]P[X] \frac{\mu_n[X]}{\mu_p[X]}, \quad (6.15)$$

$$0 = P[X]^2 + P[X]E[X] \frac{d\mu_p[X]}{dX} \frac{1}{\mu_p[X]} + E[X] \frac{dP[X]}{dX} - \frac{kT}{eV} \frac{d\mu_p[X]}{dX} \frac{1}{\mu_p[X]} \frac{dP[X]}{dX} - \frac{kT}{eV} \frac{d^2P[X]}{dX^2} [X] + N[X]P[X] \frac{\mu_n[X]}{\mu_p[X]}. \quad (6.16)$$

While it is possible to write Poisson's equation in terms of V directly, it is instructive to solve for the shape of the field (as determined by $N[X]$ and $P[X]$) while using V to set the boundary conditions. This matches well with actual device operation, where a potential is applied to the electrodes and the field may vary depending on the local electron and hole charge densities. The boundary conditions imposed are:

$$N[0] = P[1] = 0, \quad (6.17)$$

$$N[1] = P[0] = 1, \quad (6.18)$$

$$V[1] = 0, \quad (6.19)$$

$$V[0] = 1. \quad (6.20)$$

The boundary conditions in Eqn. 6.17 constrain the system such that there is no electron leakage to the anode, no hole leakage to the cathode, and all current comes from the recombination of carriers. This scenario is valid given the high efficiencies obtained in Chapter 3 for single-layer G-EML OLEDs. Together with the boundary conditions of Eqn. 6.18, an equal number of holes and electrons are present in the device. This last constraint ensures that the model reflects the steady-state behavior of the device and can be confirmed by comparing the integrated charge densities. The boundary conditions of Eqns. 6.19 and 6.20 reflect a system where one side is grounded and a potential is applied at the opposite side. The magnitude of the applied voltage is varied in the coupled equations. Finally, the product of the electron ($N[X]$) and hole ($P[X]$) charge densities

(the 'NP product') is equivalent to the exciton density profile, and thus reflects the extent of the exciton recombination zone with exciton diffusion assumed to be negligible. This last assumption is valid for cases where the exciton is well-confined to the guest and the guest concentration is low, both of which are typical conditions in an OLED.

6.3 Experimental Methods

The Förster radius was calculated using the extinction coefficient of TPTBP as measured by spectroscopic ellipsometry, the PL spectrum of Ir(ppy)₃, an average index of refraction ($n = 1.8$) for the TCTA:BPhen host at the peak in Ir(ppy)₃ emission as determined by spectroscopic ellipsometry, and the photoluminescence quantum yield of Ir(ppy)₃, taken as $\eta_{PL} = 95\%$ based on previous work.²¹ The formula weight of TPTBP is 816.99 g mol⁻¹ and a density 1.2 g cm⁻¹ was measured via X-ray reflectivity. Using Eqn. 6.2 and the above parameters, a Förster radius of $R_0 = 3.9$ nm is calculated. The Förster radius is primarily determined by the overlap of sensitizer absorption cross-section with the guest PL.

All devices are fabricated by the vacuum thermal evaporation methods described in Chapter 2. Green-emitting devices were fabricated using 4,4',4''-tris(carbazol-9-yl)triphenylamine (TCTA) and 4,7-diphenyl-1,10-phenanthroline (BPhen) as the HTM and ETM, respectively, with Ir(ppy)₃ as the luminescent guest and TPTBP (Frontier Scientific) as the quencher in sensitized devices; all materials were used as received. All organic layers were deposited in high vacuum ($<10^{-7}$ Torr) with independent quartz crystal monitors measuring the deposition rate of each material, allowing for careful

control of the concentration and location of TPTBP within the devices. The G-EML devices were fabricated using time-varying deposition rates as described previously, with an optimal Ir(ppy)₃ doping concentration of 2 wt.%. Sensitized G-EML devices included a 4-nm-thick strip of 1 wt. % TPTBP with concentrations of TCTA, BPhen and Ir(ppy)₃ that are matched to the spatial location of the strip. The D-EML and M-EML devices were fabricated using the following optimized structures: ITO/40 nm TCTA:Ir(ppy)₃ (5 wt.)/40 nm BPhen:Ir(ppy)₃ (5 wt.%) for the D-EML, and ITO/20 nm TCTA/60nm TCTA:BPhen:Ir(ppy)₃ (1:1:5 wt.)/20 nm BPhen for the M-EML. The additional TCTA and BPhen layers present in the M-EML device serve to confine charge the emissive layer; M-EML devices fabricated without such blocking layers have large leakage currents and show poor device performance. Sensitized M-EML devices contained a 4-nm-thick strip of 1 wt.% TPTBP and D-EML devices contained a 2-nm-thick strip of 1 wt.% TPTBP with concentrations of TCTA, BPhen, and Ir(ppy)₃ corresponding to the spatial location within each device. The ratio of the strip width to measured recombination zone width remains <10% in all device architectures, ensuring a high degree of spatial accuracy

6.4 Measurements of the Exciton Recombination Zone

The current density-voltage (J-V) characteristics for selected sensitized devices are shown in Figures 6.3a-c for D-EML, M-EML, and G-EML devices, respectively, as a function of strip position, along with control devices that do not contain the sensitizing strip. To ensure that variations in the J-V characteristics are not strip-position dependent

and are instead the result of minor sample-to-sample variations, the current density of each sensitized device at 5 V is plotted versus strip position in Figures 6.3d-f for D-EML,

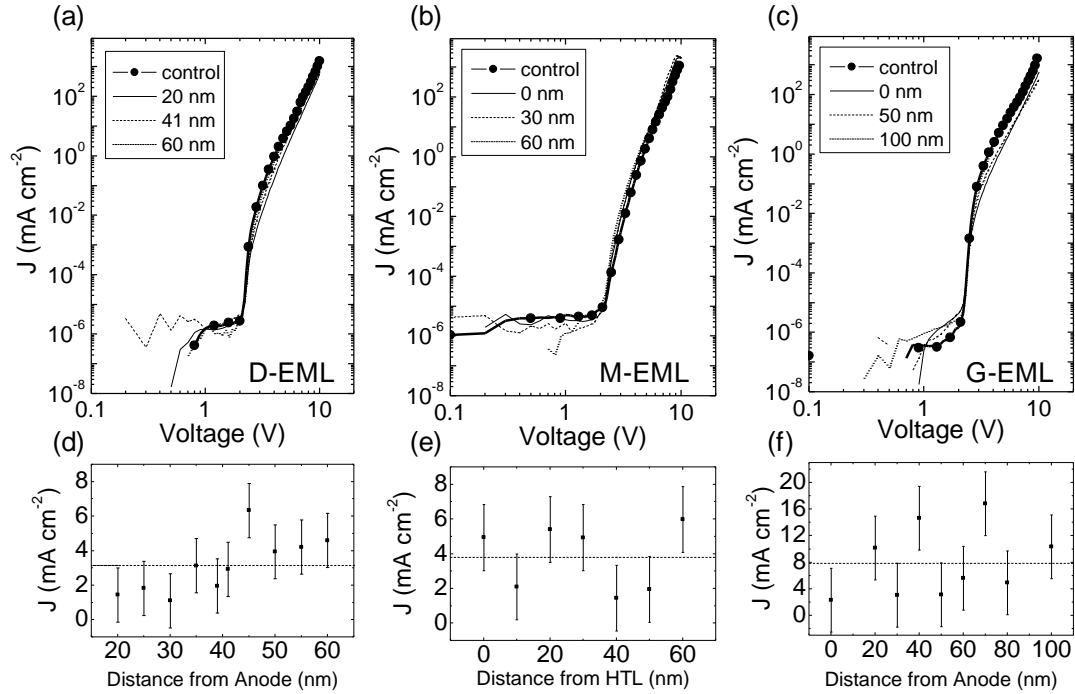


Figure 6.3: Current density-voltage characteristics (J-V) for (a) D-EML, (b) M-EML, and (c) G-EML devices with a sensitizing strip located at different positions within the emissive layer (as measured from anode, in the case of the D-EML and G-EML, or from the TCTA/M-EML interface, for M-EML devices). Data for devices with intermediate strip positions are omitted for clarity. A control device which does not contain the sensitizing strip is shown (closed symbols) for each of the device architectures of interest. The current density at an applied voltage of 5 V for each device is shown in (d) for D-EML devices, (e) for M-EML devices, and (f) for G-EML devices; the horizontal line represents the average current density of the devices and error bars are calculated from the current density variation of control devices fabricated in different runs.

M-EML, and G-EML devices, respectively. The error bars are taken as the device-to-device variation observed for control devices fabricated in different runs. For each of the architectures, differences in the current densities do not trend systematically with sensitizer position, suggesting that the inclusion of the doped sensitizing strip does not substantially impact charge transport, satisfying condition (iii) discussed previously.

Chapter 6: Measurement of the Recombination Zone of Organic Light-Emitting Devices

The measured exciton recombination zone for a D-EML device is shown in Figure 6.4a at an applied current density of 10 mA cm^{-2} and is found to be pinned at the HTM:ETM interface. The total spatial extent of the recombination zone is $\sim 15 \text{ nm}$ and does not shift in position or spatial extent throughout the range of current densities probed. Previous studies on the hole and electron mobilities of TCTA and BPhen have suggested that holes are slightly more mobile in TCTA than electrons in BPhen.^{89,152} This is reflected here in the observation of an increased width in the recombination zone on the BPhen side of the D-EML. In terms of device operation, holes are arriving at the interface of the HTM:ETM more quickly and are penetrating into the ETM, likely by injection onto molecules of Ir(ppy)_3 . The low concentration of Ir(ppy)_3 confines holes on the ETM side close to the interface, where they may form excitons with incoming electrons. More generally, the recombination zone in D-EML devices is dominated by the extent to which a minority carrier may penetrate the majority host. Minority charge carriers on each side of the D-EML are usually confined to the emissive guest in configurations where the guest energy levels lie within those of the host materials. To attain high photoluminescence efficiencies (η_{PL}), guest doping concentrations are typically $<10 \text{ wt.}\%$, likely inhibiting efficient charge transport along the guest. Effectively, the product $n[x] \times p[x]$ is confined to a narrow region centered on the interface between the HTM and ETM in D-EML-based OLEDs.

The recombination zone profile of the M-EML device is shown in Figure 6.4b at an applied current density of 10 mA cm^{-2} . In comparison to the case of the D-EML, the

recombination zone width in the M-EML is substantially larger, approaching a value

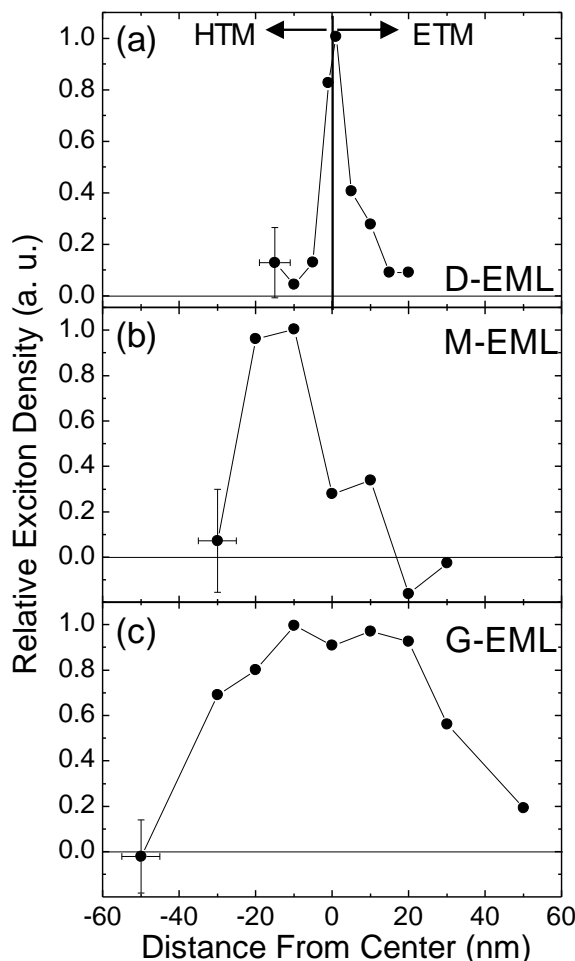


Figure 6.4: The relative exciton density versus position in (a) D-EML, (b) M-EML, and (c) G-EML devices, at an applied current density of 10 mA cm^{-2} . For the D-EML device, the recombination zone is centered at the TCTA/BPhen interface and has a spatial extent of $\sim 15 \text{ nm}$. In the case of the M-EML device, the spatial extent of the recombination zone approaches $\sim 40 \text{ nm}$ and is centered on the TCTA side of the emissive layer. The G-EML shows the largest recombination zone, with a spatial extent $> 80 \text{ nm}$, and is centered in the middle of the device.

of $\sim 40 \text{ nm}$. The peak exciton density is shifted towards the TCTA side of the M-EML, with the density decreasing to a negligible amount $\sim 40 \text{ nm}$ from the TCTA/M-EML interface. The shape of the recombination zone is indicative of a device that is limited by

the spatial extent of the hole density, potentially indicating that electrons are more mobile in the M-EML layer. Generally, the recombination zone in an M-EML-based device will depend on the transport properties of the emissive layer, transport layers, and blocking layers, but may be enhanced relative to the D-EML architecture due the ability of the M-EML to carry both electrons and holes.

The recombination zone profile of the G-EML is presented in Figure 6.4c for an applied current density of 10 mA cm^{-2} and spans the majority of the device, realizing a total spatial extent of $>80 \text{ nm}$ with a peak at the center of the layer. The measured exciton densities at the edge of the G-EML are within the experimental resolution of zero, indicating that excitons are not likely to form directly adjacent to the metal cathode. The large spatial extent of the recombination zone reflects a broad distribution of the electron and hole densities in the G-EML device. The observed symmetry and well-centered peak position in the exciton density is a result of the relative symmetry of the magnitude and spatial dependence of the electron and hole mobilities throughout the G-EML device. Generally, it is expected that the spatial extent and peak location of the recombination zone in a G-EML-based OLED will reflect the spatial dependence of the electron and hole mobilities. This is addressed in the following section.

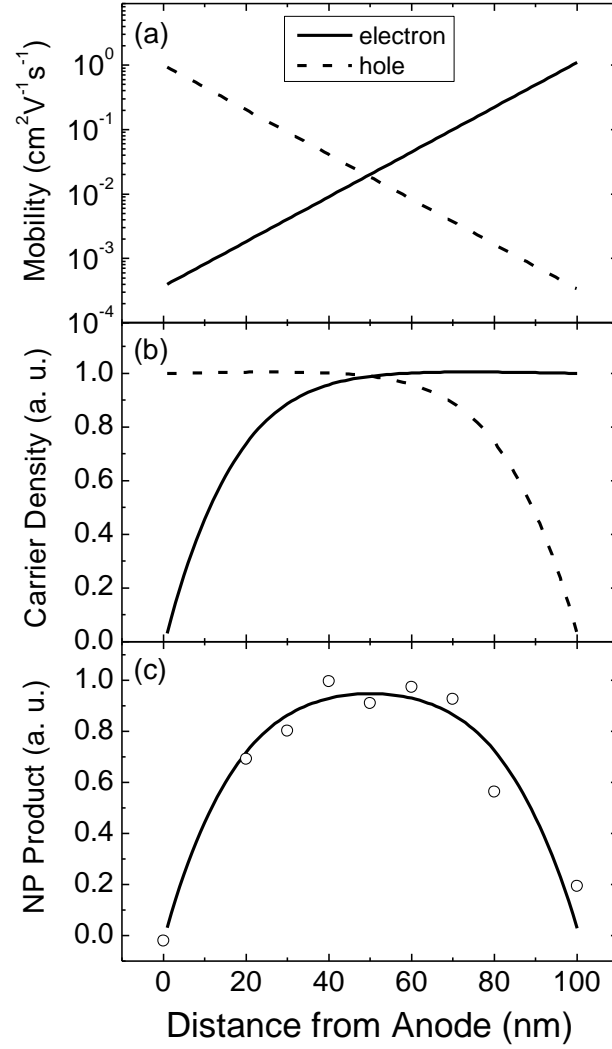


Figure 6.5: Functions chosen to describe the spatial variation electron and hole mobilities of a G-EML device. (b) Calculated electron and hole densities; both carrier densities vanish at the opposing electrode, reflecting the boundary conditions and situation where there is no leakage current. (c) The product $N[X] \times P[X]$ (NP product) is plotted along with the measured recombination zone data of Figure 4. The NP product has been scaled vertically, as the injected current density is arbitrarily set via the boundary condition in Eqn. 6.18.

6.5 Electronic Model of G-EML OLEDs

Using the boundary conditions described in Eqns. 6.17-6.20, the set of coupled differential equations describing the spatial overlap of the electron and hole densities have been solved numerically for the G-EML. The functions used to describe the spatial variation of the electron and hole mobilities of the TCTA:BPhen-based G-EML are shown in Figure 6.5a. These represent well the measured mobilities of a G-EML OLED described previously using the same materials. In Figure 6.5b the spatial dependence of $N[X]$ and $P[X]$ is shown with the resulting NP product, $N[X] \times P[X]$, plotted in Figure 6.5c along with the experimentally measured recombination zone data, with the NP product scaled vertically. The simulated recombination zone matches well with measured data, reproducing both the peak position and breadth of the experimental data. In accordance with Eqn. 6.17 $N[X]$ and $P[X]$ vanish at the opposite electrode which drives the exciton density to zero, confirming that no substantial exciton density is present near the electrodes in the G-EML device.

Given the good agreement between the model and experimental data, it is instructive to model the electron and hole charge densities, and NP product, for a series of G-EML devices which have HTM and ETM mobilities that are not well matched in magnitude, but retain the spatial dependence characteristic of the G-EML architecture. These simulations allow for characterization of the recombination zone in devices where particular materials may be desired due to beneficial optical properties, but where electrical transport may suffer. The magnitude and spatial dependence of the electron and

hole mobilities examined are shown in Figure 6.6a and 6.6b. To simplify comparisons going forward, each case is identified by the ratio of the electron-to-hole mobility at the midpoint of the device, $\mu_R = 0.01, 0.1, 10, 100$. The resulting $N[X]$ and $P[X]$ are shown in Figure 6.6c and 6d for $\mu_R = 0.01$ and 0.1 , and $\mu_R = 10$ and 100 , respectively. The NP products for $\mu_R = 0.01$ and 0.1 is shown in Figure 6.6e, with the NP products for $\mu_R = 10$ and 100 shown in Figure 6.6f.

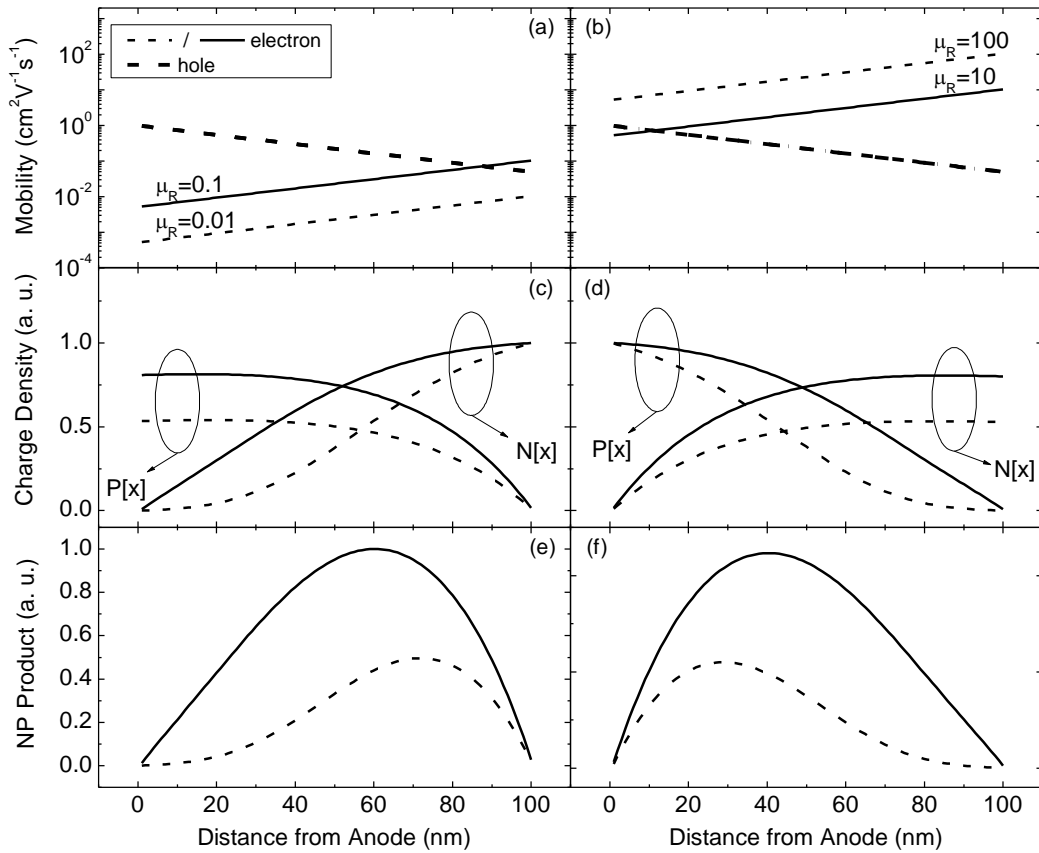


Figure 6.6: Spatial variation of electron and hole mobilities for G-EML devices where the ratio of electron to hole mobility is: $\mu_R = 0.01$ and $\mu_R = 0.1$. (b) Spatial variation of electron and hole mobilities for G-EML devices where $\mu_R = 10$ and $\mu_R = 100$. The calculated $N[X]$ and $P[X]$ for the mobilities shown in (a) and (b) are shown in (c) and (d), respectively. The resulting NP product of the carrier densities of (c) are shown in (e), while the NP product for the carrier densities of (d) are shown in (f).

For devices with a moderate mobility mismatch (i.e. μ_R between 0.01 and 100), the recombination zone is shifted away from the majority carrier injecting electrode, as seen in Fig 6.6c and 6.6d. The total extent of the recombination zone is not affected greatly, indicating the flexibility of the G-EML architecture to accommodate a wide range of HTM and ETM host combinations. For devices with large mobility mismatches, the recombination zone peak shifts greatly towards the minority carrier side. This is a result of the majority charge density extending far into the device. At extreme mobility mismatches the majority charge density extends far enough into the device that injected minority carriers rapidly encounter majority carriers, form excitons, and recombine. As the recombination zone encounters the electrode, additional losses may be incurred such as a loss in charge confinement, dissociation of the exciton by the nearby metal, or by exciton coupling to the surface plasmon modes.^{124,125} These effects may be particularly important for devices with large mobility mismatches and have not been considered in this model as they apply to extreme cases where the HTM and ETM are poorly chosen.

Generally, in a G-EML-based device, materials with moderate mobility mismatches may be used by tuning the concentration gradient profile of the G-EML device. By tuning the relative deposition rates of the HTM, ETM, and guest material, a G-EML device with a composition favorable to electron or hole charge transport may be fabricated. Previously, in Chapter 3, a G-EML device with an electron-favorable composition profile was shown to be optimal for blue light-emitting devices. These devices extend the minority carrier density further in to the device, improving electron-

hole overlap while maintaining charge and exciton confinement, retaining the large recombination zone. High efficiency may then be realized in a wide range of simplified devices where particular active materials are desirable, despite a mismatch in mobilities.

6.6 Impact of Recombination Zone on Efficiency Roll-Off

The four main parameters which govern the η_{EQE} roll-off of an OLED are: the relative rate constants of TTA and TPQ, τ , and the recombination zone width. While the first three parameters depend primarily on materials selection, the recombination zone, as has been demonstrated here, is strongly device design-dependent. One way to quantitatively compare the efficiency roll-off of different architectures is to note the current density at which the η_{EQE} has rolled-off to half of its maximum, or “ J_0 .”¹¹ Therefore, the peak-normalized η_{EQE} of the three device structures of interest are shown in Figure 6.7, with relevant device parameters presented in Table 1. Here, a reduction in the efficiency roll-off with current density is observed in devices characterized by a larger exciton recombination zone, as shown by an increased value for J_0 in the M-EML and G-EML structures relative to the D-EML. It is interesting to note that despite the larger recombination zone of the G-EML device relative to the M-EML, the efficiency roll-off in these devices is very similar. This may suggest that important parameters, such as the polaron density and the degree of charge confinement, differ significantly in each device. Further work is needed to fully quantify and decouple the role of the exciton recombination zone from other contributing factors that determine the efficiency roll-off.

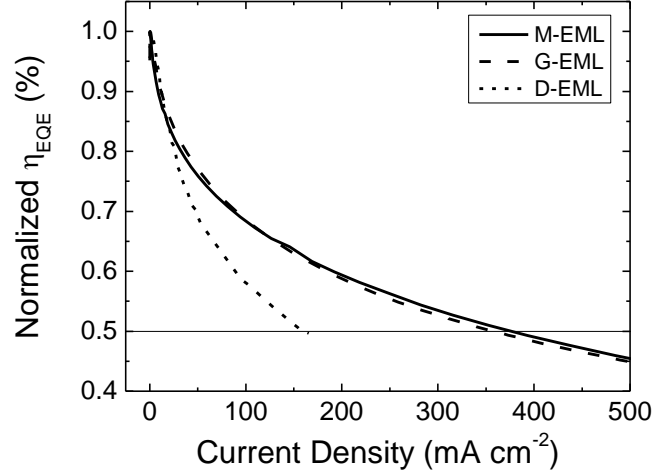


Figure 6.7: Peak-normalized η_{EQE} for D-EML, M-EML, and G-EML OLEDs. The J_0 for each device is: 160 mA cm^{-2} , 375 mA cm^{-2} , and 360 mA cm^{-2} , for D-EML, M-EML, and G-EML, respectively.

Table I: Device parameters for the architectures of interest: Peak η_{EQE} , measured recombination zone (RZ) width, and roll-off parameter J_0 , defined as the current density where η_{EQE} rolls-off to half its peak value, for the D-EML, M-EML, and G-EML device architectures

Device Architecture	Peak η_{EQE} (%)	RZ width (nm)	J_0 (mA cm^{-2})
D-EML	11.8	15	160
M-EML	12.2	40	375
G-EML	16.9	80	360

The efficiency roll-off in these devices is addressed in greater detail in Chapter 8.

6.7 Conclusions and Acknowledgments

A method to quantitatively measure the width and location of the exciton recombination zone in an OLED has been developed and is generally independent of emissive layer architecture. This technique demonstrates a high sensitivity to the presence of guest excitons, a high degree of spatial resolution, and does not alter charge transport in the OLED. We demonstrate a strong dependence of both the location and spatial extent of the exciton recombination zone on the emissive layer architecture.

Chapter 6: Measurement of the Recombination Zone of Organic Light-Emitting Devices

OLEDs based on M- and G-EML architectures have much larger recombination zones than devices based on a D-EML architecture, with the G-EML architecture showing a recombination zone which spans the entire device. This strong correlation emphasizes the need to couple efforts aimed at engineering OLED architecture with direct measurements of the exciton recombination zone. Quantitative insight into the exciton recombination zone is essential as a tool to guide OLED design and to better inform and evaluate critically needed models of operation.

Chapter 7 Engineering Efficiency Roll-Off in Organic Light-Emitting Devices

As mentioned previously, one development which has enabled high peak external quantum efficiency (η_{EQE}) is the ability to harvest triplet excitons for electroluminescence (EL). The utilization of triplet excitons occurs via three pathways: (1) directly as radiative decay, i.e. electrophosphorescence,^{10,54,55,57,66} or indirectly, from (2) triplet-triplet annihilation processes which result in the formation of a singlet exciton,^{153–157} or (3) singlet states which are populated through reverse intersystem crossing from triplet states, as in thermally activated delayed fluorescence (TADF).^{47,158–160} All of these routes, however, require population of the triplet exciton state through electrical excitation. Triplet excitons typically have long natural lifetimes, on the order of 10^{-6} - 10^{-3} s.^{10–13} A consequence of the long lifetime is that at the high current densities often necessary to achieve high brightness levels, large triplet exciton densities are produced. These high densities result in exciton density-driven quenching processes, which are observed as a decrease in the η_{EQE} with increasing current density (and thus increasing brightness), a characteristic termed the “efficiency roll-off.”^{12,79,120,121,136,161} The efficiency roll-off is one factor which limits the implementation of OLEDs in high brightness applications. Further, it has been suggested that device operating lifetimes may suffer in devices with a high degree of efficiency roll-off, as higher current densities are needed to reach high operating brightness levels.^{79,162–165}

7.1 Density-Driven Exciton Quenching Processes

The physical processes which are responsible for exciton quenching in phosphorescence-based OLEDs have been previously identified as triplet-triplet annihilation and triplet-polaron quenching.^{11,12,120,121,135,137} The impact of these processes on the triplet exciton population can be written separately as:

$$\frac{dn_{ex}}{dt} = -\frac{n_{ex}}{\tau} - \frac{1}{2}\kappa_{TT}n_{ex}^2 + G \quad (7.1)$$

for triplet-triplet annihilation, and

$$\frac{dn_{ex}}{dt} = -\frac{n_{ex}}{\tau} - \kappa_{TP}\rho n_{ex} + G \quad (7.2)$$

for triplet-polaron quenching, where n_{ex} is the triplet exciton population, which may depend on position within the emissive layer, τ is the exciton lifetime, κ_{TT} is the rate of triplet-triplet annihilation, κ_{TP} is the rate of triplet-polaron annihilation, G is an exciton generation term, and ρ is the polaron density, which depends on position and which may be a function of the current density, J , or voltage, V , depending on the description of charge transport.^{112,135,166} In Eqn. (7.2), the spatial overlap of polarons and excitons in the device is of particular importance. This property, however, is difficult to probe directly, thus the rate constant κ_{TP} reflects not only the strength of the interaction of polarons and excitons but also the spatial overlap.¹² Under device operating conditions, the exciton population becomes:^{11,12}

$$\frac{dn_{ex}}{dt} = -\frac{n_{ex}}{\tau} - \frac{1}{2}\kappa_{TT}n_{ex}^2 - \kappa_{TP}\rho n_{ex} + \frac{J}{eW} \quad (7.3)$$

where the final term represents electrical generation of excitons, e is the elementary charge, and W is the width of exciton recombination zone in the device. Written this way, the generation term assumes all injected carriers form excitons, which may be the

case for devices with a high degree of charge balance. Previously, loss of charge balance has been identified as a contributing factor to the efficiency roll-off observed in devices.¹²⁰ Loss of charge balance may be mitigated through device design, either through material selection or the incorporation of charge blocking layers. Whereas κ_{TT} , κ_{TP} , and τ are typically considered material parameters and are generally independent of device design in typical OLED architectures, the exciton recombination zone in an OLED is dependent on the overlap of electron and hole charge densities, and thus is sensitive to the architecture of the device, particularly the emissive layer design.

7.2 Experimental Design

7.2.1 Device Architectures of Interest

There are a variety of emissive layer architectures which have shown high peak efficiencies, including double-emissive layer (D-EML), mixed-emissive layer (M-EML), and graded-emissive layer (G-EML) devices.^{77,78,81–83,103,104,139} The D-EML consists of two distinct layers, a hole-transport layer (HTL) and an electron transport layer (ETL), both doped uniformly with a dilute emissive guest. This architecture can achieve high a degree of charge balance and strongly confines the charge carriers to a region near the HTM:ETM interface. The M-EML design consists of a uniformly mixed layer of HTM and ETM that is doped with the emissive guest. This design allows for the charge carrier mobilities of the composite layer to be tuned by varying the HTM:ETM ratio, ideally achieving ambipolar characteristics to maximize charge balance and efficient exciton formation.⁸³ The G-EML device is a single-layer device architecture which consists of a

continuously varying composition profile, from nearly 100% HTM at the anode to nearly 100% ETM at the cathode, doped throughout with an emissive guest.¹⁰³ This device architecture has been previously used to achieve high η_{EQE} in red-, green-, and blue-light emitting devices.¹⁰⁴

Whereas the G-EML device may be optimized by tuning the composition gradient profile, the D-EML and M-EML device architectures often require the use of charge and exciton blocking and transport layers to achieve high peak performance. Optimization in these devices is done by adjusting the doping concentration, thickness of each layer, and mixing ratio of HTM:ETM, in the M-EML devices. These parameters are most often tuned to give low-voltage operation and high peak-performance, though the impact these changes have on the spatial extent and location of the recombination zone is rarely considered.

The recombination zone width of D-EML and G-EML-based devices has previously been measured in Chapter 6, and it was found that the D-EML architecture had a significantly reduced width ($W \approx 15$ nm) compared to that of the G-EML device ($W \approx 80$ nm).¹⁶⁷ In that Chapter, it was observed that the G-EML device exhibited a reduction in the efficiency roll-off compared to the D-EML-based device. In this Chapter we quantitatively examine the exciton quenching processes present in both device architectures using both transient and steady state photo- and electro-luminescence measurements. The important quenching parameters κ_{TT} , κ_{TP} , and τ are measured

independently, and the impact of the recombination zone width on efficiency roll-off is examined directly.

7.2.2 Device Fabrication and Test Film Design

Optimized OLEDs and thin film test devices were fabricated using 4,4',4''-tris(carbazol-9-yl)triphenylamine (TCTA) as an HTM, 4,7-diphenyl-1,10-phenanthroline (BPhen) as an ETM, and the archetypal green phosphorescent molecule tris(2-phenylpyridine)iridium(III) (Ir(ppy)₃) as the emitter. These host materials are common to many OLEDs and have been previously used in the fabrication of high-efficiency G-EML OLEDs.¹⁰⁴ To characterize the κ_{TT} and τ , thin films having a thickness of 30 nm were fabricated on glass substrates with TCTA:Ir(ppy)₃ (2 wt.%), BPhen:Ir(ppy)₃ (2 wt.%), or a uniform mixture of [TCTA:BPhen]:Ir(ppy)₃ ([50:50]:2 wt.%). An optical pulse from an N₂ laser ($\lambda=337$ nm, 1 ns pulse width, 10 Hz rate) was used to generate a population of singlet excitons on the guest which rapidly intersystem cross to the triplet state. It is likely that under optical excitation that excitons are formed on the hosts, with host-guest energy transfer occurring rapidly and efficiently.¹¹

Hole-only single carrier devices were fabricated on pre-cleaned glass substrates with ITO as a bottom contact and Au as a top contact. Films for transient photoluminescence (PL) measurements were deposited on pre-cleaned glass substrates with each host:guest combination of interest. Transient PL experiments were conducted using a pulsed nitrogen laser (Optical Building Blocks) with an excitation wavelength of $\lambda=337$ nm and a pulse length of approximately 0.5 ns. The transient PL signal was

collected with a set of lenses and focused down on to a fast photodiode (Thorlabs PDA10A). The photodiode signal was recorded using a 1GHz bandwidth oscilloscope (Tektronix TDS5104b). The laser pulse energy was measured with a powermeter (Coherent EnergyMax 10MB-HE). Electroluminescent transient experiments were conducted using a pulse generator (HP 8114a) and the collection setup described above. For the steady-state photoluminescence quenching experiments, an LED laser with a pump wavelength $\lambda=405$ nm (B&W Tek 405-40E) was used to excite the samples, while a large-area silicon photodiode was used to detect the emission (Hamamatsu S3584-08).

7.3 Characterizing Triplet-Triplet Annihilation

Assuming a high photoluminescence efficiency for emission,²¹ the luminescent output, L , is linearly proportional to the exciton density ($L[t] \sim n_{ex}[t]/\tau$), Eqn. 1 may be solved to describe the transient decay of triplet excitons

$$L[t] = \frac{L[0]}{\left(1 + \frac{\tau}{2} n_{ex}[0] \kappa_{TT} e^{\frac{t}{\tau}}\right) - \frac{\tau}{2} n_{ex}[0] \kappa_{TT}}, \quad (7.4)$$

where $n_{ex}[0]$ is the initial population of excitons, calculated from measurements of the initial laser intensity and the optical absorption coefficients of each sample. The normalized transient photoluminescence (PL) decay of each material system and the fits to Eqn. 7.4 are shown in Figure 7.1a-c for multiple initial exciton densities. In all material systems, an initial fast decay is observed which increases with increasing excitation density. This feature is attributed to strong exciton-exciton quenching at high exciton densities. As the exciton population falls at longer times, due to both radiative

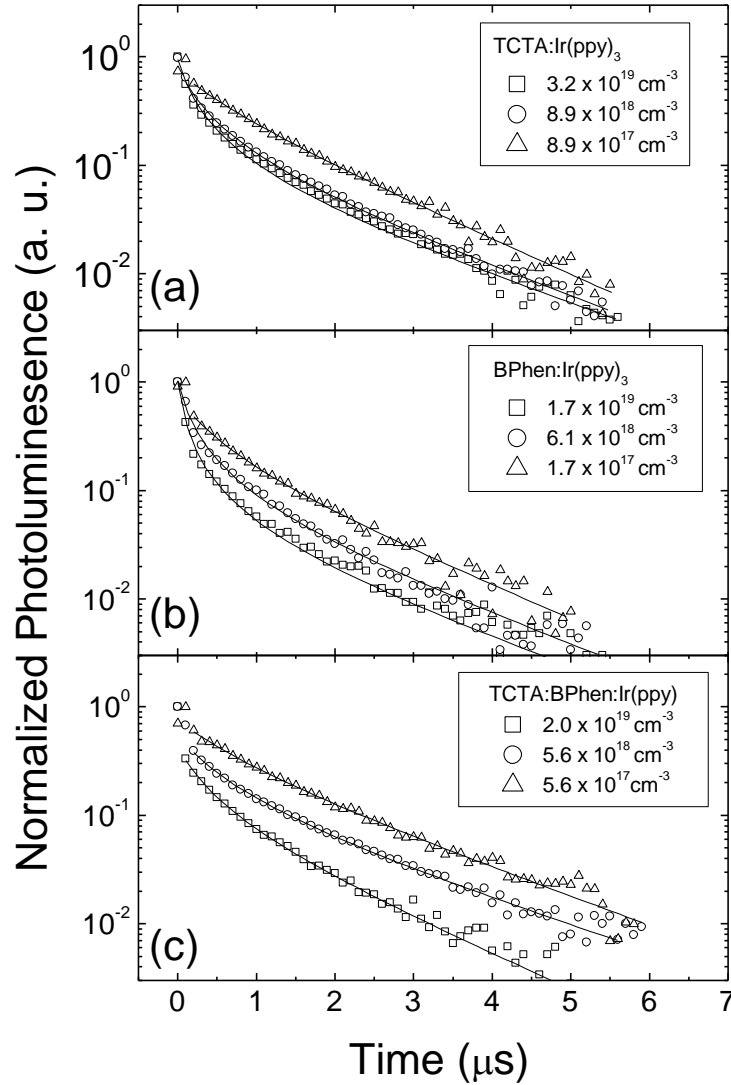


Figure 7.1: Transient photoluminescence decays for (a) TCTA:Ir(ppy)₃, (b) BPhen:Ir(ppy)₃ and (c) TCTA:BPhen:Ir(ppy)₃ thin films at different initial exciton densities. Fits to Eqn. 7.4 for each measurement are shown as solid lines.

decay and quenching events, exciton-exciton interactions decrease and the decay is dominated by the natural exciton lifetime. The κ_{TT} and τ extracted for each system do not vary within experimental error, and have average values of $\kappa_{TT} = (1.9 \pm 4.1) \times 10^{-12} \text{ cm}^3 \text{ s}^{-1}$ and $\tau = (1.62 \pm 0.19) \times 10^{-6} \text{ s}$. The average is used hereafter as κ_{TT} reflects the

interaction of the emissive guest with itself; these values are in good agreement with previous data reported for Ir(ppy)₃-based systems.^{11,12,168}

7.4 Characterizing Triplet-Polaron Quenching

To realize an independent measurement of the exciton-polaron interaction, Eqn. 2 is solved in the steady-state:

$$L = \frac{L[0]}{1 + \tau \kappa_{TP} \rho[V]}. \quad (7.5)$$

Here, the polaron density, $\rho[V]$, is described as a function of applied voltage. Theoretically, the charge carrier density (and equivalently, the polaron density) may be predicted from the applied voltage, V (and consequently applied field, assumed to be uniform across the device thickness, d , $F=V/d$), in a device which is in the injection-current limit (ILC).¹¹¹ This model has been previously used to describe single-carrier devices with contacts which inject and extract either electrons-only, or holes-only.¹¹² Under a continuous-wave optical pump and an applied DC voltage, the luminescence of a single-carrier D-EML or G-EML device is given by Eqn. 7.5. With τ measured in the previous measurements, κ_{TP} may be extracted independently, without the need to correct for triplet-triplet annihilation, which is independent of the polaron density. Plots of the steady-state PL decay versus polaron density are shown in Figure 7.2a for D-EML and Figure 7.2b for G-EML, hole-only devices. As the polaron density is increased, a clear decrease in steady-state PL is observed, indicating significant exciton-polaron quenching.

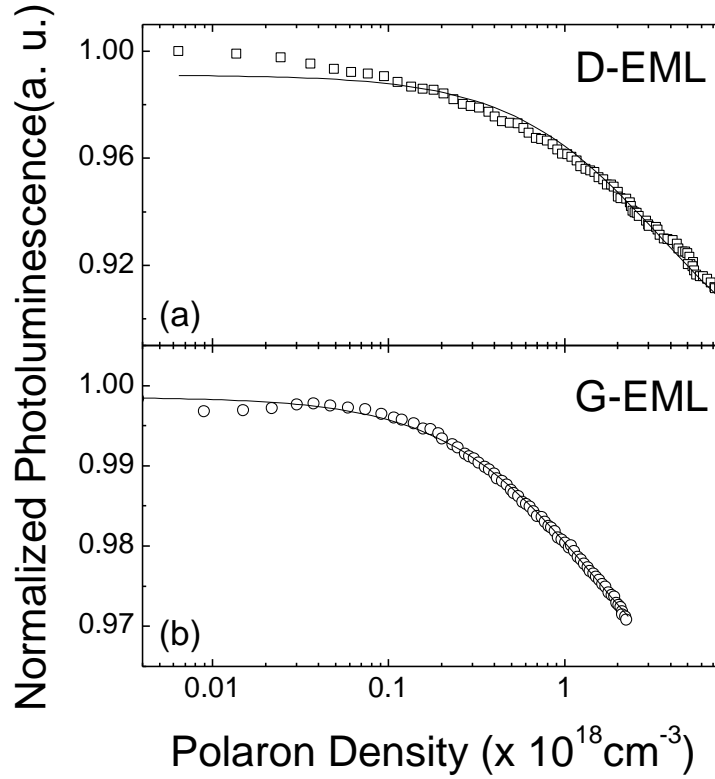


Figure 7.2: Steady-state photoluminescence of hole-only (a) D-EML and (b) G-EML devices at varying polaron densities. Fits to Eqn. 7.5 are shown as solid lines for each device.

Electric field-induced exciton quenching has been previously suggested as a loss pathway, however, such effects are only observed at very high fields ($F > 2.5$ MV/cm), greater than those used in the present study ($F < 2.0$ MV/cm). Interestingly, the values of κ_{TP} extracted for D-EML and G-EML devices are similar, $\kappa_{TP} = (6.3 \pm 4.7) \times 10^{-13} \text{ cm}^3 \text{ s}^{-1}$ and $\kappa_{TP} = (2.8 \pm 1.6) \times 10^{-13}$, respectively. These values are in good agreement with those previously reported by Reineke et al.¹² for TCTA:Ir(ppy)₃ devices. In that work, the single-carrier devices were designed to be in the space-charge limited current (SCLC) regime and the polaron density was related to the current density in a trap-filling SCLC model.

7.5 Predicting Efficiency Roll-Off in OLEDs

7.5.1 η_{EQE} Predictions for D-EML and G-EML Devices

A steady-state solution to Eqn. 7.3 may be found which describes the photon output per electron input, which is equivalent to the normalized external quantum efficiency, η_{EQE} , of a device. That solution, after Reineke et al., is:¹²

$$\frac{\eta_{EQE}}{\eta_0} = \Theta \left(\sqrt{\frac{\Delta^2 + \Gamma \kappa_{TT}}{\kappa_{TT}^2}} - \frac{\Delta}{\kappa_{TT}} \right), \quad (7.6)$$

with

$$\Theta = \frac{e W}{\tau J}, \quad (7.7)$$

$$\Delta = \left(\frac{1}{\tau} + \kappa_{TP} C J^{1/(l+1)} \right), \quad (7.8)$$

and

$$\Gamma = \frac{2J}{eW}, \quad (7.9)$$

where a relationship between the current density and polaron density in a full device is assumed, $\rho = C J^{1/(l+1)}$, and C is a constant which describes the electronic properties of the device.¹² The current density-voltage and brightness-voltage characteristics for the D-EML and G-EML are shown in Figure 7.3a and 7.3c, respectively. The corresponding normalized η_{EQE} for the devices are shown versus current density in Figure 7.3b and 7.3d for D-EML and G-EML devices, respectively; the peak η_{EQE} of the D-EML device is $\eta_{EQE} = 11.3\%$, while the G-MEL device reaches a peak $\eta_{EQE} = 16.3\%$. The best-fits of Eqn. 7.6 to each device are also shown in Figure 7.3b and 7.3d (solid line); the model parameters for each fit are shown in Table 7.1. To compare the roll-off of devices with

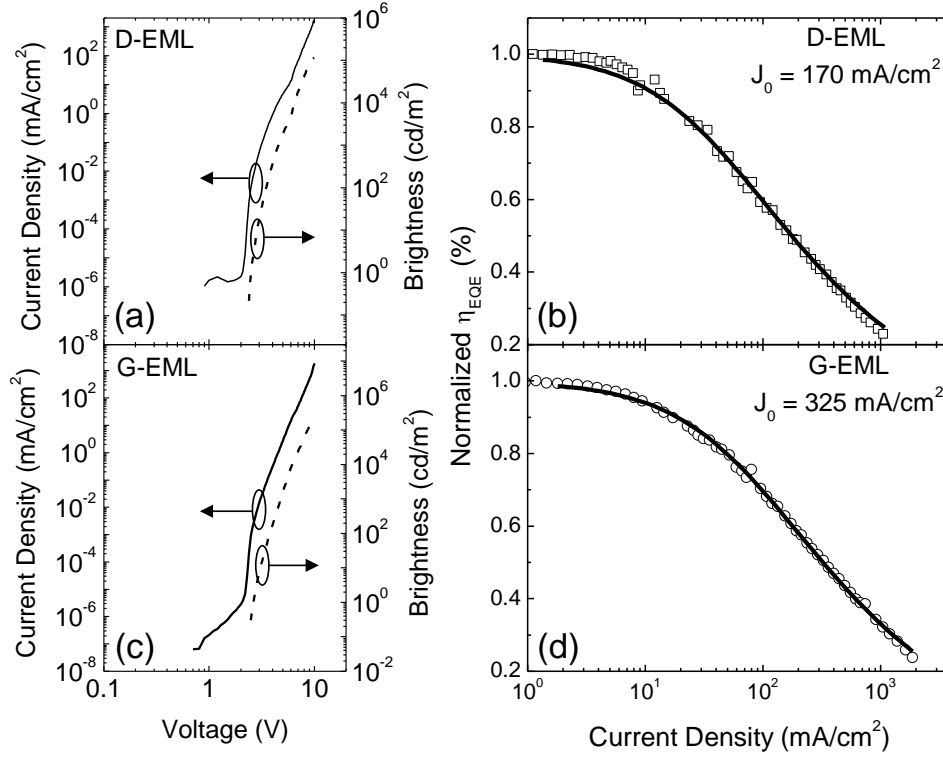


Figure 7.3: (a) Current density-voltage, brightness-voltage and (b) normalized η_{EQE} for the D-EML device. (c) Current density-voltage, brightness-voltage and (d) normalized η_{EQE} for the G-EML device. Fits to Eqn. 6 of the η_{EQE} of each device are shown as solid lines. The J_0 of each device is noted, $J_0 = 170 \text{ mA/cm}^2$ for the D-EML device, $J_0 = 325 \text{ mA/cm}^2$ for the G-EML device.

	$\kappa_{TT}^{3^{-1}}$ (cm s^{-1})	$\kappa_{TP}^{3^{-1}}$ (cm s^{-1})	τ (s)	W (nm)
D-EML (Measured)	1.9×10^{-12}	6.3×10^{-13}	1.62×10^{-6}	15
D-EML (Best Fit)	2.1×10^{-12}	0		
G-EML (Measured)	1.9×10^{-12}	2.8×10^{-13}		80
G-EML (Best Fit)	5.7×10^{-12}	2.8×10^{-13}		

Table 7.1: Measured rate constants for triplet-triplet annihilation (κ_{TT}), triplet-polaron quenching (κ_{TP}), measured exciton lifetime (τ), and measured recombination zone width (W) for D-EML and G-EML OLEDs.

different peak η_{EQE} , the current density at which the efficiency decreases to half of its maximum, termed “ J_0 ,” is noted, $J_0 = 170 \text{ mAcm}^{-2}$ for the D-EML and $J_0 = 325 \text{ mAcm}^{-2}$. As has been observed previously, the G-EML device exhibits significantly less efficiency roll-off than the D-EML device.

For the G-EML device, best-fits of Eqn. 7.6 were achieved by allowing κ_{TT} and κ_{TP} to vary; the resulting values are *within* the experimental error bars, indicating the high degree of accuracy with which the model (and measured values of W , κ_{TT} , κ_{TP} , and τ) replicates the measured η_{EQE} . In the case of the D-EML device, the best-fit κ_{TT} constant is similarly within experimental error, see Table 7.1. However, the best-fit value of κ_{TP} for the D-EML devices is essentially zero, in contrast to the measured value of κ_{TP} from the above experiments. This discrepancy likely arises from the different distributions of excitons and polarons within the test films compared to actual device operation. In the test films, excitons are created throughout the film, according to the optical field distribution and the absorption properties of the materials; however, in the D-EML device, excitons are only present near the HTM:ETM interface. This likely results in a much lower exciton-polaron density overlap in the D-EML device, which in turn reduces the best-fit value of κ_{TP} , which, in the framework of Eqn. (7.2), reflects both the interaction and spatial overlap of excitons and polarons.

To verify this impact, the steady-state PL of hole-only devices with an alternate D-EML structure of: ITO (150 nm) / TCTA (45 nm) / TCTA:Ir(ppy)₃ (5 wt.%, 5 nm) / BPhen:Ir(ppy)₃ (5 wt.% 5 nm) / UGH2 (45 nm) / Au (50 nm), where UGH2 is the wide-

gap molecule: 1,4-bis(triphenylsilyl)benzene.⁶⁶ In this configuration, excitons are only generated on the Ir(ppy)₃ molecules, which is present in a narrow region of the device, such as in the narrow-recombination zone D-EML OLEDs. In that test device, no decrease in steady-state PL was observed with polaron densities up to 10^{19} cm^{-3} (see Figure 7.4), giving $\kappa_{TP} \approx 0$, in agreement with the fits of device η_{EQE} . Clearly, both

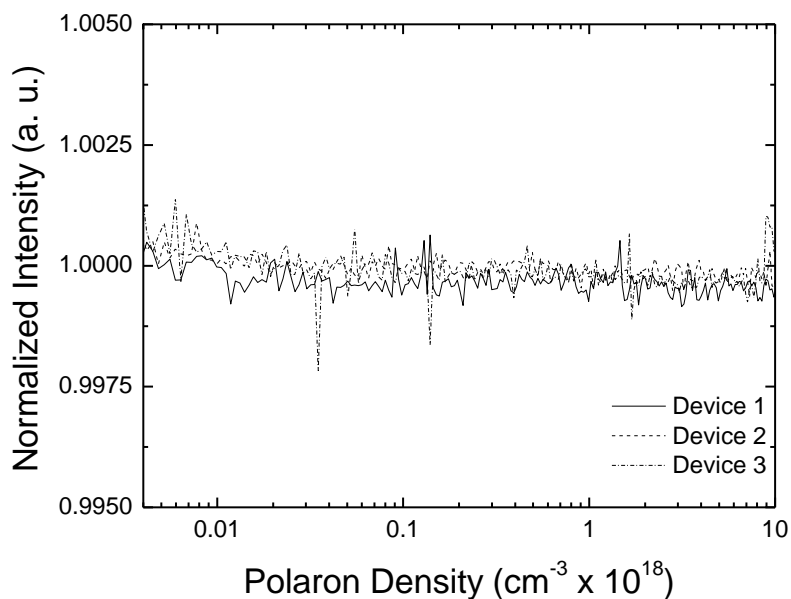


Figure 7.4: Triplet polaron quenching for a D-EML device with a narrow spatial overlap of charges and excitons. Data from three devices show no observable decrease in steady-state luminescence with increasing injected polaron density.

triplet-triplet annihilation and triplet-polaron quenching are processes which affect the roll-off of G-EML devices, while the roll-off of D-EML is dominated by triplet-triplet annihilation. In both cases, the recombination zone width is fixed to experimentally-measured values, and, given the good agreement of the η_{EQE} data and fits to Eqn. 7.6, is a key parameter in determining the efficiency roll-off.

7.5.2 Transient Electroluminescence of D-EML and G-EML Devices

The cumulative effects of triplet-triplet annihilation and triplet-polaron quenching can be seen under device operating conditions in transient electroluminescence (EL). These quenching processes are observed as a reduction in the total exciton lifetime, particularly under high excitation. Transient EL may therefore be used to show the impact of recombination zone width on the quenching processes in an OLED. Voltage pulses with a pulse width of 250 ns and period of 200 μ s were applied to D-EML and G-EML devices with varying peak voltage, V , the resulting transient EL decays are shown in Figure 7.5a for $V = 25$ V. In transient EL, the effects of triplet-triplet annihilation and triplet-polaron quenching can be seen as reduction in the effective exciton lifetime. Previously, transient EL decays have been fit using bi-exponential equations with short and long lifetimes, τ_1 and τ_2 , respectively.¹¹ The short lifetime has been previously associated with host-guest interactions, while the long lifetime has been associated with guest exciton decay.¹¹ The fitted values of τ_1 and τ_2 are shown in Figure 7.5b for a range of voltages for both D-EML and G-EML devices. At low peak voltage pulses, both devices approach a common value of τ_2 which is close agreement with the lifetime value measured in the PL transient experiments. At high peak voltage pulse, the value of τ_2 decreases drastically in the D-EML devices, relative to the G-EML device. The longer-lived EL transients of the G-EML devices, compared to the D-EML devices, indicate the role the wide recombination zone plays in mitigating the exciton density-dependent

quenching effects.

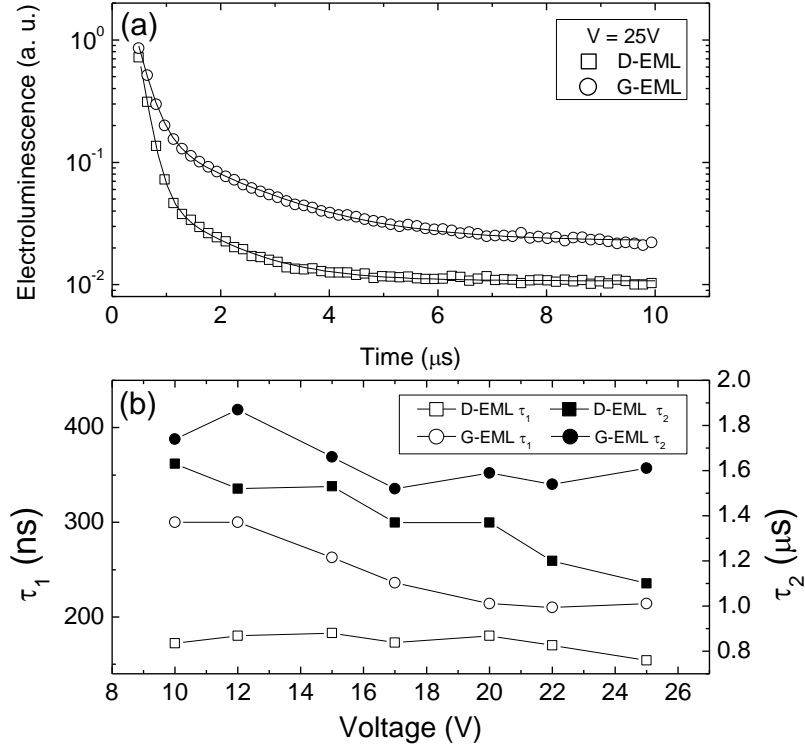


Figure 7.5: (a) Transient electroluminescence decays for D-EML (squares) and G-EML (circles) devices for a voltage pulse of 250ns, with a peak voltage, $V = 25\text{V}$. Bi-exponential fits to the transient decay of each device are shown as solid lines. (b) Transient fit lifetimes, τ_1 (open) and τ_2 (closed) as a function of voltage for D-EML (squares) and G-EML (circles).

7.5.3 η_{EQE} Predictions for Large-Recombination Zone G-EML Devices

Given the good agreement of the fits to Eqn. 7.6 to the efficiency roll-off of the G-EML devices, it is instructive to predict the efficiency roll-off of G-EML devices with a range of recombination zone widths, keeping κ_{TT} , κ_{TP} , and τ fixed to the measured values. Figure 7.6a shows the efficiency roll-off of G-EML devices having recombination zone widths which vary from 2-200 nm, together with the η_{EQE} of the reported G-EML device. To compare the devices, the predicted J_0 of each device is

plotted versus recombination zone width in Figure 7.6b. As seen in Figure 7.6b, there is a sharp increase in J_0 for a moderate increase in W , particularly at low recombination zone widths. For devices with inherently small recombination zones, engineering a small improvement in recombination zone width may have a large impact on the efficiency roll-off. In all devices, engineering the recombination zone width offers a route towards improving the efficiency roll-off in OLEDs.

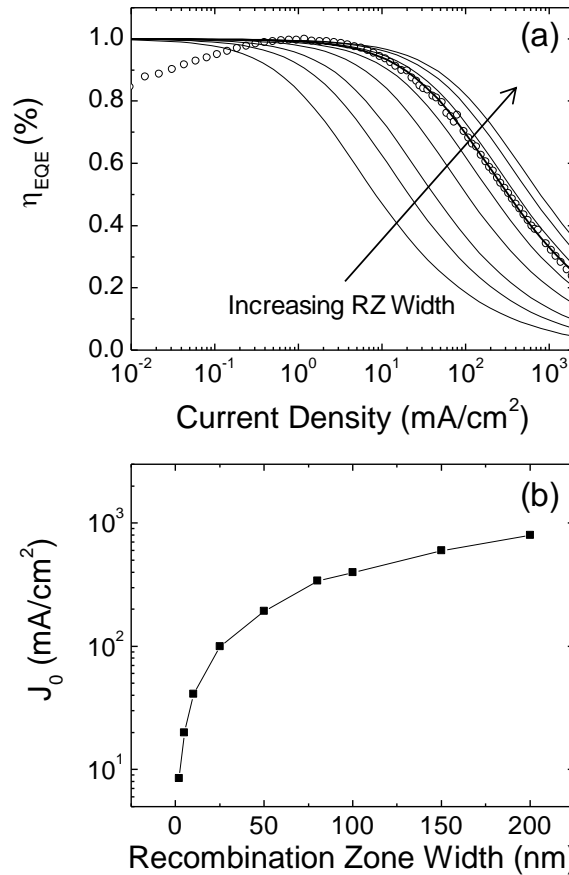


Figure 7.5: (a) Normalized η_{EQE} s for G-EML devices with varying recombination zone widths, as predicted from Eqn. 6. Measured data for the G-EML device used in the present study is shown (circles) together with the best fit to Eqn. 6. (bold line). (b) The J_0 of each predicted device is shown versus recombination zone width.

7.6 Conclusions

In summary, the four main parameters which impact efficiency roll-off in OLEDs (κ_{TT} , κ_{TP} , τ , and W) have been measured independently for D-EML and G-EML devices. A model of the efficiency roll-off which is based on those parameters was used to accurately predict the performance of the OLEDs of interest. In the case of the G-EML device, it was found that the η_{EQE} was well-predicted by measured values of κ_{TT} and κ_{TP} , with the recombination zone fixed according to previous experimental results. In the D-EML device, the η_{EQE} was best-predicted using only κ_{TT} , with $\kappa_{TP} \sim 0$. These results indicate that triplet-triplet annihilation and triplet-polaron quenching are processes which impact the efficiency roll-off of G-EML devices, while the D-EML device efficiency roll-off is dominated by triplet-triplet annihilation. Further, the G-EML device exhibited significantly less efficiency roll-off, due in large part to the wide recombination zone present in that device. Using the model of efficiency roll-off, predictions of the efficiency roll-off of G-EML devices with varying recombination zones were shown to have drastically different degrees of efficiency roll-off, further evidence of the large role the exciton recombination zone plays in efficiency roll-off. In the future, the G-EML device architecture may offer a route towards engineering efficient, single-layer OLEDs which have large recombination zones, thus reducing the efficiency roll-off and extending the range of useful brightness levels in OLED applications.

Chapter 8 Optical Modeling of OLEDs

Previous models in this thesis have been aimed at understanding and predicting the electronic properties of OLEDs. Equally important to consider is the optical design of the OLEDs, i.e. the spatial distribution of the optical electric field within the device. The optical field within a structure impacts the angular distribution and efficiency of far-field light extraction and, in some cases, may alter the lifetime of the exciton.^{169–173} The efficiency with which photons generated in the device escape in the forward viewing direction, or outcoupling efficiency (η_{OC}) has been briefly introduced in Chapter 2. In that chapter a rough estimate of $\eta_{OC} = 20\%$ was made, in accordance with typical values reported in the literature. However, the exact value and wavelength dependence of η_{OC} is more complicated, and may vary greatly depending on the layer structure of the device. A more accurate prediction of η_{OC} requires knowledge of the optical density of states which couple to the far-field at each emitter molecule location.¹⁷⁴ This is done by calculating the optical electric field throughout the multilayer structure of an OLED. A predictive model of the optical field requires knowledge of the complex index of refraction and thickness of each material. These properties are independently measureable; in this work they are measured by spectroscopic ellipsometry.

8.1 Theory of Optical Fields in OLEDs

8.1.1 *Transfer-Matrix Model of Optical Electric Fields*

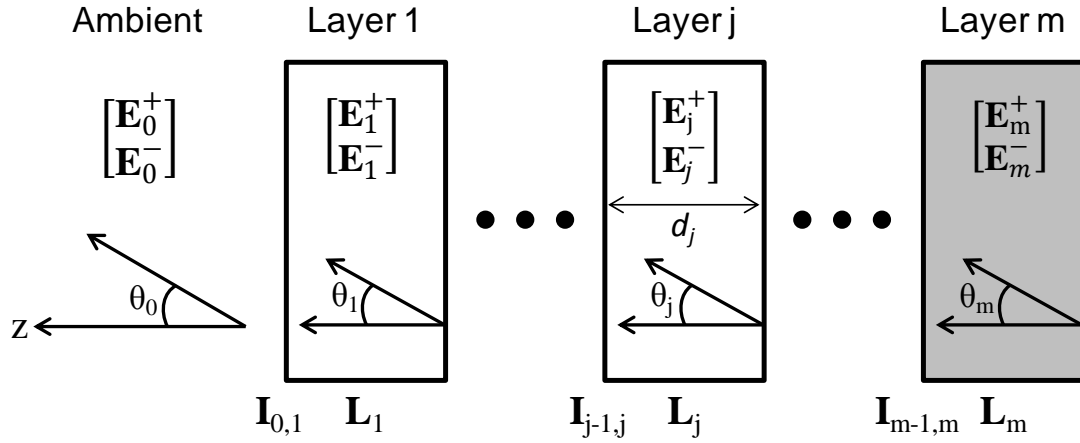


Figure 8.1: General representation of a multilayer optical structure having m layers. Each layer has a thickness of d_j and an angle of refraction, θ_j . The electric field in each layer is represented by two components propagating in positive and negative direction (normal to layer, \mathbf{E}_j^+ and \mathbf{E}_j^- , respectively). The impact on the electric field due to propagation across interfaces is described by the matrix $\mathbf{I}_{j,k}$ and propagation through layers is described by the matrix \mathbf{L}_j .

In this optical model,¹⁷⁰ the OLED is represented by a series of 2×2 matrices which describe the transmission, reflection, and absorption of light at each interface and within each layer. Each layer in the OLED is assumed to be homogeneous and isotropic, with respect to its complex index of refraction, and each interface is assumed to be planar and parallel to the other layers of the device. Light propagation in the structure is assumed to be normal to the plane of the device (designate as the z -axis), with off-axis components specified at angles relative to the normal axis (θ_j), this scheme is depicted in Figure 8.1. The propagation of the optical electric field through layer j is given by:

$$L_j = \begin{bmatrix} e^{-i\xi_j d_j} & 0 \\ 0 & e^{i\xi_j d_j} \end{bmatrix}. \quad (8.1)$$

And the propagation of the electric field across an interface between layers j and k is given by:

$$I_{jk} = \frac{1}{t_{jk}} \begin{bmatrix} 1 & r_{jk} \\ r_{jk} & 1 \end{bmatrix}. \quad (8.2)$$

Where r_{jk} and t_{jk} are the complex Fresnel reflection and transmission coefficients:

$$r_{jk} = \frac{q_j - q_k}{q_j + q_k} \quad (8.3)$$

and

$$t_{jk} = \frac{2 q_j}{q_j + q_k}, \quad (8.4)$$

for s-polarized (TE) light, and:

$$r_{jk} = \frac{-n_k^2 q_j + n_j^2 q_k}{n_k^2 q_j + n_j^2 q_k} \quad (8.5)$$

and

$$t_{jk} = \frac{2 n_j n_k q_j}{n_k^2 q_j + n_j^2 q_k} \quad (8.6)$$

for p-polarized (TM) light. Here, d_j is the layer thickness,

$$\xi = \frac{2\pi q_j}{\lambda}, \quad (8.7)$$

and

$$q_j = n_j \cos[\theta_j], \quad (8.8)$$

where θ_j is the angle of refraction in layer j and n_j is the complex index of refraction ($n_j = \eta_j + i\kappa$, where η_j is the index of refraction and κ is the extinction coefficient). The optical electric field propagating in to (\mathbf{E}_0^+) and out of (\mathbf{E}_0^-) the stack is then described by a total system transfer matrix, \mathbf{S} , and the optical electric fields propagating at the furthest interface (\mathbf{E}_m^+ and \mathbf{E}_m^- , respectively) are:

$$\begin{bmatrix} \mathbf{E}_0^+ \\ \mathbf{E}_0^- \end{bmatrix} = \mathbf{S} \begin{bmatrix} \mathbf{E}_m^+ \\ \mathbf{E}_m^- \end{bmatrix}. \quad (8.9)$$

The complete computer code for the model may be found in Appendix D. As an example, the optical electric field of a typical D-EML device (glass with ITO (150 nm) / TCTA:Ir(ppy)₃ (40 nm) / BPhen:Ir(ppy)₃ (40 nm) / Al (100 nm)) is shown in Figure 8.2a for a single wavelength ($\lambda = 520\text{nm}$) and a contour plot of the field versus wavelength and device thickness is shown in Figure 8.2b.

8.1.2 Dipole Emission within OLEDs

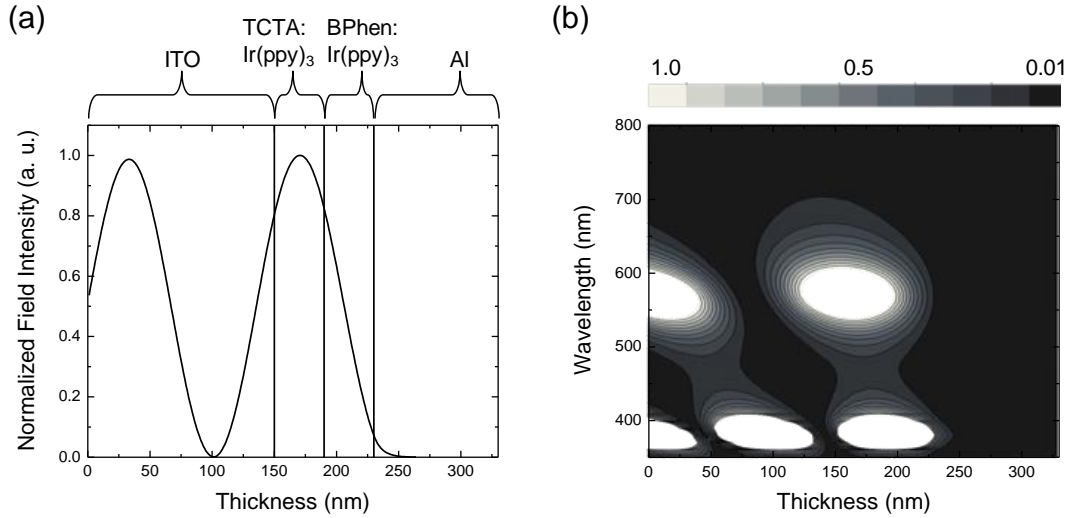


Figure 8.2: (a) Optical electric field of a D-EML device at $\lambda = 520\text{nm}$. The field peaks in the TCTA:Ir(ppy)₃ layer and decays rapidly in the BPhen:Ir(ppy)₃ layer. (b) The full optical electric field for the visible wavelengths at each thickness in the device. Dark colors represent low intensity optical fields. The ITO thickness spans the 0-150 nm, the TCTA:Ir(ppy)₃ spans 150-190 nm, BPhen:Ir(ppy)₃ spans 190-230 nm, and the Al cathode spans the 230-330nm thicknesses.

To simulate the far-field light extraction efficiency of photons generated at various positions within an OLED, emission source terms must be included in the above optical model. Emitting molecules act as local additions to the electric field:^{171,175}

$$\begin{bmatrix} \mathbf{E}_a^+ \\ \mathbf{E}_a^- \end{bmatrix} + \begin{bmatrix} A^+ \\ A^- \end{bmatrix} = \begin{bmatrix} \mathbf{E}_b^+ \\ \mathbf{E}_b^- \end{bmatrix}, \quad (8.10)$$

where \mathbf{E}_a and \mathbf{E}_b are the electric fields (propagating in the positive and negative z-axis direction) on either side of the emitting dipole, represented here as an infinitesimally small plane at the interface between two layers in the OLED stack. Benisty et al.¹⁷¹ has previously described the emission pattern of an organic molecule as randomly oriented vertical and horizontal electric dipoles with normalized power per unit solid angle (P) given by:

$$P_v^p = \frac{3}{8\pi} \sin^2[\theta], \quad (8.11)$$

$$P_h^s = \frac{3}{16\pi}, \quad (8.12)$$

and:

$$P_h^p = \frac{3}{8\pi} \cos^2[\theta], \quad (8.13)$$

where the subscripts v and h refer to the orientation of the dipole (vertical or horizontal) and the super scripts p and s refer to the polarization of the light emission (TM and TE, respectively). The A terms of equation 8.10 are given by $A^{+, -} = \pm\sqrt{P}$ for each dipole and polarization.

8.2 Optical Modeling Results for D-, M-, and G-EML OLEDs

8.2.1 Optical Electric Field Results

To illustrate the power of the optical modeling technique, the optical electric fields of the Ir(ppy)₃-based D-, M-, and G-EML OLEDs are shown in Figures 8.3a-c, respectively. Most important in these figures is the peak height and location of the

optical electric field within the emissive layers. As will be seen below, this peak shape and height directly relate the optical density of states which couple to the far-field, i.e. the outcoupling efficiency at each point within the emissive layers.

8.2.2 Predictions of Outcoupling Efficiency

With the models of Section 8.1 the outcoupling efficiency of the D-EML device shown in Figure 8.3a was simulated. Given the narrow recombination zone measured in Chapter 6, a single dipole emission plane was used at the interface between the TCTA:Ir(ppy)₃ and BPhen:Ir(ppy)₃ layers; an $\eta_{OC} = 18.3\%$ was calculated. This represents the upper limit to η_{EQE} in this device. The use of Ir(ppy)₃ allows $\chi \sim 1.0$ and $\eta_{PL} \approx 100\%$.²¹ Thus, with a peak observed $\eta_{EQE} = 11.7\%$, this gives a charge balance factor of $\gamma = 64\%$. For the M-EML and G-EML systems, the recombination zone is significantly wider, requiring multiple dipole emission plane locations. With the above model, this is achieved by independently calculating the outcoupling efficiency at many points within the emissive layer. This assumes that the inclusion of the dipole emission does not fundamentally alter the optical density of states which couple to the far-field. For the M-EML device, the simulated η_{OC} versus position within the emissive layer is shown in Figure 8.4. The simulated outcoupling efficiency generally follows the shape of the optical electric field in Figure 8.3b.

The simulated η_{OC} of the G-EML device architecture of Figure 8.3c is shown in Figure 8.5. Again, the η_{OC} follows the shape of the optical field, with a maximum ~30 nm from the ITO anode and a minimum at points nearest the LiF/Al cathode. The

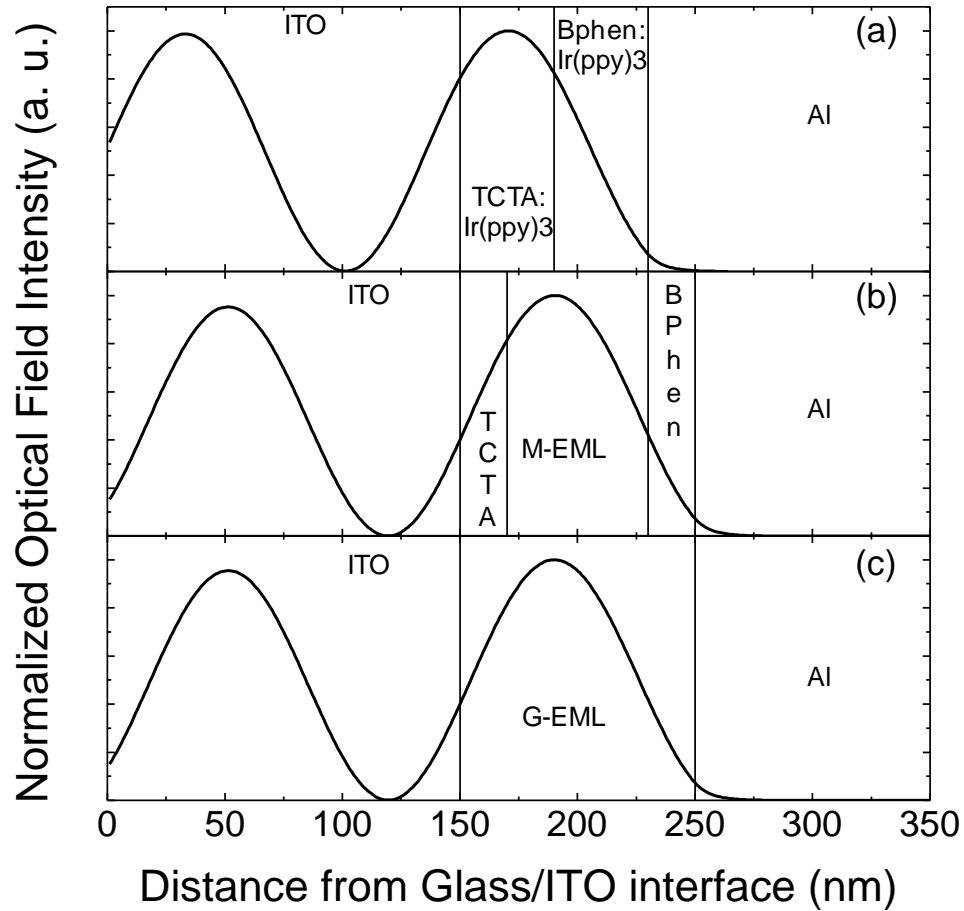


Figure 8.3: (a) optical electric field distributions for the D-EML OLED which has the structure: ITO (150 nm) / TCTA:Ir(ppy)₃ (5 wt. %, 40 nm) / BPhen:Ir(ppy)₃ (5 wt.%, 40 nm) / LiF (1 nm) / Al (100 nm). (b) The optical electric field for M-EML OLEDs with the structure: ITO (150 nm) / TCTA (20 nm) / TCTA:BPhen:Ir(ppy)₃ [50:50] (5 wt.%, 60 nm) / BPhen (20 nm) / LiF (1 nm) / Al (100 nm). (c) The optical electric field for G-EML OLEDs with the structure: ITO (150 nm) / TCTA:BPhen:Ir(ppy)₃ 1:1 gradient (2 wt.%, 100 nm) / LiF (1 nm) / Al (100 nm). All fields are shown for a wavelength $\lambda = 520$ nm.

simulated η_{OC} can be weighted by the known location of excitons within the G-EML device, i.e. the recombination zone data from Chapter 6. The recombination zone-corrected η_{OC} of the entire G-EML structure is 18.9%.

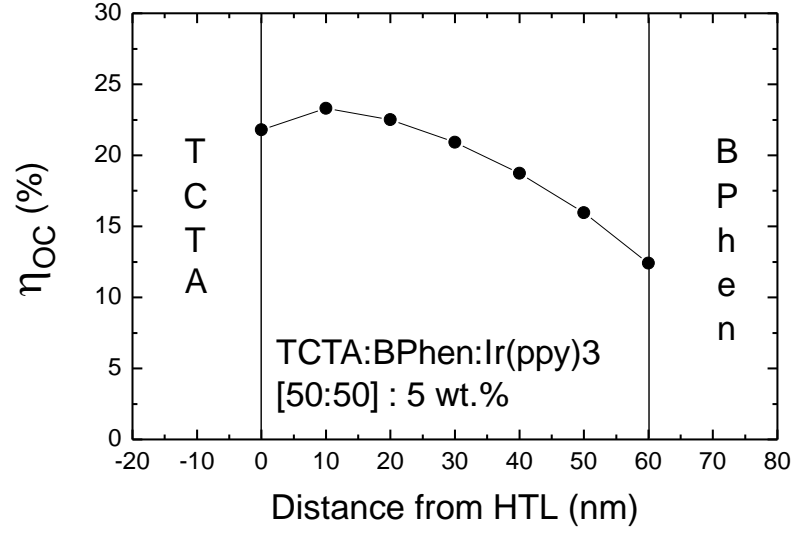


Figure 8.4: Simulated η_{OC} for an M-EML device with the structure: glass / ITO (150 nm) / TCTA (20 nm) / TCTA:BPhen:Ir(ppy)₃ [50:50] : 5 wt.% (60 nm) / BPhen (20nm) / Al (100 nm). The simulated η_{OC} closely follows the optical field simulated in Figure 8.3b.

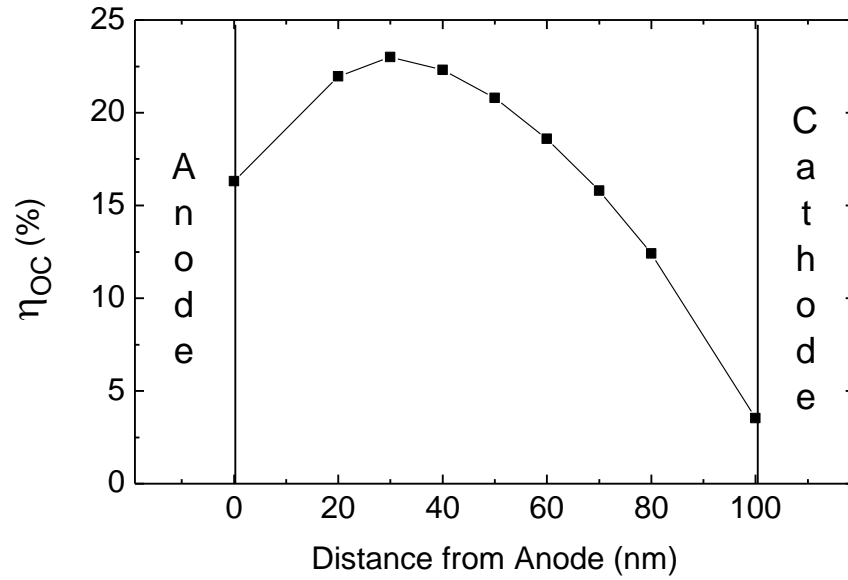


Figure 8.5: Simulated outcoupling efficiency (η_{OC}) for the G-EML device architecture. A peak $\eta_{OC} = 23.0\%$ is predicted at a distance of 30 nm from the anode. An average $\eta_{OC} = 17.2\%$ is predicted.

8.3 Summary

The realization of high-efficiency OLED operation requires the simultaneous optimization of charge-to-exciton conversion, radiative exciton decay, and the outcoupling of generated photons. As the results of Section 8.2 show, the η_{OC} of a device is strongly dependent on device design, as the optical field shape and peak determines the efficiency of far-field light extraction. Often, the optimization of an OLED includes adjusting transport or emissive layer thicknesses, with the intention of reducing drive voltage or improving charge balance in a device. However, even small changes in the position of the emissive layer will impact the outcoupling efficiency and subsequently the observed η_{EQE} . Thus the convolution of changing optical and electronic properties masks the contribution of each in the observed performance. With the model presented in this chapter, the impact of device design on the optical performance of an OLED may be predicted, allowing for a more complete understanding of effects of device design on OLED operation.

Chapter 9 Single-Dopant, Single-Layer White Light-Emitting OLEDs

Many of the properties which make OLEDs attractive for use in displays, i.e. wide and tunable color gamut, high efficiency, compatibility with flexible substrates, etc., are similarly attractive for solid-state white lighting (SSL) applications. There are some important differences, however, when considering the development of OLEDs for SSL. The high production volume applications of lighting, industrial and home lighting, first and foremost require cost and efficiency competitiveness with available technology. Also important is the “quality” of the light source, how well it recreates the color spectrum of a blackbody source, often considered an ideal human light source. OLEDs certainly offer potentially high efficiencies, evidenced by the efficiencies of single-color devices reported in previous chapters. The issue of the quality of a light source must be an ongoing design parameter, while the cost of a light source must be addressed at the manufacturing level. Low-cost manufacturing may be enabled, however, if a device architecture which meets both efficiency and quality metrics, is ‘simple,’ i.e. has low numbers of constituent materials and few processing steps. The following chapter presents work towards simple, efficient, and high quality white-emitting OLEDs.

9.1 Simultaneous Monomer and Excimer Emission

Recently, an interesting class of cyclometalated organic compounds have been demonstrated which show high efficiency emission from both a monomer (i.e. triplet) and excimer state.^{74,176} Excimer emission in these molecules comes from an excited state

wave function which overlaps two of the guest molecules (the term excimer is short for “excited dimer” implying two identical species, rather than an excited complex of two dissimilar species, termed an exciplex).¹⁷⁷ The excimer state emission is generally broad and red-shifted with respect to the monomer. When the molecule is designed to give blue monomer phosphorescence, the simultaneous emission of phosphorescence and red-shifted excimer gives a broadband emission spectrum which may be suitable for white light applications.^{75,178,179} Devices fabricated with these emitters are often referred to as “excimer whites.” Excimer white OLEDs have been previously shown to achieve high efficiency with a variety of molecules in multilayer device architectures. In these devices, the concentration of the emissive guest has been shown to strongly impact the balance of monomer (blue) and excimer (red) emission. At the higher concentrations necessary to achieve balanced white light emission, charge confinement to the guest molecule is difficult, requiring the inclusion of special electron-blocking layers (EBLs) to achieve high performance.¹⁸⁰

9.2 Pt-17 in Single-Layer G-EML Devices

To address the challenges facing organic SSL, a molecule known to emit simultaneously from monomer and excimer states was obtained from the research group of Prof. Jian Li at Arizona State University. This molecule, platinum(II) bis(N-methylimidazolyl)-toluene chloride (Pt-17),¹⁷⁹ has shown some promise in multi-layer OLEDs, achieving peak $\eta_{EQE} = 15.7\%$ and $\eta_P = 27.3$ lm/W with a CRI = 80. To assess the use of Pt-17 in consort with the single-layer G-EML architecture, a series of devices with varying concentrations of Pt-17 were fabricated. These devices used TCTA as an HTM and 3TYMB as an ETM, in a 1:2 gradient profile with constant concentrations of Pt-17 throughout. This device architecture was previously found to be optimal for blue phosphorescent OLEDs.

9.2.1 G-EML Devices with Pt-17

An initial device with 2 wt.% Pt-17 was fabricated to establish a baseline characterization for the molecule and the resulting spectra. The current density-voltage characteristics are shown in Figure 9.1a and the resulting EL spectra are shown in Figure 9.1b, the chemical structure of the molecule is shown in the inset. The current density-voltage characteristics show low leakage currents at low voltage, indicative of the good charge confinement observed in G-EML devices. The brightness of the device reaches a peak output of ~ 1700 cd/m². The CRI of the device reaches a factor of 76, indicating the feasibility of Pt-17 to operate as a single-dopant in a high quality SSL source. The EL of the device shows a decreasing contribution of the excimer emission with increasing

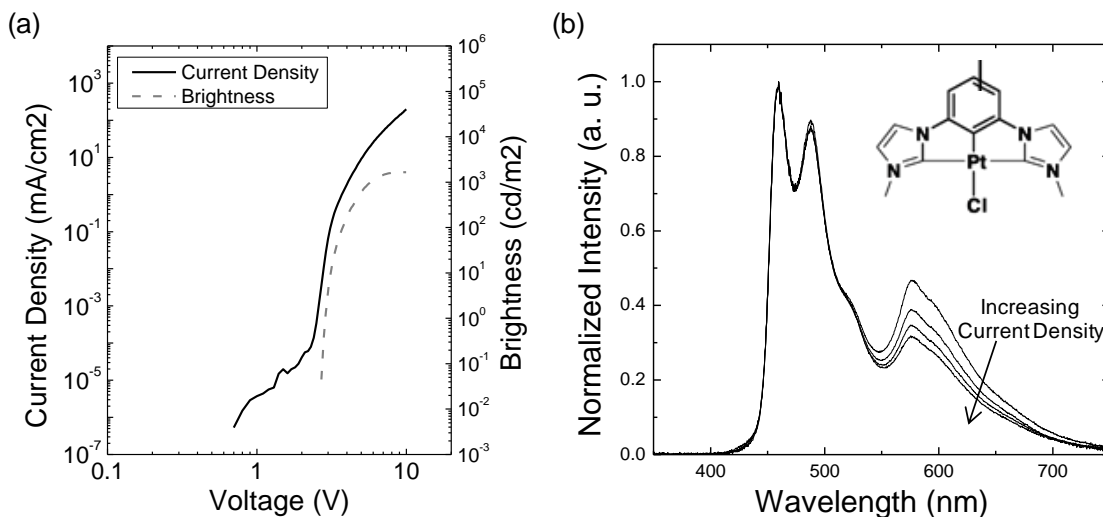


Figure 9.1: (a) Current density-voltage and brightness-voltage characteristics of a 2 wt.% Pt-17 G-EML device, the EL spectra of the device is shown in (b). The spectra shows decreasing contributions from the excimer emission with the current density increasing from 1 to 10 mA/cm².

current density. This may be due to a range of factors, including a shift in the recombination zone as a function of current density or an electric field or charge density effect on the population of the lower-energy excimer state. More work is required to

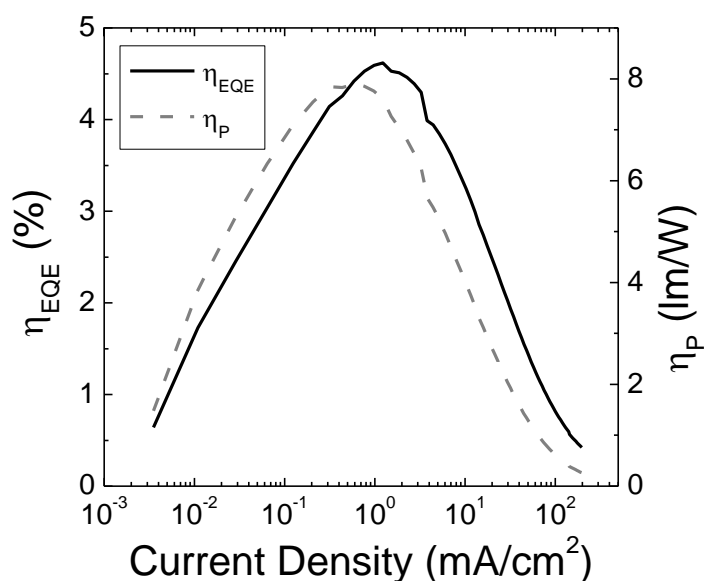


Figure 9.2: η_{EQE} and η_P of the 2 wt.% Pt-17 G-EML OLED as a function of current density.

establish and minimize the cause of the shift, as the change may result in a noticeable change in the color quality of the white light source. The η_{EQE} and η_P of the device is shown in Figure 9.2 as a function of current density. Peak values of $\eta_{EQE} = 4.6\%$ and $\eta_P = 7.9 \text{ lm/W}$ are recorded at brightness levels of ~ 110 and 50 cd/m^2 , respectively.

9.2.2 G-EML Devices with 10 wt. % Pt-17

A second G-EML device was fabricated with 10 wt.% Pt-17 doped throughout. The current density-voltage and brightness-voltage characteristics are shown in Figure 9.3a with the EL spectra shown in Figure 9.3b. Again, the current-density voltage characteristics show low leakage currents. The brightness reaches much higher peak values than in the 2 wt.% case, reaching $13,000 \text{ cd/m}^2$ at 10 V. The EL of the device again shows a decrease in excimer emission with increasing current density, but the overall balance of monomer and excimer emission is more equal. The broadband spectra of the 10 wt.% device achieves a CRI of 82 and CCT of $\sim 4100 \text{ K}$, metrics better than many current multi-layer, multi-dopant OLEDs. The η_{EQE} and η_P of the device is shown in Figure 9.4 as a function of current density with peak values of $\eta_{EQE} = 7.1\%$ and $\eta_P = 15.4 \text{ lm/W}$. These values represent a 54% enhancement in η_{EQE} and a nearly 95% enhancement in η_P .

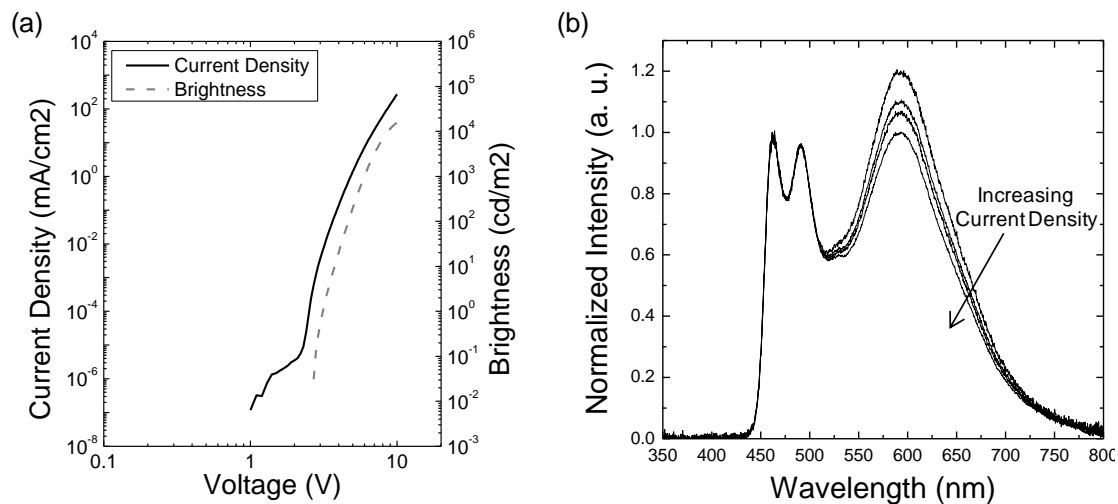


Figure 9.3: (a) Current density-voltage and brightness-voltage characteristics of a 10 wt.% Pt-17 G-EML device, the EL spectra of the device is shown in (b). The spectra shows decreasing contributions from the excimer emission with the current density increasing from 1 to 10 mA/cm².

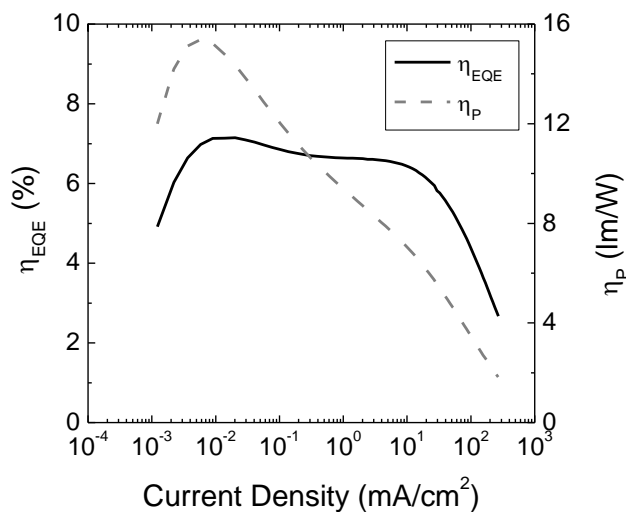


Figure 9.4: η_{EQE} and η_P of the 2 wt.% Pt-17 G-EML OLED as a function of current density.

9.2.3 Summary of Pt-17 Performance in G-EML Devices

Together with the spectral shift in the EL of devices with 2 and 10 wt.% Pt-17, the performance data indicates the large role doping concentration plays in the operation of the excimer white devices. A range of devices with varying doping concentrations were

fabricated, and a summary of the lighting-relevant spectral data is presented in Figure 9.5. Clearly, increased concentrations of Pt-17 push the CCT to lower values, indicating a spectrum with increasing red emission. Higher doping concentrations result in higher

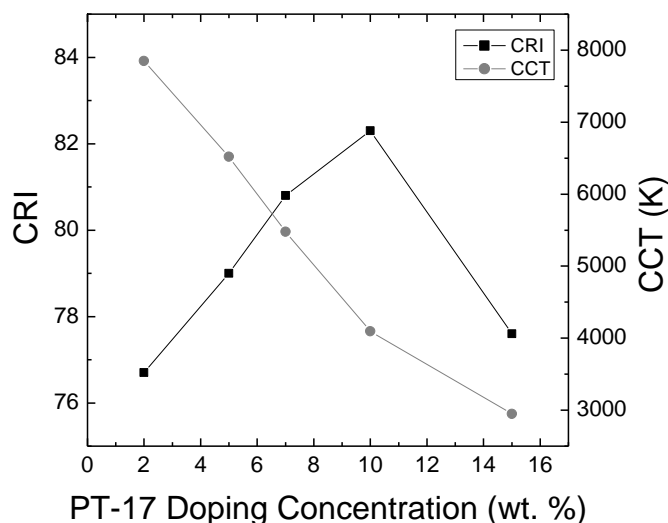


Figure 9.5: Color render index (CRI) and color coordinated temperature (CCT) versus Pt-17 concentration (wt. %) in 1:2 TCTA:3TPYMB G-EML devices.

densities of the Pt-17 molecules and greater probabilities of excimer formation, which results in relatively higher ratios of excimer to monomer emission. As the spectrum of the device trends from monomer (blue) to excimer (red) emission, a greater percentage of the visible spectrum, relative to a blackbody at the same temperature, is represented. This is observed as an increase in the CRI of the devices, with increasing doping concentration, until a critical point is reached where excimer emission dominates the monomer, finally lowering the CRI. This transition occurs around 10 wt.%, but it is unclear how sharply this transition occurs without more concentration data points around 10 wt.%.

The peak η_{EQE} and η_P of the devices is shown in Figure 9.6 versus doping concentration. The η_{EQE} and η_P trend to higher performance with increasing doping concentration, peaking near 10 wt.%, though there is a broad range of doping concentrations which give high performance. Coupled with the ability to tune CRI and CCT of the spectrum, the broad range of doping concentrations which give good performance makes the Pt-17-based G-EML devices attractive for further study

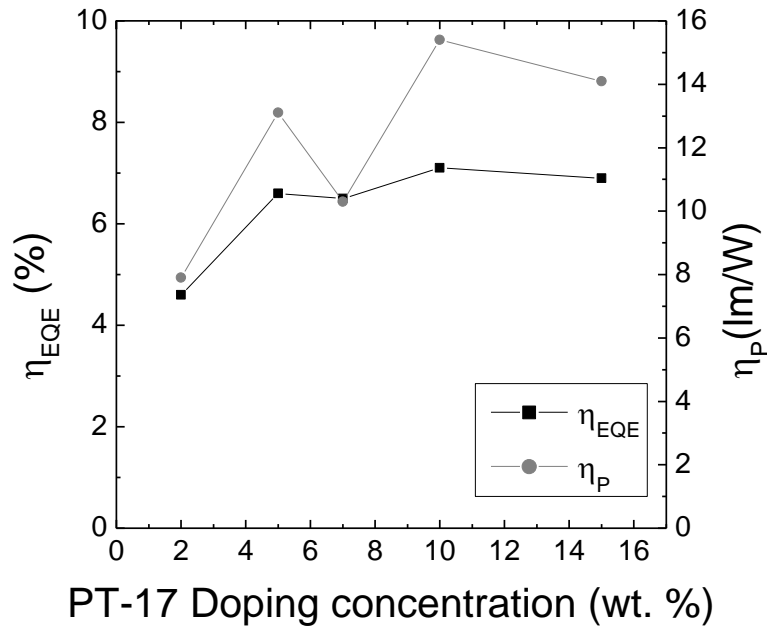


Figure 9.6: Peak η_{EQE} and η_P for varying PT-17 doping concentrations (wt. %). Best performance is observed in the 10 wt.% device, with a corresponding CRI = 82 and CCT = 4000 K.

9.3 Conclusions

The above study has yielded promising results in the pursuit of simply-fabricated, high performing, and quality solid-state light white light sources. The ability to tune the doping concentration of an excimer white dopant to simultaneously maximize the quality and efficiency of a device renders the single-dopant, single-layer devices presented here attractive for use in SSL applications. Given the high η_{EQE} of multi-layer devices with similar molecules,¹⁷⁹ it is conceivable that further optimization of the G-EML devices could yield $\eta_P > 30$ lm/W, a significant milestone in the pursuit of simple white OLEDs. Further optimization of the G-EML structure should focus on the impact of doping concentration on the electrical properties of the G-EML device. At concentrations of 10 wt.% or greater, the dopant may significantly participate in charge transport, by trapping or by conducting charge through dopant energy levels. Further, a greater range of host materials should be explored to maximize the charge density overlap in the device, improving exciton (and excimer) formation, and further increasing the efficiency.

Chapter 10 Future Research Directions

10.1 Summary of This Thesis

This thesis has sought understanding of the device design and materials selection rules which result in particular OLED properties: high peak efficiency, simple fabrication, tunable charge carrier and exciton densities, low efficiency roll-off, color, and others. There are several areas of OLED research which can build from these device and model results. In the following sections, potential research topics are presented which extend concepts from the previous chapters. The goals of these research topics reflect the state of the field; some are related to device engineering for efficiency and operating lifetime, while others seek to drastically shift the current understanding of the interplay between device design, device performance, and materials properties.

While organic light-emitting devices are currently being commercialized in the form of small, mobile displays, other promised applications, such as large-area displays, fully flexible displays, and solid-state white lighting, are not yet commercially viable.^{181,182} There are several areas of OLED research with significant scientific merit which deserve academic investigations. Chapter 9 presented work on simplified white light-emitting devices. As stated in that chapter, the lighting market is particularly sensitive to cost, efficiency, and quality of the light source. Additional work on achieving highly-efficient, quality lighting in a simple device design is one important area of future research. Related to the issue of cost in white lighting applications (and in all OLED applications), is the longevity of device operation. Current devices exhibit

marked efficiency decrease over time, requiring higher voltages to achieve consistent brightness output. The physical process which lead to the decrease in the observed efficiency are not well understood, nor are the degradation mechanisms or chemical reactions well detailed. Chapter 7 showed promising work on reducing the efficiency roll-off of OLEDs, however, there are several possible routes towards improving the roll-off. Finally, the realization of an electrically-pumped organic laser has eluded this field, one intermediate step is presented as a thought experiment.

10.2 Simple, High-Quality White OLEDs

The white light-emitting OLEDs presented in Chapter 9 utilized a single dopant to achieve broad-band emission. This design is attractive for its simplicity, and promising results were shown. However, the range of molecules which have shown simultaneous phosphorescent monomer and excimer emission is narrow, potentially limiting the performance and quality of single-doped white OLEDs. One device design which expands the library of possible dopants while maintaining processing simplicity is the use of a multi-dopant, single-layer gradient.

The results of Chapter 6 clearly indicate the presence of a large exciton recombination zone in G-EML devices. It is possible, then, that doping strips of the G-EML device separately with red-, green-, and blue-emitting molecules would give broadband emission, as the each molecule would ‘sample’ the exciton recombination zone. A schematic of this concept is shown in Figure 10.1 for a 1:2 G-EML device.

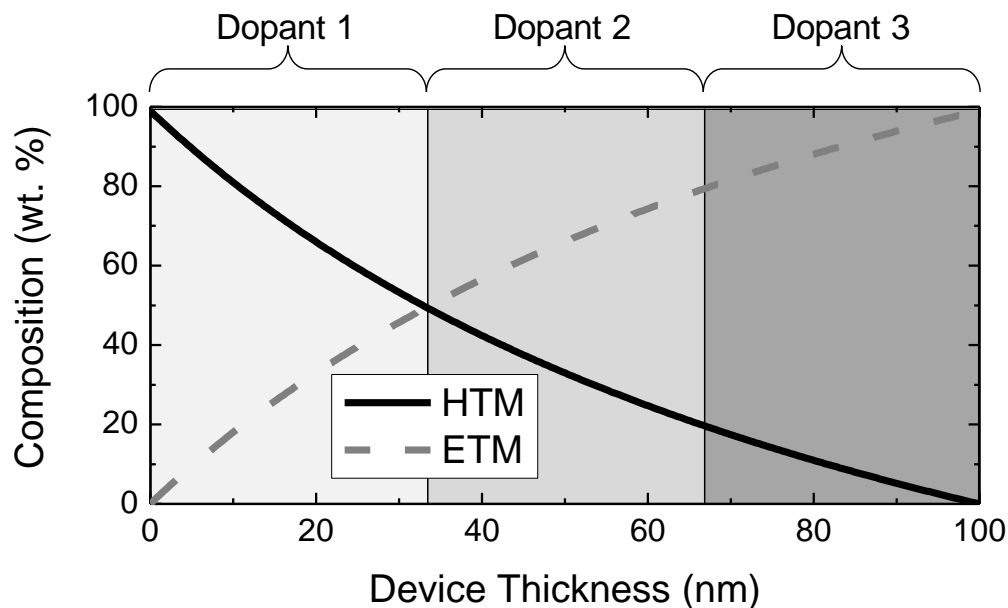


Figure 10.1: Schematic of a multi-dopant, single-layer OLED with a 1:2 HTM:ETM gradient profile. The position of the dopant, doping concentration, thickness of the doped regions, and gradient profile might all be adjusted to give peak white light-emission performance.

There are many ways in which a device like this might be tuned for both high efficiency and high quality. The thickness of each dopant region, doping concentration, and the order of the dopants might be adjusted (red-green-blue (RGB) or blue-green-red (BGR), etc.) to tune color and efficiency. The gradient profile might be adjusted such that the recombination zone, predicted from Chapter 6, has a larger or smaller overlap with a particular doped region. First and foremost, however, the optical field of any structure of interest must be known. As was shown in Chapter 8, the outcoupling efficiency of a G-EML OLED may vary greatly with respect to the position of the emitting molecule within the device, this effect must be considered when analyzing any multi-dopant, single-layer white OLED.

To illustrate the potential use of this device design, several multi-dopant, single-layer devices were fabricated using TCTA as an HTM, TPBi as an ETM, with 1:2 gradient profile, previously shown to be optimal for TCTA:TPBi-based gradients. For emitters, FIrpic, Ir(ppy)₃, and PQIr were chosen for their blue, green, and red emission, respectively. The η_{EQE} and η_P of each device together with its EL spectrum is shown in Figure 10.2a-c for three devices having dopants in the order: GBR, BGR, and RGB, respectively. From each EL spectrum, it is clear that order of the dopant within the device plays a large role in determining the observed spectra, though the exact dependence is not clear. The efficiencies of each device reflect the dominant emitter, i.e. the devices with predominant Ir(ppy)₃ emission show high efficiency, while devices with greater shares of FIrpic and PQIr show lower efficiencies. Some of the differences in efficiency can be ascribed to the lower η_{PL} of PQIr and, according to Chapter 3, 3TPYMB might be a more suitable host for future devices which contain FIrpic. Not considered here, however, is the role that outcoupling in the device might play. Chapter 8 clearly demonstrates the rather large dependence outcoupling has on position within a G-EML device. This dependence (together with the wavelength dependence of outcoupling) must be taken into account in order to understand the EL spectra observed for each device. In the future, outcoupling effects in multi-dopant, single-layer devices should be fully predicted and analyzed prior to experimental device fabrication and

characterization.

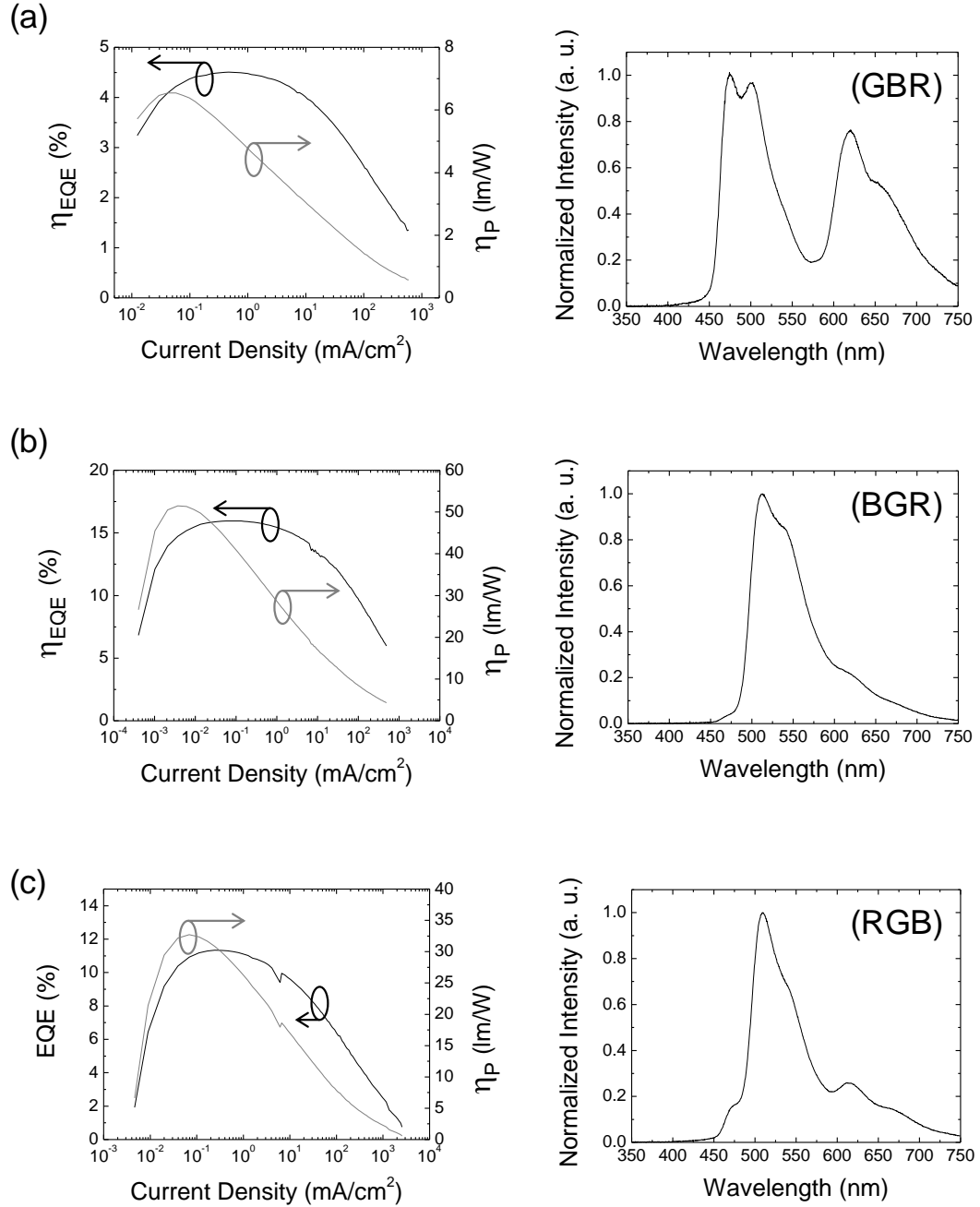


Figure 10.2: η_{EQE} , η_P and EL spectrum for a set of multi-dopant, single-layer OLEDs with dopant orders of: (a) green-blue-red, (b) blue-green-red, and (c) red-green-blue.

Another method which may be used to achieve broadband emission relies on the use of the solid state solvation effect (SSSE).^{183,184} This effect describes the impact that a polar host has on the emission characteristics of the dipole-like exciton. If a molecular has a larger dipole moment in its excited state than in its ground state, the presence of a polar host may stabilize the exciton, resulting in a higher binding energy and red-shifting the emission. If the ground state has a larger dipole moment than the exciton, a polar host will lead to blue-shift in the emission. This effect has been used previously to shift the color of a polar dopant, where the concentration of a uniformly-mixed dopant changed the polarity of the film, leading to a shift in emission.¹⁸⁴ Unfortunately, and as is typical for emissive organic molecules, the η_{PL} of the material depends greatly on doping concentration, and the higher concentrations, while showing a large shift in peak emission wavelength (up to 50 nm), have shown lower emission efficiencies. With the fine control of local concentration demonstrated by the G-EML devices, introduced in Chapter 3, the local polarity of a device may be tuned, either through adjusting the concentration of a polar dopant, or through the gradient in composition of a polar host. Ideally, a device with a gradient in host (or dopant) polarity would show broadband emission, as the large recombination zone present in G-EML allows excitons to sample a large range of host polarities.

To demonstrate the potential of the SSSE to shift the emission color of a polar, a fluorescent OLED molecule, 2,3,6,7-tetrahydro-1,1,7,7-tetramethyl-1H,5H,11H-10-(2-benzothiazolyl)quinolizino[9,9a,1gh]coumarin (C545T), was mixed in varying

concentrations in to solution with chloroform. The PL spectra, the peak, and the wavelengths at half-maximum intensity are shown in Figure 10.3a and b, respectively, for the solutions. The molecular structure of C545T is shown in the inset of Figure 10.3a.

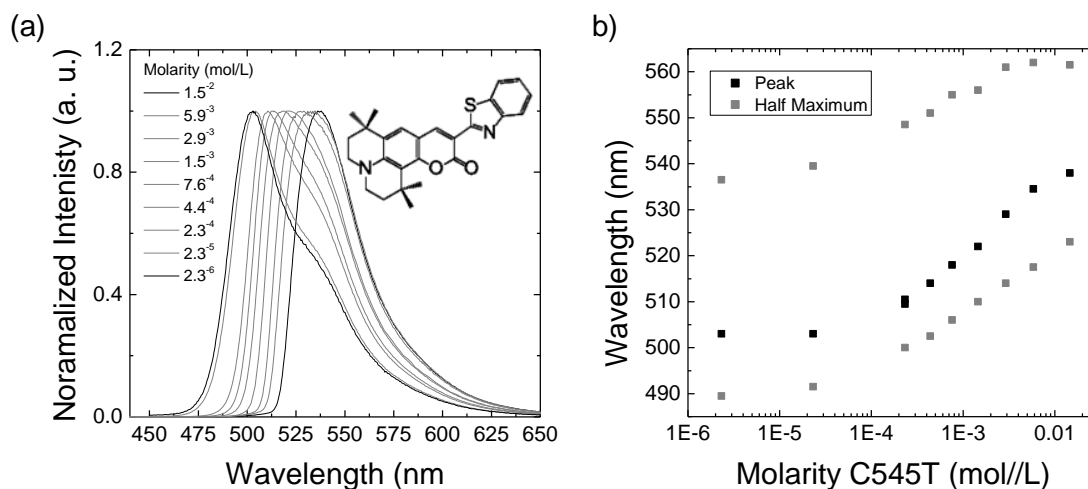


Figure 10.3: (a) Normalized photoluminescence spectra for varying concentrations of the polar emitter C545T, shown in the inset. (b) Peak wavelength and the wavelengths at one-half of the maximum intensity as a function of concentration.

As expected, the C545T solutions show a shift to longer wavelength with increasing concentration, indicating the stabilization of the exciton with increasing polarity of the solution. With a strong demonstration of the SSSE of C545T in solution, thin films of varying concentrations of C545T in a TCTA host were fabricated to characterize the change in emission possible. The PL spectra and the peak, and half-maximum wavelengths, of the thin film system are shown in Figure 10.4a and b, respectively. Interestingly, C545T shows an even greater shift in wavelength in thin film, achieving a peak shift of nearly 70 nm and the full-width, half-maximum (FWHM) of the spectra doubles, from ~55 nm to ~110 nm. The range of wavelengths covered by this range of

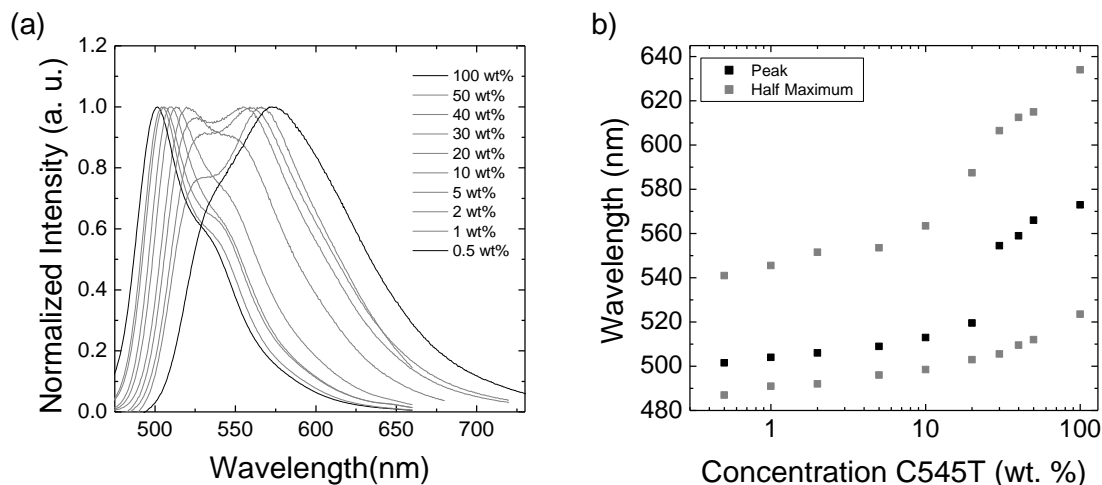


Figure 10.4: (a) Normalized photoluminescence spectra for varying concentrations of the polar emitter C545T in TCTA in thin films. (b) Peak wavelength and the wavelengths at one-half of the maximum intensity as a function of concentration. A peak wavelength shift of ~ 70 nm is observed.

C545T concentrations in thin film represents a large part of the green to red portion of the visible spectrum. Pairing this range of wavelengths of emission with a blue-emitting material could result in a very broadband, and thus high-quality, white light emission. More studies are needed to establish the range of concentrations which give good device performance as well as good color. Additionally, it would be ideal if a polar transport host was discovered and used. This would eliminate the need to adjust the concentration of the emitter, leading to more stable device operation, and likely better performance (through a high and unchanging η_{PL}). The solution and thin film photoluminescence data in this section were collected by Luke Balhorn, UMN, under the direction of the author and Russell J. Holmes.

10.3 Understanding device operating lifetimes

It is well known that many of the organic materials used in OLEDs are sensitive to water and oxygen exposure.^{98,185} Devices which are left in ambient atmosphere degrade quickly, often on the order of hours. Even under hermetic encapsulation, however, devices show a pronounced decrease in luminescence at constant applied current densities, concomitant with a decrease in the efficiency of the device.¹⁸⁶ Though there has been much focus on developing better encapsulation technologies, less work has been devoted to understanding the origin of the efficiency decrease. Considering the conceptual equation for η_{EQE} presented in Chapter 2 (Eqn. 2.3), $\eta_{EQE} = \chi \times \gamma \times \eta_{OC} \times \eta_{PL}$, we may surmise that the decrease is *not* due to a change in the outcoupling efficiency, η_{OC} , nor a change in the spin fraction, χ , as these would require extraordinary changes in molecular properties. Decreases in the η_{EQE} must then come from a loss of charge balance or a loss of the effective η_{PL} . Here “effective η_{PL} ” is used to describe the efficiency with which excitons are converted in to photons *within* a device, rather than as an individual material property. It is under this factor that exciton quenching events, such as energy transfer to a degradation product, can be accounted for.

10.3.1 Characterizing Degradation-Induced Exciton Quenching

The basic tools and theory for studying exciton quenching have been established previously and are described in Chapter 7, and it stands to reason that additional quenching routes may be described in a similar framework. Under optical excitation, the exciton population was previously described as:

$$\frac{dn_{ex}}{dt} = -\frac{n_{ex}}{\tau} - \frac{1}{2}k_{TT}n_{ex}^2. \quad (10.1)$$

We may modify that equation to include a term which describes exciton quenching by a nearby degradation product:

$$\frac{dn_{ex}}{dt} = -\frac{n_{ex}}{\tau} - \frac{1}{2}k_{TT}n_{ex}^2 - k_d n_{ex}m, \quad (10.2)$$

where k_d is the rate of exciton quenching by a density of degradation products, m . In this way, the impact (or existence) of exciton quenching by degradation products may be illuminated. Overall, the existence of a quenching mechanism such as this will serve to reduce the observed PL lifetime. If this is not observed in a degraded device which still shows a reduced efficiency, another factor may be considered. If the emissive dopant molecules degrade and leave behind inert products, a reduction in steady-state photoluminescence may be observed which does not affect the exciton lifetime. This effect, in normal device operating conditions, should appear as a decrease in the EL intensity associated with the dopant and an increase in host emission, if exciton formation has not been changed (i.e. charge balance is the same).

10.3.2 Characterizing Degradation-Induced Loss of Charge Balance

Changes in charge balance due to host or guest degradation may be more difficult to quantify and observe. This might be done by monitoring the J - V characteristics of single-carrier devices as a function of degradation. If the degradation products affect charge balance (or current transport), a change in the magnitude of J , or functional dependence on V , might be observed. In this case, under particular conditions (such as a space-charge limited current, SCLC), the trap distribution and trap depth due to degradation products might be deduced.

The pairing of the above characterization techniques may give better information about the mechanisms which are responsible for the efficiency drop as OLEDs degrade. This information could be used to design devices which minimize the probability that degradation interferes with device operation.

10.4 Mitigating Efficiency Roll-Off

10.4.1 Extraordinary Recombination Zone Widths

Chapter 7 clearly shows, both experimentally and theoretically, the impact the exciton recombination zone has on efficiency roll-off. The large recombination zone present in those G-EML devices effectively lowers the exciton density and reduces triplet-triplet annihilation. With the tunability of the G-EML devices, the concept of the large recombination zone device should be explored further. For example, a very large G-EML device, with a thickness of >150 nm should be fabricated and tested. Given the accuracy of the fits of η_{EQE} shown in Chapter 7, a fit of the η_{EQE} of a thick G-EML device should yield the recombination zone thickness, holding τ , k_{TT} , and k_{TP} constant. In this way, the maximum recombination zone width, independent of peak efficiency, might be discovered for various G-EML profiles and materials combinations. According to the trend in J_0 presented in Chapter 7, doubling the recombination zone width could yield $J_0 = 1 \text{ A/cm}^2$, a feat not yet demonstrated for phosphorescent OLEDs.

10.4.2 Engineering Exciton Lifetime through Device Design

Of the four parameters which influence efficiency roll-off (W , τ , k_{TT} , and k_{TP}), only W has been addressed in this thesis. So far, k_{TT} , and k_{TP} seem to be inaccessible via

device design, though the spatial dependence of the polaron density and exciton densities may be influenced. The lifetime of the exciton, τ , has been previously described as a material property; while this is true, it may be influenced by engineering the optical properties of the OLED. As has been demonstrated previously, the radiative decay rate (or rate of spontaneous emission) is dependent on the optical environment present, this is known as the Purcell effect.^{128,133,173,187,188} When described in the context of a Fermi's golden rule framework, the rate of a transition (such as radiative decay, or exciton recombination) depends not only on the strength of the transition, but on the density of resonant states between the initial and final states. In conventional OLEDs, such as those simulated in Chapter 8, the simulated optical field represents the photonic density of states. If the density of states could be greatly enhanced, the radiative decay rate must

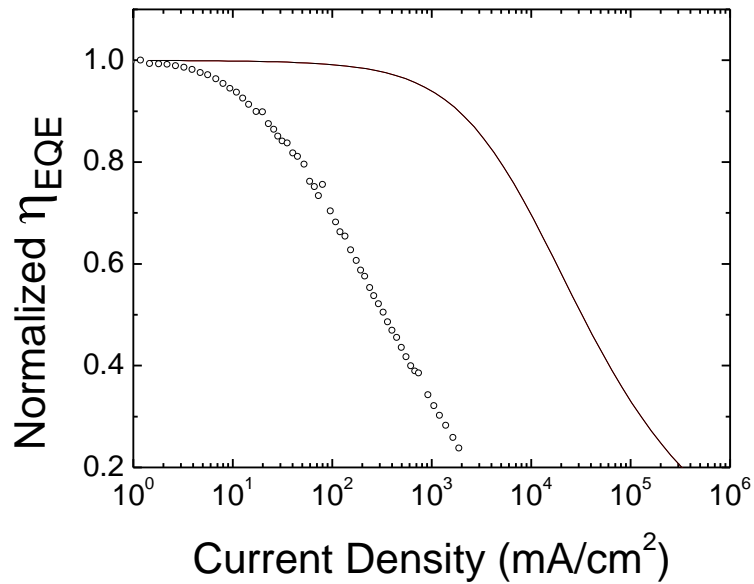


Figure 10.5: Normalized η_{EQE} for a conventional G-EML device (open circles) with a predicted η_{EQE} for a device with $\tau = 1.62 \times 10^{-7}$ s (solid line).

increase, giving a shorter exciton lifetime. To demonstrate the substantial impact exciton lifetime has on efficiency roll-off, a G-EML device is imagined with identical quenching parameters to those presented in Chapter 7, except with $\tau = 1.62 \times 10^{-7}$ s, an enhancement of \sim one order of magnitude. The predicted normalized η_{EQE} of the device is shown in Figure 10.5 with a conventional device, for comparison. While the efficiency roll-off retains the shape of a conventional device, the current densities at which the roll-off occurs are drastically larger. A $J_0 = 32,000$ mA/cm² is predicted, a nearly 100x improvement relative to the conventional G-EML device. Efficiency characteristics such as those predicted here reach the $\eta_{EQE} \times J$ product which has been previously predicted as a threshold for electrically pumped lasing ($\eta_{EQE} \times J = 5$ A/cm²), which has eluded the field thus far.

Chapter 11 Bibliography

- ¹ M. Pope and C.E. Swenberg, *Electronic Processes in Organic Crystals* (Oxford University Press, 1982).
- ² H. Ishii, K. Sugiyama, E. Ito, and K. Seki, *Adv. Mater.* **11**, 605 (1999).
- ³ P.I. Djurovich, E.I. Mayo, S.R. Forrest, and M.E. Thompson, *Org. Electron.* **10**, 515 (2009).
- ⁴ S.M. Tadayyon, H.M. Grandin, K. Griffiths, L.L. Coatsworth, P.R. Norton, H. Aziz, and Z.D. Popovic, *Org. Electron.* **5**, 199 (2004).
- ⁵ S.R. Forrest, *Nature* **428**, 911 (2004).
- ⁶ M. Hack, A. Chwang, Y.-J. Tung, R. Hewitt, J. Brown, J. Lu, C. Shih, J. Ho, R.A. Street, L. Moro, X. Chu, T. Krajewski, N. Rutherford, and R. Visser, *Mater Res Soc Symp Proc* **870E**, H3.1.1 (2005).
- ⁷ S. Choi, J. Jortner, S.A. Rice, and R. Silbey, *J. Chem. Phys.* **41**, 3294 (1964).
- ⁸ M. Pope, J. Burgos, and J. Giachino, *J. Chem. Phys.* **43**, 3367 (1965).
- ⁹ C. Kittel, *Introduction to Solid State Physics* (Wiley, 2004).
- ¹⁰ M.A. Baldo, D.F. O'Brien, Y. You, A. Shoustikov, S. Sibley, M.E. Thompson, and S.R. Forrest, *Nature* **395**, 151 (1998).
- ¹¹ M.A. Baldo, C. Adachi, and S.R. Forrest, *Phys. Rev. B* **62**, 10967 (2000).
- ¹² S. Reineke, K. Walzer, and K. Leo, *Phys. Rev. B* **75**, 125328 (2007).
- ¹³ R.J. Holmes, S.R. Forrest, Y.-J. Tung, R.C. Kwong, J.J. Brown, S. Garon, and M.E. Thompson, *Appl. Phys. Lett.* **82**, 2422 (2003).
- ¹⁴ R.J. Holmes, S.R. Forrest, T. Sajoto, A. Tamayo, P.I. Djurovich, and M.E. Thompson, *Org. Electron. Phys. Mater. Appl.* **7**, 163 (2006).
- ¹⁵ N.J. Turro, *Modern Molecular Photochemistry* (University Science Books, 1991).
- ¹⁶ M.A. Baldo, D.F. O'Brien, M.E. Thompson, and S.R. Forrest, *Phys Rev B* **60**, 14422 (1999).
- ¹⁷ M. Segal, M.A. Baldo, R.J. Holmes, S.R. Forrest, and Z.G. Soos, *Phys. Rev. B* **68**, 075211 (2003).
- ¹⁸ F.L. Pilar, *J. Chem. Educ.* **61**, A248 (1984).
- ¹⁹ M. Kasha, *Discuss Faraday Soc* **9**, 14 (1950).
- ²⁰ S. Lamansky, P. Djurovich, D. Murphy, F. Abdel-Razzaq, H.-E. Lee, C. Adachi, P.E. Burrows, S.R. Forrest, and M.E. Thompson, *J. Am. Chem. Soc.* **123**, 4304 (2001).
- ²¹ Y. Kawamura, K. Goushi, J. Brooks, J.J. Brown, H. Sasabe, and C. Adachi, *Appl. Phys. Lett.* **86**, 071104 (2005).
- ²² C. Adachi, M.A. Baldo, M.E. Thompson, and S.R. Forrest, *J. Appl. Phys.* **90**, 5048 (2001).
- ²³ T. Förster, *Discuss Faraday Soc* **27**, 7 (1959).
- ²⁴ M. Schober, M. Anderson, M. Thomschke, J. Widmer, M. Furno, R. Scholz, B. Lüssem, and K. Leo, *Phys. Rev. B* **84**, 165326 (2011).
- ²⁵ H. Bässler, *Phys. Status Solidi B* **175**, 15 (1993).

- ²⁶ J.D. Wright, *Molecular Crystals* (Cambridge University Press, 1995).
- ²⁷ A.R. Duggal, C. Heller, J.J. Shiang, J. Liu, and L. Lewis, *J Disp. Technol* **3**, 184 (2007).
- ²⁸ M. Shtein, P. Peumans, J.B. Benziger, and S.R. Forrest, *J. Appl. Phys.* **96**, 4500 (2004).
- ²⁹ B.W. D'Andrade and S.R. Forrest, *Adv. Mater.* **16**, 1585 (2004).
- ³⁰ K. Jain, M. Klosner, M. Zemel, and S. Raghunandan, *Proc. IEEE* **93**, 1500 (2005).
- ³¹ A.A. Zakhidov, J.-K. Lee, H.H. Fong, J.A. DeFranco, M. Chatzichristidi, P.G. Taylor, C.K. Ober, and G.G. Malliaras, *Adv. Mater.* **20**, 3481 (2008).
- ³² C.D. Muller, A. Falcou, N. Reckefuss, M. Rojahn, V. Wiederhirn, P. Rudati, H. Frohne, O. Nuyken, H. Becker, and K. Meerholz, *Nature* **421**, 829 (2003).
- ³³ B. Marheineke, in (2005), pp. 596101–596101–13.
- ³⁴ M.A. Baldo, V.G. Kozlov, P.E. Burrows, S.R. Forrest, V.S. Ban, B. Koene, and M.E. Thompson, *Appl. Phys. Lett.* **71**, 3033 (1997).
- ³⁵ S.R. Forrest, *Chem. Rev.* **97**, 1793 (1997).
- ³⁶ G. Sauerbrey, *Z. Für Phys.* **155**, 206 (1959).
- ³⁷ S.J. Martin, V.E. Granstaff, and G.C. Frye, *Anal. Chem.* **63**, 2272 (1991).
- ³⁸ T. Oyamada, C. Maeda, H. Sasabe, and C. Adachi, *Jpn. J. Appl. Phys.* **42**, L1535 (2003).
- ³⁹ L.S. Hung, C.W. Tang, and M.G. Mason, *Appl. Phys. Lett.* **70**, 152 (1997).
- ⁴⁰ S.Y. Park, C.H. Lee, W.J. Song, and C. Seoul, *Curr. Appl. Phys.* **1**, 116 (2001).
- ⁴¹ L.S. Hung, C.W. Tang, M.G. Mason, P. Raychaudhuri, and J. Madathil, *Appl. Phys. Lett.* **78**, 544 (2001).
- ⁴² X.J. Wang, J.M. Zhao, Y.C. Zhou, X.Z. Wang, S.T. Zhang, Y.Q. Zhan, Z. Xu, H.J. Ding, G.Y. Zhong, H.Z. Shi, Z.H. Xiong, Y. Liu, Z.J. Wang, E.G. Obbard, X.M. Ding, W. Huang, and X.Y. Hou, *J. Appl. Phys.* **95**, 3828 (2004).
- ⁴³ P.C. Rusu, G. Giovannetti, C. Weijtens, R. Coehoorn, and G. Brocks, *Phys Rev B* **81**, 125403 (2010).
- ⁴⁴ H. Heil, J. Steiger, S. Karg, M. Gastel, H. Ortner, H. Von Seggern, and M. StoBel, *J. Appl. Phys.* **89**, 420 (2001).
- ⁴⁵ S.R. Forrest, D.D.C. Bradley, and M.E. Thompson, *Adv. Mater.* **15**, 1043 (2003).
- ⁴⁶ A. Endo, M. Ogasawara, A. Takahashi, D. Yokoyama, Y. Kato, and C. Adachi, *Adv. Mater.* **21**, 4802 (2009).
- ⁴⁷ Q. Zhang, J. Li, K. Shizu, S. Huang, S. Hirata, H. Miyazaki, and C. Adachi, *J. Am. Chem. Soc.* **134**, 14706 (2012).
- ⁴⁸ F.B. Dias, K.N. Bourdakos, V. Jankus, K.C. Moss, K.T. Kamtekar, V. Bhalla, J. Santos, M.R. Bryce, and A.P. Monkman, *Adv. Mater.* **25**, 3707 (2013).
- ⁴⁹ W. Helfrich and W.G. Schneider, *Phys. Rev. Lett.* **14**, 229 (1965).
- ⁵⁰ C.W. Tang and S.A. VanSlyke, *Appl. Phys. Lett.* **51**, 913 (1987).
- ⁵¹ C.H. Chen, C.W. Tang, J. Shi, and K.P. Klubeck, *Macromol Symp* **125**, 49 (1997).
- ⁵² C. Adachi, M.E. Thompson, and S.R. Forrest, *Sel. Top. Quantum Electron. IEEE J. Of* **8**, 372 (2002).
- ⁵³ D.F. O'Brien, M.A. Baldo, M.E. Thompson, and S.R. Forrest, *Appl. Phys. Lett.* **74**, 442 (1999).

- ⁵⁴ M.A. Baldo, S. Lamansky, P.E. Burrows, M.E. Thompson, and S.R. Forrest, Appl. Phys. Lett. **75**, 4 (1999).
- ⁵⁵ D. Tanaka, H. Sasabe, Y.-J. Li, S.-J. Su, T. Takeda, and J. Kido, Jpn. J. Appl. Phys. Part 2-Lett. Express Lett. **46**, L10 (2007).
- ⁵⁶ G. He, O. Schneider, D. Qin, X. Zhou, M. Pfeiffer, and K. Leo, J. Appl. Phys. **95**, 5773 (2004).
- ⁵⁷ N. Chopra, J. Lee, Y. Zheng, S.-H. Eom, J. Xue, and F. So, Appl. Phys. Lett. **93**, 143307 (2008).
- ⁵⁸ S. Watanabe, N. Ide, and J. Kido, Jpn. J. Appl. Phys. **46**, 1186 (2007).
- ⁵⁹ B.W. D'Andrade, R.J. Holmes, and S.R. Forrest, Adv. Mater. **16**, 624 (2004).
- ⁶⁰ Y. Sun and S.R. Forrest, Appl. Phys. Lett. **91**, 263503 (2007).
- ⁶¹ S. Reineke, F. Lindner, G. Schwartz, N. Seidler, K. Walzer, B. Lüssem, and K. Leo, Nature **459**, 234 (2009).
- ⁶² Q. Xin, W.L. Li, W.M. Su, T.L. Li, Z.S. Su, B. Chu, and B. Li, J. Appl. Phys. **101**, (2007).
- ⁶³ J. Lee, J.-I. Lee, K.-I. Song, S.J. Lee, and H.Y. Chu, Appl. Phys. Lett. **92**, (2008).
- ⁶⁴ I. Tanaka, Y. Tabata, and S. Tokito, J. Appl. Phys. **99**, (2006).
- ⁶⁵ W.-Y. Hung, Z.-W. Chen, H.-W. You, F.-C. Fan, H.-F. Chen, and K.-T. Wong, Org. Electron. **12**, 575 (2011).
- ⁶⁶ R.J. Holmes, B.W. D'Andrade, S.R. Forrest, X. Ren, J. Li, and M.E. Thompson, Appl. Phys. Lett. **83**, 3818 (2003).
- ⁶⁷ E. Polikarpov, J.S. Swensen, N. Chopra, F. So, and A.B. Padmaperuma, Appl. Phys. Lett. **94**, (2009).
- ⁶⁸ A. Chaskar, H.-F. Chen, and K.-T. Wong, Adv. Mater. **23**, 3876 (2011).
- ⁶⁹ X. Qiao, Y. Tao, Q. Wang, D. Ma, C. Yang, L. Wang, J. Qin, and F. Wang, J. Appl. Phys. **108**, 034508 (2010).
- ⁷⁰ *Solid-State Lighting Research and Development: Multi-Year Program Plan* (U.S. Department of Energy, Office of Energy Efficiency and Renewable Energy, 2013), pp. 1–89.
- ⁷¹ T.-Y. Cho, C.-L. Lin, and C.-C. Wu, Appl. Phys. Lett. **88**, 111106 (2006).
- ⁷² H. Kanno, R.J. Holmes, Y. Sun, S. Kena-Cohen, and S.R. Forrest, Adv. Mater. **18**, 339 (2006).
- ⁷³ F. Yan and X. Wei Sun, Appl. Phys. Lett. **102**, (2013).
- ⁷⁴ B. D'Andrade and S.R. Forrest, Chem. Phys. **286**, 321 (2003).
- ⁷⁵ E.L. Williams, K. Haavisto, J. Li, and G.E. Jabbour, Adv. Mater. **19**, 197 (2007).
- ⁷⁶ N. Chopra, J.S. Swensen, E. Polikarpov, L. Cosimbescu, F. So, and A.B. Padmaperuma, Appl. Phys. Lett. **97**, 033304 (2010).
- ⁷⁷ G. He, M. Pfeiffer, K. Leo, M. Hofmann, J. Birnstock, R. Pudzych, and J. Salbeck, Appl. Phys. Lett. **85**, 3911 (2004).
- ⁷⁸ J. Lee, J.-I. Lee, J.Y. Lee, and H.Y. Chu, Appl. Phys. Lett. **94**, 193305 (2009).
- ⁷⁹ C. Murawski, K. Leo, and M.C. Gather, Adv. Mater. **25**, 6801 (2013).
- ⁸⁰ C. Adachi, M.A. Baldo, S.R. Forrest, and M.E. Thompson, Appl. Phys. Lett. **77**, 904 (2000).

- ⁸¹ X. Zhou, D.S. Qin, M. Pfeiffer, J. Blochwitz-Nimoth, A. Werner, J. Drechsel, B. Maennig, K. Leo, M. Bold, P. Erk, and H. Hartmann, *Appl. Phys. Lett.* **81**, 4070 (2002).
- ⁸² J.-H. Lee, C.-I. Wu, S.-W. Liu, C.-A. Huang, and Y. Chang, *Appl. Phys. Lett.* **86**, 103506 (2005).
- ⁸³ M.E. Kondakova, T.D. Pawlik, R.H. Young, D.J. Giesen, D.Y. Kondakov, C.T. Brown, J.C. Deaton, J.R. Lenhard, and K.P. Klubek, *J. Appl. Phys.* **104**, 094501 (2008).
- ⁸⁴ Y. Zhao, J. Chen, W. Chen, and D. Ma, *J. Appl. Phys.* **111**, (2012).
- ⁸⁵ N. Koch, S. Duhm, J.P. Rabe, A. Vollmer, and R.L. Johnson, *Phys. Rev. Lett.* **95**, 237601 (2005).
- ⁸⁶ X. Zhou, M. Pfeiffer, J. Blochwitz, A. Werner, A. Nollau, T. Fritz, and K. Leo, *Appl. Phys. Lett.* **78**, 410 (2001).
- ⁸⁷ T.-Y. Hwu, T.-C. Tsai, W.-Y. Hung, S.-Y. Chang, Y. Chi, M.-H. Chen, C.-I. Wu, K.-T. Wong, and L.-C. Chia, *Chem Commun* 4956 (2008).
- ⁸⁸ S. Olthof, R. Meerheim, M. Schober, and K. Leo, *Phys. Rev. B* **79**, 245308 (2009).
- ⁸⁹ S. Naka, H. Okada, H. Onnagawa, and T. Tsutsui, *Appl. Phys. Lett.* **76**, 197 (2000).
- ⁹⁰ J.-W. Kang, S.-H. Lee, H.-D. Park, W.-I. Jeong, K.-M. Yoo, Y.-S. Park, and J.-J. Kim, *Appl. Phys. Lett.* **90**, 223508 (2007).
- ⁹¹ Z.W. Liu, M.G. Helander, Z.B. Wang, and Z.H. Lu, *Appl. Phys. Lett.* **94**, 113305 (2009).
- ⁹² S. Reineke, M. Thomschke, B. Lüssem, and K. Leo, *Rev. Mod. Phys.* **85**, 1245 (2013).
- ⁹³ H. Sasabe, J. Takamatsu, T. Motoyama, S. Watanabe, G. Wagenblast, N. Langer, O. Molt, E. Fuchs, C. Lennartz, and J. Kido, *Adv. Mater.* **22**, 5003 (2010).
- ⁹⁴ X. Cai, A.B. Padmaperuma, L.S. Sapochak, P.A. Vecchi, and P.E. Burrows, *Appl. Phys. Lett.* **92**, (2008).
- ⁹⁵ C.W. Tang, S.A. VanSlyke, and C.H. Chen, *J. Appl. Phys.* **65**, 3610 (1989).
- ⁹⁶ J. Huang, M. Pfeiffer, A. Werner, J. Blochwitz, K. Leo, and S. Liu, *Appl. Phys. Lett.* **80**, 139 (2002).
- ⁹⁷ Y.-Y. Chen, B.-Y. Yu, W.-B. Wang, M.-F. Hsu, W.-C. Lin, Y.-C. Lin, J.-H. Jou, and J.-J. Shyue, *Anal. Chem.* **80**, 501 (2007).
- ⁹⁸ S. Ninomiya, K. Ichiki, H. Yamada, Y. Nakata, T. Seki, T. Aoki, and J. Matsuo, *Rapid Commun. Mass Spectrom.* **23**, 3264 (2009).
- ⁹⁹ B.-Y. Yu, Y.-Y. Chen, W.-B. Wang, M.-F. Hsu, S.-P. Tsai, W.-C. Lin, Y.-C. Lin, J.-H. Jou, C.-W. Chu, and J.-J. Shyue, *Anal. Chem.* **80**, 3412 (2008).
- ¹⁰⁰ S.H. Kim, J. Jang, and J.Y. Lee, *Appl. Phys. Lett.* **91**, 083511 (2007).
- ¹⁰¹ S.W. Liu, C.A. Huang, J.H. Lee, K.H. Yang, C.C. Chen, and Y. Chang, *Proc. Symp. H Photonic Process. Surf. Thin Films Devices E-MRS 2003 Spring Conf.* **453–454**, 312 (2004).
- ¹⁰² S.-W. Liu, J.-H. Lee, C.-C. Lee, C.-T. Chen, and J.-K. Wang, *Appl. Phys. Lett.* **91**, 142106 (2007).
- ¹⁰³ N.C. Erickson and R.J. Holmes, *Appl. Phys. Lett.* **97**, 083308 (2010).
- ¹⁰⁴ N.C. Erickson and R.J. Holmes, *J. Appl. Phys.* **110**, 084515 (2011).
- ¹⁰⁵ J. Wang, X. Shi, J. Liu, S. Huang, X. Wu, Z. Ye, J. Lu, Y. Su, and G. He, *SID Symp. Dig. Tech. Pap.* **44**, 1400 (2013).

- ¹⁰⁶ S. Lee and C.W. Tang, *J. Vac. Sci. Technol. B Microelectron. Nanometer Struct.* **29**, 062401 (2011).
- ¹⁰⁷ A.G. Shard, P.J. Brewer, F.M. Green, and I.S. Gilmore, *Surf. Interface Anal.* **39**, 294 (2007).
- ¹⁰⁸ S. Ninomiya, K. Ichiki, H. Yamada, Y. Nakata, T. Seki, T. Aoki, and J. Matsuo, *Rapid Commun. Mass Spectrom.* **23**, 1601 (2009).
- ¹⁰⁹ T. Miyayama, N. Sanada, M. Suzuki, J.S. Hammond, S.-Q.D. Si, and A. Takahara, *J. Vac. Sci. Technol. A* **28**, L1 (2010).
- ¹¹⁰ F.J. Grunthaner, *MRS Bull.* **12**, 60 (1987).
- ¹¹¹ J.C. Scott and G.G. Malliaras, *Chem. Phys. Lett.* **299**, 115 (1999).
- ¹¹² Z.B. Wang, M.G. Helander, M.T. Greiner, J. Qiu, and Z.H. Lu, *J. Appl. Phys.* **107**, (2010).
- ¹¹³ J. Frenkel, *Phys. Rev.* **54**, 647 (1938).
- ¹¹⁴ P.W.M. Blom, M.J.M. de Jong, and M.G. van Munster, *Phys. Rev. B* **55**, R656 (1997).
- ¹¹⁵ W.D. Gill, *J. Appl. Phys.* **43**, 5033 (1972).
- ¹¹⁶ S.V. Rakhmanova and E.M. Conwell, *Appl. Phys. Lett.* **76**, 3822 (2000).
- ¹¹⁷ L. Bozano, S.A. Carter, J.C. Scott, G.G. Malliaras, and P.J. Brock, *Appl. Phys. Lett.* **74**, 1132 (1999).
- ¹¹⁸ X.-W. Zhang, M.A. Khan, X.-Y. Jiang, J. Cao, W.-Q. Zhu, and Z.-L. Zhang, *Phys. B Condens. Matter* **404**, 1247 (2009).
- ¹¹⁹ T.C. Wong, J. Kovac, C.S. Lee, L.S. Hung, and S.T. Lee, *Chem. Phys. Lett.* **334**, 61 (2001).
- ¹²⁰ N.C. Giebink and S.R. Forrest, *Phys. Rev. B* **77**, 235215 (2008).
- ¹²¹ J. Kalinowski, W. Stampor, J. Mężyk, M. Cocchi, D. Virgili, V. Fattori, and P. Di Marco, *Phys. Rev. B* **66**, 235321 (2002).
- ¹²² J. Kalinowski, W. Stampor, J. Szmytkowski, D. Virgili, M. Cocchi, V. Fattori, and C. Sabatini, *Phys. Rev. B* **74**, 085316 (2006).
- ¹²³ B.P. Rand, J. Xue, S. Uchida, and S.R. Forrest, *J. Appl. Phys.* **98**, 124902 (2005).
- ¹²⁴ P.A. Hobson, S. Wedge, J.A.E. Wasey, I. Sage, and W.L. Barnes, *Adv. Mater.* **14**, 1393 (2002).
- ¹²⁵ L.H. Smith, J.A.E. Wasey, and W.L. Barnes, *Appl. Phys. Lett.* **84**, 2986 (2004).
- ¹²⁶ J. Meyer, S. Hamwi, T. Bulow, H.-H. Johannes, T. Riedl, and W. Kowalsky, *Appl. Phys. Lett.* **91**, 113506 (2007).
- ¹²⁷ W.S. Jeon, T.J. Park, K.H. Kim, R. Pode, J. Jang, and J.H. Kwon, *Org. Electron.* **11**, 179 (2010).
- ¹²⁸ M. Furno, R. Meerheim, S. Hofmann, B. Lüssem, and K. Leo, *Phys. Rev. B* **85**, 115205 (2012).
- ¹²⁹ I.-S. Park, S.-R. Park, D.-Y. Shin, J.-S. Oh, W.-J. Song, and J.-H. Yoon, *Org. Electron.* **11**, 218 (2010).
- ¹³⁰ V. Bulović, V.B. Khalfin, G. Gu, P.E. Burrows, D.Z. Garbuzov, and S.R. Forrest, *Phys. Rev. B* **58**, 3730 (1998).

- ¹³¹ E.F. Schubert, N.E.J. Hunt, M. Micovic, R.J. Malik, D.L. Sivco, A.Y. Cho, and G.J. Zydzik, *Science* **265**, pp. 943 (1994).
- ¹³² Q. Huang, S. Reineke, K. Walzer, M. Pfeiffer, and K. Leo, *Appl. Phys. Lett.* **89**, 263512 (2006).
- ¹³³ S. Mladenovski, S. Reineke, and K. Neyts, *Opt. Lett.* **34**, 1375 (2009).
- ¹³⁴ D. Song, S. Zhao, and H. Aziz, *Adv. Funct. Mater.* **21**, 2311 (2011).
- ¹³⁵ S. Reineke, G. Schwartz, K. Walzer, and K. Leo, *Phys. Status Solidi RRL Rapid Res. Lett.* **3**, 67 (2009).
- ¹³⁶ D. Song, S. Zhao, Y. Luo, and H. Aziz, *Appl. Phys. Lett.* **97**, 243304 (2010).
- ¹³⁷ W. Staroske, M. Pfeiffer, K. Leo, and M. Hoffmann, *Phys. Rev. Lett.* **98**, 197402 (2007).
- ¹³⁸ C.-H. Hsiao, Y.-H. Chen, T.-C. Lin, C.-C. Hsiao, and J.-H. Lee, *Appl. Phys. Lett.* **89**, 163511 (2006).
- ¹³⁹ S.-J. Su, E. Gonmori, H. Sasabe, and J. Kido, *Adv. Mater.* **20**, 4189 (2008).
- ¹⁴⁰ U.S. Bhansali, H. Jia, M.A.Q. Lopez, B.E. Gnade, W.-H. Chen, and M.A. Omary, *Appl. Phys. Lett.* **94**, 203501 (2009).
- ¹⁴¹ M.C. Gather, M. Flammich, N. Danz, D. Michaelis, and K. Meerholz, *Appl. Phys. Lett.* **94**, 263301 (2009).
- ¹⁴² J. Kalinowski, L.C. Palilis, W.H. Kim, and Z.H. Kafafi, *J. Appl. Phys.* **94**, 7764 (2003).
- ¹⁴³ J. Lee, J.-I. Lee, K.-I. Song, S.J. Lee, and H.Y. Chu, *Appl. Phys. Lett.* **92**, 133304 (2008).
- ¹⁴⁴ S.L.M. van Mensfoort, M. Carvelli, M. Megens, D. Wehenkel, M. Bartyzel, H. Greiner, R.A.J. Janssen, and R. Coehoorn, *Nat Photon* **4**, 329 (2010).
- ¹⁴⁵ N. Chopra, J. Lee, Y. Zheng, S.-H. Eom, J. Xue, and F. So, *ACS Appl. Mater. Interfaces* **1**, 1169 (2009).
- ¹⁴⁶ W.H. Choi, C.H. Cheung, and S.K. So, *Org. Electron.* **11**, 872 (2010).
- ¹⁴⁷ C. Weichsel, L. Burtone, S. Reineke, S.I. Hintschich, M.C. Gather, K. Leo, and B. Lüssem, *Phys. Rev. B* **86**, 075204 (2012).
- ¹⁴⁸ J. Staudigel, M. Stossel, F. Steuber, and J. Simmerer, *J. Appl. Phys.* **86**, 3895 (1999).
- ¹⁴⁹ F. Neumann, Y.A. Genenko, R. Schmechel, and H. von Seggern, *Synth. Met.* **150**, 291 (2005).
- ¹⁵⁰ G.G. Malliaras and J.C. Scott, *J. Appl. Phys.* **85**, 7426 (1999).
- ¹⁵¹ R. Coehoorn and S.L.M. van Mensfoort, *Phys. Rev. B* **80**, 085302 (2009).
- ¹⁵² S. Noh, C.K. Suman, Y. Hong, and C. Lee, *J. Appl. Phys.* **105**, 033709 (2009).
- ¹⁵³ J. Partee, E.L. Frankevich, B. Uhlhorn, J. Shinar, Y. Ding, and T.J. Barton, *Phys. Rev. Lett.* **82**, 3673 (1999).
- ¹⁵⁴ D. Yokoyama, Y. Park, B. Kim, S. Kim, Y.-J. Pu, J. Kido, and J. Park, *Appl. Phys. Lett.* **99**, (2011).
- ¹⁵⁵ Z.D. Popovic and H. Aziz, *J. Appl. Phys.* **98**, (2005).
- ¹⁵⁶ D.Y. Kondakov, *J. Appl. Phys.* **102**, (2007).
- ¹⁵⁷ D.Y. Kondakov, T.D. Pawlik, T.K. Hatwar, and J.P. Spindler, *J. Appl. Phys.* **106**, (2009).

- ¹⁵⁸ H. Uoyama, K. Goushi, K. Shizu, H. Nomura, and C. Adachi, *Nature* **492**, 234 (2012).
- ¹⁵⁹ A. Endo, K. Sato, K. Yoshimura, T. Kai, A. Kawada, H. Miyazaki, and C. Adachi, *Appl. Phys. Lett.* **98**, (2011).
- ¹⁶⁰ K. Masui, H. Nakanotani, and C. Adachi, *Org. Electron.* **14**, 2721 (2013).
- ¹⁶¹ M.-T. Lee, J.-S. Lin, M.-T. Chu, and M.-R. Tseng, *Appl. Phys. Lett.* **94**, 083506 (2009).
- ¹⁶² K.T. Kamtekar, A.P. Monkman, and M.R. Bryce, *Adv. Mater.* **22**, 572 (2010).
- ¹⁶³ P. Wellmann, M. Hofmann, O. Zeika, A. Werner, J. Birnstock, R. Meerheim, G. He, K. Walzer, M. Pfeiffer, and K. Leo, *J. Soc. Inf. Disp.* **13**, 393 (2005).
- ¹⁶⁴ M.C. Gather, S. Köber, S. Heun, and K. Meerholz, *J. Appl. Phys.* **106**, (2009).
- ¹⁶⁵ R. Meerheim, S. Scholz, S. Olthof, G. Schwartz, S. Reineke, K. Walzer, and K. Leo, *J. Appl. Phys.* **104**, (2008).
- ¹⁶⁶ M.A. Lampert and P. Marks, *Current Injection in Solids* (Academic Press Inc, 1970).
- ¹⁶⁷ N.C. Erickson and R.J. Holmes, *Adv. Funct. Mater.* **23**, 5190 (2013).
- ¹⁶⁸ J. Kalinowski, J. Mężyk, F. Meinardi, R. Tubino, M. Cocchi, and D. Virgili, *J. Appl. Phys.* **98**, (2005).
- ¹⁶⁹ Y.H. Kim, J. Lee, W.M. Kim, C. Fuchs, S. Hofmann, H.-W. Chang, M.C. Gather, L. Müller-Meskamp, and K. Leo, *Adv. Funct. Mater.* n/a (2013).
- ¹⁷⁰ L.A.A. Pettersson, L.S. Roman, and O. Inganäs, *J. Appl. Phys.* **86**, 487 (1999).
- ¹⁷¹ H. Benisty, R. Stanley, and M. Mayer, *J Opt Soc Am A* **15**, 1192 (1998).
- ¹⁷² K.A. Neyts, *J Opt Soc Am A* **15**, 962 (1998).
- ¹⁷³ S. Mladenovski, S. Hofmann, S. Reineke, L. Penninck, T. Verschueren, and K. Neyts, *J. Appl. Phys.* **109**, (2011).
- ¹⁷⁴ M. Furno, R. Meerheim, M. Thomschke, S. Hofmann, B. Lüssem, and K. Leo, in (2010), pp. 761716–761716–12.
- ¹⁷⁵ Z.B. Wang, M.G. Helander, X.F. Xu, D.P. Puzzo, J. Qiu, M.T. Greiner, and Z.H. Lu, *J. Appl. Phys.* **109**, (2011).
- ¹⁷⁶ B.W. D’Andrade, J. Brooks, V. Adamovich, M.E. Thompson, and S.R. Forrest, *Adv. Mater.* **14**, 1032 (2002).
- ¹⁷⁷ J. Han, L. Shen, X. Chen, and W. Fang, *J Mater Chem C* **1**, 4227 (2013).
- ¹⁷⁸ V. Adamovich, J. Brooks, A. Tamayo, A.M. Alexander, P.I. Djurovich, B.W. D’Andrade, C. Adachi, S.R. Forrest, and M.E. Thompson, *New J Chem* **26**, 1171 (2002).
- ¹⁷⁹ T. Fleetham, J. Ecton, Z. Wang, N. Bakken, and J. Li, *Adv. Mater.* **25**, 2573 (2013).
- ¹⁸⁰ B.W. D’Andrade and S.R. Forrest, *J. Appl. Phys.* **94**, 3101 (2003).
- ¹⁸¹ Y.-S. Tsai, S.-H. Wang, S.-Y. Chen, S.-Y. Su, and F.-S. Juang, 4th Int. Conf. Technol. Adv. Thin Films Surf. Coat. **517**, 5338 (2009).
- ¹⁸² S. Ie, J.-H. Kim, B.T. Bae, D.-H. Park, J.-W. Choi, and W.-K. Choi, *Proc. 1st Int. Conf. Microelectron. Plasma Technol. ICMAP 2008* **517**, 4015 (2009).
- ¹⁸³ V. Bulovic, *Chem Phys Lett* **287**, 455 (1998).
- ¹⁸⁴ V. Bulovic, R. Deshpande, M.E. Thompson, and S.R. Forrest, *Chem Phys Lett* **308**, 317 (1999).
- ¹⁸⁵ N. Grossiord, J.M. Kroon, R. Andriessen, and P.W.M. Blom, *Org. Electron.* **13**, 432 (2012).

- ¹⁸⁶ K.S. Yook, S.O. Jeon, C.W. Joo, and J.Y. Lee, Appl. Phys. Lett. **94**, (2009).
- ¹⁸⁷ E.M. Purcell, H.C. Torrey, and R.V. Pound, Phys. Rev. **69**, 37 (1946).
- ¹⁸⁸ F. Gourdon, M. Chakaroun, N. Fabre, J. Solard, E. Cambril, A.-M. Yacomotti, S. Bouchoule, A. Fischer, and A. Boudrioua, Appl. Phys. Lett. **100**, (2012).

Appendix

A: List of Publications, Presentations, and Patents

Publications:

- 1) **N.C. Erickson** and R.J. Holmes, "Highly efficient, single-layer organic light-emitting devices based on a graded-composition emissive layer," Appl. Phys. Lett. 97, 083308 (2010)
- 2) **N.C. Erickson** and R.J. Holmes, "Relating charge transport and performance in single-layer graded-composition organic light-emitting devices," J. Appl. Phys. 110, 084515 (2011)
- 3) D. Braga, **N.C. Erickson**, M. Renn, R.J. Holmes and C.D. Frisbie, "High transconductance organic thin film electrochemical transistors for driving low voltage red-green-blue active matrix organic light-emitting devices," Adv. Func. Mater., 22, 1623 (2012)
- 4) **N.C. Erickson** and R.J. Holmes "Investigating the role of emissive layer architecture on the exciton recombination zone in organic light-emitting devices," Adv. Func. Mater. 23, 5190 (2013)
- 5) **N.C. Erickson** and R. J. Holmes, "Engineering Efficiency Roll-Off in Organic Light-Emitting Devices," (2013) *In Preparation*
- 6) **N.C. Erickson**; S. N. Raman; J. S Hammond; and R. J. Holmes, "Probing the composition depth profile of organic light-emitting devices by gas-cluster ion beam sputtering and X-ray photoelectron spectroscopy," (2013) *In Preparation*

Presentations:

- 1) **Erickson, N.C.**; Holmes, R.J. "Single Layer Organic Light-Emitting Devices Based on a Graded Composition Emissive Layer," 2010, American Vacuum Society Annual Meeting, Albuquerque NM
- 2) **Erickson, N.C.**; Holmes, R.J., "Efficient, single-layer organic light-emitting devices based on a graded composition emissive layer," 2011, Materials Research Society (MRS) Spring Meeting, San Francisco CA

- 3) **Erickson, N.C.;** Holmes, R.J., "High-efficiency, single-layer RGB organic light-emitting devices based on a graded-composition emissive layer architecture," 2011, Industrial Partnership for Research in Interfacial and Materials Engineering (iPrime), Minneapolis MN
- 4) **Erickson, N.C.;** Holmes, R.J., "Experimental Determination of the Exciton Recombination Zone Width in Double- and Graded-Emissive Layer Organic Light-Emitting Devices," 2012, Materials Research Society (MRS) Spring Meeting, San Francisco CA
- 5) **Erickson, N.C.;** Holmes, R.J., "Engineering the spatial extent of exciton formation in organic light-emitting devices," 2012, Industrial Partnership for Research in Interfacial and Materials Engineering (iPrime), Minneapolis MN
- 6) **Erickson, N.C.;** Holmes, R.J., "The graded-composition emissive layer: a route to efficient, single-layer organic light-emitting devices," 2012, American Vacuum Society Annual MN Chapter Meeting, Minneapolis MN
- 7) **Erickson, N.C.;** Raman, S.; Bryan, S.; Holmes, R.J.; "Direct measurement of the composition profile in graded emissive layer organic light-emitting devices and its relation to device performance," 2013, SPIE Optics + Photonics, San Diego CA

Patents:

- 1) "Organic light emitting devices having graded emission regions," R.J. Holmes and **N.C. Erickson**, International Patent Application Number: 13/701,208

B: G-EML Electronic Simulation Code

The simulation of the electronic properties, including the spatial dependence of the electron and hole charge carrier densities, and their overlap (the NP product) was developed performed using the following code, developed using Wolfram Alpha's Mathematica.

```

a = 100;

100;

un=a .14□3x-1 ;

up=□(-3x) ;

LogPlot[{up,un},{x,0,1},PlotRange□{.0001,10}]

D[un,x]

D[up,x]

un/D[un,x]

up/D[up,x]

un/up

q=1.6 10-19;

v=.01;

kT=300 1.38 10-23;

sol=NDSolve[{

  V'[x]□-F[x],

  F'[x]□p[x]-n[x],

  -n[x]2+n[x] F[x] D[un,x]/un+F[x]n'[x]+kT/(q v) D[un,x]/un n'[x]+kT/(q v) n''[x]-n[x]
p[x] up/un□0,p[x]2+p[x] F[x] D[up,x]/up+F[x] p'[x]-kT/(q v) D[up,x]/up p'[x]-kT/(q v)
p''[x]+n[x] p[x] un/up□0,

  V[1]□0,
```

```

V[0]□1,
n[0]□0,
p[1]□0,
n[1]□.527,
p[0]□1},
{p[x],n[x],F[x],V[x]},{x,0,1}]
Integrate[Evaluate[n[x]/.sol],{x,0,1}]
Integrate[Evaluate[p[x]/.sol],{x,0,1}]
Plot[{Evaluate[p[x]/.sol],Evaluate[n[x]/.sol],Evaluate[F[x]/.sol],Evaluate[V[x]/.sol]},{x,
0,1}]
Plot[{Evaluate[n[x] p[x]/.sol]},{x,0,1}]

{0.423302}
{0.422972}
Pplot = Partition[Flatten[Table[{i/100., Integrate[Evaluate[p[x] /. sol], {x, .01 i, .01 (i +
1)}/.01], {i, 0, 99}]], 2];
ListPlot[Pplot]
Plot[Evaluate[p[x] /. sol], {x, 0, 1}]

Plist = Flatten[Table[Integrate[Evaluate[p[x] /. sol], {x, .01 i, .01 (i + 1)}/.01, {i, 0,
99}]]];
Export["P(x).txt", Plist]
"P(x).txt"
Nplot = Partition[Flatten[Table[{i/100., Integrate[Evaluate[n[x] /. sol], {x, .01 i, .01 (i +
1)}/.01], {i, 0, 99}]], 2];

```

```
ListPlot[Nplot]
```

```
Plot[Evaluate[n[x] /. sol], {x, 0, 1}]
```

```
Nlist = Flatten[Table[Integrate[Evaluate[n[x] /. sol], {x, .01 i, .01 (i + 1)}]/.01, {i, 0, 99}]];
```

```
Export["N(x).txt", Nlist]
```

```
ListPlot[Plist Nlist]
```

```
"P(x).txt"
```

```
"P(x).txt"
```

```
"N(x).txt"
```

C: Optical Simulation Code

Optical Field Simulation

The optical field simulations presented in Chapter 9 were performed using the code below. The code was developed for use in Wolfram Alpha's Mathematica.

Nick Erickson

University of Minnesota

Department of Electrical and Computer Engineering

Holmes Research Group

This program will calculate the optical electrical field (proportional to $|E|^2$) for a defined layer structure. Required data is complex index of refraction vs wavelength and layer thickness.

v.9.5

09/15/10

09/16/10

Added For loop to import data from tsv files on optical properties of the user-specified number of materials in the stack. Material information is stored in array "Materials"

Added For loop to ask user for each layer thickness

05/17/11

Added contour plot, integrated global constants into first import section.

The following imports material data (lambda vs n) for the user - specified number of materials, beginning with glass

```
(* Global Constants *)
```

```
h = 6.626 10^-34;(* Js *)
```

```
c = 3 10^8; (* m/s *)
```

```
(* set Air index and angle of incidence *)
```

```
\[Eta]0=1.0;
```

```
\[Phi]0=0;
```

```
number=Input["How many layers are there (include glass)?"];
```

```

Glass=InputString["Enter glass n file name (include .txt) "]
Initial=Import[Glass,"Table",Path-> {"H:\\desktop"}];
Materials={ { 1,Initial} };
For[i=2,i<= number,i++,

material=InputString["Enter next layer file name"];

mats=Import[material,"Table",Path->{ "H:\\desktop" }];

Materials=Append[Materials,{i,mats}];
];
ComplexGlass=InputString["Enter k file name (include .txt) "];
initialcomplex=Import[ComplexGlass,"Table",Path-> {"H:\\desktop" }];

Complexk={ { 1,initialcomplex} };
For[i=2,i<= number,i++,
kname=InputString["Enter next layer k file name"];
kfile=Import[kname,"Table",Path->{ "H:\\desktop" }];

Complexk=Append[Complexk,{i,kfile}];
];
Glassthickness=Input["What is the thickness of the first material (begin with glass)"];
Thicknesses=Glassthickness;
For[a=2,a<= number , a++,
thick=Input["What is the thickness of the next material?"];
Thicknesses=Append[{ Thicknesses},{thick}];
];
Thicknesses=Flatten[Thicknesses];
dummyvar=Flatten[Materials,1];
Points=Map[Length,dummyvar];
Points[[2]];
\\[Lambda]=Table[Materials[[1,2,b,1]],{b,1,Points[[2]]}];

(*\\[Eta]0 is refractive index of transparent ambient,\\[Phi]0 is angle of incidence*)
q[j_,Lindex_]:=Sqrt[n[[j,Lindex]]^2-\\[Eta]0^2 Sin[\\[Phi]0]^2];
(*Fresnel complex reflection and transmission coefficients for s-polarized (E-field
perpendicular to plane of incidence,TE waves) at interface jk*)
rsjk[j_,Lindex_]:= (q[j,Lindex] - q[(j+1),Lindex])/(q[j,Lindex]+q[(j+1),Lindex])

```



```

tsjk[j_,Lindex_]:= (2 q[j,Lindex])/(q[j,Lindex]+q[(j+1),Lindex])
(*Fresnel complex reflection and transmission coefficients for p-polarized (E-Field
parallel to the plane of incidence,TM waves) at interface jk *)
rpjk[j_,Lindex_]:= (-n[(j+1),Lindex]^2 q[j,Lindex]+n[j,Lindex]^2
q[(j+1),Lindex])/(n[(j+1),Lindex]^2 q[j,Lindex]+n[j,Lindex]^2 q[(j+1),Lindex])
tpjk[j_,Lindex_]:= (2 n[j,Lindex] n[(j+1),Lindex] q[j,Lindex])/(n[(j+1),Lindex]^2
q[j,Lindex]+n[j,Lindex]^2 q[(j+1),Lindex])

(*[Xi][j] d[j] is the layer phase thickness corresponding to the phase change the wave
experiences as it traverses layer j:*)
\[Xi][j_,Lindex_]:= (2 \[Pi])/(\[Lambda][[Lindex]] q[j,Lindex])
(*Interface matrix (matrix of refraction) for interface jk for p-polarized incident light:*)
Ipjk[j_,Lindex_]:= 1/tpjk[j,Lindex] (1 rpjk[j,Lindex]
rpjk[j,Lindex] 1

)
(*Interface matrix (matrix of refraction) for interface jk for s-polarized incident light:*)
Isjk[j_,Lindex_]:= 1/tsjk[j,Lindex] (1 rsjk[j,Lindex]
rsjk[j,Lindex] 1

)
(* Layer matrix (phase matrix) describing propagation through layer j *)
Lj[j_,Lindex_]:= (E^(-I \[Xi][j,Lindex] Thicknesses[[j]])) 0
0 E^(I \[Xi][j,Lindex] Thicknesses[[j]])

)
totalthick=Sum[Thicknesses[[i]],{i,1,Length[Thicknesses]}];
Length[\[Lambda]];

n={Table[(Materials[[1,2,b,2]]+I Complexk[[1,2,b,2]]),{b,1,Points[[2]]}]];

For[d=2,d<= number,d++,

n=Append[n,Table[Materials[[d,2,b,2]]+I Complexk[[d,2,b,2]],{b,1,Points[[2]]}]];
];

(* This is an alternate thickness input which does not require inputing optical constants *)
Glassthickness = Input["What is the thickness of the first material (begin with glass)"];

```

```

Thicknesses = Glassthickness;
For[a = 2, a <= number , a++,
  thick = Input["What is the thickness of the next material?"];
  Thicknesses = Append[{Thicknesses}, {thick}];

];
Thicknesses = Flatten[Thicknesses];
totalthick = Sum[Thicknesses[[i]], {i, 1, Length[Thicknesses]}];
Length[\\[Lambda]];
dummyvar = Flatten[Materials, 1];
Points = Map[Length, dummyvar];
Points[[2]];
Thicknesses = Flatten[Thicknesses]
totalthick = Sum[Thicknesses[[i]], {i, 1, Length[Thicknesses]}];
Length[\\[Lambda]];

dummyvar = Flatten[Materials, 1];
Points = Map[Length, dummyvar];
Points[[2]];

{0, 0, 150, 10, 10, 10, 10, 10, 10, 10, 10, 10, 100, 0}

For s-polarized light, calculate the system matrices, field and reflection

Timing[
Rglass=((1-n[[1]])/(1+n[[1]]))^2;
Tglass=(4 n[[1]])/(1+n[[1]])^2;

Rs={2};
Ts={3};
Ex={1};
For[l=1,l<= 451,l+=10,

  Ss=Isjk[1,l];

  For[f=2, f<= (Length[Thicknesses]-1), f++,
    Ss=Ss.Lj[f,l].Isjk[f,l];
  ];

```

```

Rs=Append[Rs,Re[Conjugate[Ss[[2,1]]/Ss[[1,1]]]*(Ss[[2,1]]/Ss[[1,1]])]];
Ts=Append[Ts,Re[Conjugate[1/Ss[[1,1]]]*(1/Ss[[1,1]])]];

For[m=2, m<= (Length[Thickesses]), m++,

    Sprime=Isjk[1,l];

    For[p=3,p<= m,p++,

        Sprime=Sprime.Lj[(p-1),l].Isjk[(p-1),l];

    ];

    Sdoubleprime= (1      0
0      1

);

    For[r=m,r<= (Length[Thickesses]-1),r++,
        Sdoubleprime=Sdoubleprime .Isjk[r,l]. Lj[(r+1),l];
    ];

    For[x=1,x<= Thickesses[[m]],x++,

        Ex=Append[Ex,
Ts[(((1-1)/10+2))]*((Sdoubleprime[[1,1]] E^(-I \[Xi][m,l] (Thickesses[[m]]-
x))+Sdoubleprime[[2,1]] E^(I \[Xi][m,l] (Thickesses[[m]]-
x)))/(Sprime[[1,1]]Sdoubleprime[[1,1]] E^(-I \[Xi][m,l] Thickesses[[m]])+Sprime[[1,2]]
Sdoubleprime[[2,1]] E^(I \[Xi][m,l] Thickesses[[m]])))]
];
];

];

Reflection=Table[(Rglass[[wave]]+Rs[((wave-1)/10+2]]-2 Rglass[[wave]]*Rs[((wave-
1)/10+2]])/(1-Rglass[[wave]]*Rs[((wave-1)/10+2]]),{ wave,1,450,10}];

Field={Table[Ex[[i]],{i,2,totalthick+1}]}];
For[in=1,in<451/10,in++,

```

```
Field=Append[Field,Table[Ex[[i+in*totalthick+1]],{i,1,totalthick}]];
];
]
```

Thicknesses

```
{0, 0, 90, 30, 90, 30, 90, 30, 90, 30, 0}
```

```
Lambda=Input["What wavelength?"];
```

```
ListPlot[Re[Conjugate[Field[[(Lambda-350)/10]]]*Field[[(Lambda-
350)/10]]],DataRange->{0,totalthick},PlotRange-> All,AxesOrigin->{0,0},GridLines-
->{ { Thicknesses[[2]],
Thicknesses[[3]]+Thicknesses[[2]],
Thicknesses[[2]]+Thicknesses[[3]]+Thicknesses[[4]],
Thicknesses[[2]]+Thicknesses[[3]]+Thicknesses[[4]]+Thicknesses[[5]],
Thicknesses[[2]]+Thicknesses[[3]]+Thicknesses[[4]]+Thicknesses[[5]]+Thicknesses[[6]]
,
Thicknesses[[2]]+Thicknesses[[3]]+Thicknesses[[4]]+Thicknesses[[5]]+Thicknesses[[6]]
+Thicknesses[[7]],
Thicknesses[[2]]+Thicknesses[[3]]+Thicknesses[[4]]+Thicknesses[[5]]+Thicknesses[[6]]
+Thicknesses[[7]]+Thicknesses[[8]],
Thicknesses[[2]]+Thicknesses[[3]]+Thicknesses[[4]]+Thicknesses[[5]]+Thicknesses[[6]]
+Thicknesses[[7]]+Thicknesses[[8]]+Thicknesses[[9]],
Thicknesses[[2]]+Thicknesses[[3]]+Thicknesses[[4]]+Thicknesses[[5]]+Thicknesses[[6]]
+Thicknesses[[7]]+Thicknesses[[8]]+Thicknesses[[9]]+Thicknesses[[10]],
Thicknesses[[2]]+Thicknesses[[3]]+Thicknesses[[4]]+Thicknesses[[5]]+Thicknesses[[6]]
+Thicknesses[[7]]+Thicknesses[[8]]+Thicknesses[[9]]+Thicknesses[[10]]+Thicknesses[[
11]],
Thicknesses[[2]]+Thicknesses[[3]]+Thicknesses[[4]]+Thicknesses[[5]]+Thicknesses[[6]]
+Thicknesses[[7]]+Thicknesses[[8]]+Thicknesses[[9]]+Thicknesses[[10]]+Thicknesses[[
11]]+Thicknesses[[12]],
Thicknesses[[2]]+Thicknesses[[3]]+Thicknesses[[4]]+Thicknesses[[5]]+Thicknesses[[6]]
+Thicknesses[[7]]+Thicknesses[[8]]+Thicknesses[[9]]+Thicknesses[[10]]+Thicknesses[[
11]]+Thicknesses[[12]]+Thicknesses[[13]],
Thicknesses[[2]]+Thicknesses[[3]]+Thicknesses[[4]]+Thicknesses[[5]]+Thicknesses[[6]]
+Thicknesses[[7]]+Thicknesses[[8]]+Thicknesses[[9]]+Thicknesses[[10]]+Thicknesses[[
11]]+Thicknesses[[12]]+Thicknesses[[13]]+Thicknesses[[14]],
```

```
Thicknesses[[2]]+Thicknesses[[3]]+Thicknesses[[4]]+Thicknesses[[5]]+Thicknesses[[6]]
+Thicknesses[[7]]+Thicknesses[[8]]+Thicknesses[[9]]+Thicknesses[[10]]+Thicknesses[[
11]]+Thicknesses[[12]]+Thicknesses[[13]]+Thicknesses[[14]]+Thicknesses[[15]]},{ } }
```

```
ListPlot[Re[Reflection],AxesOrigin->{0,0},Filling->Axis]
```

```
Sorted = Table[Table[{j*10 + 340, i, Re[Conjugate[Field[[j, i]]]*Field[[j, i]]]}, {i, 1,
totalthick}], {j, 1, Length[Field]}];
```

```
ListPointPlot3D[Flatten[Sorted, 1], PlotStyle -> PointSize[Tiny], Axes -> True,
PlotRange -> All, AxesLabel -> {"Wavelength", "Thickness", "Field"}]
```

```
ListContourPlot[Flatten[Sorted, 1], Contours -> 20]
```

For p-polarized light, calculate the system matrices, field and reflection

p-polarized simulation has discontinuities at interfaces

```
Timing[
```

```
RPglass=((1-n[[1]])/(1+n[[1]]))^2;
```

```
TPglass=(4 n[[1]])/(1+n[[1]])^2;
```

```
Rp={2};
```

```
Tp={3};
```

```
ExP={1};
```

```
For[lp=1,lp<= 451,lp+=10,
```

```
    Sp=Ipjk[1,lp];
```

```
        For[fp=2, fp<= (Length[Thicknesses]-1), fp++,
```

```
            Sp=Sp.Lj[fp,lp].Ipjk[fp,lp];
```

```
        ];
```

```
Rp=Append[Rp,Re[Conjugate[Sp[[2,1]]/Sp[[1,1]]*(Sp[[2,1]]/Sp[[1,1]])]];
Tp=Append[Tp,Re[Conjugate[1/Sp[[1,1]]*(1/Sp[[1,1]])]];

```

```
For[mp=2, mp<= (Length[Thicknesses]), mp++,
```

```
    SPprime=Ipjk[1,lp];
```

```
        For[pp=3,pp<= mp,pp++,
```

```

        SPprime=SPprime.Lj[(pp-1),lp].Ipjk[(pp-1),lp];
    ];

    SPdoubleprime= (1  0
0      1

);

    For[rp=mp,rp<= (Length[Thickesses]-1),rp++,
        SPdoubleprime=SPdoubleprime .Ipjk[rp,lp]. Lj[(rp+1),lp];
    ];

    For[xp=1,xp<= Thickesses[[mp]],xp++,
        ExP=Append[ExP,
        Tp[((lp-1)/10+2)]]*((SPdoubleprime[[1,1]] E^(-I \[Xi][mp,lp] (Thickesses[[mp]]-
xp))+SPdoubleprime[[2,1]] E^(I \[Xi][mp,lp] (Thickesses[[mp]]-
xp)))/(SPprime[[1,1]]SPdoubleprime[[1,1]] E^(-I \[Xi][mp,lp]
Thickesses[[mp]]))+SPprime[[1,2]] SPdoubleprime[[2,1]] E^(I \[Xi][mp,lp]
Thickesses[[mp]])))
    ];
    ];

    ];

    PReflection=Table[(RPglass[[wave]]+Rp[((wave-1)/10+2]]-2
RPglass[[wave]]*Rp[((wave-1)/10+2]])/(1-RPglass[[wave]]*Rp[((wave-
1)/10+2]]),{wave,1,450,10}];

    FieldP={Table[ExP[[i]],{i,2,totalthick+1}]}];
    For[inp=1,inp<451/10,inp++,
        FieldP=Append[FieldP,Table[ExP[[i+inp*totalthick+1]],{i,1,totalthick}]];
    ];
    ]

    LambdaP=Input["What wavelength?"];

```

```
ListPlot[Re[Conjugate[FieldP[((LambdaP-340)/10)]]]*FieldP[((LambdaP-
340)/10)]]],DataRange->{0,totalthick},PlotRange-> All,AxesOrigin->{0,0},GridLines-
>{ { Thicknesses[[2]],
Thicknesses[[3]]+Thicknesses[[2]],
+Thicknesses[[2]]+Thicknesses[[3]]+Thicknesses[[4]],
+Thicknesses[[2]]+Thicknesses[[3]]+Thicknesses[[4]]+Thicknesses[[5]]},{ } }
```

```
ListPlot[Re[Prefflection],AxesOrigin->{0,0}]
```

```
SortedP = Table[Table[{j*10 + 340, i, Re[Conjugate[FieldP[[j, i]]]*FieldP[[j, i]]}], {i, 1,
totalthick}], {j, 1, Length[FieldP]}];
ListPointPlot3D[Flatten[SortedP, 1], PlotStyle -> PointSize[Tiny], Axes -> True,
PlotRange -> All, AxesLabel -> {"Wavelength", "Thickness", "Field"}]
```

Optical Emission and Outcoupling Simulation

The optical emission and outcoupling efficiency simulations presented in Chapter 10 were performed using the code below, developed in Wolfram Alpha's Mathematica.

```
Glassthickness = Input["What is the thickness of the first material (begin with glass)"];
```

```
Thicknesses = Glassthickness;
```

```
For[a = 2, a <= number, a++, _thick = Input["What is the thickness of the next material?"]; _
```

```
Thicknesses = Append[{Thicknesses}, {thick}];
```

```
_];
```

```
Thicknesses = Flatten[Thicknesses]; _
```

```
dummyvar = Flatten[Materials, 1];
```

```
Points = Map[Length, dummyvar];
```

```
Points[[2]];
```

```
□ = Table[Materials[[1, 2, b, 1]], {b, 1, Points[[2]]}]; _
```

```
totalthick = Sum[Thicknesses[[i]], {i, 1, Length[Thicknesses]}];
```

```
Length[□];
```

```
(* The following asks for the PL spectrum of the emitter (in 1nm steps from 350-800nm *) _
```

```
plshape = InputString["Enter the normalized PL lineshape file name"];
```

```
PL = Import[plshape, "Table", Path -> { "H:\desktop" }];
```

```
(* This initializes the n array with glass n & k, the loop adds the other materials *) _
```

```
n = {Table[(Materials[[1, 2, b, 2]] + I Complexk[[1, 2, b, 2]]), {b, 1, Points[[2]]}]; _
```

```
For[d = 2, d <= number, d++, _n = Append[n, Table[Materials[[d, 2, b, 2]] + I
```

```
Complexk[[d, 2, b, 2]], {b, 1, Points[[2]]}]]];
```

```
];
```

```
Thicknesses
```

```
{0, 0, 120, 10, 10, 10, 10, 10, 10, 10, 10, 100, 0}
```

This Subsection defines all system functions called in the loops

```
(* Global Constants *)
```

```
(* □0 is refractive index of transparent ambient, □0 is angle of incidence*)
```

```
□0=1.0;
```

```
h = 6.626 10-34; (* Js *) \.01
```

```
c = 3 108; (* m/s *)
```

$$q[j_ , Lindex_ , \square_] := \sqrt{n[j_ , Lindex_]^2 - \square0^2 \sin\left[\frac{t}{180}\right]^2};$$


```

(*Fresnel complex reflection and transmission coefficients for s-polarized (E-field
perpendicular to plane of incidence,TE waves) at interface jk*)
rsjk[j_,Lindex_,□_]:= (q[j,Lindex,□] -
q[(j+1),Lindex,□])/(q[j,Lindex,□]+q[(j+1),Lindex,□])
tsjk[j_,Lindex_,□_]:= (2 q[j,Lindex,□])/(q[j,Lindex,□]+q[(j+1),Lindex,□])
(*Fresnel complex reflection and transmission coefficients for p-polarized (E-Field
parallel to the plane of incidence,TM waves) at interface jk *)
rpjk[j_,Lindex_,□_]:= (-n[(j+1),Lindex]^2 q[j,Lindex,□]+n[j,Lindex]^2
q[(j+1),Lindex,□])/(n[(j+1),Lindex]^2 q[j,Lindex,□]+n[j,Lindex]^2 q[(j+1),Lindex,□])
tpjk[j_,Lindex_,□_]:= (2 n[j,Lindex] n[(j+1),Lindex]
q[j,Lindex,□])/(n[(j+1),Lindex]^2 q[j,Lindex,□]+n[j,Lindex]^2 q[(j+1),Lindex,□])

(*□[j] d[j] is the layer phase thickness corresponding to the phase change the wave
experiences as it traverses layer j:*)
□[j_,Lindex_,□_]:= (2 □)/□[[Lindex]] q[j,Lindex,□]
(*Interface matrix (matrix of refraction) for interface jk for p-polarized incident light:*)
Ipjk[j_,Lindex_,□_]:= 1/tpjk[j,Lindex,□] ( {
  {1, rpjk[j,Lindex,□]},
  {rpjk[j,Lindex,□], 1}
})
(*Interface matrix (matrix of refraction) for interface jk for s-polarized incident light:*)
Isjk[j_,Lindex_,□_]:= 1/tsjk[j,Lindex,□] ( {
  {1, rsjk[j,Lindex,□]},
  {rsjk[j,Lindex,□], 1}
})
(* Layer matrix (phase matrix) describing propagation through layer j *)
Lj[j_,Lindex_,□_]:= ( {
  {□-□ □[j,Lindex,□] Thicknesses[[j]], 0},
  {0, □ □[j,Lindex,□] Thicknesses[[j]]}
})

The following imports material data (lambda vs n) for the user-specified number of
materials, beginning with glass
number = Input["How many layers are there (include glass)?"];
Glass = InputString["Enter glass n file name (include .txt) "];_
Initial = Import[Glass, "Table", Path -> {"H:\\desktop"}];

Materials = { {1, Initial} };

```

```

For[i = 2, i <= number, i++, _
  material = InputString["Enter next layer file name"];_
  mats = Import[material, "Table", Path -> { "H:\\desktop" }];_
  Materials = Append[Materials, {i, mats}];
];

ComplexGlass = InputString["Enter k file name (include .txt) "];

initialcomplex = Import[ComplexGlass, "Table", Path -> { "H:\\desktop" }];

Complexk = {{1, initialcomplex}};
For[i = 2, i <= number, i++, _

  kname = InputString["Enter next layer k file name"];
  kfile = Import[kname, "Table", Path -> { "H:\\desktop" }];
  Complexk = Append[Complexk, {i, kfile}];
];
Glassthickness = Input["What is the thickness of the first material (begin with glass)"];
Thicknesses = Glassthickness;

For[a = 2, a <= number , a++, _thick = Input["What is the thickness of the next
material?"];_
  Thicknesses = Append[{Thicknesses}, {thick}];
  _];
Thicknesses = Flatten[Thicknesses];_
dummyvar = Flatten[Materials, 1];
Points = Map[Length, dummyvar];
Points[[2]];
□ = Table[Materials[[1, 2, b, 1]], {b, 1, Points[[2]]}];_
totalthick = Sum[Thicknesses[[i]], {i, 1, Length[Thicknesses]}];
Length[□];
(* The following asks for the PL spectrum of the emitter (in 1nm steps from 350-800nm
*)_
plshape = InputString["Enter the normalized PL lineshape file name"];
PL = Import[plshape, "Table", Path -> { "H:\\desktop" }];
(* This initializes the n array with glass n & k, the loop adds the other materials *)_
n = {Table[(Materials[[1, 2, b, 2]] + I Complexk[[1, 2, b, 2]]), {b, 1, Points[[2]]}];_

```

```

For[d = 2, d <= number, d++,_n = Append[n, Table[Materials[[d, 2, b, 2]] + I
Complexk[[d, 2, b, 2]], {b, 1, Points[[2]]}]];
];

```

(* This is an alternate thickness input which does not require inputting optical constants *)

For s-polarized light, calculate the system matrices and field

```

Clear[□,ASvp,AShp,ASvm,AShm]
ASvp[Lindex_,□_]:=0;
AShp[Lindex_,□_]:=√ $\frac{3}{16^l}$  *PL[[Lindex,2]];
ASvm[Lindex_,□_]:=0;
AShm[Lindex_,□_]:=√ $\frac{3}{16^l}$  *PL[[Lindex,2]];
Timing[
  SSL = {1};
  SSR = {1};
  For[Lindex = 1, Lindex < 451, Lindex++,
    SSSL = {{1, 1}, {1, 1}};
    SSSR = {{1, 1}, {1, 1}};
    For[□ = -89, □ <= 89, □++,
      SSSL = Append[SSSL,
        Isjk[1, Lindex, □].Lj[2, Lindex, □].Isjk[2, Lindex, □].Lj[3, Lindex, □].Isjk[3,
        Lindex, □].Lj[4, Lindex, □].Isjk[4, Lindex, □].Lj[5, Lindex, □].Isjk[5, Lindex, □].Lj[6,
        Lindex, □].Isjk[6, Lindex, □].Lj[7, Lindex, □]];

      SSSR = Append[SSSR,
        Isjk[7, Lindex, □].Lj[8, Lindex, □].Isjk[8, Lindex, □].Lj[9, Lindex, □].Isjk[9,
        Lindex, □].Lj[10, Lindex, □].Isjk[10, Lindex, □].Lj[11, Lindex, □].Isjk[11, Lindex,
        □].Lj[12, Lindex, □].Isjk[12, Lindex, □].Lj[13, Lindex, □].Isjk[13, Lindex, □].Lj[14,
        Lindex, □]];
    ];
  SSL = Append[SSL, SSSL];
  SSR = Append[SSR, SSSR];
];
]
{390.782505, Null}
Timing[

```

```

E0Svm = {1};
For[j = 3, j < 182, j++,
  E0Svm2 = {1};
  For[l = 2, l < 452, l++, E0Svm2 = Append[E0Svm2, (SSR[[l, j, 2, 1]]*ASvp[l - 1, j - 2]
- SSR[[l, j, 1, 1]]*ASvm[l - 1, j - 2])/(SSL[[l, j, 2, 2]]*SSR[[l, j, 1, 1]] - SSR[[l, j, 2,
1]]*SSL[[l, j, 1, 2]])];
  ];
  E0Svm = Append[E0Svm, E0Svm2];
];

E0Shm = {1};
For[j = 3, j < 182, j++,
  E0Shm2 = {1};
  For[l = 2, l < 452, l++,
    E0Shm2 = Append[E0Shm2, (SSR[[l, j, 2, 1]]*AShp[l - 1, j - 2] - SSR[[l, j, 1,
1]]*AShm[l - 1, j - 2])/(SSL[[l, j, 2, 2]]*SSR[[l, j, 1, 1]] - SSR[[l, j, 2, 1]]*SSL[[l, j, 1,
2]])];
  ];
  E0Shm = Append[E0Shm, E0Shm2];
];
]

{15.350498, Null}
Timing[
  Field = E0S = Table[Table[.5*Conjugate[E0Svm[[i, j]]]*E0Svm[[i, j]] +
.5*Conjugate[E0Shm[[i, j]]]*E0Shm[[i, j]], {i, 2, 180}], {j, 2, 451}];
]
{0.514803, Null}
Field[[180, 90]]
AShp[180, 90]
0.0271067 + 0. I
0.208721
SumField = Table[Sum[Field[[i, l]], {i, 1, 450}], {l, 1, 179}];
SumFieldL = Table[Sum[Field[[i, l]], {l, 1, 179}], {i, 1, 450}];
ListPlot[Re[SumField]]
ListPlot[Re[SumField], PlotRange -> All]
ListPlot[Re[SumFieldL]]
ListPlot[Re[SumFieldL], PlotRange -> All]

```

For p-polarized light, calculate the system matrices and field

$$APvp[Lindex_ , \square_] := \sqrt{\frac{3}{8^l} \sin\left|\left|\frac{l}{2} - 89\right|, \frac{l}{180}\right|^2} * PL[[Lindex, 2]];$$

$$APhp[Lindex_ , \square_] := \sqrt{\frac{3}{16^l} \cos\left|\left|\frac{l}{2} - 89\right|, \frac{l}{180}\right|^2} * PL[[Lindex, 2]];$$

$$APvm[Lindex_ , \square_] := -\sqrt{\frac{3}{8^l} \sin\left|\left|\frac{l}{2} - 89\right|, \frac{l}{180}\right|^2} * PL[[Lindex, 2]];$$

$$APhm[Lindex_ , \square_] := -\sqrt{\frac{3}{16^l} \cos\left|\left|\frac{l}{2} - 89\right|, \frac{l}{180}\right|^2} * PL[[Lindex, 2]];$$

Timing[

PSL = {1};

PSR = {1};

For[Lindex = 1, Lindex < 451, Lindex++,

PSSL = {{1, 1}, {1, 1}};

PSSR = {{1, 1}, {1, 1}};

For[\square = -89, \square < 90, \square++,

PSSL = Append[PSSL,

Ipjk[1, Lindex, \square].Lj[2, Lindex, \square].Ipjk[2, Lindex, \square].Lj[3, Lindex, \square].Ipjk[3,

Lindex, \square].Lj[4, Lindex, \square].Ipjk[4, Lindex, \square].Lj[5, Lindex, \square].Ipjk[5, Lindex, \square].Lj[6,

Lindex, \square].Ipjk[6, Lindex, \square].Lj[7, Lindex, \square]];

PSSR = Append[PSSR,

Ipjk[7, Lindex, \square].Lj[8, Lindex, \square].Ipjk[8, Lindex, \square].Lj[9, Lindex, \square].Ipjk[9,

Lindex, \square].Lj[10, Lindex, \square].Ipjk[10, Lindex, \square].Lj[11, Lindex, \square].Ipjk[11, Lindex,

\square].Lj[12, Lindex, \square].Ipjk[12, Lindex, \square].Lj[13, Lindex, \square].Ipjk[13, Lindex, \square].Lj[14,

Lindex, \square]];

];

PSL = Append[PSL, PSSL];

PSR = Append[PSR, PSSR];

];

]

{421.655103, Null}

Timing[

EOPvm = {1};

For[j = 3, j < 182, j++,

EOPvm2 = {1};

```

For[l = 2, l < 452, l++, E0Pvm2 = Append[E0Pvm2, (PSR[[l, j, 2, 1]]*APvp[l - 1, j - 2]
- PSR[[l, j, 1, 1]]*APvm[l - 1, j - 2])/(PSL[[l, j, 2, 2]]*PSR[[l, j, 1, 1]] - PSR[[l, j, 2,
1]]*PSL[[l, j, 1, 2]])];
];
E0Pvm = Append[E0Pvm, E0Pvm2];
];

E0Phm = {1};
For[j = 3, j < 182, j++,
E0Phm2 = {1};
For[l = 2, l < 452, l++,
E0Phm2 = Append[E0Phm2, (PSR[[l, j, 2, 1]]*APhp[l - 1, j - 2] - PSR[[l, j, 1,
1]]*APhm[l - 1, j - 2])/(PSL[[l, j, 2, 2]]*PSR[[l, j, 1, 1]] - PSR[[l, j, 2, 1]]*PSL[[l, j, 1,
2]])];
];
E0Phm = Append[E0Phm, E0Phm2];
];
]
{61.979197, Null}
Timing[
FieldP = E0P = Table[Table[.5*Conjugate[E0Pvm[[i, j]]]*E0Pvm[[i, j]] +
.5*Conjugate[E0Phm[[i, j]]]*E0Phm[[i, j]], {i, 2, 180}], {j, 2, 451}];

SumFieldP = Table[Sum[FieldP[[i, l]], {i, 1, 450}], {l, 1, 179}];
SumFieldLP = Table[Sum[FieldP[[i, l]], {l, 1, 179}], {i, 1, 450}];
]
{10.873270, Null}
ListPlot[Re[SumFieldP]]
ListPlot[Re[SumFieldP], PlotRange -> All]
ListPlot[Re[SumFieldLP]]
ListPlot[Re[SumFieldLP], PlotRange -> All]
This Section puts the S and P simulations together
(* Total field versus wavelength *)
TotalFieldAngle = Table[.5*SumFieldP[[i]] + .5*SumField[[i]], {i, 1, 179}];
(* Total Field versus Angle *)
TotalFieldWave = Table[.5*SumFieldL[[i]] + .5*SumFieldLP[[i]], {i, 1, 450}];
ListPlot[Re[TotalFieldWave]]
ListPlot[Re[TotalFieldWave], PlotRange -> All]

```

```

ListPlot[Re[TotalFieldAngle]]
ListPlot[Re[TotalFieldAngle], PlotRange -> All];

Sum[Re[TotalFieldAngle[[i]]], {i, 1, 179}]
Sum[Re[TotalFieldWave[[i]]], {i, 1, 450}]
288.597
288.597
Angle=Table[{i*0.0174533,
  Re[TotalFieldAngle[[i]]],{i,1,179}}];
ListPolarPlot[{Angle,1.7*Table[Cos[(90-x) °/180 ],{x,0,360}]]}
Output = Table[Angle[[i, 2]], {i, 1, 179}];
WaveOutput = Table[Re[TotalFieldWave[[i]]], {i, 1, 450}];
Angle2=Table[{i*0.0174533,
  Re[TotalFieldAngle[[i]]*(°3 Cos[((i-90)*°)/180]2)/(Mean[Abs[n[[5]]]]3-°2
  Mean[Abs[n[[5]]]] Sin[((i-90)*°)/180]2)},{i,1,179}];
a2=Max/@Transpose[Angle2];
AnglePlot2=Table[{i*0.0174533,Angle2[[i,2]]/a2[[2]]},{i,1,179}];
ListPolarPlot[{Table[Cos[(90-x) °/180 ],{x,0,360}],AnglePlot2}]
Export["angle.txt", Output]
Export["wave.txt", WaveOutput]
"angle.txt"
"wave.txt"
CorAngle=Table[
  Re[TotalFieldAngle[[i]]*(°3 Cos[((i-90)*°)/180]2)/(Mean[Abs[n[[5]]]]3-°2
  Mean[Abs[n[[5]]]] Sin[((i-90)*°)/180]2)},{i,1,179}];
Export["CorAngle.txt", CorAngle]
"CorAngle.txt"
ListPlot[WaveOutput]
indexedPL = Table[PL[[i, 2]], {i, 1, 451}];
ListPlot[{indexedPL, Re[TotalFieldWave]/Re[Max[TotalFieldWave]]}, PlotRange ->
All]
SourceP=Table[Sum[Re[APhp[l,a]2+APvp[l,a]2],{a,0,360}],{l,1,451}];
Sum[SourceP[[i]],{i,1,451}]
SourceS=Table[Sum[Re[AShp[l,a]2+ASvp[l,a]2],{a,0,360}],{l,1,451}];
Sum[SourceS[[i]],{i,1,451}]
1535.28
1022.58
Sum[SumFieldLP[[i]], {i, 1, 450}]

```

Sum[SumFieldL[[i]], {i, 1, 450}]

Outcoupling = Re[(Sum[SumFieldLP[[i]], {i, 1, 450}] + Sum[SumFieldL[[i]], {i, 450}])/(Sum[SourceP[[i]], {i, 1, 451}] + Sum[SourceS[[i]], {i, 1, 451}])]

403.162 + 0. I

174.032 + 0. I

0.225656

D: Copyright Notices

Applied Physics Letters:

AIP PUBLISHING LLC LICENSE

TERMS AND CONDITIONS

Nov 12, 2013

All payments must be made in full to CCC. For payment instructions, please see information listed at the bottom of this form.

License Number 3266671423036

Order Date Nov 12, 2013

Publisher AIP Publishing LLC

Publication Applied Physics Letters

Article Title Highly efficient, single-layer organic light-emitting devices based on a graded-composition emissive layer

Author Nicholas C. Erickson, Russell J. Holmes

Online Publication Date Aug 27, 2010

Volume number 97

Issue number 8

Type of Use Thesis/Dissertation

Requestor type Author (original article)

Format Print and electronic

Portion Excerpt (> 800 words)

Will you be translating? No

Title of your thesis / dissertation

On the Design and Properties of Organic Light Emitting Devices

Expected completion date Jan 2014

Estimated size (number of pages) 180

Total 0.00 USD

Terms and Conditions

AIP Publishing LLC -- Terms and Conditions: Permissions Uses

AIP Publishing LLC ("AIPP") hereby grants to you the non-exclusive right and license to use and/or distribute the Material according to the use specified in your order, on a one-time basis, for the specified term, with a maximum distribution equal to the number that you have ordered. Any links or other content accompanying the Material are not the subject of this license.

Journal of Applied Physics

AIP PUBLISHING LLC LICENSE

TERMS AND CONDITIONS

Nov 12, 2013

All payments must be made in full to CCC. For payment instructions, please see information listed at the bottom of this form.

License Number 3266680185258

Order Date Nov 12, 2013

Publisher AIP Publishing LLC

Publication Journal of Applied Physics

Article Title Relating charge transport and performance in single-layer graded composition organic light-emitting devices

Author Nicholas C. Erickson, Russell J. Holmes

Online Publication Date Oct 31, 2011

Volume number 110

Issue number 8

Type of Use Thesis/Dissertation

Requestor type Author (original article)

Format Print and electronic

Portion Excerpt (> 800 words)

Will you be translating? No

Title of your thesis / dissertation

On the Design and Properties of Organic Light Emitting Devices

Expected completion date Jan 2014

Estimated size (number of pages) 180

Total 0.00 USD

Terms and Conditions

AIP Publishing LLC -- Terms and Conditions: Permissions Uses AIP Publishing LLC ("AIPP") hereby grants to you the non-exclusive right and license to use and/or distribute the Material according to the use specified in your order, on a one-time basis, for the specified term, with a maximum distribution equal to the number that you have ordered. Any links or other content accompanying the Material are not the subject of this license.

Advanced Functional Materials:

JOHN WILEY AND SONS LICENSE

TERMS AND CONDITIONS

Nov 12, 2013

This is a License Agreement between Nicholas C Erickson ("You") and John Wiley and Sons

("John Wiley and Sons") provided by Copyright Clearance Center ("CCC"). The license consists of your order details, the terms and conditions provided by John Wiley and Sons, and the payment terms and conditions. All payments must be made in full to CCC. For payment instructions, please see information listed at the bottom of this form.

License Number 3266680649617

License date Nov 12, 2013

Licensed content publisher John Wiley and Sons

Licensed content publication Advanced Functional Materials

Licensed content title High-Transconductance Organic Thin-Film Electrochemical Transistors for Driving Low-Voltage Red-Green-Blue Active Matrix Organic Light-Emitting Devices

Licensed copyright line Copyright © 2012 WILEY-VCH Verlag GmbH & Co. KGaA, Weinheim

Licensed content author Daniele Braga, Nicholas C. Erickson, Michael J. Renn, Russell J. Holmes, C. Daniel Frisbie

Licensed content date Feb 14, 2012

Start page 1623

End page 1631

Type of use Dissertation/Thesis

Requestor type Author of this Wiley article

Format Print and electronic

Portion Full article

Will you be translating? No

Total 0.00 USD

Terms and Conditions

TERMS AND CONDITIONS

This copyrighted material is owned by or exclusively licensed to John Wiley & Sons, Inc. or one of its group companies (each a "Wiley Company") or a society for whom a Wiley Company has exclusive publishing rights in relation to a particular journal (collectively "WILEY"). By clicking "accept" in connection with completing this licensing transaction, you agree that the following terms and conditions apply to this transaction (along with the billing and payment terms and conditions established by the Copyright Clearance Center/ Inc., ("CCC's Billing and Payment terms and conditions"), at the time that you opened your Rights Link account (these are available at any time at <http://myaccount.copyright.com>). Rights link Printable License

JOHN WILEY AND SONS LICENSE

TERMS AND CONDITIONS

Nov 12, 2013

This is a License Agreement between Nicholas C Erickson ("You") and John Wiley and Sons ("John Wiley and Sons") provided by Copyright Clearance Center ("CCC"). The license consists of your order details, the terms and conditions provided by John Wiley and Sons, and the payment terms and conditions.

All payments must be made in full to CCC. For payment instructions, please see information listed at the bottom of this form.

License Number 3266671022250

License date Nov 12, 2013

Licensed content publisher John Wiley and Sons

Licensed content publication Advanced Functional Materials

Licensed content title Investigating the Role of Emissive Layer Architecture on the Exciton

Recombination Zone in Organic Light-Emitting Devices

Licensed copyright line Copyright © 2013 WILEY-VCH Verlag GmbH & Co. KGaA, Weinheim

Licensed content author Nicholas C. Erickson, Russell J. Holmes

Licensed content date Apr 19, 2013

Start page 5190

End page 5198

Type of use Dissertation/Thesis

Requestor type Author of this Wiley article

Format Print and electronic

Portion Full article

Will you be translating? No

Total 0.00 USD

TERMS AND CONDITIONS

This copyrighted material is owned by or exclusively licensed to John Wiley & Sons, Inc. or one of its group companies (each a "Wiley Company") or a society for whom a Wiley Company has exclusive publishing rights in relation to a particular journal (collectively "WILEY"). By clicking "accept" in connection with completing this licensing transaction, you agree that the following terms and conditions apply to this transaction (along with the

Appendix

billing and payment terms and conditions established by the Copyright Clearance Center Inc., ("CCC's Billing and Payment terms and conditions"), at the time that you opened your Rights Link account (these are available at any time at <http://myaccount.copyright.com>).